UNIVERSITAT DE BARCELONA

Interface Engineering in Mixed Ionic Electronic Conductor Thin Films for Solid State Devices

Francesco Maria Chiabrera

Tesis doctoral

Interface Engineering in Mixed Ionic Electronic Conductor Thin Films for Solid State Devices

Autor

Francesco Maria Chiabrera

Directores

Albert Tarancón Rubio y Iñigo Garbayo Senosiain

UNIVERSITAT DE BARCELONA

Interface Engineering in Mixed Ionic Electronic Conductor Thin Films for Solid State Devices

Memoria presentada para optar al grado de doctor por la

Universidad de Barcelona

Programa de Doctorado en Nanociencias

Autor:

Francesco Maria Chiabrera

Directores:

Albert Tarancón Rubio y Iñigo Garbayo Senosiain

Tutor:

Joan Ramón Morante Lleonart

Institut de Recerca en Energia de Catalunya (IREC)

UNIVERSITAT DE BARCELONA

El Dr. Albert Tarancón Rubio y el Dr. Iñigo Garbayo, investigadores del Instituto de Investigación en Energía de Cataluña (IREC), CERTIFICAN:

Que la memoria titulada **Interface Engineering in Mixed Ionic Electronic Conductor Thin Films for Solid State Devices** presentada por Francesco Maria Chiabrera para optar al grado de Doctor en el Programa de Nanociencias de la Universitat de Barcelona ha sido realizada bajo su dirección en el Instituto de Investigación en Energía de Cataluña (IREC).

Barcelona, marzo de 2019

Dr. Albert Tarancón Rubio

Dr. Iñigo Garbayo Senosiain

Acknowledgments

Many different people contributed to this thesis and made possible finishing this long journey. First, I want to thank my thesis directors Albert and Iñigo for all the support that they provided me in these years. Albert, thank you for the opportunity you gave me the day you offered me a PhD, for the assistance you have always offered me every time I needed help, for the enthusiasm you showed when I had a new idea and for making the Nanoionic group a *creative* place to work. Iñigo, thank you for all the help you gave me every day, for all our discussions that made our work a funny and exciting experience, for your patience when I came up with "esta es la clave!" at 6:30 pm and for all the important suggestions without which I couldn't have finished this thesis.

I would like also to thank all the people that contribute to this thesis offering me help with the different experimental techniques present in this work. Monica and Dolors, thank you for offered me the possibility of performing some exciting experiments at the Synchrotron of Grenoble. Thanks to Nini Pryds and Simone Sanna for hosting me during my external stay at DTU. Thanks to Santi for helping me to understanding the reciprocal space maps. Thanks to Francesca Peiró, Luis Lopez, Sonia Estradé and Marc for the wonderful TEM experiments. A special thanks to Alex, who introduced me to many of the different techniques of this work and offered me his help every time I had some problem during these years.

Without doubt, my PhD journey was a wonderful experience also thanks to all my colleagues at IREC. Thanks for enduring my papers discussions every Monday morning, for all the fun we had at the calçotadas, at the paellas and at the Cangrejos (not so much at the Beach volleys). Thanks to Nerea, Marco and Iñigo, for making pleasant our work together. To all my PhD colleagues, Elba, Simone, Marco, Gerard, José, Arianna, Valerie, Yunquing, Hemesh thank you for sharing your experiences during these years together. Marc T., Alex, Marc N., Mercé, Aitor, Lucile, Miguel, Aneta, thank you for supporting me and for offering me advices when I needed. Grazie a Federico, per il suo costante aiuto sul lavoro, per i suoi consigli davanti ai vermut e per le discussioni su Bob e Laura.

Grazie a Elena, per tutto quello che abbiamo condiviso, senza il quale questo viaggio non sarebbe stato cosí piacevole. Grazie ai miei genitori, a cui devo tutto quello che sono diventato e tutto quello che saró.

Abstract

Advanced energy conversion and storage devices, such as batteries, solar-to-fuel converters, fuel cells and supercapacitors, as well as novel solid state electrochemical information storage and logic devices, such are resistive switching memories, are largely based on Mixed Ionic-Electronic Conductors (MIECs) perovskite oxides. The optimization and engineering of MIEC materials for each specific application was classically tackled by the selection of the metal transition element and/or by doping it with aliovalent atoms. However, in the last years a new enthralling approach to tailor functional properties in these perovskite oxides has emerged, based on the use of interface-dominated oxides such as nanocrystalline thin films. In this direction, it has been recently proved that grain boundaries (GBs) in the perovskite $La_{1-x}Sr_xMnO_{3\pm\delta}$ (manganite) deeply impact its functional properties, boosting the oxygen mass transport while abating the electronic and magnetic order. The impact of grain boundaries in manganite nanocrystalline thin films is so relevant that these can radically change the behaviour of the material, transforming an electronic conductor into a functional MIEC for redox-based solid state devices. Based on these preliminary studies, it became crucial to understand the origin of this enhancement, in order to gain engineering capabilities and potentially extend it to other functional perovskite materials.

Following this approach, this thesis focuses in analysing the remarkable properties of GBs in manganites and, ultimately, investigating the possibility of engineering these interfaces. The thesis develops through three different parts: (i.) structural and compositional characterization of grain and GBs in $La_{0.8}Sr_{0.2}MnO_{3\pm\delta}$ (LSM) thin films; (ii.) effect of GBs on functional properties of LSM thin films; (iii.) effect of B-site Co substitution on the bulk and GBs functional properties of $La_{0.8}Sr_{0.2}Mn_{1-y}Co_yO_{3\pm\delta}$ (LSMC) thin films.

First, the structural and chemical characterization of the LSM thin films deposited by pulsed laser deposition (PLD) is presented. The compositional analysis of the layers revealed a severe Mn deficiency, ascribed to the plasma-background interactions during the deposition. Transmission Electron Microscopy (TEM) and Electron Energy Loss Spectroscopy (EELS) analysis of the GBs of these Mn-deficient thin films revealed a remarkable local modification of both anionic and cationic composition in the vicinity of the strained regions. In detail, a significant Mn and O depletion along with a La and Sr enrichment was observed (*viz.* GB_{def}). Then, through a PLD combinatorial approach, LSM films with progressively increasing Mn content were deposited, altering the overall cationic ratio on the thin films (Mn/(La+Sr)). The variation of cationic chemical potential on the thin films was observed to significantly affect the GB composition, which passed from Mn depletion/La-enrichment (GB_{def}) to Mn enrichment/La-depletion (*viz.* GB_{rich}) when surpassing a certain overall Mn content. Meanwhile, the O deficiency character of the GBs was maintained. This behaviour suggests that, through the tuning of the overall cationic concentration in the thin films, the GB composition can be

altered, offering an innovative way for engineering the chemical defects of strained interfaces.

The effect of these different interfaces on the electrical conductivity and the oxygen mass transport properties of LSM thin films was then investigated. In the *in-plane* electrical measurements, the effect of GBs was analysed by comparing polycrystalline LSM films with a set of epitaxial LSM thin films prepared under similar deposition conditions and thus expected to behave similarly to the grain bulk of the polycrystalline films. The *out-of-plane* high temperature electrochemical properties of LSM thin films with variable Mn content was studied by electrochemical impedance spectroscopy as a function of temperature and oxygen partial pressure, using YSZ (001) single crystals as substrate for deposition and subsequently as active electrolyte for the measurement.

It was found that in the layers characterized by GB_{def}, the lack of Mn hinders the low temperature metal insulator transition. Instead, a variable range hopping mechanism occurs, where electrons tunnels across the GBs for reaching distant Mn atoms. Remarkably, in these films n-type behaviour was found in the high temperature pO_2 experiments, indicating that the complex defect distribution found strongly affects the equilibration mechanism. Also, a simultaneous decrease of activation energies of both GB oxygen diffusivity and GB oxygen surface exchange coefficient was observed when lowering the Mn concentrations in the films, indicating a strong interdependence between these two phenomena. Moreover, the constant oxygen partial pressure dependence of the GB diffusivity, together with the direct TEM observation of oxygen deficiency in the GBs, suggest that the GB accumulation of oxygen vacancies is at the origin of the large improvement of both oxygen mass transport parameters observed in LSM polycrystalline thin films.

On the contrary, in the LSM thin films characterized by GB_{rich}, the low temperature metallic behaviour is restored and an increase of electronic conductivity is observed in the entire temperature range. Also, in the paramagnetic state the increase of Mn atoms originate an interesting increase of the pre-exponential factor, which can be explained by the increase of Mn sites in the GBs available for the polaron hopping. Finally, a p-type pO_2 trend was measured in these films, similar to the one expected from the bulk defect chemistry model. In these layers, the variation of Mn does not give rise to a variation of the oxygen diffusivity, meaning that the GBs oxygen vacancy concentration is not altered anymore. Overall, the results demonstrate the possibility of engineering the functional properties of LSM polycrystalline thin films by modifying the GB cationic composition.

In the third part of the thesis, the effect of Co substitution on LSMC functional properties was investigated. The LSMC thin films were produce by combinatorial PLD, which allow a direct measure of a real-continuous composition spread LSMC system. The oxygen mass transport properties of bulk and GB were evaluated by finite element model (FEM) fitting of O^{18} exchange profiles. The results revealed that GBs enhance

the transport properties of the whole material in the range of compositions under study, although for high Co concentration the GB effect is already concealed by the high bulk diffusion.

Finally, as appendixes of the thesis, two further studies on the electrochemical properties of complementary oxide thin films able to operate as an electrolyte (BICUVOX) and electrode (photoactivated LSF) at low temperature are presented. The first one deals with the deposition and characterization of BICUVOX thin films as electrolyte for low temperature micro Solid Oxide Fuel Cells (μSOFC). The results showed that by a proper selection of PLD parameters, high quality BICUVOX thin films can be deposited, characterized by outstanding oxygen ion conductivity at low temperature and a good electrochemical stability. The second appendix presents an *in-situ* ellipsometry study of the intermediate temperature oxygen partial pressure behaviour in $La_{0.8}Sr_{0.2}FeO_{3-\delta}$. The results disclosed that this technique can be used for tracking the point defect concentration evolution of oxide thin films.

Resumen

Hoy en día, buena parte de los dispositivos avanzados de conversión y almacenamiento de energía, como baterías, convertidores de energía solar a combustible, pilas de combustible y supercapacitores, así como nuevos sistemas electroquímicos de almacenamiento de información y dispositivos lógicos, tales como memorias de resistive switching, están basados en gran medida en óxidos tipo perovskita conductores mixtos iónicos y electrónicos (MIEC, por sus siglas en inglés). Tradicionalmente, la optimización de estos materiales MIEC para cada aplicación específica se abordaba desde la selección de los metales de transición que componen el óxido perovskita, o bien desde el dopaje del mismo óxido con elementos aliovalentes. Sin embargo, en los últimos años está emergiendo una nueva estrategia muy prometedora para moldear las propiedades de las perovskitas según su uso, basado en la fabricación de óxidos en los que sus propiedades funcionales están dominadas por las intercaras (por ejemplo, en capas delgadas nanocristalinas). En este sentido, se ha probado recientemente que los bordes de grano en la perovskita $La_{1-x}Sr_xMnO_{3\pm\delta}$ (manganita) pueden modificar profundamente las propiedades del material, potenciando el transporte de oxígeno y minimizando el orden electrónico y magnético. El impacto de los bordes de grano en capas delgadas de manganita nanocristalina es tan relevante que es posible cambiar completamente el comportamiento del material, transformando un buen conductor electrónico en un MIEC, con aplicación en dispositivos sólidos basados en reacciones redox. En este contexto, es crucial entender el origen de estos cambios, con el fin de poder moldear las propiedades del material en función de la aplicación, así como potencialmente extender este efecto a otros materiales funcionales.

Siguiendo esta idea, esta tesis se enfoca en el análisis de los bordes de grano en manganitas y en el estudio de sus propiedades excepcionales para, finalmente, tratar de manipular estas intercaras y así moldear las propiedades del material. La tesis se estructura de la siguiente manera: (i.) caracterización estructural y composicional del grano y borde de grano en capas delgadas de $La_{0.8}Sr_{0.2}MnO_{3\pm\delta}$ (LSM); (ii.) efecto de los bordes de grano en las propiedades funcionales de capas delgadas de LSM; (iii.) efecto de la sustitución de Mn por Co en las propiedades del grano y borde de grano, en capas delgadas de $La_{0.8}Sr_{0.2}Mn_{1-y}Co_yO_{3\pm\delta}$ (LSMC).

En primer lugar, se presenta la caracterización estructural y química de capas delgadas de LSM depositadas por la técnica de depósito por laser pulsado (PLD, de sus siglas en inglés). El análisis composicional de las capas reveló una deficiencia severa de Mn, relacionada con interacciones plasma-ambiente durante el depósito. El análisis de los bordes de grano en estas capas delgadas deficientes en Mn, estudiado por microscopía electrónica de transmisión (TEM) y por espectroscopía electrónica de pérdida de energía (EELS) reveló una alteración importante de la composición aniónica y catiónica alrededor de las regiones con mayor estrés. En concreto, se observó una disminución de Mn y O y un aumento de La y Sr en el borde de grano. Posteriormente, usando la

técnica de deposición combinatoria por PLD, se fabricaron capas delgadas de LSM con contenido de Mn variable, de forma que se alteraba progresivamente el ratio Mn/(La+Sr). Se observó que el cambio en el potencial químico catiónico en las capas afecta significativamente a la composición del borde de grano, pasando éste de presentar deficiencia en Mn y enriquecimiento en La (GB_{def}) a presentar enriquecimiento en Mn y deficiencia en La (GB_{rich}), al sobrepasar un cierto nivel de contenido en Mn. Al mismo tiempo, el carácter deficiente en oxígeno de los bordes de grano se mantiene inalterado. Según los resultados obtenidos, es posible alterar la composición del borde de grano mediante la modificación de la concentración de cationes en las capas delgadas, ofreciendo una forma innovadora para moldear los defectos químicos de estas intercaras.

En la segunda parte de la tesis, se estudia el efecto de estas intercaras de composición variable en la conductividad eléctrica y las propiedades de transporte de oxígeno, en capas delgadas de LSM. Por un lado, el efecto de los bordes de grano en las medidas eléctricas *en plano* se estudia comparando capas de LSM policristalinas con un set de capas delgadas epitaxiales de LSM preparadas en condiciones de depósito similares, por lo que se espera un comportamiento similar al de los granos en las capas policristalinas. Por otro lado, las propiedades electroquímicas de capas delgadas de LSM a alta temperatura, medidas *a través del plano*, se estudian por espectroscopía de impedancias electroquímica, en función de la temperatura y de la presión parcial de oxígeno. Para estas medidas, se utilizan monocristales de YSZ (001) como sustrato para el depósito de LSM y posteriormente como electrolito activo durante las medidas de impedancia.

En las capas caracterizadas por GB_{def}, se descubrió que la falta de Mn imposibilita la transición metal-aislante a baja temperatura. Por el contrario, estas capas presentan un mecanismo de conducción basado en saltos de rango variable, según el cual los electrones tienen que atravesar los bordes de grano por efecto túnel, para alcanzar átomos de Mn más distantes. Es interesante remarcar que estas capas presentan un comportamiento tipo n, según los experimentos *vs.* pO_2 a alta temperatura. Esto parece indicar que la compleja distribución de defectos que se encontró en estos bordes de grano afecta el mecanismo de equilibrio químico. Así mismo, se observó un descenso simultáneo de las energías de activación para la difusión de oxígeno y el coeficiente de intercambio superficial de oxígeno en el borde de grano, lo cual revela una fuerte interdependencia entre estos dos fenómenos. Además, la dependencia de la difusión en el borde de grano con la presión parcial de oxígeno, sumado a la observación directa por TEM de la deficiencia de oxígeno en el borde de grano, sugiere que la acumulación de vacantes de oxígeno en el borde de grano se encuentra en el origen de la gran mejora en las propiedades de transporte de oxígeno en las capas policristalinas de LSM.

En capas delgadas de LSM caracterizadas por GB_{rich}, el comportamiento metálico a baja temperatura se recupera, a la vez que se observa un incremento de la conductividad electrónica en todo el rango de temperaturas estudiado. Además, en el estado paramagnético del LSM, el incremento de átomos de Mn origina un interesante

incremento del factor pre-exponencial, lo cual puede explicarse por el aumento en el borde de grano de Mn disponibles para saltos polarónicos. Finalmente, en estas capas se midió un comportamiento tipo p frente a la pO_2, similar a lo que se esperaría según el modelo de química de defectos del material. Igualmente, la variación de Mn no conlleva una variación de la difusión de oxígeno, lo que conlleva que la concentración de vacantes de oxígeno en el borde de grano ya no se ve afectada por el contenido de Mn. En definitiva, este estudio demuestra la posibilidad de moldear las propiedades funcionales de capas delgadas policristalinas de LSM mediante la modificación de la composición catiónica en el borde de grano.

En la tercera parte de la tesis, se estudia el efecto de la sustitución de Mn por Co en las propiedades funcionales del material LSMC. Las capas delgadas de LSMC se depositaron por PLD combinatorio, lo cual permitió medir directamente un único sistema LSMC con una distribución continua de composiciones. Las propiedades de transporte de oxígeno en el grano y en el borde de grano se evaluaron por medio de un ajuste de los perfiles de intercambio de O^{18} con un modelo de elementos finitos. Los resultados del estudio revelaron que los bordes de grano mejoran las propiedades de transporte del material en el rango de concentraciones de Co estudiado, aunque para altos contenidos de Co el efecto del borde de grano queda enmascarado por la alta difusión de oxígeno del propio grano.

Dos estudios adicionales se presentan como apéndices en esta tesis. El primero se centra en el depósito de capas delgadas de BICUVOX y su caracterización como electrolito de baja temperatura para micro pilas de combustible de óxido sólido (μSOFC, por sus siglas en inglés). Este estudio demuestra que, seleccionando unas condiciones de depósito adecuadas para el PLD, se pueden obtener capas de BICUVOX de alta calidad, que se caracterizan por una alta conductividad iónica a baja temperatura y buena estabilidad electroquímica. El segundo estudio recoge un estudio *in-situ* de elipsometría, enfocado en el comportamiento frente a la presión parcial de oxígeno a temperaturas intermedias del $La_{0.8}Sr_{0.2}FeO_{3-\delta}$. Los resultados muestran que esta técnica puede utilizarse para estudiar la evolución de la concentración de defectos puntuales en capas delgadas de óxidos funcionales.

Index

List of acronyms

3PB	Triple phase boundaries
ADF	Annular Dark Field Detector
AFM	Atomic Force Microscopy
b	Bulk
BUCUVOX	$Bi_4V_{1.8}Cu_{0.2}O_{10.7}$
CCS	Continuous Composition Spread
CMR	Colossal Magnetoresistance
C-PLD	Combinatorial Pulsed Laser Deposition
CSL	Coincidence Site Lattice method
CTEM	Convectional Transmission Electron Microscopy
CVD	Chemical Vapour Deposition
DFT	Density Functional Theory
EDS	Energy Dispersive X-ray Spectroscopy
EELS	Electron Energy Loss Spectroscopy
EIS	Electrochemical Impedance Spectroscopy
FEM	Finite Element Method
FeRAM	Ferroelectric Random-Access Memories
FFT	Fast Fourier transform
GB	Grain Boundary
HAADF	High Angle Annular Dark Field Detector
HRTEM	High Resolution Transmission Electron Microscopy
IEDP	Isotope Exchange Depth Profiling
IR	Infrared
JT	Jahn-Teller
LA-PLD	Large Area Pulsed Laser Deposition
LMO	$LaMnO_{3\pm\delta}$
LSC	$La_{0.8}Sr_{0.2}MnO_{3\pm\delta}$
LSF	$La_{0.8}Sr_{0.2}FeO_{3-\delta}$
LSM	$La_{1-x}Sr_xMnO_{3\pm\delta}$
$LSM_{0.85}$	$La_{0.8}Sr_{0.2}Mn_{0.85}O_{3\pm\delta}$
LSMC	$La_{0.8}Sr_{0.2}(Mn_{1-y}Co_y)_{0.85}O_{3\pm\delta}$
LSM_y	$La_{0.8}Sr_{0.2}Mn_yO_{3\pm\delta}$
MBE	Molecular beam Epitaxy
MIEC	Mixed Ionic Electronic Conductor
MRAM	Magnetoreristive Random-Access Memories
M-VRH	Mott Variable Range Hopping
NGO	$NdGaO_3$
NNH	Nearest Neighbour Hopping
ORR	Oxygen Reduction Reactions
pc	Pseudo-cubic

PLD	Pulsed Laser Deposition
PVD	Physical Vapour Deposition
RAM	Random-Access Memories
ReRAM	Resistive Random-Access Memories
rms	Mean square roughness
SEM	Scanning Electron Microscopy
SE-VRH	Shklovskii–Efros Variable Range Hopping
SIMS	Secondary Ion Mass Spectroscopy
SOFC	Solid Oxides Fuel Cells
STEM	Scanning Transmission Electron Microscopy
STO	$SrTiO_3$
TEM	Transmission Electron Microscopy
ToF	Time of Flight
UV	Ultra-Violet
VAN	Vertical Aligned Nanocomposite
VRH	Variable Range Hopping
WDS	Wavelength Dispersive Spectroscopy
XANES	X-ray Absorption Near-Edge Structure
XRD	X-ray Diffraction
YSZ	Yttria stabilized Zirconia
μSOFC	micro Solid Oxides Fuel Cells

1. Introduction

1.1 Motivation*

There is a growing interest in the development of functional metal oxides with mixed ionic electronic conduction for their application in different strategic fields. In particular, ionic transport-related phenomena are of primary importance in energy transformation and storage devices, such as solid oxides fuel cells (SOFC) or batteries. Traditionally, the main issue that hindered a wide spread of solid state electrochemical devices is the slow ionic conduction and the sluggish Oxygen Reduction Reactions (ORR) related with the oxygen incorporation in oxides.

In these materials, the poor ionic motion, mainly related to the low mobility of the ionic charge carriers and their mechanical and coulombic interactions with their host crystal structures, imposes operating at high temperatures, which is incompatible with some applications such as portable electronics. The conductivity of a charged species in a solid solution is proportional to the product of its concentration c_i and its mobility u_i ($\sigma_i \propto c_i \cdot u_i$). Typically, the ionic conductivity in oxides has been controlled by doping them with aliovalent cations, which naturally creates charged defects to maintain the electroneutrality, or by trying to stabilize high-conductive crystallographic phases in polymorphic materials. Nonetheless, limitations came across in terms of materials instability, reactivity and defect interactions when trying to implement and operate these ionic conductors in real devices.

A different strategy for the enhancement of the ionic conductivity in a material is based on the use of nanoionics effects, which take place when reducing the dimensions to the nanoscale.[1–3] In interface-dominated materials, like thin films, both the concentration of charge carriers c_i and the mobility μ_i can be modified. Engineering nanostructures allow tuning these two parameters, to maximize their impact on the ionic conduction.[4,5] Moreover, interfaces in interface-dominated materials can also be used to enhance other mass transport phenomena, such as, for instance, the Oxygen Reduction Reaction (ORR) capabilities of a cathode for solid oxide fuel cells[6,7] or the redox reversibility of a material employed in resistive switching.[8]

In this chapter, the most significant nanoionics effects involving interfaces and to explore their effect on ionic-related phenomena will be described. In section **1.2**, the applications and characteristics of perovskite based oxides are reviewed, particularly focusing on the effect of point defects on their functional properties. Then, in section **1.3** the grain boundary (GB) composition and effects commonly found in oxides are described. Finally, the scope of this thesis is presented.

* This introduction is adapted from "Nanoionics and interfaces for energy and information technologies" Chiabrera, F., Garbayo, I. & Tarancón, A. in *Metal Oxide-Based Thin Film Structures* 409–439 (Elsevier, 2018) with the permission of Elsevier.[1]

1.2 Perovskite oxides: structure, applications and impact of the point defects

1.2.1 The structure of a perovskite oxide

Perovskite metal oxide materials are a family of compounds that share the same type of crystal structure of the archetypal $CaTiO_3$.[9] The general formula of perovskites is ABO_3, where A^{n+} is a large radius cation, $B^{(6-n)+}$ is a small radius cation and O^{2-} is the oxide anion. In this structure, the charge n of the cation can assume different values, *e.g.* n= 1, 2, 3. The ideal cubic structure of a perovskite is shown in **Figure 1.1**. The B-site cations are surrounded by six oxygen atoms, forming an octahedron, whereas the A-site ions have 12 oxygen atoms in the direct proximity.

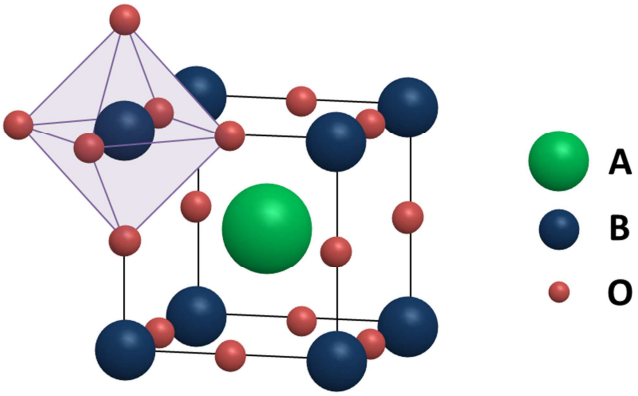

Figure 1.1 Structure of the cubic perovskite ABO_3

Although some perovskites effectively show the cubic structure, most of them present different types of structural distortions, which lower the symmetry of the system. The stability of a perovskite compound can be predicted by the Goldschmidt factor (t), defined as:

$$t = \frac{r_A + r_O}{\sqrt{2}(r_B + r_O)} \qquad \text{Eq. 1.1}$$

Where r_A, r_B, r_O are the ionic radii of A, B and O ions respectively. A Goldschmidt factor equal to one denotes the ideal cubic lattice, whereas for values approximately between 0.8 and 1.1 structural distortions tend to appear (i.e. orthorhombic and rhombohedral structures). For values of Goldschmidt factor larger than 1.1 or smaller than 0.8, other structures are likely to stabilize, since the relative difference between cations radii impedes the stabilization of the perovskite phase.

It was demonstrated that the majority of elements of the periodic table can form a perovskite compound, either occupying the A or the B site of the structure.[9] This flexibility in the choice of the metal cations has raised a large interest in the perovskite family, mainly because of the different physical properties that can be designed. For

example, perovskite metal oxides can display: ferromagnetic properties, piezoelectricity, superconductivity, catalytic properties, high ion conductivity and many others. Furthermore, the substitution of A and/or B ions with other cations offer an additional degree of freedom in modifying the physical properties of perovskite materials. In this thesis, the perovskite materials $La_{1-x}B_xMO_{3\pm\delta}$ are studied, where B sands for a divalent alkaline ion and M is a transition metal such as Mn, Co or Fe. In the following, some examples of strategic applications of $La_{1-x}B_xMO_{3\pm\delta}$ perovskite directly related with this thesis are commented.

1.2.2 Applications of $La_{1-x}B_xMO_{3\pm\delta}$ perovskite oxides

1.2.2.1 Solid Oxide Fuel Cells (SOFC)

One of the most relevant applications of these oxides is in Solid Oxide Fuel Cells (SOFC). SOFCs are among the most efficient devices for the conversion of chemical fuel into electrical power. The three main components of a SOFC are: the anode, the electrolyte and the cathode. In the SOFC cathode, the gaseous oxygen is reduced and incorporated into the electrolyte as oxide ion. The electrolyte is a pure oxygen-ion conducting material, which allows oxygen ions to move from the cathode to the anode side due to the difference in chemical potential. At the anode side, the oxide ions react with the gaseous fuel (for instance H_2), generating water, heat and electrons, which can be used to produce electrical power.

Perovskite materials have found application as anode, cathode, electrolyte and interconnectors in SOFC.[9,10] The large development of this family of oxides directly derives from the possibility of tailoring their electronic, ionic, structural and chemical characteristics, allowing designing materials suited for each specific SOFC component. In particular, many efforts have been devoted to the development of perovskite mixed ionic electronic conductors (MIECs) for cathode electrodes. Indeed, the cathode was identified to be the limiting component in SOFCs operating in an intermediate temperature range, as required for a broad deployment of the technology.[11,12]

At first, precious metals (*i.e.* Pt, Ag) were used as cathode materials in SOFC, due to their high electrochemical properties and despite their limiting oxygen reduction reaction (ORR) sites (restricted to the triple phase boundaries, 3PBs, the points in which gaseous oxygen (gas phase), electrons (metal) and oxygen ions (electrolyte) encounter). In order to increase the 3PB length and to reduce the cathodic polarization resistance, the use of composites made by an electronic conductor and an ionic one were proposed. Several composites based on the combination of a precious metal and a ceramic ionic conductor were studied, but replacing the metals by pure electronic conducting perovskites meant a leap on the performance of the cathodes by gaining chemical and mechanical stability and compatibility with other components of the cell. Among the various composites studied, $La_{1-x}Sr_xMnO_{3\pm\delta}$ /Yttria stabilized Zirconia (YSZ) was

selected as the best candidate and still remains as one of the most common choices for the cathode in SOFCs.[13]

The use of perovskite MIECs represents another important strategy for increasing the electrochemically active area for oxygen incorporation in the cathodes. Indeed, the high oxygen diffusion of these compounds allows enlarging the electrochemical active area to, ideally, the entire electrode material, which determines a substantial decrease of the electrochemical resistance associated to the oxygen reactions. In this sense, perovskite materials such as $La_{1-x}Sr_xFeO_{3-\delta}$ and $La_{1-x}Sr_xCoO_{3-\delta}$ were found to present both electronic and ionic conduction under typical SOFC operating conditions and excellent ORR properties. Nevertheless, the integration of these compounds in SOFC systems was not straightforward, due to a poor chemical stability and a thermal expansion mismatch with the other components.[14] One possible solution proposed to overcome this problem is doping the B-site of the MIECs with other transition metal (such as Mn), which partially reduce their electrochemical properties but enhances the compatibility with the entire system. Alternatively, the use of cation diffusion barrier layers based on ceria was suggested to avoid insulating phase typically produced at the electrolyte-electrode interface.

Beyond the classical SOFC, the miniaturization of this technology for portable power sources represents an innovative application of perovskite materials in thin film form. The so called micro-SOFC (μSOFC) is a technology that has the potential to meet the growing demand of modern portable electronics, not sustainable by current Li-ion batteries.[15–18] μSOFCs are based on the use of thin films as main functional component (cathode, anode, electrolyte), integrated into Si technology[19] (see **Figure 1.2**) or porous substrates.[20] The use of electrolyte thin films of hundreds of nanometres allows to substantially decrease the operation temperature (down to 400 ºC using state-of-the-art YSZ[21]). Despite representing a breakthrough compared to the traditional operating temperature of SOFC, at this temperature, standard thin film metallic electrodes undergo severe structural degradation with time, hindering a broad deployment of μSOFC technology. Opposed to that, thin film perovskite electrodes present much better chemomechanical stability, thus representing a promising solution for the development of intermediate temperature μSOFC. However, their electrochemical properties still need to be significantly improved in this temperature range.[19,22]

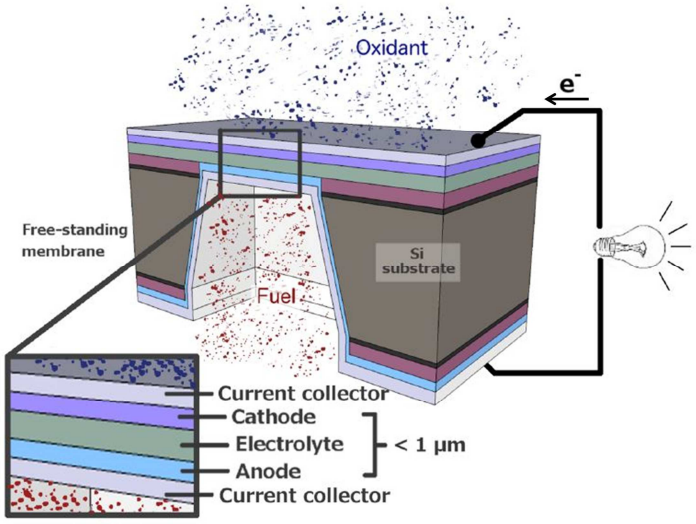

Figure 1.2 Sketch of a µSOFC integrated in Si technology reproduced from Garbayo's doctoral thesis.[23]

1.2.2.2 Non-volatile random-access memories

Non-volatile random-access memories (RAM) are a form of computer data storage that does not require constant power for retrieving information. The different types of non-volatile RAM are generally classified by the physical mechanism involved in the data storage, *viz.* ferroelectric RAM (FeRAM), mangetoresistive RAM (MRAM) and resistive RAM (ReRAM). Perovskite-based compounds find application in all these types of memories, due to their different physical and chemical properties. Here, the use of $La_{1-x}B_xMO_{3\pm\delta}$ family in MRAM and ReRAM is briefly discussed.

In MRAM, the data are stored by magnetic tunnel junctions, that varies their resistance through the application of a magnetic field.[24] In this type of memory, $La_{1-x}B_xMnO_{3\pm\delta}$ perovskites (*e.g.* manganites) may find a perfect application of their colossal negative magnetoresistance (CMR). CMR is an intrinsic property of manganites that involves a large decrease of resistivity when a magnetic field is applied near the Curie temperature (T_c).[25] The origin of this phenomenon is related to the delocalization of electrons naturally occurring in the ferromagnetic phase ($T < T_c$), which give rise to a metallic behaviour and a decrease of resistivity in the material.[26,27] By forcing a magnetic field when $T > T_c$, the electronic spins tends to align along one direction, promoting the delocalization of electrons and giving rise to the negative CMR. Unfortunately, this phenomenon requires large magnetic fields (up to several teslas), hindering the practical employment in real devices. Nevertheless, promising results have been recently obtained across disordered interfaces (*i.e.* polycrystalline thin films,[28] artificial grain boundaries,[29] micro bridges,[30] etc.), where considerably lower magnetic fields are necessary to influence the resistivity.[31]

In ReRAM, the data storage is based on the variation of resistance taking place in some oxides upon the application of electric fields (called resistive switching). One of the major advantages of ReRAM technology is the possibility of using thin films with a

simple capacitor-like structure (metal-oxide-metal), which allows a facile scalability of the system (see **Figure 1.3**).[32] Since the discovery of resistive switching phenomena in $Pr_{0.7}Ca_{0.3}MnO_3$,[33] perovskite oxides have been largely investigated as possible ReRAM materials. Many different resistive switching mechanisms have been proposed in literature. In the particular case of manganites, the two main phenomena that can give rise to a variation of resistance upon the application of an electric field are the filamentary and the interface switching.[34,35] In the former, a conductive filament is formed when a large potential is applied across a thin film, giving rise to a decrease of the electronic resistance through it. By applying an electric field with opposite polarity, the filament breaks and the low resistance state is restored. On the contrary, the interface pathway involves a valence variation of the surface material's atoms, due to the migration of oxygen ions, the trapping of charge carriers or other phenomena related to the equilibrium of point defects in the material. For further details on the switching mechanisms proposed for perovskites, the interested reader may refer to the reviews from Waser *et al.*[36,37]

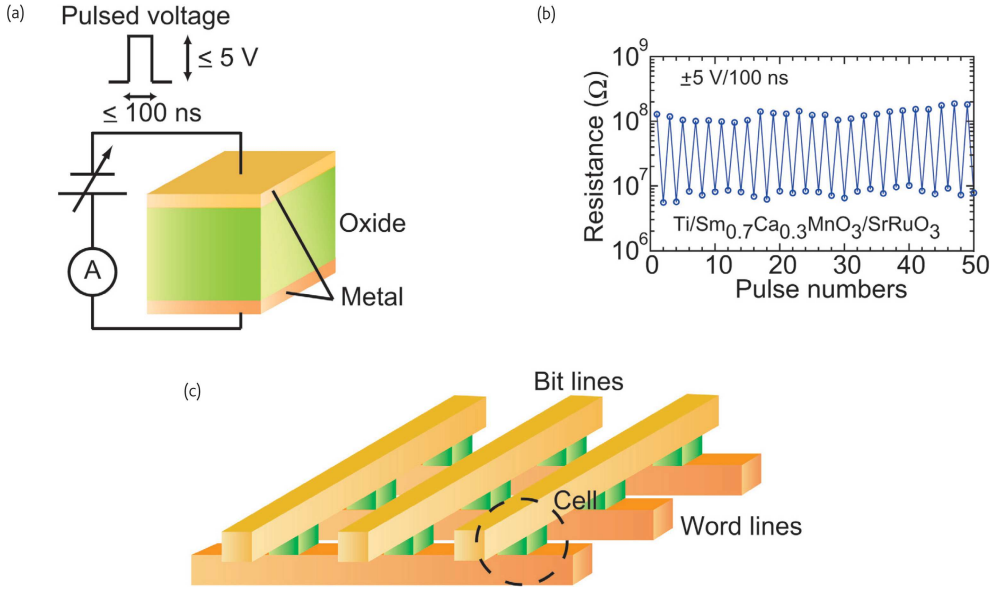

Figure 1.3 a, Sketch of a ReRAM memory cell where an oxide layer is inserted between two metal electrodes. **b**, Example of resistive switching behaviour of a $Ti/Sm_{0.7}Ca_{0.3}MnO_3/SrRuO_3$ cell at room temperature. **c**, Illustration of a highly scalable "cross-point" ReRAM memory. The word and bit lines can be used for selecting one memory cell and write on it. Reprinted from "*Resistive switching in rapid advances in information technology rely on high-speed and large-capacity nonvolatile memories*", 11, Sawa, A., 28-36, (2008), with permission from Elsevier.[38]

1.2.3 The defect chemistry of $La_{1-x}Sr_xMO_{3\pm\delta}$

In this section, a brief overview of the defect chemistry of $La_{1-x}Sr_xMO_{3\pm\delta}$ is presented. The defect chemistry of a certain material is the set of reactions and mechanisms that fully describe the concentration of point defects in its structure. A point defect is defined as a single lattice site deviation from the long range periodicity of the crystal

lattice.[39] These kind of 0-D defects forms naturally at temperature T > 0 K, as a result of the minimization of the Gibbs free energy of the system. Point defects can be intrinsic of the material, such as the formation of Schottky vacancies and Frenkel interstitials, or extrinsic, such as the equilibrium with oxygen in the environment or the insertion of a dopant in the lattice. Considering the $La_{1-x}Sr_xMO_{3\pm\delta}$ family, a qualitative model describing the main regimes of oxygen equilibria in p-doped perovskite oxides was developed by Anderson.[40,41] This model, although it may be considered just as a first approximation of the real behaviour of these oxides, offers a good overview of the properties expected for this family as a function of pO_2. In the following, the main equations and results of the model are discussed.

In the perovskite structure, the presence of cation or oxygen atoms in interstitial positions is highly unfavourable, due to the small distances between anionic and cationic species. This means that one can exclude the presence of Frenkel (i.e. $M_M^x \leftrightarrow V_M''' + M_i^{\bullet\bullet\bullet}$) or Anti-Frenkel (i.e. $O_O^x \leftrightarrow O_i''' + M_i^{\bullet\bullet\bullet}$) disorder.[†] Instead, the generation of intrinsic Schottky type defects has to be considered:

$$nil \leftrightarrow V_M''' + V_{La}''' + 3V_O^{\bullet\bullet} \qquad \text{Eq. 1.1}$$

With constant of equilibrium:

$$K_s = [V_M'''][V_{La}'''][V_O^{\bullet\bullet}]^3 \qquad \text{Eq. 1.2}$$

The electronic charges may be localized on the M ion (i.e. $M_M^{\bullet}$ and M_M') or delocalized on the structure (i.e. holes $h^{\bullet}$ and electrons e'). For simplicity, here it is assumed that these are just delocalized on the material, allowing for an easier qualitative description of the defect chemistry. Nevertheless, it must be noted that for a more accurate description, polaron effect must be considered as well (see for example the defect chemistry model of $La_{0.8}Sr_{0.2}MnO_{3\pm\delta}$ in Chapter **2**). The introduction of divalent Sr ions into the trivalent A-site of $LaMO_{3\pm\delta}$ perovskite gives rise to an increase of negative charges, which needs to be compensated by positive defects. Two types of compensation mechanisms can be considered for the introduction of Sr:

$$2SrO + \frac{1}{2}O_2 \rightarrow 2Sr_{La}' + 2h^{\bullet} + 3O_O^x \qquad \text{Eq. 1.3}$$

$$2SrO \rightarrow 2Sr_{La}' + 2O_O^x + 3V_O^{\bullet\bullet} \qquad \text{Eq. 1.4}$$

Eq. **1.3** involves pure electronic charge compensation while Eq. **1.4** encompasses an oxygen ionic one. In real systems, both mechanisms may be active and the prevalence of one over the other is determined by the equilibrium with the oxygen environment, as:

[†] In this thesis, the Kröger-Vink notation is adopted.[136] The general form of this notation is Q_z^y where Q stands for the ionic species (*e.g.* M for metal, O for oxygen, V for vacancy), z the lattice site occupied (*e.g.* M for the metal site, O for the oxygen site, i for interstitial) and y the charge of the ion (*e.g.* x for zero charge compared to the neutral ABO_3 lattice, • for a positive and ' for a negative extra charge).

$$\frac{1}{2}O_2 + V_O^{\bullet\bullet} \leftrightarrow 2h^{\bullet} + O_O^x \quad \text{Eq. 1.5}$$

The constant of equilibrium of Eq. **1.5** reads as:

$$K_{ox} = \frac{[O_O^x][h^{\bullet}]^2}{[V_O^{\bullet\bullet}]pO_2{}^{1/2}} \quad \text{Eq. 1.6}$$

Finally, the charge equilibration mechanism must be considered:

$$nil \leftrightarrow h^{\bullet} + e' \quad \text{Eq. 1.7}$$

With equilibrium constant:

$$K_{el} = [h^{\bullet}][e'] \quad \text{Eq. 1.8}$$

Considering all the charged species introduced, the charge neutrality equilibrium equation is:

$$2[V_O^{\bullet\bullet}] + [h^{\bullet}] = [Sr'_{La}] + [e'] + 3[V_M'''] + 3[V_{La}'''] \quad \text{Eq. 1.9}$$

Following Anderson's approach,[40,41] the overall pO_2 regime can be divided into regions in which a simplified version of Eq. **1.9** can be applied, see **Figure 1.4**. In this way, the set of equations become easily solvable and an approximate solution can be found for each region. For instance, in highly oxidizing conditions (high pO_2) the concentration of electrons and oxygen vacancies is negligible and the presence of cation vacancies dominates the neutrality equilibrium (Region **I**), leading to:

$$[h^{\bullet}] = 3[V_M'''] + 3[V_{La}'''] \quad \text{Eq. 1.10}$$

Considering the concentration of A site and B site vacancies equivalent ($[V_M'''] = [V_{La}''']$) and substituting Eq. **1.10** into Eq. **1.2** and Eq. **1.6**, one finds:

$$[V_M'''] = [V_{La}'''] = \frac{1}{6}[h^{\bullet}] \propto pO_2{}^{3/16} \quad \text{Eq. 1.11}$$

From Eq **1.11**, the behaviour of the other defect species in region **I** can be calculated. **Figure 1.4** shows the evolution of oxygen content, oxygen vacancies, holes and electrons obtained for five different charge neutrality conditions (depicted in the upmost panel). The oxygen content in the material progressively reduces decreasing the pO_2, first passing from a hyper-stoichiometric condition ($\delta > 0$, Region **I**) to a stoichiometric plateau ($\delta = 0$, region **II**), where the negative defects are entirely compensated by holes. At a certain pO_2, the increasing concentration of oxygen vacancies is high enough to influence the charge neutrality equilibrium. This gives rise to a hypo-stoichiometric behaviour, with a constant reduction of the O content ($\delta < 0$, region **III**). Further decreasing the pO_2, another oxygen plateau is found, characterized by a fully ionic compensation of the negative charges introduced by the Sr doping ($\delta = -1/2[Sr'_{La}]$, region **IV**). Finally, in region **V** the electrons become the most numerous negative defect ($[e'] > [Sr'_{La}]$), giving rise to a further decrease of oxygen content till the

solubility limit of oxygen vacancy is reached and the decomposition of the perovskite phase takes place.

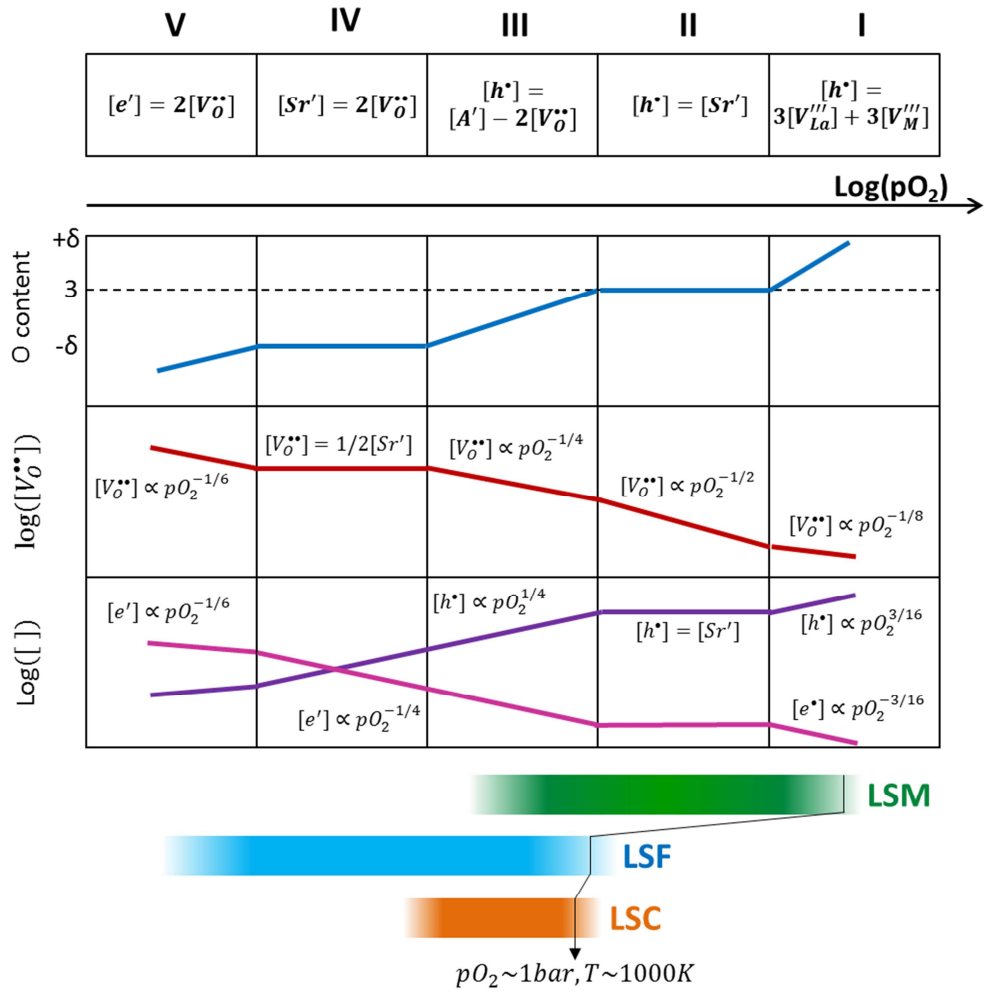

Figure 1.4 Brower diagram corresponding to the perovskite oxide $La_{1-x}Sr_xMO_{3\pm\delta}$ showing the evolution of oxygen content, oxygen vacancy, holes and electrons as a function of the pO_2.[40,41] The upmost panel shows the neutrality equilibrium conditions valid for each region. In the bottom part, the regions of interest for $La_{0.8}Sr_{0.2}MnO_{3\pm\delta}$ (LSM), $La_{0.8}Sr_{0.2}FeO_{3-\delta}$ (LSF) and $La_{0.8}Sr_{0.2}CoO_{3-\delta}$ (LSC) are depicted. The black arrow crossing the three materials marks the approximate regime observed at $pO_2 \sim 1$ bar, T ~1000 K.[42–44] The diagram is adapted from Steele.[45]

Although this model offers a complete picture of all the possible oxygen regimes in $La_{1-x}Sr_xMO_{3\pm\delta}$, it must be noted that none of the different transition metals M considered in this thesis (Mn, Fe, Co) undergoes through all the five regimes described. Indeed, each specific material generally displays only a limited number of regions between pO_2 = 1 bar and the lowest partial pressure achievable before the perovskite decomposition, see **Figure 1.4**. The type of predominant charge neutrality mechanism mainly depends on the reducibility of the transition metal, the electronic properties and stability of the structure. For instance, it was found that $La_{0.8}Sr_{0.2}MnO_{3\pm\delta}$ (LSM) shows a behaviour in agreement with the first three regions (**I**, **II** and **III**) for a pO_2 range between 1 and 10^{-20} bar, but no ionic plateau (region **IV**) was observed.[44,46] Instead, $La_{0.8}Sr_{0.2}FeO_{3-\delta}$ (LSF)

presents a concentration of point defects well described by regions **II** to **V**, also demonstrated by the n-type conductivity commonly observed at low pO_2.[43,47] The $La_{0.8}Sr_{0.2}CoO_{3-\delta}$ (LSC) compound is highly reducible, showing an oxygen stoichiometry in agreement with region **II** and **III**. The absence of the ionic plateau (region **IV**) is believed to be caused by the mostly metallic behaviour of electronic species in Co-based perovskites.[42]

It is important to point out the relevance of the divalent dopant concentration (*i.e.* Sr) in the material, as a way to tailor the concentration of point defects in the structure. Indeed, increasing the dopant concentration not only results in an increase of the positive charges to maintain electro-neutrality (see Eq. **1.9**), but also affects the equilibrium constants, generally making more reducible the oxide.[43] As an example, **Figure 1.5a** shows the oxygen content in $La_{1-x}Sr_xMnO_{3\pm\delta}$ and $La_{1-x}Sr_xCoO_{3-\delta}$ compounds for different values of Sr (x = 0.2, 0.3 and 0.5) at 1073 K. The increase of Sr in the Co-based perovskite directly generates larger concentration of oxygen vacancies already in pure oxygen ($\delta < 0$). Also the $La_{1-x}Sr_xMnO_{3\pm\delta}$ compound shows a more reducible behaviour for higher dopant concentration but, even for x = 0.5, it maintains an almost stoichiometric behaviour ($\delta = 0$) up to $pO_2 \sim 10^{-10}$ bar. This means that the Mn-based perovskite is expected to present mainly an electronic behaviour in air, with an extremely low concentration of oxygen vacancies.

Due to the similarity of the structure among the various $La_{1-x}Sr_xMO_{3\pm\delta}$ perovskites, another option to alter the functional properties of the material is to dope the B-site with another transition metal. In this sense, the substitution of an easily reducible metal into a perovskite mainly governed by electronic compensation can lead to an increase of oxygen vacancy concentration. This is the case of $La_{1-x}Sr_xMn_{1-y}Co_yO_{3\pm\delta}$ compound, also studied in this thesis, which progressively reduces the oxygen content increasing the Co concentration (see **Figure 1.5b**).[48]

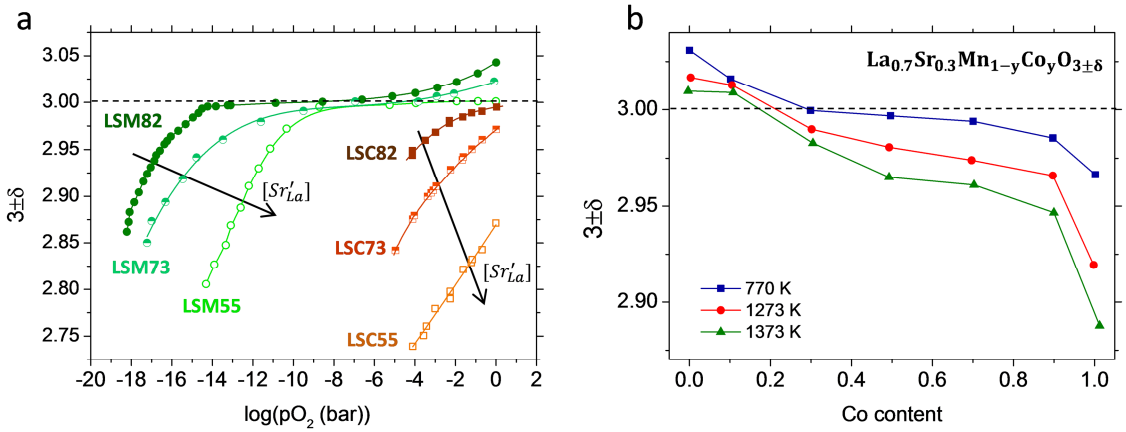

Figure 1.5 a, Effect of Sr doping on the oxygen content of $La_{1-x}Sr_xMnO_{3\pm\delta}$ and $La_{1-x}Sr_xCoO_{3-\delta}$ at 1073 K. The data of LSM82 (x=0.2), LSM73 (x=0.3), LSM55 (x=0.5), LSC82 (x=0.2), LSC73 (x=0.3) and LSC55 (x=0.5) are derived from Mizusaki *et al.*[42,44] **b**, Effect of Co content on the oxygen stoichiometry of $La_{1-x}Sr_xMn_{1-y}Co_yO_{3\pm\delta}$ compound measured at different temperature in air.[48]

1.2.4 The impact of point defects on $La_{1-x}Sr_xMO_{3\pm\delta}$ functional properties

In perovskite oxides, the concentration of point defects severely impacts the oxygen transport, electronic, structural and magnetic properties. In this section, two examples are described: the variation of oxygen mass transport properties in $La_{1-x}Sr_xMn_{1-y}Co_yO_{3\pm\delta}$ and the variation of electronic resistivity in $La_{1-x}Sr_xMO_{3\pm\delta}$.

1.2.4.1 Oxygen mass transport properties

The electrochemical properties of a cathode material are strictly related to its oxygen mass transport properties, namely the oxygen self-diffusion coefficient D^* and the surface exchange coefficient k^*. On one side, the diffusion coefficient governs the portion of cathode active for the ORR reaction. This can take place mainly close to the electrolyte (small values of D^* for electronic conductors) or up to the entire cathode surface (high values of D^* for MIEC). At the same time, the surface exchange coefficient determines the ORR and incorporation rates, directly affecting the polarization resistance of the electrode. For these reasons, these two parameters are generally used to describe oxide materials for SOFC applications.[49,50] The surface exchange and oxygen diffusion coefficients can be measured by tracer, electrical or chemical relaxation experiments.[51] In particular, tracer experiments offer a direct measure of D^* and k^* of oxide materials (see Chapter **2** for more details on the technique).

An illustrative example of the effect of A- and B-site substitution on the mass transport properties of perovskite oxides was presented by De Souza *et al.*,[52,53] who analysed the oxygen diffusivity and surface exchange of $La_{1-x}Sr_xMn_{1-y}Co_yO_{3\pm\delta}$ for different values of Sr and Co (see **Figure 1.6**). First, it is possible to observe that both parameters progressively increase passing from Mn to Co rich materials. Moreover, a similar trend is found when increasing the Sr content, although it must be noted that in $La_{1-x}Sr_xMnO_{3\pm\delta}$ the variation is not so significant, especially at low temperature.

In these perovskites, it is generally accepted that the diffusion of oxygen is vacancy mediated.[54] In the light of the defect chemistry shown in the previous section, De Souza *et al.* suggested that the increase oxygen diffusivity is mainly due to an increase of carriers in the system (i.e. oxygen vacancy) passing from Mn-rich to Co-rich compounds or increasing the Sr content.[52,53] Indeed, the oxygen diffusivity is related through the vacancy diffusivity (D_v) through:

$$D^*[O_O^x] = f[V_O^{\bullet\bullet}]D_v \qquad \text{Eq. 1.12}$$

Where f is the correlation factor.[55] Since the vacancy diffusivity was calculated to be similar for the whole perovskite family,[52,53,55,56] the increase of oxygen vacancies generated by a A- and B-site substitution will directly originate an increase of D^*. In the

case of k^*, a direct correlation with the available oxygen vacancies in the system can be also established, although other factors such as the electronic structure, adsorption properties of the B-site ion or the surface concentration of Sr can influence this parameter as well. This issue will be more carefully addressed in Chapters **5** and **6**.

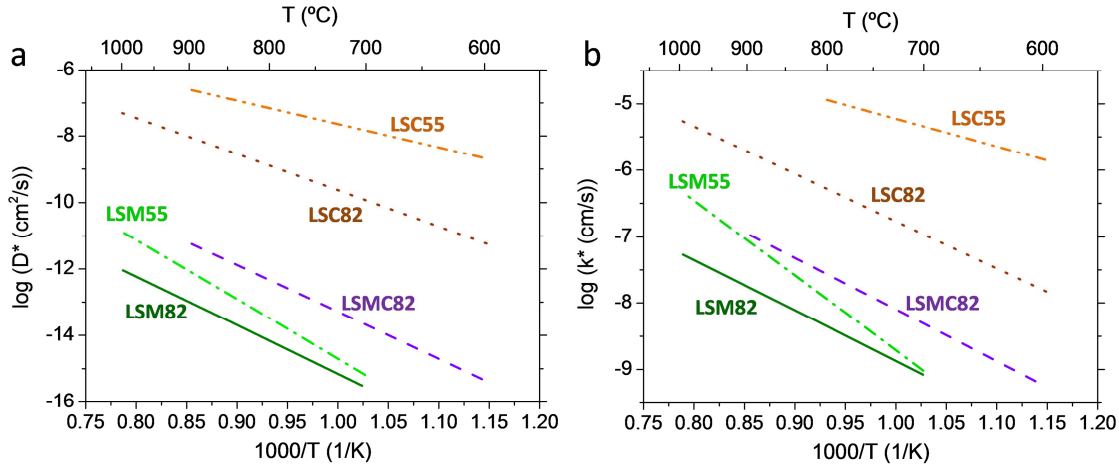

Figure 1.6 Oxygen diffusivity (**a**) and surface exchange coefficient (**b**) of $La_{1-x}Sr_xMn_{1-y}Co_yO_{3\pm\delta}$ perovskites as a function of temperature at pO_2 = 1 bar. The data of LSM82 ($La_{0.8}Sr_{0.2}MnO_{3\pm\delta}$), LSM55 ($La_{0.5}Sr_{0.5}MnO_{3\pm\delta}$), LSMC82 ($La_{0.8}Sr_{0.2}Mn_{0.5}Co_{0.5}O_{3\pm\delta}$), LSC82 ($La_{0.8}Sr_{0.2}MnO_{3-\delta}$), and LSC55 ($La_{0.5}Sr_{0.5}MnO_{3-\delta}$) are taken from De Souza *et al.*[52,53]

1.2.3.2 Electronic properties

In the qualitative defect chemistry model presented in the previous section, the electrons and holes were considered to be delocalized over the entire lattice. Nevertheless, in perovskite oxides strong structural and electronic effects can localize the electrons over the B-O bonds, giving rise to semiconducting behaviour even for half-filled bands near the Fermi level.[57] Moreover, in $La_{1-x}Sr_xMO_{3\pm\delta}$ oxides where M can easily change its oxidation state (such as Mn, Co and Fe), different electronic configurations can be found which can have a large impact on the structural, electronic and magnetic properties of these materials. This is the case of $La_{1-x}Sr_xMnO_{3\pm\delta}$, where the different oxidation states of Mn (Mn^{2+}, Mn^{3+}, Mn^{4+}) give rise to radically different electronic transport properties.

The electronic structure of perovskites is determined by the MO_6 octahedra.[57] The crystal field potential splits the degenerated 3d electrons of the metal into t_{2g} and e_g orbitals in a cubic environment. Due to the spatial overlap of the oxygen 2p electrons with the M orbitals, bonding and antibonding orbitals of mixed covalent-ionic types are created, with a strong σ-type character for the e_g orbitals and π-type for the t_{2g} ones.[58] The electronic configuration near the Fermi level is characterized by the antibonding t_{2g} and e_g orbitals, which possesses a mixed O2p - M3d character depending on the energy position of the O2p band centre.[59] The occupancy of these orbitals in the MnO_6 octahedra is schematically shown in **Figure 1.7** for Mn^{2+}, Mn^{3+} and Mn^{4+} ions (spin up

configuration). In the case of Mn^{3+}, the half filling of the e_g orbital gives rise to a tetragonal distortion of the unit cell and the breaking of the degeneracy of $d_{z^2-r^2}$ (e_g^1) and $d_{x^2-y^2}$ (e_g^2) orbitals. This phenomenon is called Jahn-Teller distortion and is the main responsible of the high temperature semiconducting behaviour commonly found in lightly doped manganites. Indeed, even if the Sr doping induces a mixed Mn^{3+}/Mn^{4+} valence, the holes are strongly localized in the Mn-O lattice distance, originating a polaron type conduction in the paramagnetic phase of $La_{1-x}Sr_xMnO_{3\pm\delta}$ ($T>T_c$).[25,27,60]

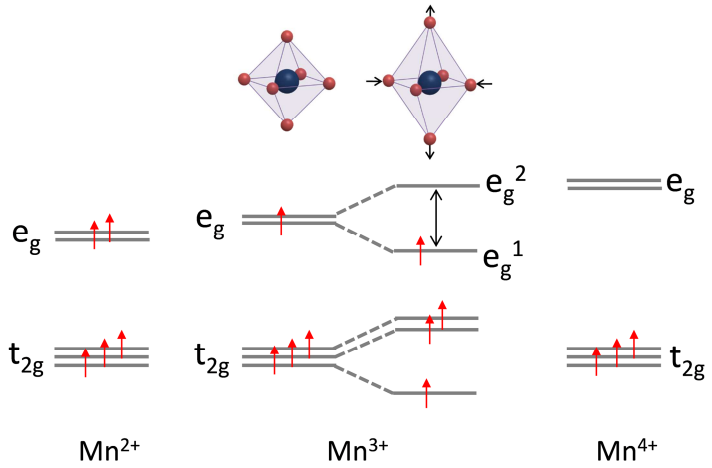

Figure 1.7 Electron occupancy of energy levels in Mn^{2+}, Mn^{3+} and Mn^{4+}. The tetragonal JT distortion is schematically shown above Mn^{3+} configuration.[25]

One of the most characteristic aspects of the electronic transport in mixed valence manganites is the onset of a metallic behaviour below Curie temperature (T_c). The metal transition is generated by a Jahn-Teller mediated double exchange mechanism, which take place through the tunnelling of an electron from one Mn^{3+} to a neighbour Mn^{4+} hole through the oxygen orbital (see Chapter **4** for more details). **Figure 1.8a** shows the evolution of resistivity in $La_{1-x}Sr_xMnO_{3\pm\delta}$ for different Sr content.[61] It is observed that the metal insulator transition only take place for $x > 0.15$, while for $x < 0.1$ a semiconducting resistivity is observed for the entire temperature range. This behaviour is associated in bulk $La_{1-x}Sr_xMnO_{3\pm\delta}$ to the increasing presence of Mn^{4+} generated by the A-site substitution, which reduces the JT distortions and allows the double exchange mechanism.

Similar effects on the low temperature electrical resistivity can be generated by increasing the oxygen deficiency. **Figure 1.8b** shows the results obtained by Baikov *et al.* in bulk $La_{0.67}Sr_{0.33}MnO_{3-\delta}$ varying the oxygen content in the material.[62] In this case, the increase of oxygen vacancies produces a decrease of Mn^{4+}, generating an increase of JT distortions and a suppression of the metal-insulator transition. It is necessary to note that some differences arise in the electronic behaviour when comparing the effect of Sr doping or δ, probably related to the effect of the A-site dopant on the tetragonal distortions and/or to the presence of oxygen vacancies hindering the double exchange mechanism through the oxygen orbital.[25,27] Nevertheless, this example well illustrates

the large impact of the defect concentration on the electronic behaviour of perovskite oxides.

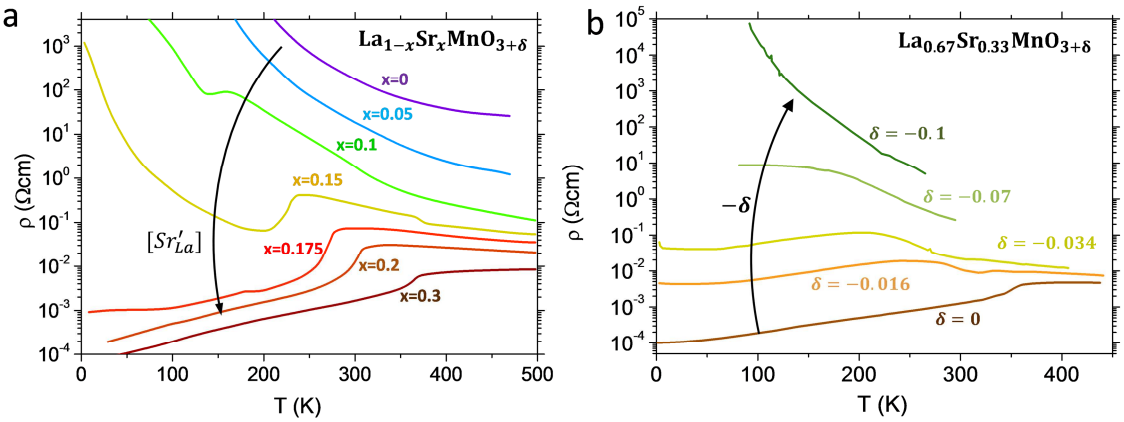

Figure 1.8 Temperature dependence of the resistivity in $La_{1-x}Sr_xMnO_{3\pm\delta}$ bulk as a function of Sr (**a**) and oxygen (**b**) content. The data are taken respectively from Urushibara *at al.*[61] and Baikov *et al.*[62]

1.3 Grain boundaries in functional metal transition oxides

In the previous sections, the importance of point defects on the perovskite oxides was introduced. It was shown that by doping the A- or B-site it is possible to tailor the defect concentration, giving rise to severe modifications of their functional properties. Here, another strategy for engineering the defect chemistry and the functionalities of perovskites is described, *i.e.* taking advantage of the unique properties of their interfaces and, in particular, of grain boundaries (GBs). An interface is defined as an interruption of the symmetry in a crystal structure, which brings strong modifications on the atomic properties as compared to the bulk. Two main type of interfaces may be distinguished on the basis of the constituent phases, *viz.* homo-interfaces (one single material) and hetero-interfaces (two different materials).[63] Examples of homo-interfaces are grain boundaries or dislocations (see **Figure 1.9a**), while hetero-interfaces are for instance surfaces, thin film multilayers and Vertical Aligned Nanocomposite structures (VANs) (see **Figure 1.9b** and **c**). All these interfaces are characterized by complex interactions between strain, structural disorder, electrical and ionic compensation effects, which give rise to a modification of the bulk properties and, sometimes, the rise of unexpected phenomena.[1,63,64] Indeed, it was shown that interfaces may impact both the mobility and the concentration of charge species. This is for instance the case of ionic diffusion in elastically strained layers, where the tensile strain was observed to both reduce the vacancy energy formation and to decrease the energy barrier of ion mobility.[65]

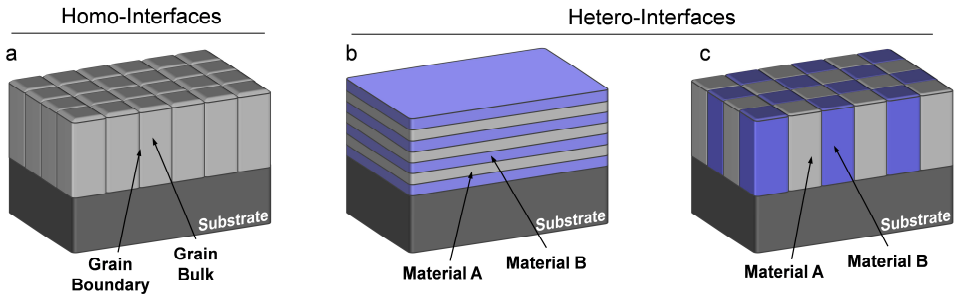

Figure 1.9 Sketch of types of interfaces-dominated ceramic oxide thin films: Homointerfaces, i.e. grain boundary-dominated materials (**a**) and heterointerfaces, *viz.* multilayers (**b**) and vertically aligned nanocomposite structures (**c**).

Grain boundaries are known to strongly influence functional properties of polycrystalline bulk materials[5] and, more interestingly, to even control the behaviour of the so-called interface-dominated nanomaterials, *e.g.* polycrystalline thin films. Typically, the active use of GBs for modifying the functionality of materials has been found difficult to implement, despite polycrystalline materials being vastly deployed in bulky systems and also in many thin film-based devices. The random orientation of the grains and their relatively big size (compared to the grain boundary width) have contributed to classically see the grain boundaries rather as a problem than as an opportunity.[4,66] However, the great advances in thin film deposition and characterization technologies attained in the last decades opened new possibilities to actively use grain

boundaries for improving the performance of certain materials. Thin films with reduced dimensions and customized microstructures (grain size, density, crystallinity…) can be fabricated with high reproducibility, thus making grain boundaries accessible not only for their study and better understanding,[67–71] but also for actively profiting from their modified properties.[6,72,73] For example, thin films of functional oxides can be deposited by pulsed laser deposition (PLD) in the form of fully packed vertically aligned columnar grains.[7] This configuration opens a new avenue for the integration of nanoionics effect into novel devices by allowing the use of enhanced properties of grain boundaries *through* the films in vertical configurations.[64] In the following, the grain boundary characteristics and properties commonly found in oxides materials are reviewed.

1.3.1 Grain boundary composition in oxides

The large impact of grain boundaries on the behaviour of polycrystalline materials received increasing attention in the last decades, especially due to the interest in structural metals and ceramics.[74] However, a full comprehension of the nature and effects of grain boundaries in functional oxides is still lacking, despite their profound influence in the electrical properties of these materials. It is only lately that computational simulations and high-resolution characterization techniques (primarily Atomic Force and Electron Microscopy) reached the required maturity for significantly contributing to the atomistic picture of grain boundaries. In this section, it is shown how the presence of structural defects in a GB can severely modify its ionic composition. In Section 1.3.1.1, the correlation between composition and structural properties taking place in the proximity of a grain boundary interface (namely in the *grain boundary core*) is presented. Then, Section 1.3.1.2 examines the consequences of the accumulation of these defects in the core of a grain boundary. Indeed, a volume is formed in the surroundings of the charged GB, in which a concentration profile of the different species is generated in order to preserve the overall charge neutrality. This volume is called *space charge region* or electrical GB.

1.3.1.1 Grain boundary core composition

A grain boundary is an interface composed by two crystals of the same composition joined together. It is usually defined by the orientation of the grain boundary plane and the angle of misorientation θ between the principal crystallographic directions of the two grains (the rotation angle necessary to align both grains in the same orientation).[75] In general, low-θ angle grain boundaries can accommodate differences in the lattice orientation by forming arrays of dislocations. It is possible to forecast the periodicity of the rearrangement by using the Frank's equation,[76] which shows that the dislocation spacing decreases with increasing θ. Opposed to that, for high values of misorientation angle the dislocations tend to overlap and several more complex accommodation structures can be originated. One useful way to describe high and low angle grain

boundaries is the so-called *coincidence site lattice* method (CSL).[76,77] Let us image a grain boundary where two crystals are rotated through the grain boundary plane by a certain angle θ; in such situation, certain atomic positions from both crystal orientations would coincide, periodically repeating through the grain boundary´s lattice structure. The CSL method uses the reciprocal density of these coincident states, Σ, to describe the grain boundary. In particular, Σ is defined as the ratio between the number of coincident sites and the total number of sites. This way, a grain boundary formed by two grains with parallel orientations corresponds to Σ=1, since every single atomic position coincides in the interface between both grains. Meanwhile, an increasing Σ value represents a less coherent structure (see **Figure 1.10**).

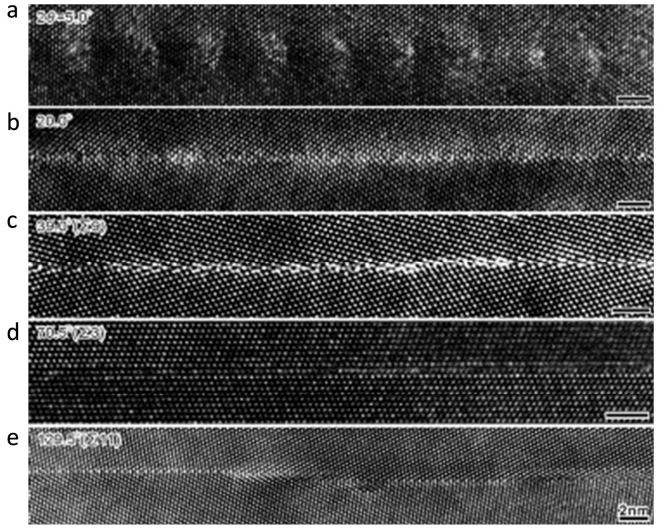

Figure 1.10 High-resolution TEM images of [110] symmetric tilt grain boundaries of YSZ with different misorientation angles 2θ: 5.0° (**a**), 39.0° (Σ9) (**b**), 70.5° (Σ3) (**d**) and 129.5° (Σ11) (**d**). Reprinted from High-temperature grain boundary sliding behavior and grain boundary energy in cubic zirconia bicrystals, 53, Yoshida, H., Yokoyama, K., Shibata, N., Ikuhara, Y., Sakuma, T., 2349-2357, (2004), with permission from Elsevier.[78]

The high degree of structural disorder found in the different types of grain boundaries can influence on the defect chemistry of the material, leading to a local change in its chemical composition. Many studies have found that, for several oxides, oxygen vacancies are created within the firsts atomic planes around the grain boundary interface.[67,70,71,79–83] For example, An and co-workers analysed an 8% mol. Yttria stabilized Zirconia (YSZ) Σ13 (510)/[001] symmetric tilt grain boundary by aberration-corrected TEM and quantified the atomistic composition by Electron Energy Loss Spectroscopy (EELS).[71] They found that a large oxygen deficiency is detectable in the first 0.5 nm from the grain boundary plane. A higher concentration of oxygen vacancies in the proximities of grain boundaries has been found also in other oxides such as ceria,[67,79,80] strontium titanate[82] and barium titanate.[81] Feng *et al.* studied the atomic composition of different grain boundary orientations of ceria by High Angle Annular Dark Field (HAADF) Scanning Transmission Electron Microscopy (STEM).[80] Interestingly, they discovered that only some orientations present oxygen vacancy

accumulation, while others do not show any compositional change. Supported by theoretical calculations, they discovered that the oxygen vacancies were present just in the grain boundaries with larger degrees of structural distortion. They concluded that, by reducing the oxygen content, the most distorted structures could relax while the lattice defects were reduced. Other studies by Liu *et al.* and by Hoyo *et al.* also found that the rearrangement of oxygen vacancies is a way through which different crystal structures (*e.g.* fluorites, perovskites) are able to accommodate the loss of coherency.[79,84]

Along with the oxygen vacancies, also cations and dopants can modify their concentration to accommodate lattice defects.[66,68,85,86] A recent study by Frechero *et al.* found that a symmetrical 33° [001] tilt grain boundary in YSZ films not only presents an accumulation of oxygen vacancies, but also of Yttrium (see **Figure 1.11**).[66] Lee and co-workers also studied the defect distribution around Σ5(310)/[001] grain boundary of YSZ, as well as Ceria, by a hybrid Monte Carlo–molecular dynamics simulations.[87] They discovered that oxygen vacancies are accumulated firstly in the grain boundary due to lower vacancy formation enthalpy, whereas the dopant appears to accumulate as a result of a strong vacancy-dopant interaction.

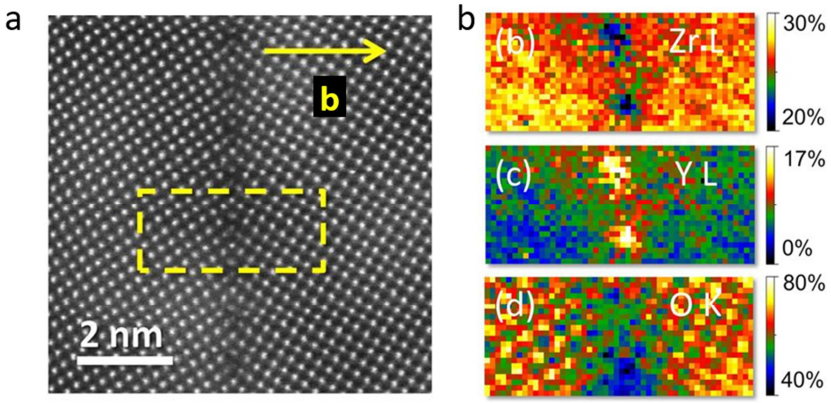

Figure 1.11 a, TEM atomic resolution Z-contrast image of a symmetrical 33° [001] tilt YSZ grain boundary. **b**, Chemical compositional maps measured by electron energy-loss spectroscopy (EELS). The area corresponds to the yellow square in **a**. The image is modified with permission from Frechero *et al.*[66]

A general conclusion that arises from these works is that the GB core is a region where the point defects formation energies differ from the bulk values. The trend that emerges is of a more reducible interface that, in some cases, can also present an accumulation of other defects (*e.g.* segregated dopants).

1.3.1.2 Grain boundary: space charge formation

The modification of the defect energy formation in the grain boundary leads to a restricted zone in which charged defects accumulate, *i.e.* the grain boundary core. Therefore, the electroneutrality is no longer preserved and an electric field is developed in the volume adjacent to the grain boundary plane. In order to keep the charge neutrality, charged species in the surroundings of the grain boundary tend to modify

their concentration, to compensate the generated charge in the core. The volume of material affected by the electric potential created in the grain boundary and the subsequent redistribution of charged defects is called the *space charge region*. While the grain boundary core takes place in a very restricted zone, *ca.* 1 nm, the space charge region can be extended to even several tens of nanometers. The grain boundary core and the space charge region constitute the "*electrical grain boundary*", which is on the basis of the space charge theory described in the following.[5]

Different models have been proposed in literature to describe the depletion and accumulation of species in the space charge region.[1,5,88–91] In this introduction, the grain core is considered just as a two-dimensional interface with a potential $\phi_0 = \phi(0) - \phi(\infty)$, where $\phi(\infty)$ is the potential in the bulk. The interface potential is originated by the accumulation of point defects in the grain core, as described in the previous section. Due to the local non-equilibrium, the potential in the space charge layer distributes according to the Poisson equation (1-D problem):[5,90–92]

$$\frac{\partial^2 \Phi(\mathrm{x})}{\partial \mathrm{x}^2} = -\frac{1}{\varepsilon_0 \varepsilon_r} \cdot \zeta(\mathrm{x}) \qquad \text{Eq. 1.13}$$

Being ε_0 and ε_r the vacuum and material specific dielectric constants, respectively, and ζ the charge density at position x. Considering the mobile species as diluted and not interacting, one can obtain their concentration in the space charge region by:

$$c_i(x) = c_{i,b} \cdot \exp\left(\frac{-z_i e \cdot \Delta\phi(x)}{k_b T}\right) \qquad \text{Eq. 1.14}$$

With $\Delta\phi(x) = \phi(x) - \phi(\infty)$ being the potential at a position *x*, $c_i(x)$ and $c_{i,b}$ the concentration of defects in the space charge region and in the bulk, respectively and z_i, e, k_b and T the charge carrier number, the electron charge, the Boltzmann constant and the temperature. Since the charge density is equal to the sum of the charge of all the individual species ($\zeta = \sum_{i=1}^{n} z_i e c_i(x)$), the general expression of the Poisson equation becomes:

$$\frac{\partial^2 \Phi}{\partial \mathrm{x}^2} = -\frac{1}{\varepsilon_0 \varepsilon_r} \cdot \sum_{i=1}^{n} z_i e \, c_{i,b} \cdot \exp\left(\frac{-z_i e \cdot \Delta\phi(x)}{k_b T}\right) \qquad \text{Eq. 1.15}$$

Equation 1.15 is general but, unfortunately, there is no analytical solution to it. In order to obtain simple expressions to predict the space charge behaviour, one has to adopt approximations that make the solutions valid under certain conditions. The different models are based on estimations of the charge density. The most relevant approximations are the Gouy-Chapman and Mott-Schottky models.[5,90,92–94] The Gouy-Chapman model is a limit solution valid in case of large accumulation of defects in the space charge zone.[5,93] In the model, the charge compensation is considered to be mainly controlled by the dopant cation distribution in the space charge region (with charge $\mathrm{z_c}$ and concentration $c_{c,b}$). The Mott-Schottky model considers that the dopant cation is immobile and gives the most predominant contribution to the charge density. This

approximation is found to be valid for describing the grain boundary behaviour in many oxides below 1000°C, due to the low diffusion of cations. For example, it is to be highlighted here the studies made by Guo *et al.* on lightly doped zirconia [94,95] and by Kim *et al.* and Guo *et al.* on ceria.[93,96,97]

In the Mott-Schottky approximation, the charge density in the case of constant dopant concentration is:

$$\rho = -z_c e c_{c,b} \qquad \text{Eq. 1.16}$$

The solution of the potential redistribution under this assumption is:

$$\Delta\phi(x) = \phi_0 \left(\frac{x}{\lambda^*} - 1\right)^2 \qquad \text{For } x < \lambda^* \qquad \lambda^* = \lambda\sqrt{\frac{4|z_c|e}{k_b T}\Phi_0} \qquad \text{Eq. 1.17}$$

Where λ^* is the width of the space charge zone and λ is the Debye length ($\lambda = \sqrt{(\varepsilon_0 \varepsilon_r k_b T)/(2 z_c^2 e^2 c_c)}$). As an example, **Figure 1.12** shows the redistribution of potential and main charged species (cations, oxygen vacancies, electrons and holes) according to this model for Fe-doped $SrTiO_3$ at 600°C and 0.01 bar, considering an interface potential of 0.3 V and 0.5 V as well as different Fe contents.

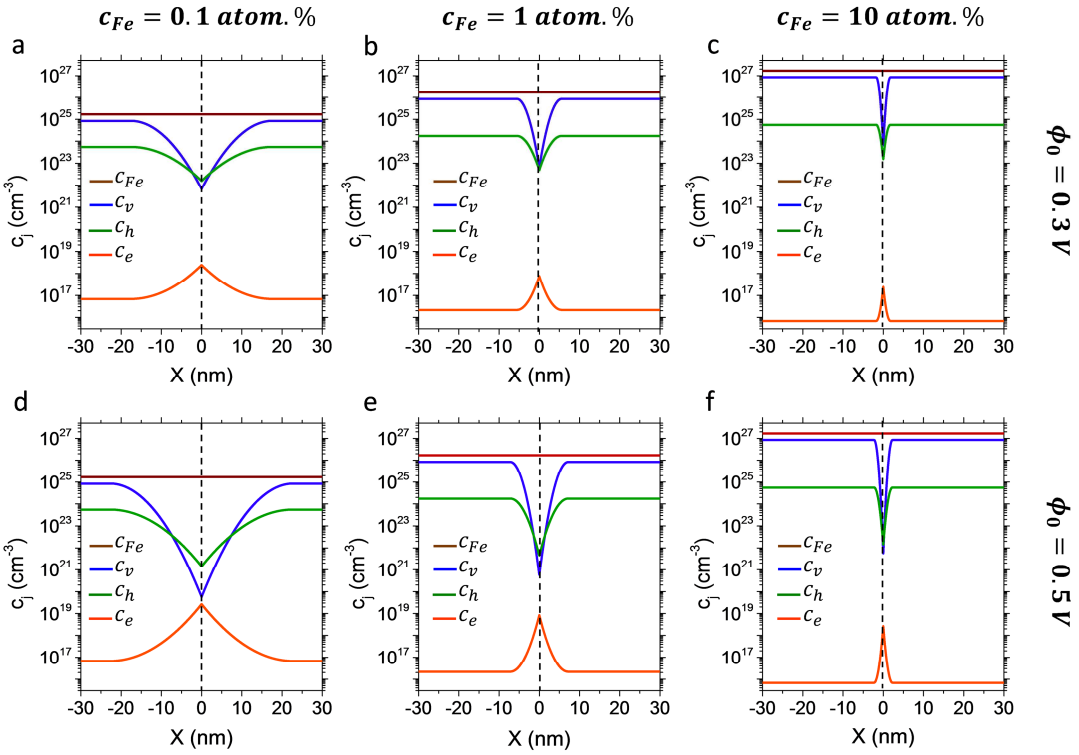

Figure 1.12 Mott-Schottky space charge approximation of a Fe-doped $SrTiO_3$ grain boundary, calculated for Φ_0=0.3 V (**a – c**) and Φ_0=0.5 V (**d – f**), as well as different values of dopant concentration: c_{Fe} = 0.1 at.% (**a, d**), c_{Fe} =1 at.% (**b, e**) and c_{Fe} = 10 at.% (**c, f**). The dielectric constant of the material is set at ε_r=160 and the temperature is T=600ºC. The concentration values of oxygen vacancies (c_v), holes (c_h) and electrons (c_e) are derived from the defect chemistry model at 600ºC and 0.1 bar.[98,99]

From **Figure 1.12**, it is possible to note that large space charge effects are expected for small doping concentrations, while when increasing the Fe content the space charge width tends to become smaller. The positive potential gives rise to an accumulation of negative species (electrons) and a depletion of positive ones (holes and oxygen vacancies). Under certain conditions (i.e. high surface potential ϕ_0, not shown here) the concentration of electrons in the space charge can even exceed the holes in an acceptor doped material. This phenomenon has been indeed found for $SrTiO_3$[100,101] and ceria oxides.[96,97,102] It is possible to consider the electron enrichment and hole depletion as a downward band bending of both the valence and conduction bands, with a constant Fermi level.[88,90] Another possible effect of space charge in oxides is an increase of electronic transport number (the ratio between electronic and ionic conductivity), due to both the increase of electrons and a sharper decrease of oxygen vacancies than holes, as found in $LaGaO_3$.[103,104]

When decreasing the grain size to the nanometric scale, the effect of the space charge layer on the overall conductivity becomes more relevant, due to the increasing significance of the space charge region. For values of grain size approaching the space charge width, the overall conductivity is expected to change drastically, due to mesoscopic effects.[2,4,5,105] Indeed, for grain sizes comparable to the Debye length, the concentration of mobile defects does not relax to the bulk values, because the space charge of two consecutive grain boundaries overlaps. This mesoscopic behaviour has been found in nanocrystalline $SrTiO_3$ with grain size lower than 100 nm.[106] Due to the increase of electrons concentration, in mesoscopic $SrTiO_3$ the change from p-type to n-type behaviour occurs at oxygen partial pressures far higher than the bulk ones. This particular example illustrates the great impact of nanoionics effects, eventually being able to alter the nature of a material just by controlling the grain size.[101]

1.3.2 The effect of grain boundaries in the functional properties of oxides

In previous sections, it was shown that grain boundaries effectively affect the charge carrier concentration in the grain boundary core and its surroundings. Based on the depletion or enhancement of different charge carriers in either the grain boundary core or the space-charge region, great differences are expected in the functional properties. In the following, the main effects of GBs on ionic conductivity and electrochemical properties are resumed.

1.3.2.1 Grain boundaries effect on ionic conductivity

As mentioned beforehand, a significant increase of oxygen vacancies concentration is generally found in the GB core; but, are these mobile enough to provide a preferential conduction pathway? If so, this could be actively used for modifying bulk properties at the nanoscale. Unfortunately, no clear evidences of enhanced ionic conduction along the

grain boundaries have been found in classical ionic conductors such as YSZ[107] or ceria.[108] Even a negative effect on oxygen diffusion was reported for ceria, in the case of accumulation of charged cations in the GB core, which was mainly associated to an increase of the association energy between the defects.[109] In the case of perovskite structures, it is worth mentioning the work by Marocchelli *et al.,* who calculated by large scale atomistic simulations the impact of an array of dislocations on the oxygen ion diffusion of $SrTiO_3$.[110] They found that the oxygen vacancy formation energy is substantially lowered in the tensile strained part of the dislocation, resulting in an accumulation of point defects that may enhance the diffusion of lightly doped $SrTiO_3$ perovskites (see **Figure 1.13a**). Nevertheless, they also found that the mobility of these defects is far lower in the dislocation core respect to the bulk one, which substantially decreases the beneficial effect of the rise of charge carriers (**Figure 1.13b**). Overall, no preferential transport along the GBs was predicted in $SrTiO_3$. Similar results were reported by De Souza and co-workers.[111,112]

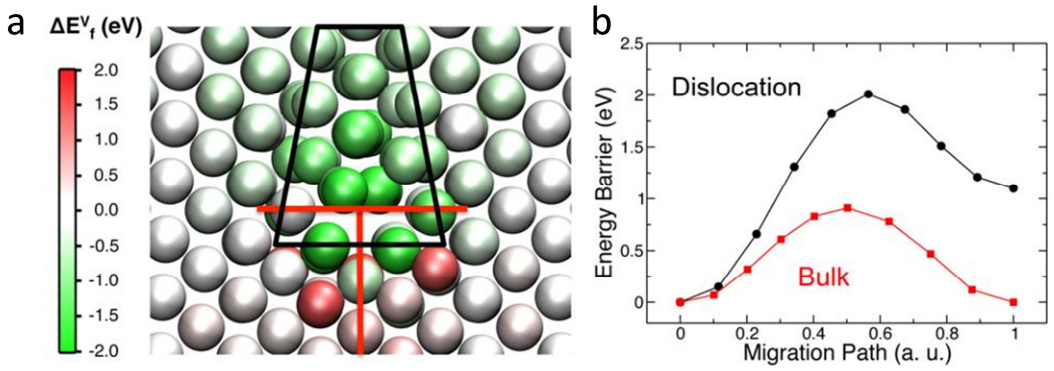

Figure 1.13 Effect of one dislocation on the formation of oxygen vacancies (ΔE^{v}_{f}, relative to the bulk) (**a**) and on the energy barrier mobility of oxygen diffusion (**b**) in $SrTiO_3$. Although being more reducible, the dislocation does not provide a preferential pathway for oxygen diffusion. Reprinted with permission from Marrocchelli, D., Sun, L. & Yildiz, B. Dislocations in $SrTiO_3$: Easy to Reduce but Not so Fast for Oxygen Transport. *J. Am. Chem. Soc.* 137, 4735–4748 (2015).[110] Copyright American Chemical Society.

Yet, it is important to mention that recent experimental results in some particular materials have also shown an enhancement of ion mobility in the grain boundaries. This is the case of strontium-doped lanthanum manganite (LSM) mixed ionic-electronic conductors, one of the scoped materials in this thesis. Independent works from Fleig's and Tarancón's groups recently discovered fast oxide-ionic conductivity along grain boundaries in LSM, reporting up to 6 orders of magnitude of improvement in oxide-ion diffusivity compared to the bulk, which might be associated to strain-induced defects and/or corresponding changes in the concentration of $La_{1-x}Sr_xMnO_{3\pm\delta}$ constituent species.[72,113,114] Other examples are the dominating ionic conductivity at the grain boundary level reported by Druce *et al.* for PLD-grown thin films of $LaCo_{0.6}Ni_{0.4}O_3$,[115] or by Develos-Bagarinao *et al.* for $La_{0.6}Sr_{0.4}Co_{0.2}Fe_{0.8}O_{3-\delta}$ and $La_{0.6}Sr_{0.4}CoO_{3-\delta}$.[116,117] This difference in behaviour between materials with similar structure (*e.g.* LSM and STO) stands as one of the most interesting topics in ion conducting oxides, since its

comprehension may reveal new strategies for the smart design of hetero-interfaces for solid state devices.

Beyond the GB core effects, also the creation of space charge region is generally considered to hinder the ionic conductivity in oxides. This is mainly due to the positive character of these interfaces that, as shown in Section 1.3.1.2, gives rise to a depletion of oxygen vacancy concentration in the GB surroundings. Tuning the properties of oxides by changing the accumulation or depletion of certain charge carriers in the grain boundaries is a fascinating challenge. The positive potential in the GB core mainly arises from the accumulation of positive defects that, as shown before, are mainly represented by oxygen vacancies both in perovskites such as $SrTiO_3$,[88,118–120] $LaGaO_3$,[103,104] $BaTiO_3$,[121–123] $BaZrO_3$[124] and fluorites, such as acceptor doped ZrO_2 [71,92,94,95] and CeO_2.[93,96,102,125,126] Few examples of negative core charge can however be found in literature, such as the case of the TiO_2. In titania, a negative surface potential can be developed by the accumulation of cations vacancies in the grain core.[127–129] Unlikely, the sign of the core charge is not easily switchable, because it depends on complex interactions between grain boundary misorientations and the material's defect chemistry (see section 1.3.1.1). The width and influence of the space charge can however be modified, for instance by changing the doping level. As a general rule, it is possible to expect large space charge effects in lightly doped oxides while, for higher values of dopant concentration, other effects such as defects association may prevail, resulting in limited space charge effects.

1.3.2.2 Grain boundaries effect on electrochemical properties

Contrary to what is generally found for oxygen diffusion, several examples are present in literature on the enhancement of electrochemical properties in oxides by the effect of GBs. For instance, Lee *et al*. studied the oxygen surface exchange at grain boundaries in GDC.[6] They concluded that higher grain boundary densities in GDC results in a higher exchange current density, evidencing the effect of grain boundaries on surface kinetics. Importantly, they also showed an interesting analysis of the charge distribution near the grain boundaries measured by Kelvin probe microscopy, finding a positively charged core for GDC. Similar results also were found in other pure ionic conductors, such as yttria-stabilized zirconia[130,131] and ceria.[80,132,133] Moreover, evidences of enhanced electrochemical activity has been also found in the grain boundaries of strontium-doped lanthanum manganite (LSM)[72,113,114] and $La_{0.6}Sr_{0.4}Co_{0.2}Fe_{0.8}O_{3-\delta}$,[116,117] in accordance with the previously mentioned enhancement of the ionic conductivity along grain boundaries.

The origin of the enhancement is not yet fully understood and may have different causes depending on the specific properties of each material. Still, this enhancement appears to be strictly related to changes in the ionic composition and/or the electronic structure taking place in the GB core or in the space charge region. Indeed, both an increase of oxygen vacancies and a more facile transfer of electrons could generate a boost of ORR

and oxygen incorporation, depending on the rate limiting reaction of the process. Interestingly, the enhancement of electrochemical properties in GBs also extends to other fields, such as water splitting. Indeed, recently Heo *et al.* showed that in $LaMnO_3$ and $LaCoO_3$ GBs are responsible for an increase of Oxygen Evolution Reactions (OER) activity, mainly caused by an increase of structural distortions that promotes the electronic transfer between the metal and the oxygen.[134]

Overall, two main conclusions may arise from this brief discussion. On one side, according to current literature, it appears that GBs and structural defects may enhance the electrochemical activity in oxides. On the other side, it is evidenced that a more fundamental understanding of GB-related phenomena is needed for allowing a rational design of the next generation of RedOx solid state devices. Notably, the use of interfacial effects in metal oxide thin films have been indeed already proposed for the fabrication of new resistive switching functional films based on interfacial oxidation/reduction of MIECs.[37] In particular, the modified electronic concentration and band structure in the grain boundaries could potentially help to separate in the nanoscale ionic and electronic channels at high density. However, as highlighted by Messerschmitt *et al*., the specific role of thin film microstructural properties is still not fully understood, and further work is needed for understanding the effects of grain boundary density, and also strain, in the resistive switching mechanisms.[135]

1.4 Scope of the thesis

This thesis is devoted to the investigation, understanding and, ultimately, engineering of grain boundaries functional properties in perovskite MIEC thin films. The work is encompassed on the project ULTRASOFC (H2020-ERC-CG, grant agreement 681146), which aims to break the low temperature operating limits of μSOFC, nowadays set at *ca.* 400 ºC. The strategy explored for the improvement of electrochemical properties of cathode materials is the GB engineering in $La_{0.8}Sr_{0.2}MnO_{3\pm\delta}$, which, as shown in this introduction, was previously found to present a remarkable increase of oxygen mass transport properties when nanostructured in polycrystalline thin films. In detail, the thesis deals with the comprehension of physical and chemical characteristics of GBs in manganite thin films and their impact on the overall electrical and oxygen mass transport properties. Two strategies are explored for tuning the GB composition and functional properties: (i.) variation of Mn/(La+Sr) content in $La_{0.8}Sr_{0.2}Mn_yO_{3\pm\delta}$ (LSM_y) thin films and (ii.) substitution of Mn with Co in $La_{0.8}Sr_{0.2}Mn_{1-y}Co_yO_{3\pm\delta}$ (LSMC) thin films.

The thesis is organized as follows:

- **Chapter 2** presents the experimental techniques and the computational methods used in this thesis. A detailed explanation of the Pulsed Laser Deposition (PLD) technique used for the thin film growth is included.

- **Chapter 3** deals with the chemical and structural characterization of bulk and GBs in $La_{0.8}Sr_{0.2}Mn_yO_{3\pm\delta}$ thin films with variable Mn content. Here, the combinatorial approach used for depositing the LSM_y layers is also described. Finally, the chapter presents a discussion on the effects of varying the overall Mn chemical potential on the bulk and GBs compensation mechanisms. The results obtained are used to rationalize the functional properties presented in the following chapters.

- **Chapter 4** investigates the low temperature and high temperature electrical properties of LSM_y polycrystalline layers deposited on dielectric substrates. The GB properties are differentiated from the bulk ones by comparison with LSM_y epitaxial thin films with the same Mn content. Also, the defect chemistry of these layers is investigated by measuring the variation of electrical conductivity in different oxygen partial pressure environments.

- **Chapter 5** is devoted to the study of the high temperature electrochemical properties of LSM_y polycrystalline layers deposited on cells based on pure ionic conductor electrolyte substrates. The films are studied as a function of temperature, Mn content and oxygen partial pressure by electrochemical impedance spectroscopy, allowing differentiating the diffusion and surface

exchange contribution for each composition. The results are used to discuss the effect of Mn on the oxygen mass transport properties of LSM_y GBs.

- **Chapter 6** describes the effect of adding Co to the oxygen mass transport properties of LSMC thin films. These properties are measured by tracer experiments (oxygen isotopes) and the GB and bulk contribution are differentiated by fitting the oxygen profiles with a finite element method (FEM) model. Also, the electronic and optical properties of the thin films are measured. Finally, a discussion on the effect of Co on the surface exchange properties of LSMC GBs is reported.

As appendixes of the thesis, two complementary studies on the electrochemical properties of oxides thin films for low temperature solid state ionic devices (a novel electrolyte and a photoactivated electrode) are presented. In **Appendix A**, the deposition of superior oxygen ion conductive BICUVOX thin films for low temperature electrolyte in μSOFCs is investigated. In **Appendix B**, an *in-situ* study of point defects concentration in $La_{0.8}Sr_{0.2}FeO_{3-\delta}$ thin films by ellipsometry is reported. Both appendixes represent further strategies to decrease the operating temperature of μSOFCs within the framework of ULTRASOFC project, namely the substitution of state of art YSZ electrolyte by improved ionic conductors and the use of light to improve the oxygen incorporation in cathode thin films. Finally, in order to discuss the variation of defect chemistry at the interface level in the main part of the thesis, **Appendix C** shortly describes the description of the current understanding of the bulk defect chemistry of the $La_{0.8}Sr_{0.2}MnO_{3\pm\delta}$ parent compound.

References

1. Chiabrera, F., Garbayo, I. & Tarancón, A. in *Metal Oxide-Based Thin Film Structures* 409–439 (Elsevier, 2018). doi:10.1016/B978-0-12-811166-6.00017-0
2. Maier, J. Nanoionics: ionic charge carriers in small systems. *Phys. Chem. Chem. Phys.* **11,** 3011–3022 (2009).
3. Maier, J. Nanoionics: ion transport and electrochemical storage in confined systems. *Nat. Mater.* **4,** 805–815 (2005).
4. Tuller, H. L. Ionic conduction in nanocrystalline materials. *Solid State Ionics* **131,** 143–157 (2000).
5. Maier, J. Ionic conduction in space charge regions. *Prog. Solid State Chem.* **23,** 171–263 (1995).
6. Lee, W. *et al.* Oxygen Surface Exchange at Grain Boundaries of Oxide Ion Conductors. *Adv. Funct. Mater.* **22,** 965–971 (2012).
7. Saranya, A. M. *et al.* Engineering Mixed Ionic Electronic Conduction in $La_{0.8}Sr_{0.2}MnO_{3+\delta}$ Nanostructures through Fast Grain Boundary Oxygen Diffusivity. *Adv. Energy Mater.* **5,** 1500377 (2015).
8. Schweiger, S., Pfenninger, R., Bowman, W. J., Aschauer, U. & Rupp, J. L. M. Designing Strained Interface Heterostructures for Memristive Devices. *Adv. Mater.* **29,** 1605049 (2017).
9. Ishihara, T. *Perovskite Oxide for Solid Oxide Fuel Cells*. *Perovskite oxide for solid oxide fuel cells* (Springer, 2009). doi:10.1007/978-0-387-77708-5
10. Stambouli, A. B. & Traversa, E. Solid oxide fuel cells (SOFCs): a review of an environmentally clean and efficient source of energy. *Renew. Sustain. Energy Rev.* **6,** 433–455 (2002).
11. Adler, S. B. Factors governing oxygen reduction in solid oxide fuel cell cathodes. *Chem. Rev.* **104,** 4791–4843 (2004).
12. Carter, J. D., Cruse, T. A., Ingram, B. J. & Krumpelt, M. in *Handbook of Fuel Cells* (John Wiley & Sons, Ltd, 2010). doi:10.1002/9780470974001.f500040
13. Jiang, S. P. Development of lanthanum strontium manganite perovskite cathode materials of solid oxide fuel cells: A review. *J. Mater. Sci.* **43,** 6799–6833 (2008).
14. Sun, C., Hui, R. & Roller, J. Cathode materials for solid oxide fuel cells: A review. *J. Solid State Electrochem.* **14,** 1125–1144 (2010).
15. Bieberle-Hütter, A. *et al.* A micro-solid oxide fuel cell system as battery replacement. *J. Power Sources* **177,** 123–130 (2008).
16. Chiabrera, F., Garbayo, I., Alayo, N. & Tarancón, A. Micro solid oxide fuel cells: a new generation of micro-power sources for portable applications. in *Smart Sensors, Actuators, and MEMS VIII* **10246,** 102460S (2017).
17. Evans, A., Bieberle-Hütter, A., Rupp, J. L. M. M. & Gauckler, L. J. Review on microfabricated micro-solid oxide fuel cell membranes. *J. Power Sources* **194,** 119–129 (2009).
18. Evans, A. *et al.* Micro-solid oxide fuel cells: status, challenges, and chances. *Monatshefte für Chemie - Chem. Mon.* **140,** 975–983 (2009).
19. Garbayo, I. *et al.* Full ceramic micro solid oxide fuel cells: Towards more reliable MEMS power generators operating at high temperatures. *Energy Environ. Sci.* **7,** (2014).

20. Joo, J. H. & Choi, G. M. Simple fabrication of micro-solid oxide fuel cell supported on metal substrate. *J. Power Sources* **182,** 589–593 (2008).

21. Garbayo, I. *et al.* Electrical characterization of thermomechanically stable YSZ membranes for micro solid oxide fuel cells applications. *Solid State Ionics* **181,** 322–331 (2010).

22. Garbayo, I. *et al.* Porous $La_{0.6}Sr_{0.4}CoO_{3-\delta}$ thin film cathodes for large area micro solid oxide fuel cell power generators. *J. Power Sources* **248,** 1042–1049 (2014).

23. Garbayo, I. Integration of thin film based micro solid oxide fuel cells in silicon technology. (Universitat de Barcelona, 2013). at <http://hdl.handle.net/2445/52027>

24. Prinz, G. A. Magnetoelectronics. *Science (80-.).* **282,** 1660–1663 (1998).

25. Haghiri-Gosnet, A.-M. & Renard, J.-P. CMR manganites: physics, thin films and devices. *J. Phys. D. Appl. Phys.* **36,** R127–R150 (2003).

26. Copyright, C., Corporation, F., Salamon, M. B. & Jaime, M. The physics of manganites : Structure and transport Edited by Foxit Reader. *Rev. Mod. Phys.* **73,** 2005–2009 (2009).

27. Tokura, Y. & Tomioka, Y. Colossal magnetoresistive manganites. *J. Magn. Magn. Mater.* **200,** 1–23 (1999).

28. Gupta, A. *et al.* Grain-boundary effects on the magnetoresistance properties of perovskite manganite films. *Phys. Rev. B* **54,** R15629–R15632 (1996).

29. Mathur, N. D. *et al.* Large low-field magnetoresistance in $La_{0.7}Ca_{0.3}MnO_3$ induced by artificial grain boundaries. *Nature* **387,** 266–268 (1997).

30. Raveau, B. *et al.* Large domain wall magnetoresistance up to room temperature in $La_{0.7}Sr_{0.3}MnO_3$ bridges with nanoconstrictions. *J. Appl. Phys.* **89,** 6955–6957 (2002).

31. Siwach, P. K., Singh, H. K. & Srivastava, O. N. Low field magnetotransport in manganites. *J. Phys. Condens. Matter* **20,** (2008).

32. Pershin, Y. V. & Di Ventra, M. Memory effects in complex materials and nanoscale systems. *Adv. Phys.* **60,** 145–227 (2011).

33. Asamitsu, A., Tomioka, Y., Kuwahara, H. & Tokura, Y. Current switching of resistive states in magnetoresistive manganites. *Nature* **388,** 50–52 (1997).

34. Panda, D. & Tseng, T. Y. Perovskite oxides as resistive switching memories: A review. *Ferroelectrics* **471,** 23–64 (2014).

35. Yan, Z. B. & Liu, J. M. Resistance switching memory in perovskite oxides. *Ann. Phys. (N. Y).* **358,** 206–224 (2015).

36. Waser, R., Dittmann, R., Staikov, C. & Szot, K. Redox-based resistive switching memories nanoionic mechanisms, prospects, and challenges. *Adv. Mater.* **21,** 2632–2663 (2009).

37. Waser, R. & Aono, M. Nanoionics-based resistive switching memories. *Nat. Mater.* **6,** 833–840 (2007).

38. Sawa, A. Resistive switching in rapid advances in information technology rely on high-speed and large-capacity nonvolatile memories. *Mater. Today* **11,** 28–36 (2008).

39. Tuller, H. L. & Bishop, S. R. Point Defects in Oxides: Tailoring Materials Through Defect Engineering. *Annu. Rev. Mater. Res.* **41,** 369–398 (2011).

40. Anderson, H. U., Zhou, X.-D. & Dogan, F. in *Mixed Ionic Electronic Conducting Perovskites for Advanced Energy Systems* (eds. Orlovskaya, N. & Browning, N.) 303–312 (Springer Netherlands, 2004). doi:10.1007/978-1-4020-2349-1_30

41. Anderson, H. U. Defect chemistry of p-type perovskites. in *Proceedings of the 14th Risø International Symposium on Materials Science* (eds. Poulsen, F. W., Bentzen, J. ., Jacobsen, T., Skou, E. & Østergard, M. J. .) 1–18 (The Electrochemical Society, 1994).

42. Mizusaki, J., Yamauchi, S., Tagawa, H., Mima, Y. & Fueki, K. Nonstoichiometry of the perovskite-type oxides $La_{1-x}Sr_xCoO_{3-\delta}$. *J. Solid State Chem.* **80,** 102–111 (2003).

43. Mizusaki, J., Yoshihiro, M., Yamauchi, S. & Fueki, K. Nonstoichiometry and defect structure of the perovskite-type oxides $La_{1-x}Sr_xFeO_{3-\delta}$. *J. Solid State Chem.* **58,** (1985).

44. Mizusaki, J. *et al.* Oxygen nonstoichiometry and defect equilibrium in the perovskite-type oxides $La_{1-x}Sr_xMnO_{3+d}$. *Solid State Ionics* **129,** 163 (2000).

45. Steele, B. C. H. Oxygen Ion Conductors and Their Technological Applications. *Mater. Sci. Eng. B* **13,** 79–87 (1992).

46. Mizusaki, J. *et al.* Electronic conductivity , Seebeck coefficient , defect and electronic structure of nonstoichiometric $La_{1-x}Sr_xMnO_3$. *Solid State Ionics* **132,** 167–180 (2000).

47. Mizusaki, J., Sasamoto, T., Cannon, W. R. & Bowen, M. Electronic Conductivity, Seebeck Coefficient, and Defect Structure of $La_{1-x}Sr_xFeO_3$ (x=0.1, 0.25). *J. Am. Ceram. Soc.* **66,** 247–252 (1983).

48. Petrov, A. N., Voronin, V. I., Norby, T. & Kofstad, P. Crystal Structure of the Mixed Oxides $La_{0.7}Sr_{0.3}Co_{1-z}Mn_zO_{3-y}$ ($0<z<1$). *J. Solid State Chem.* **143,** 52–57 (1999).

49. Kuklja, M. M., Kotomin, E. a, Merkle, R., Mastrikov, Y. a & Maier, J. Combined theoretical and experimental analysis of processes determining cathode performance in solid oxide fuel cells. *Phys. Chem. Chem. Phys.* **15,** 5443–5471 (2013).

50. Adler, S. B. Limitations of charge-transfer models for mixed-conducting oxygen electrodes. *Solid State Ionics* **135,** 603–612 (2000).

51. Maier, J. On the correlation of macroscopic and microscopic rate constants in solid state chemistry. *Solid State Ionics* **112,** 197–228 (1998).

52. De Souza, R. & Kilner, J. a. Oxygen transport in $La_{1-x}Sr_xMn_{1-y}Co_yO_{3\pm\delta}$ perovskites Part I. Oxygen tracer diffusion. *Solid State Ionics* **106,** 175–187 (1998).

53. De Souza, R. A. & Kilner, J. a. Oxygen transport in $La_{1-x}Sr_xMn_{1-y}Co_yO_{3\pm\delta}$ perovskites: Part II. Oxygen surface exchange. *Solid State Ionics* **126,** 153–161 (1999).

54. Maier, J. *Physical Chemistry of Ionic Materials*. *Physical Chemistry of Ionic Materials* (John Wiley & Sons, Ltd, 2005). doi:10.1002/0470020229

55. Ishigaki, T., Yamauchi, S., Kishio, K., Mizusaki, J. & Fueki, K. Diffusion of oxide ion vacancies in perovskite-type oxides. *J. Solid State Chem.* **73,** 179–187 (1988).

56. De Souza, R. A. De, Kilner, J. A. & Walker, J. F. A SIMS study of oxygen tracer diffusion and surface exchange in $La_{0.8}Sr_{0.2}MnO_{3+\delta}$. *Mater. Lett.* **43,** 43–52 (2000).

57. Cooper, S. L., Egami, T., Goodenough, J. B. & Zhou, S. *Localized to Itinerant Electronic Transition in Perovskite Oxides*. (Springer, 2007).

58. Groot, F. M. F. d. *et al.* Oxygen 1s x-ray-absorption. *Phys. Rev. B* **40,** 5715–5723 (1989).

59. Wolfram, T. & Ellialtioglu, S. *Electronic and optical properties of D-band perovskites*. (Cambridge University Press, 2006). doi:10.1017/CBO9780511541292

60. To, J. & Goodenough, J. B. $LaMnO_{3+\delta}$ Revisited. *J. Solid State Chem.* **128,** 117–128 (1997).

61. Urushibara, A. *et al.* Insulator-metal transition and giant magnetoresistance in La_{1-}

$_xSr_xMnO_3$. *Phys. Rev. B* **51,** 103–109 (1995).

62. Baikov, Y. M., Nikulin, E. I., Melekh, B. T. & Egorov, V. M. Conductivity, Magnetoresistance, and Specific Heat of Oxygen-Deficient $La_{0.67}Sr_{0.33}MnO_{3-a}$ ($0 \leq a \leq 0.16$). *Phys. Solid State* **46,** 2086–2093 (2004).

63. Aidhy, D. S. & Weber, W. J. Microstructure design for fast oxygen conduction. *J. Mater. Res.* **31,** 2–16 (2016).

64. Garbayo, I., Baiutti, F., Morata, A. & Tarancón, A. Engineering mass transport properties in oxide ionic and mixed ionic- electronic thin film ceramic conductors for energy applications. *J. Eur. Ceram. Soc.* **39,** 101–114 (2019).

65. Wen, K., Lv, W. & He, W. Interfacial lattice-strain effects on improving the overall performance of micro-solid oxide fuel cells. *J. Mater. Chem. A* **3,** 20031–20050 (2015).

66. Frechero, M. Paving the way to nanoionics: atomic origin of barriers for ionic transport through interfaces. *Sci. Rep.* 1–9 (2015). doi:10.1038/srep17229

67. Diercks, D. R. *et al.* Three-dimensional quantification of composition and electrostatic potential at individual grain boundaries in doped ceria. *J. Mater. Chem. A* **4,** 5167–5175 (2016).

68. Feng, B. *et al.* Atomically ordered solute segregation behaviour in an oxide grain boundary. *Nat. Commun.* **7,** 11079 (2016).

69. Feng, B. *et al.* Atomic structure of a Σ3 [110]/(111) grain boundary in CeO_2. *Appl. Phys. Lett.* **100,** 3–6 (2012).

70. An, J. *et al.* Aberration-corrected TEM imaging of oxygen occupancy in YSZ. *J. Phys. Chem. Lett.* **4,** 1156–1160 (2013).

71. An, J. *et al.* Atomic scale verification of oxide-ion vacancy distribution near a single grain boundary in YSZ. *Sci. Rep.* **3,** 2680 (2013).

72. Navickas, E. *et al.* Fast oxygen exchange and diffusion kinetics of grain boundaries in Sr-doped $LaMnO_3$ thin films. *Phys. Chem. Chem. Phys.* **17,** 7659–7669 (2015).

73. Bae, J. *et al.* Influence of the grain size of samaria-doped ceria cathodic interlayer for enhanced surface oxygen kinetics of low-temperature solid oxide fuel cell. *J. Eur. Ceram. Soc.* **34,** 3763–3768 (2014).

74. Balluffi, R. W. & Mehl, R. F. Grain boundary diffusion mechanisms in metals. *Metall. Trans. A* **13,** 2069–2095 (1982).

75. Lejček, P. in *Grain Boundary Segregation in Metals* 5–24 (Springer Berlin Heidelberg, 2010). doi:10.1007/978-3-642-12505-8_2

76. Sutton, A. P. & Balluffi, R. W. *Interfaces in crystalline materials*. (Clarendon Press, 1995).

77. Brandon, D. G. *The structure of high angle grain boundaries*. *Acta Metallurgica* **14,** (1966).

78. Yoshida, H., Yokoyama, K., Shibata, N., Ikuhara, Y. & Sakuma, T. High-temperature grain boundary sliding behavior and grain boundary energy in cubic zirconia bicrystals. *Acta Mater.* **52,** 2349–2357 (2004).

79. Hojo, H. *et al.* Atomic structure of a CeO_2 grain boundary: The role of oxygen vacancies. *Nano Lett.* **10,** 4668–4672 (2010).

80. Feng, B. *et al.* Atomic structures and oxygen dynamics of CeO_2 grain boundaries. *Sci. Rep.* **6,** 20288 (2016).

81. Jia, C. L. & Urban, K. Atomic-Resolution Measurement of Oxygen Concentration in Oxide Materials. *Science (80-.).* **303,** 2001–2004 (2004).

82. Zhang, Z., Sigle, W. & Rühle, M. Atomic and electronic characterization of the a[100] dislocation core in $SrTiO_3$. *Phys. Rev. B* **66,** 094108 (2002).

83. Choi, S. Y. *et al.* Assessment of Strain-Generated Oxygen Vacancies Using $SrTiO_3$ Bicrystals. *Nano Lett.* **15,** 4129–4134 (2015).

84. Liu, B., Cooper, V. R., Zhang, Y. & Weber, W. J. Segregation and trapping of oxygen vacancies near the $SrTiO_3$ Σ3 (112) [1¯10] tilt grain boundary. *Acta Mater.* **90,** 394–399 (2015).

85. Aidhy, D. S., Zhang, Y. & Weber, W. J. Impact of segregation energetics on oxygen conductivity at ionic grain boundaries. *J. Mater. Chem. A* **2,** 1704–1709 (2014).

86. Arora, G. & Aidhy, D. Segregation and Binding Energetics at Grain Boundaries in Fluorite Oxides. *J. Mater. Chem. A* 4026–4035 (2017). doi:10.1039/C6TA09895A

87. Lee, H. B., Prinz, F. B. & Cai, W. Atomistic simulations of grain boundary segregation in nanocrystalline yttria-stabilized zirconia and gadolinia-doped ceria solid oxide electrolytes. *Acta Mater.* **61,** 3872–3887 (2013).

88. De Souza, R. A. The formation of equilibrium space-charge zone at grain boundaries in the perovskite oxide $SrTiO_3$. *Phys. Chem. Chem. Phys.* **11,** 9939–9969 (2009).

89. Mebane, D. S. & De Souza, R. A generalised space-charge theory for extended defects in oxygen-ion conducting electrolytes: from dilute to concentrated solid solutions. *Energy Environ. Sci.* **4,** 1166–1169 (2015).

90. Waser, R. & Hagenbeck, R. Grain boundaries in dielectric and mixed conducting ceramics. *Acta Mater.* **48,** 797–825 (2000).

91. Göbel, M. C., Gregori, G. & Maier, J. Numerical calculations of space charge layer effects in nanocrystalline ceria. Part I: comparison wih the analytical models and derivation o improved analytical solutions. *Phys. Chem. Chem. Phys.* **16,** 10214 (2014).

92. Guo, X. & Waser, R. Electrical properties of the grain boundaries of oxygen ion conductors: Acceptor-doped zirconia and ceria. *Prog. Mater. Sci.* **51,** 151–210 (2006).

93. Kim, S., Fleig, J. & Maier, J. Space charge conduction: Simple analytical solutions for ionic and mixed conductors and application to nanocrystalline ceria. *Phys. Chem. Chem. Phys.* **5,** 2268–2273 (2003).

94. Guo, X. & Maier, J. Grain Boundary Blocking Effect in Zirconia: A Schottky Barrier Analysis. *J. Electrochem. Soc.* **148,** E121 (2001).

95. Guo, X. & Ding, Y. Grain Boundary Space Charge Effect in Zirconia. *J. Electrochem. Soc.* **151,** J1 (2004).

96. Kim, S. & Maier, J. On the Conductivity Mechanism of Nanocrystalline Ceria. *J. Electrochem. Soc.* **149,** J73 (2002).

97. Guo, X., Sigle, W. & Maier, J. Blocking grain boundaries in yttria-doped and undoped ceria ceramics of high purity. *J. Am. Ceram. Soc.* **86,** 77–87 (2003).

98. Denk, I., Munch, W. & Maier, J. Partial Conductivities in $SrTiO_3$: Bulk Polarization Experiments, Oxygen Concentration Cell Measurements, and Defect-Chemical Modeling. *J. Am. Ceram. Soc.* **78,** 3265–3272 (1995).

99. Moos, R. & Hardtl, K. H. Defect chemistry of donor-doped and undoped strontium titanate ceramics between 1000 degrees and 1400 degrees C. *J. Am. Ceram. Soc.* **80,** 2549–2562 (1997).

100. Waser, R. Electronic properties of grain boundaries in $SrTi0_3$ and $BaTiO_3$ ceramics. *Solid State Ionics* **75,** 89–99 (1995).

101. Lupetin, P., Gregori, G. & Maier, J. Mesoscopic charge carriers chemistry in nanocrystalline $SrTiO_3$. *Angew. Chemie - Int. Ed.* **49,** 10123–10126 (2010).

102. Tschöpe, A., Sommer, E. & Birringer, R. Grain size dependence of electrical conductivity in polycrystalline cerium oxide I. Experiments. *Solid State Ionics* **139,** 255–265 (2001).

103. Kim, S. The intrinsic origin of the grain-boundary resistance in Sr-doped $LaGaO_3$. *Monatshefte fur Chemie* **140,** 1053–1057 (2009).

104. Park, H. J. & Kim, S. Space charge effects on the interfacial conduction in Sr-doped lanthanum gallates: A quantitative analysis. *J. Phys. Chem. C* **111,** 14903–14910 (2007).

105. Maier, J. Defect chemistry and ion transport in nanostructured materials: Part II. Aspects of nanoionics. *Solid State Ionics* **157,** 327–334 (2003).

106. Balaya, P., Jamnik, J., Fleig, J. & Maier, J. Mesoscopic Hole Conduction in Nanocrystalline $SrTiO_3$. *J. Electrochem. Soc.* **154,** P69 (2007).

107. De Souza, R. A. *et al.* Oxygen diffusion in nanocrystalline yttria-stabilized zirconia: the effect of grain boundaries. *Phys. Chem. Chem. Phys.* **10,** 2067–2072 (2008).

108. Kim, S. *et al.* Strong immobilization of charge carriers near the surface of a solid oxide electrolyte. *J. Mater. Chem.* **20,** 3855 (2010).

109. Sun, L., Marrocchelli, D. & Yildiz, B. Edge dislocation slows down oxide ion diffusion in doped CeO_2 by segregation of charged defects. *Nat. Commun.* **6,** 6294 (2015).

110. Marrocchelli, D., Sun, L. & Yildiz, B. Dislocations in $SrTiO_3$: Easy to Reduce but Not so Fast for Oxygen Transport. *J. Am. Chem. Soc.* **137,** 4735–4748 (2015).

111. Ramadan, A. H. H. & De Souza, R. A. Atomistic simulations of symmetrical low-angle [100] (011) tilt boundaries in $SrTiO_3$. *Acta Mater.* **118,** 286–295 (2016).

112. Waldow, S. P. & De Souza, R. A. Computational Study of Oxygen Diffusion along a [100] Dislocations in the Perovskite Oxide $SrTiO_3$. *ACS Appl. Mater. Interfaces* **8,** 12246–12256 (2016).

113. Saranya, A. M. *et al.* Engineering Mixed Ionic Electronic Conduction in $La_{0.8}Sr_{0.2}MnO_{3+\delta}$ Nanostructures through Fast Grain Boundary Oxygen Diffusivity. *Adv. Energy Mater.* **5,** 1500377 (2015).

114. Navickas, E. *et al.* Dislocations Accelerate Oxygen Ion Diffusion in $La_{0.8}Sr_{0.2}MnO_3$ Epitaxial Thin Films. *ACS Nano* **11,** 11475–11487 (2017).

115. Druce, J., Tellez, H., Ishihara, T. & Kilner, J. A. Surface Composition and Oxygen Exchange Properties of Alkaline Earth-Free Perovskites; $LaCo_{0.6}Ni_{0.4}O_3$. *ECS Trans.* **72,** 71–80 (2016).

116. Develos-Bagarinao, K., Kishimoto, H., De Vero, J., Yamaji, K. & Horita, T. Effect of $La_{0.6}Sr_{0.4}Co_{0.2}Fe_{0.8}O_{3-\delta}$ microstructure on oxygen surface exchange kinetics. *Solid State Ionics* **288,** 6–9 (2015).

117. Bagarinao, K. D.- *et al.* Probing Oxide Ion Transport in Fluorite and Perovskite Oxides for Solid Oxide Fuel Cells. *ECS Trans.* **72,** 139–148 (2016).

118. Guo, X., Zhang, Z. L., Sigle, W., Wachsman, E. & Waser, R. Schottky barrier formed by network of screw dislocations in $SrTiO_3$. *Appl. Phys. Lett.* **87,** 162105 (2005).

119. De Souza, R. A. *et al.* Electrical and structural characterization of a low-angle tilt grain boundary in iron-doped strontium titanate. *J. Am. Ceram. Soc.* **86,** 922–928 (2003).

120. Rodewald, S., Fleig, J. & Maier, J. Microcontact Impedance Spectroscopy at Single Grain Boundaries in Fe-doped $SrTiO_3$ Polycristals. *J. Am. Ceram. Soc.* **30,** 521–530 (2001).

121. Guo, X. Peculiar size effect in nanocrystalline $BaTiO_3$. *Acta Mater.* **61,** 1748–1756 (2013).

122. Preis, W. & Sitte, W. Electrical properties of grain boundaries in interfacially controlled functional ceramics. *J. Electroceramics* **34,** 185–206 (2014).

123. Chiang, Y.-M. & Takagi, T. Grain-Boundary Chemistry of Barium Titanate and Strontium Titanate: I, High-Temperature Equilibrium Space Charge. *J. Am. Ceram. Soc.* **73,** 3278–3285 (1990).

124. Polfus, J. M., Toyoura, K., Oba, F., Tanaka, I. & Haugsrud, R. Defect chemistry of a $BaZrO_3$ Σ3 (111) grain boundary by first principles calculations and space–charge theory. *Phys. Chem. Chem. Phys.* **14,** 12339–12346 (2012).

125. Nolan, M., Parker, S. C. & Watson, G. W. The electronic structure of oxygen vacancy defects at the low index surfaces of ceria. *Surf. Sci.* **595,** 223–232 (2005).

126. Tschöpe, A. & Saarlandes, U. Grain Size-Dependent Electrical Conductivity of Polycrystalline Cerium Oxide II : Space Charge Model Grain size-dependent electrical conductivity of polycrystalline cerium oxide II : Space charge model. *Solid State Ionics* **139,** 267–280 (2015).

127. Adepalli, K. K., Kelsch, M., Merkle, R. & Maier, J. Enhanced ionic conductivity in polycrystalline TiO_2 by‘ “one-dimensional doping”’. *Phys. Chem. Chem. Phys. Phys. Chem. Chem. Phys* **16,** 4942–4951 (2014).

128. Adepalli, K. K., Kelsch, M., Merkle, R. & Maier, J. Influence of line defects on the electrical properties of single crystal TiO_2. *Adv. Funct. Mater.* **23,** 1798–1806 (2013).

129. Ikeda, J. A. S. & Chiang, Y. Space Charge Segregation at Grain Boundaries in Titanium Dioxide: I, Relationship between Lattice Defect Chemistry and Space Charge Potential. *J. Am. Ceram. Soc.* **76,** 2437–46 (1993).

130. Park, J. S., An, J., Lee, M. H., Prinz, F. B. & Lee, W. Effects of surface chemistry and microstructure of electrolyte on oxygen reduction kinetics of solid oxide fuel cells. *J. Power Sources* **295,** 74–78 (2015).

131. Park, J. S., Holme, T. P., Shim, J. H. & Prinz, F. B. Improved oxygen surface exchange kinetics at grain boundaries in nanocrystalline yttria-stabilized zirconia. *MRS Commun.* **2,** 107–111 (2012).

132. Develos-Bagarinao, K., Yokokawa, H., Horita, T., Yamaji, K. & Kishimoto, H. Evidence for enhanced oxygen surface exchange reaction in nanostructured Gd_2O_3 - doped CeO_2 films. *Nanotechnology* **26,** 215401 (2015).

133. Bae, J. *et al.* Enhanced Oxygen Reduction Reaction in Nanocrystalline Surface of Samaria-Doped Ceria via Randomly Distributed Dopants. *J. Am. Ceram. Soc.* **99,** 4050–4056 (2016).

134. Heo, Y. *et al.* Symmetry-Broken Atom Configurations at Grain Boundaries and Oxygen Evolution Electrocatalysis in Perovskite Oxides. *Adv. Energy Mater.* **8,** 1–10 (2018).

135. Messerschmitt, F., Kubicek, M., Schweiger, S. & Rupp, J. L. M. Memristor Kinetics and Diffusion Characteristics for Mixed Anionic-Electronic $SrTiO_{3-\delta}$ Bits: The Memristor-Based Cottrell Analysis Connecting Material to Device Performance. *Adv. Funct. Mater.* **24,** 7448–7460 (2014).

136. Kröger, F. & Vink, H. Relations between the concentrations of imperfections in

crystalline solids. *Solid state Phys.* **3,** 307–435 (1956).

2. Experimental methods

2.1 Introduction

The aim of this chapter is to give a general view of the experimental techniques and methods used in this thesis. Section **2.2** is devoted to the description of the Pulsed Laser Deposition (PLD) technique used for growing the thin films under study. The main theoretical concepts behind PLD are discussed, paying particular attention to the effect of the different deposition parameters on the thin film properties (structure, composition, phase, *etc*.). Then, the particular Large Area PLD (LA-PLD) system employed in this thesis for depositing either small or large area thin films is presented; the latter mostly meant for the growth of variable continuous compositionally spread films through a combinatorial approach. In Section **2.3**, the main microstructural characterization techniques used for studying the deposited thin films are introduced. Section **2.4** describes the methods and setup used for measuring the electrical and oxygen mass transport properties of the thin films. Finally, in section **2.5**, the finite element model used for simulating the oxygen transport properties in $La_{0.8}Sr_{0.2}(Mn_{1-x}Co_x)_{0.85}O_{3\pm\delta}$ (LSMC) thin films is discussed.

2.2 Thin film fabrication by Pulsed Laser Deposition

Thin films offer an ideal system for studying interface effects in different applications, such as oxygen mass transport properties,[1–4] catalysis,[5–8] memristive devices,[9,10] high temperature superconductors[11] and many others. The great advantage of investigating thin films respect to bulk samples derives from the dominant role of interfaces in such small volumes, allowing the identification and the quantification of their impact on the material functional properties. In this sense, an interface can be found in the strained atomic layers between a thin film and the substrate, the surface of the thin film or the grain boundaries in a polycrystalline layer with nanometric grain sizes.

Among the various techniques available for the fabrication of oxide thin films, two major categories arise: Chemical Vapour Deposition (CVD) and Physical Vapour Deposition (PVD). In CVD techniques, the deposition process occurs through the surface chemical reaction of one or more volatile precursors in a controlled atmosphere. On the contrary, in PVD techniques the deposition process is characterized by the condensation of a material from the vapour phase into the thin film solid structure. Nowadays, the most important PVD systems are: sputtering, Molecular Beam Epitaxy (MBE), evaporation and Pulsed Laser Deposition (PLD). Among these techniques, MBE and PLD have emerged in the last years as the most efficient methods for the preparation of high quality thin films, due to their great versatility in the choice of growing compounds, the low level of impurities in the deposited films and the possibility of controlling the thickness down to the atomic layer.[12,13]

In this thesis, PLD is employed as a tool for fabricating epitaxial and polycrystalline Mixed Ionic Electronic Conductors and oxide ion conducting electrolyte thin films.

2.2.1 Pulsed Laser Deposition (PLD)

PLD is a technique based on the use of a high energy pulsed laser source for the evaporation of a target material into a laser plume. Although the employment of a laser for the deposition of thin films date back to the 1960s,[14] the real development of PLD started in 1987, when Dr. Venkatesan and his co-workers at Bell labs (USA) successfully deposited $YBa_2Cu_3O_{7-x}$ thin films for high temperature superconductors application.[15,16] From that moment, the potential of PLD was widely acknowledged, leading to a fast development of reliable systems for the deposition of oxide thin films for numerous applications.[12]

The PLD operation principle is based on the ablation of a target material in controlled vacuum conditions with a pulsed laser focused onto it. Due to the high energy of the laser, each pulse melt, vaporize and ionize a small amount of material from the target. The ablated material is then rapidly ejected perpendicular to the target surface, generating a plasma plume in the vacuum chamber, composed by atoms, electrons, ions,

molecules and clusters. As a result of the generation of a pressure gradient, the plume expands adiabatically towards the substrate, where the various species condense, resulting in the layer growth.

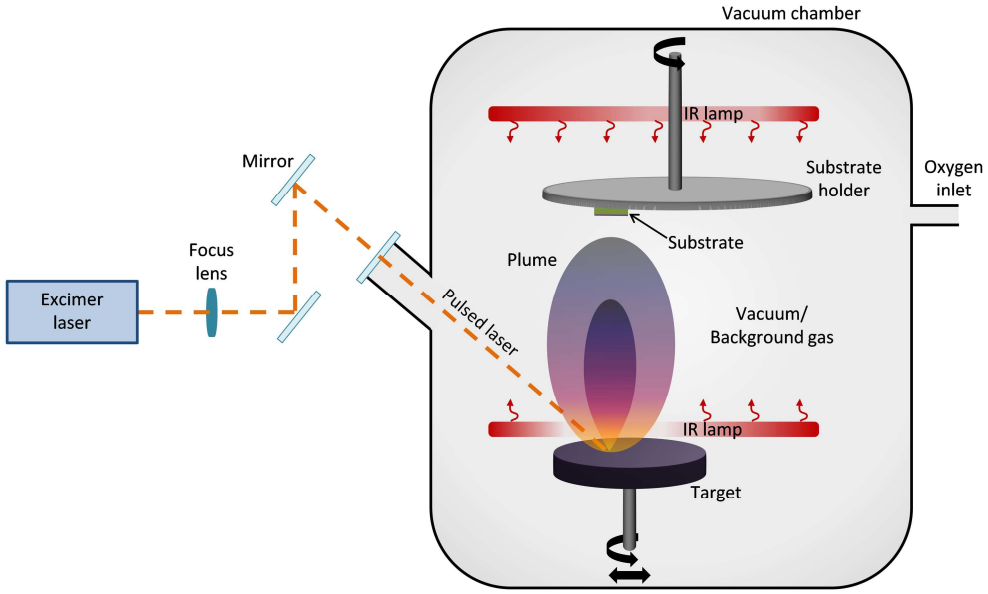

Figure 2.1 Illustration of a PLD system.

The typical configuration of a PLD system is shown in **Figure 2.1**. The main components of the system are: the excimer laser, the optical system, the vacuum chamber, the heating system, the substrate stage and the target holder. The laser used in PLD is generally based on UV emission, which is then focalized onto the target material by the optical lenses. The vacuum chamber is maintained under high vacuum condition to reduce the contaminants in the system. During the deposition of oxide materials, a certain flow of oxygen is generally introduced in the chamber, which is held to a controlled pressure (between $P = 6.67 \cdot 10^{-3} - 2.67 \cdot 10^{-1}$ mbar in the PLD used in this work). The substrate stage is heated to the desired temperature (T_d) by the heating system, which can be an ohmic resistance or infrared (IR) lamps. The target stage can be rotated and moved for homogenizing the ablated surface and avoiding the formation of macroscopic and microscopic defects.

The advantage of using PLD in the deposition of thin films comes from several different aspects, such as: (i.) the possibility of reproducing thin films with complex stoichiometry, (ii.) the decoupling of the laser-target interaction from other parameters that controls the plume dynamics (temperature, pressure, substrate-to-target distance and type of substrate), (iii.) the high nucleation rates on the substrate promoted by the high energy of the plasma plume species and (iv.) the possibility of finely control the growth rate thanks to the pulsed laser nature of the deposition.[17] Nevertheless, the optimization of deposition conditions for growing thin films with the desired phase, composition and structure is a very challenging process, which requires taking into consideration all the different aspects involved in the PLD technique. The PLD

deposition process consists of three different steps: (a.) laser-target interaction, (b.) plasma plume propagation and (c.) thin film growth dynamics. In the following, these sub-processes are briefly described, paying particular attention to the deposition conditions that most influence each deposition step and their effects on the final thin film characteristics.

In this thesis, the choice of PLD parameters is especially relevant due to the large area PLD system (LA-PLD) used for the thin films deposition, which present larger target-substrate distances and bigger laser spot sizes than usual laboratory scale PLDs (see section **2.2.2**). Therefore, some of the effects described in the following will be even more accentuated and must be taken in account for growing films with the entire set of desired characteristics. In detail, aspects of interest for this thesis are: (i.) the columnar grain growth, (ii.) the controlled porosity, (iii.) the stoichiometry of the thin films and (iv.) the epitaxial growth of the thin films.

2.2.1.1 Laser-target interaction

The formation of the plasma plume can be governed by thermal, non-thermal (electronic) and mechanical interaction between the laser photons and the target material.[12] For pulses of ns width and ceramic materials, the ablation process is mainly dominated by thermal contributions.[18] According to this phenomenon, when the laser hit the surface of the target the photons are absorbed by the material, giving rise to an increase of the surface temperature that can exceed the melting point of ceramics. This leads to a melting of the surface and a rapid evaporation of the species, which are ejected perpendicular to the surface in a plasma plume.

The laser ablation is possible if the photon energy is higher than a certain threshold energy, which depends on the optical properties of the material and the laser excitation wavelength. For this reason, UV laser are generally used in PLD system (such as KrF (248 nm), ArF (193 nm), and F_2 (157 nm)), because the short wavelength promotes the ablation of atoms closest to the surface. Although the threshold energy varies from material to material, in the perovskite family under study this value is generally close to 0.5 J/cm^2 (expressed in laser fluence, F). For instance, the energy threshold of $SrTiO_3$, was found to be closer to 0.4 J/cm^2,[18] while in $La_{0.4}Ca_{0.6}MnO_3$ to 0.5 J/cm^2.[19] For fluence energies higher than this value, the ablated material quantity (hence the thin film growth rate) increases logarithmically. Accordingly, the laser fluence is the first parameter that needs to be optimized for obtaining an acceptable and reproducible ablation rate.

Moreover, the laser fluence was also found to influence the stoichiometry of the plasma plume for multi-element materials. Indeed, high values of fluence can determine a preferential ablation of one particular element, giving rise to deviations of the stoichiometry in the deposited film. This mechanism was observed in $SrTiO_3$, where a

progressive accumulation of Sr in the target surface (i.e. preferential ablation of Ti) was observed, passing from F = 0.8 J/cm^2 to 1.7 J/cm^2.[20]

In this thesis, laser fluence was fixed to ~1 J/cm^2 for all the materials deposited, ensuring surpassing the threshold energy for ablation.

2.2.1.2 Plasma plume propagation

The continuous interaction between the laser and the material leads to the plasma formation, which rapidly expands perpendicular to the target towards the substrate. It is possible to recognize three different regimes in the plasma expansion from the target to the substrate. The initial stage is characterized by a highly anisotropic expansion of the front plume, with a velocity around 10^4 m/s (regime **1**).[21–23] Then, the plasma collisions with the background gas confine and slow down the plume expansion, giving rise to a more isotropic motion (regime **2**). In this region, the front plume tends to decrease its velocity, eventually stopping for high distances (see **Figure 2.2a**).[24] After this point, the plume enters in a pure diffusive regime (regime **3**), in which the deposition rate drastically reduces and the plume species slowly diffuse to the substrate.[25]

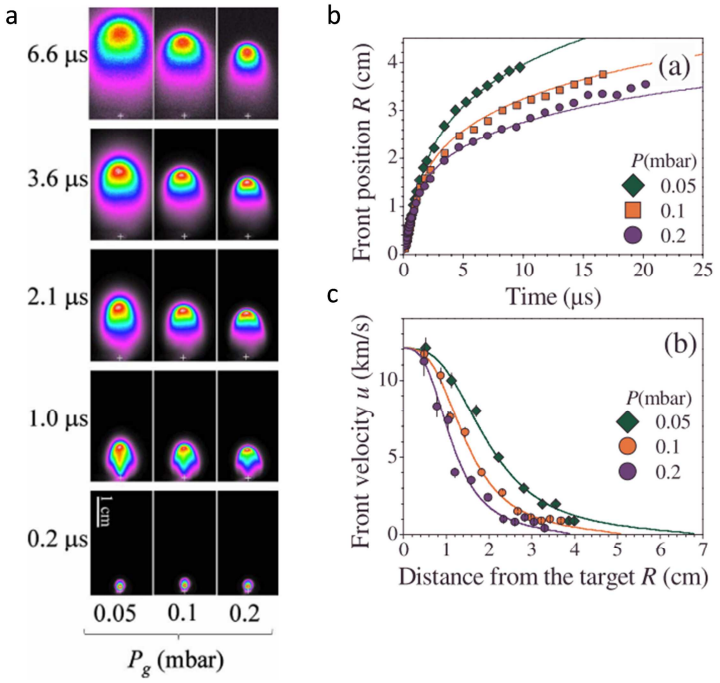

Figure 2.2 Evolution of plume dynamics in PLD deposition. **a,** Sequence of plume intensities of $La_{0.7}Sr_{0.3}MnO_3$ measured by fast intensified-charge-coupled-device (ICCD) at different delay times after the laser pulse and for different oxygen deposition pressure. The front position vs the delay time and the front velocity vs the distance from the target are depicted in **b** and **c**, respectively. The symbols refers to the experimental points measured by ICCD while the lines to the fitting of the model developed by Sambri *et al.*[24] All the figures are reproduced with permission.[24] Copyright AIP Publishing.

Many approaches were proposed in literature for describing the plume dynamics in a background gas pressure.[26,27] A rather simple but useful model was suggested by

Sambri *et al.*,[24] who considered the plume as a hemispherical front that propagates radially, experiencing the braking force due to a background pressure. As shown in **Figure 2.2b** and **c**, the model well reproduces the front velocity as a function of the time and distance from the target. The model predicts that the front velocity comes to a rest for a distance R_{st} equal to:

$$R_{st} \propto \left(\frac{M_P v_0^2}{P}\right)^{1/3} \qquad \text{Eq. 2.1}$$

Where M_p is the mass of material ejected from the target, v_0 is the velocity of the plume in the early stage and P is the deposition pressure in the chamber. The mass M_p can be estimated as: $M_p \approx \rho_t S_t \delta_a$, where ρ_t is the density of the target, S_t the spot size and δ_a the ablation rate (nm/pulse), which is in turn proportional to the laser fluence.[24] Equation **2.1** is a useful expression for estimating the type of regime in which the deposition takes place (i.e. plume-background dominated or purely diffusive).

The approach of Sambri *et al.*[24] also stresses the main deposition parameters that can influence the plume dynamics, namely the laser fluence, the deposition pressure and the target-to-substrate distance. Changing the laser energy and spot size will affect the total mass of material ablated per pulse, modifying the plasma dimensions and R_{st}. Increasing the deposition pressure confines the expansion front in a smaller plume, decreasing the growth rate and causing the diffusive regime to start at shorter distances. Finally, the target-to-substrate distance directly determines the regime at which the deposition takes place.

The plasma-background interaction are particularly important in the growth of PLD thin films, since they are believed to be one of the major causes of non-correct stoichiometric transfer in PLD thin films.[19,20,28] Indeed, many studies have shown that varying deposition pressure or the target-to-substrate distance lead to drastic variation of cationic thin film composition. As a general trend, three different zones can be identified varying the deposition pressure (or/and the target-to-substrate distance).[28] In Vacuum and for small target-substrate distances (regime **1**), the films are generally characterized by nearly a stoichiometric condition, mainly due to the absence of plume-background interactions. Increasing the deposition pressure, the frequency of scattering events between the plasma and the background gas species increases, giving rise to the decrease of front plume velocity shown in **Figure 2.2**. In this regime (regime **2**), the lighter elements (L) of the plume are scattered to higher angles than the heavier ones (H), meaning that the deposition rate of H is higher than L. Therefore, the thin films deposited perpendicular to the target may be characterized by a substantial decrease of the L/H ratio.[19] Keeping raising the background pressure, the plume velocity continually decreases and the diffusive regime starts to dominate the plasma expansion (regime **3**). Under these conditions, the scattering of plume species is less relevant, progressively reducing the differences between H and L deposition rates. Therefore, in this regime a more correct stoichiometric transfer of the target material is foreseen.

The plasma-background interactions are more relevant in materials in which the atomic mass ratio L/H is low, for instance in Li-based or Bi-based compounds.[29] It is also necessary to note that the oxygen is not generally considered in these interactions, since it was demonstrated that when depositing in oxygen background pressure (*i.e.* the most common situation when depositing ceramic films), most of the oxygen present in the thin films comes from the gas in the chamber.[30] Overall, deposition pressure and target-substrate distance are key parameters for influencing the plasma stoichiometry in PLD.

In this thesis, the influence of background pressure and target-to-substrate distance in the film stoichiometry has been found to severely impact the thin films stoichiometry, see Chapters **3** and **6**, and Appendix **A**.

2.2.1.3 Thin film growth dynamics

The films growth process starts when the plume species are adsorbed on the heated substrate surface and then continues with the reaction between arriving particles, giving rise to the film nucleation. The way in which this process takes place determines the structure and morphology of the films. In thermodynamically stable systems, three general growth modes can be considered:[12,31] (i.) the Frank-van der Merwe model (**Figure 2.3a**), consisting in a layer by layer 2 dimensional growth leading to the formation of highly ordered epitaxial films; (ii.) the Volmer-Weber model (**Figure 2.3b**), characterised by a three dimensional island growth, giving rise to the formation of polycrystalline thin films and (iii.) the Stranski-Krastinov model (**Figure 2.3b**), a mixed growth mode in which the first stages of the growth are characterized by two dimensional layer by layer formation, followed by a three dimensional growth and formation of islands, due to a change in energetics of the deposited monolayers.

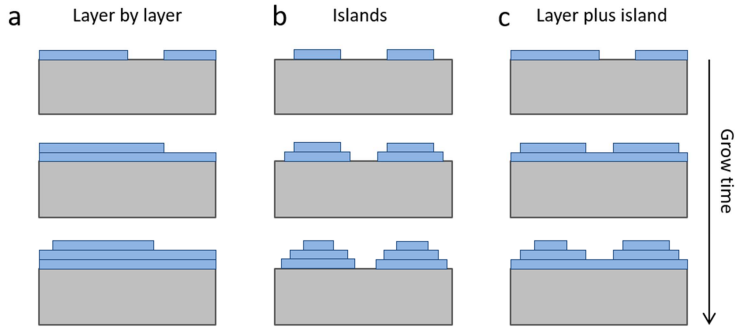

Figure 2.3 Sketch of the three basic growth modes of thin films. **a**, Frank-van der Merwe model. **b**, the Stranski-Krastinov model. **c**, the Volmer-Weber model.

In general, in order to allow an epitaxial layer by layer growth, the lattice parameters of the substrate and the film must be comparable and the energy of the plume species high enough to allow high surface mobility (high temperature, low deposition pressure). Also, the composition of the plasma plume may play a role in the diffusivity of the adsorbed species, giving rise to complex interactions between plume dynamics and film

growth.[32] If a substrate with lattice parameter strongly different from the target material is used, the thin films will be mainly characterized by a polycrystalline nature. Nevertheless, the deposition parameters still largely influence the layer microstructure, affecting the grain shape, the grain size and the micro-porosity. As a general example, **Figure 2.4** presents a sketch of the combined effect of substrate temperature and oxygen background pressure on the microstructure of yttria stabilized zirconia thin films, for intermediated temperature range (according to Thornton theory[31,33] $T_d < 0.5$ T_m, with T_m melting temperature of the material).[34] At low temperature and low pressure (case **A**), the poor mobility of the adsorbed species does not allow a sufficient diffusion, leading to random structure of the grains and possible micro-porosity. Increasing the temperature (case **B**), the surface mobility increases and a smooth dense columnar structure with nanosized grains is obtained. The pressure also influences the porosity of the thin films, due to plasma-background interactions that reduce the species energy and prevent full density (case **C** and **D**). Overall, deposition conditions needs to be carefully optimized for the growth of films with the desired composition, crystalline orientation and microstructure.

In this thesis, high temperature (T = 700 ºC) and low oxygen pressure conditions (P = 0.026 mbar) were chosen for obtaining fully-dense nanocrystalline and epitaxial thin films.

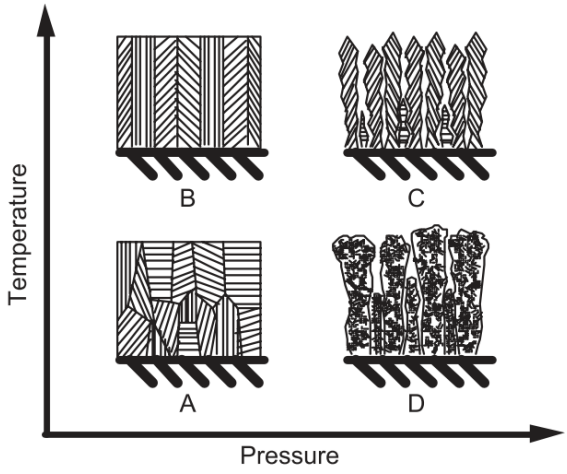

Figure 2.4 Combined effect of pressure and temperature on the microstructure of ceramic oxides thin films. The figure is reproduced with permission.[34] Copyright AIP Publishing

2.2.2 Large area pulsed laser deposition (LA-PLD)

Despite the previously described advantages of PLD techniques in the deposition of high-quality thin films, the small dimensions of the plasma plume limit the deposition to *ca.* 1 cm x 1 cm substrates, hindering the implementation of PLD at industrial level.[35] In order to overcome this problem, many efforts have been devoted in the development of a large area PLD (LA-PLD), able to deposit homogenous films in 4" and even larger

substrates (up to 12" and multi-wafer systems). This would allow the complete integration of PLD thin films in standard batch microfabrication processes.

In general, LA-PLD systems are characterized by a larger spot size and higher laser energies (in order to achieve similar laser fluence of ordinary PLD), which results in a larger quantity of material ejected with each pulse and, therefore, larger plume sizes. Also, in order to keep the film growth conditions similar to the small scale PLD, the target to substrate distances need to be adapted. Indeed, as commented in section **2.2.1.1**, since the plume stopping distance (R_{st}) is proportional to the ablated material, R_{st} will be larger in LA-PLD, meaning that the target-to-substrate distance must be increased (typical values are d = 9 – 12 cm) for avoiding the recollection of plume species in an early stage of the plume development. Another peculiar characteristic of LA-PLD is that the laser spot position on the target is not fixed but can be varied with a motorized mirror. This, along with the use of larger target materials and a rotating substrate holder, allows the deposition of highly homogenous thin films on the large substrates. In order to keep the spot size on the target material constant, a motor driven focus lens is couple to the motorized mirror. **Figure 2.5** shows the LA-PLD used in this work for the deposition of thin films on both small area substrates and on large area wafers in the combinatorial approach.

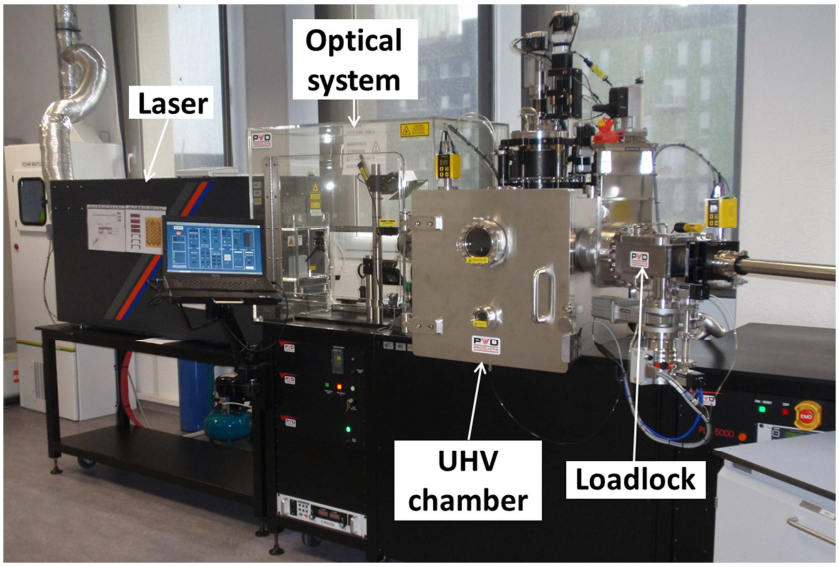

Figure 2.5 Large area PLD-5000 from PVD® located at IREC.

The conclusions drafted in the previous sections on the film growth mechanism and structure upon the variation of deposition conditions perfectly holds also in the case of LA-PLD. Indeed, especially when the position of the laser is not varied during the deposition, the effects observed in small scale PLD are also observed in LA-PLD. Nevertheless, it is necessary to note that, due to the larger target to substrate distance, some aspects connected to plasma-background interactions may be enhanced, leading to a more marked variation of stoichiometry in the thin films varying the deposition pressure (see Appendix **A**).

2.2.3 Combinatorial pulsed laser deposition (C-PLD)

Combinatorial PLD refers to the simultaneous (combined) deposition of two different target materials for the growth of a continuous composition spread thin film over large area substrates. In C-PLD, two main approaches can be adopted: (i.) the simultaneous ablation of the two different materials by splitting the laser beam or (ii.) the alternate deposition of small quantities of each material forming a multilayer.[36,37] In this work, the latter is adopted, taking advantage of the special features of the LA-PLD at IREC facilities.

The employed combinatorial PLD method is based on the superposition of large-area films deposited from two parent compounds in two different positions of a single wafer. **Figure 2.6a** shows a sketch of the C-PLD cycle deposition for the first two layers of $La_{0.8}Sr_{0.2}MnO_{3\pm\delta}$ (LSM) and $La_{0.8}Sr_{0.2}CoO_{3-\delta}$ (LSC), two parent compounds used in this thesis for the study of the variation of functional properties in $La_{0.8}Sr_{0.2}(Mn_{1-x}Co_x)_{0.85}O_{3\pm\delta}$ (LSMC) thin films (Chapter **6**). First, a thin layer of LSM is deposited centring the plume at the left edge of a large 4" substrate. Then, the substrate holder is turned 180º and a small quantity of LSC is deposited at the opposite (right) edge of the wafer. The deposition cycle is repeated till the desired thickness of the final sample is obtained. Taking advantage of the typical gaussian form of a plume thickness (see *e.g.* the calibration done for this work, Chapter **3**), a gradual variation of the composition is obtained between the two plume centres. The film composition gradient is defined by the thickness of the LSM and LSC single layers deposited at each step, as well as by the distance between the two plume centres (see **Figure 2.6b**). For allowing the intermixing of the cationic species, the thickness of each combinatorial layer and the substrate temperature must be carefully chosen, depending on the specific diffusion coefficients of each cation and the effective diffusion time. For example, for the LSMC samples deposited in this work, this *in-situ* synthesis by inter-diffusion of Mn and Co cations was achieved by depositing 1 nm alternate LSM and LSC layers at high substrate temperatures (T = 700ºC).[38–40] Also, the distance between the plume centres must be large enough to minimize the compositional gradient, allowing a simple characterization of the thin films.

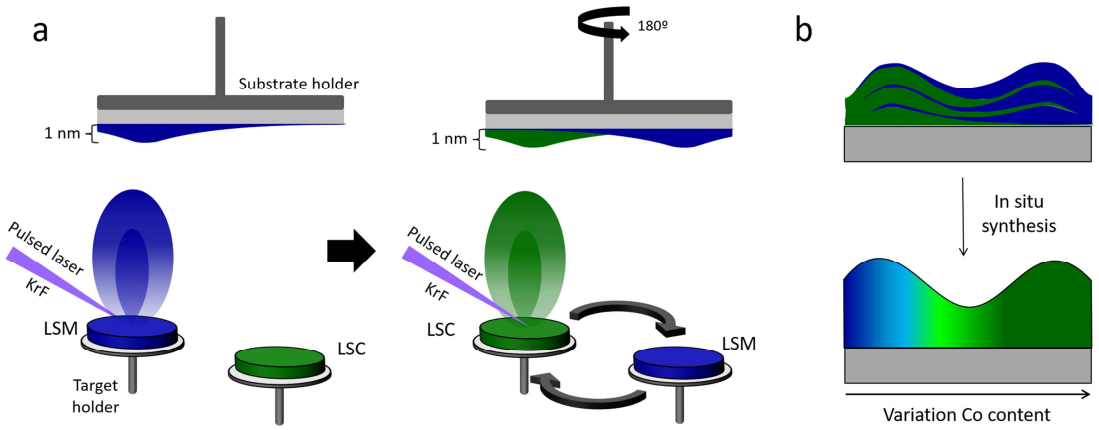

Figure 2.6 a, Sketch of the C-PLD approach employed for the deposition of LSMC films. **b**, Concentration gradient developing between the two plume centres due to high temperature in-situ synthesis of the two parent compounds.

In this thesis, PLD-5000 from *PVD Products* located at IREC facilities was used for the deposition of small area, large area and combinatorial thin films (**Figure 2.5**). The system is equipped with a KrF excimer laser from Lambda Physick COMPex PRO 205, characterized by a laser wavelength of 248 nm and a pulse duration of 20 ns.

Polycrystalline thin films of LSM were deposited on (Chapter **3**, **4** and **5**): (i.) heterostructures of 50 nm Yttria-stabilized Zirconia (YSZ) / 300 nm Si_3N_4 / 100 nm SiO_2 grown on Si (100) substrates, (ii.) Sapphire (0001) and (iii.) yttria-stabilized zirconia (001) substrates (YSZ). Commercial targets with nominal composition $La_{0.8}Sr_{0.2}MnO_3$ (LSM) and 3 mol-% Y_2O_3 stabilized ZrO_2 (3YSZ) were used for the thin films deposition. The films were deposited with an energy fluence of 1 J cm^{-2} per pulse at a frequency of 10 Hz. The substrate was kept at 700 ºC in an oxygen pressure of 0.026 mbar during the deposition and the substrate-target distance was set to 95 mm. The samples were heated at a rate of 8 K/min under 0.026 mbar of oxygen. In parallel to that, epitaxial LSM films were deposited under the same conditions but on $NdGaO_3$ (110) substrates.

Combinatorial pulsed laser deposition (C-PLD) technique was used to grow LSM_y films with variable Mn/(La+Sr) ratio and LSMC thin films with variable Co content. For the LSM_y study, commercial targets of LSM and Mn_3O_4 were used as parent compounds (Chapter **3**, **4** and **5**). The deposition conditions used were the same as for the single polycrystalline and epitaxial LSM. The thickness deposited for each cycle in the plume centre was 1 nm for LSM and 0.25 nm for Mn_3O_4. LSM_y combinatorial samples were grown on: (i.) YSZ/Si 4" wafers, (ii.) 5 mm x 10 mm Sapphire (0001) substrates, (iii.) 5 mm x 10 mm $NdGaO_3$ (110) substrates and (iv.) 3 mm x 3 mm YSZ (001) single crystal. When using pre-cut smaller substrates (i.e. sapphire, NGO and YSZ), these were attached with Silver paste to a 4" Si wafer forming a line between the two plume centres. For the LSMC study (Chapter **6**), the LSM and LSC layers were grown under the following conditions: T = 700 ºC, P = 0.026 mbar, target-to-substrate distance of 90

mm, frequency of 10 Hz, fluency of 1 J/cm^2. The number of pulses was adjusted for growing 1 nm of LSC and LSM plume centres for each cycle.

In Appendix **A**, BICUVOX thin films were deposited by LA-PLD under different background O_2 pressures (0.0067 to 0.267 mbar) and target-to-substrate distances (9 to 11 cm), from a home-made $Bi_4V_{1.8}Cu_{0.2}O_{10.7}$ pellet target. For the fabrication of the target, $Bi_4V_{1.8}Cu_{0.2}O_{10.7}$ powder was first synthesized in-house by solid state synthesis, from the basic oxide precursors (Bi_2O_3, V_2O_5 and CuO) mixed in the right stoichiometric proportion. Then, a 3" pellet was pressed by uniaxial pressing and sintered under ambient air at 850 ºC for 6 h. All BICUVOX films were deposited at a substrate temperature of 600 ºC, and on various types of substrates, including single crystal Si (100), sapphire (0001), fused silica, and Si (100) coated with Si_3N_4 (300 nm) / SiO_2 (100 nm) dielectric bilayer. For the growth of epitaxial BICUVOX films, $SrTiO_3$ (001) and Nb-doped STO (001) substrates were used, for in-plane and cross-plane electrochemical analysis, respectively.

In Appendix **B**, thin films of $La_{0.8}Sr_{0.2}FeO_{3-\delta}$ (LSF) were deposited by LA-PLD under $6.7 \cdot 10^{-3}$ mbar of oxygen and at 700 ºC. The films were grown in single crystal Sapphire (0001) substrates from a commercial LSF target. The target to substrate distance was set at 90 mm and the laser fluency to ~1 J/cm.

When needed, YSZ buffer layers were deposited by LA-PLD on $Si_3N_4/SiO_2/Si$ or bare Si 4" wafers with good thickness homogeneity, at 600 ºC, P = 0.026 mbar, target-to-substrate distance of 9 cm and frequency of 10 Hz.

2.3 Structural and microstructural characterization techniques

2.3.1 Structural properties

2.3.1.1 X-Ray Diffraction (XRD)

X-Ray Diffraction (XRD) is a non-destructive characterization technique commonly used for compositional analysis and identification of phase in crystalline materials. The principle of XRD is based on the study of the diffraction pattern obtained when a crystal is exposed to an X-ray beam with different incident angles. Since the X-rays wavelength are of the order of magnitude of the interatomic distance in crystals, the elastic scattering between the beam light and the material electrons creates constructive interferences, resulting in an increase of detected intensity at specific angular positions. According to Bragg's law, the constructive intensities occur when (see **Figure 2.7**):

$$2d_{hkl}sin(\theta) = n\lambda \qquad \text{Eq. 2.2}$$

Where d_{hkl} is the inter-planar distances between the Miller planes (h,k,l), θ the incident angle, n a positive integer number and λ is the wavelength of the X-rays. Varying the incident angle of the X-ray beam a diffraction patter can be obtained and the phase and lattice parameter of the structure identified.

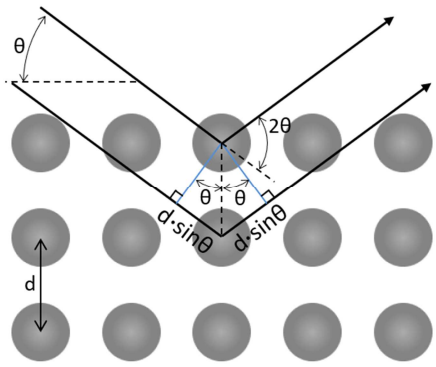

Figure 2.7 Sketch of the diffraction mechanisms of X-rays in a crystal lattice according to Bragg's law.

In this thesis, XRD was systematically employed to investigate the phase and the lattice parameter of the thin films deposited by PLD (Chapter **3**, Chapter **6**, Appendix **A** and Appendix **B**). Different XRD equipment was used: (i.) a Bruker-D8 Advance located at IREC; (ii.) a X'Pert MRD-Panalytical located at Catalan Institute of Nanoscience and Nanotechnology (ICN2) and (iii.) a X'Pert MPD-Panalytical located at University of Barcelona (UB). The basic characterization was performed in flat plate θ/2θ geometry. In order to reduce the contribution of the single crystalline substrate, in some of the experiments a small omega offset was applied. The analysis of the epitaxial LSM layers deposited on NGO was also performed using a four-angle goniometer and primary optics consisting of a parabolic mirror and a 4 x Ge (220) asymmetric

monochromator. Also, in this layer 2-D X-ray reciprocal space mapping experiments were performed to investigate the in-plane lattice relations between the substrate and the epitaxial thin films (Chapter **2** and Appendix **A**). These experiments were performed by Dr. José Santiso and Jessica Padilla at ICN2.

2.3.1.2 Scanning electron microscopy (SEM)

Scanning electron microscopy (SEM) is a very common technique in the study of microstructures and thin films. The images in SEM are generated by focusing an electron beam on a sample surface in high vacuum conditions and recording the electrons coming from it. The most common ways to collect these electrons are the low energy secondary electrons and the backscattered electrons. The former detects the electrons coming close to the impact point, which presents different angle of incidence depending on the morphology of the sample. In this sense, low energy secondary electrons detectors are surface sensitive and can be used to characterize the microstructure of the sample. In backscattering detectors, the signal recorded comes from the elastic scattering between the electron beam and the sample's atoms. This mode is also used for obtaining information about the differences of chemical composition in a material.

In this thesis, SEM was routinely used to study the morphology and the cross-section structure of the deposited thin films (see Chapter **3**, Chapter **6** and Appendix **A**). Cross section SEM was also utilized for measuring the thickness of the layers and conform them with the results obtained by ellipsometry (see section 2.3.7). Moreover, SEM was used for comparing the grain size of the polycrystalline thin films deposited by combinatorial method. The images were recorded using a Zeiss Auriga SEM located at IREC facilities.

2.3.1.3 Energy dispersive X-ray spectroscopy (EDS)

Energy dispersive X-ray spectroscopy (EDS) is a non-destructive technique that allows studying the chemical composition of a sample. EDS measures the X-ray emitted by an atom when it is exposed to an electron beam. The energy of the photons emitted is characteristic of a specific electronic transition and depends on the specific element(s) present in the sample. In this way, it is possible to investigate and quantify (previous calibration of the detector with standards) the atomic composition of a material.

In this thesis, the EDS equipped in the Zeiss Auriga SEM was used to measure the chemical composition of the thin films deposited (see Chapter **3**, Chapter **6** and Appendix **A**). The analysis especially focused on the cationic species, since the signal of light element as oxygen is not precise enough for a correct quantification. The cationic composition ratio of LSM_y and LSMC thin films was measured this way.

2.3.1.4 Wavelength dispersive spectroscopy (WDS)

Wavelength dispersive spectroscopy (WDS) is a technique used for the chemical composition analysis of the samples. Like EDS, it is based on the emission of X-rays when exposed to an electron beam. The main difference between the two techniques is that EDS measures the energy of the emitted photons while WDS sorts the X-rays based on wavelength. Indeed, in WDS the emitted X-rays passes through a single crystal before entering in a detector, resulting in diffraction peaks whose position depends on the wavelength of the emitted photons. Varying the angle between the crystal and the detector is possible to investigate different wavelengths, resulting in sharper and more separated peaks than EDS.

In this thesis, a Jeol JXA-8230 WDS located at the University of Barcelona was used to confirm the cationic composition measured by EDS in LSM (Chapter **3**) and LSMC thin films (Chapter **6**).

2.3.1.5 Transmission Electron microscopy (TEM)

Transmission Electron microscopy (TEM) is a microscopy technique based on the transmission of a focused beam of electrons through an ultrathin sample.[41] The interaction between the electron beam and the material gives rise to different phenomena, which can be collected to obtain substantial information. This interaction can generate coherent or incoherent elastically scattering, depending whether the electrons maintain or not the phase relationship between them after the scattering event. TEM images and electron diffraction are examples of incoherent elastically scattering images, whereas high angle annular dark field (HAADF) and electron energy loss spectroscopy (EELS) of incoherent elastically scattering ones. The electron beam is focused on the sample by a condenser lens in parallel or converged form. A parallel beam is used in the case of conventional TEM (CTEM) images while a convergent one is employed in Scanning TEM (STEM), where the focus beam is then moved along the sample for recording the whole image.

In TEM images, the signal can be recorded by measuring either the amplitude or the phase contrast of the electrons. The amplitude contrast gives in turn two different types of signal: bright and dark field, depending on which electrons are collected. Instead, the phase contrast is formed by the interference of more than one electron beam focused on the specimen. This mode is very sensitive to the sample characteristics and atomic scale precision can be obtained (e.g. high resolution TEM (HRTEM)). Also, information about the crystalline structure can be deduced from HRTEM by taking the Fast Fourier Transform (FFT) of the image.

In STEM images, the focused electron beam generates different signal depending on the solid angle at which the detector is positioned. There are three main types of detector: a bright field (BF) detector, for small solid angles (< 10 mrad); an annular dark field (ADF) detector for intermediate solid angles (between 10-50 mrad), and a high angle

annular dark field (HAADF) detector, for high solid angle (> 50 mrad). One of the main characteristics of HAADF is that the contrast is proportional to the atomic number Z, meaning that this mode is sensitive to the chemical composition in the sample.

In addition to the TEM imaging capabilities, spectroscopy studies can be also carried out.[42] The two main spectroscopy techniques coupled to STEM are: EDS and electron energy loss spectroscopy (EELS). In EELS measurements, a mono-energetic electronic beam is passed through the sample and the energy distribution of the transmitted beam is recorded. The intensity of the signal is then divided by a spectrometer into the kinetic energy of the arrival electrons, producing an electron energy loss spectrum. For low kinetic energies, EELS spectrum usually present a peak, originated by both elastically scattered and non-scattered electrons that do not lose energy in the transmission process. Increasing the kinetic energy, the intensity of the spectrum decreases rapidly but some peaks appear related to the inner-shell ionizations. The energy edge of these features is linked to the binding energy of the corresponding atomic shell, hence carrying evidence about the atomic specie present in the sample. Moreover, EELS can be used also for obtaining information about the relative atomic concentration and to the oxidation state of the elements.

In this thesis, TEM studies were performed in collaboration with Dr. L. López-Conesa, Dr. S. Estradé and Prof. F. Peiró from the University of Barcelona (UB) and Dr. M. Núñez from IREC, to study the atomic structure and the chemical composition of grain boundaries in LSM_y thin films (see Chapter **3**). HRTEM images were acquired in a JEOL J2010F microscope operated at 200 kV accelerating voltage. EELS experiments were carried out to investigate the elemental composition in the GBs and differences in the Mn oxidation state. EELS experiments were carried out in a JEOL ARM 200cF microscope operated at 200 kV, a FEI TITAN Low Base operated at 300 kV and a Nion UltraSTEM operated at 100 kV located at Instituto de Nanociencia de Aragón (INA). The results were analysed by DigitalMicrograph software.

2.3.1.6 Atomic force Microscopy (AFM)

Atomic Force Microscopy (AFM) is a non-destructive technique used for studying the surface of a sample. The surface topography is determined by scanning a sharp probe on the sample surface and measuring the z displacement of the tip.

There are two different types of AFM set-up for topography measurements: contact and tapping mode.[43] In tapping mode, the probe is forced to vibrate near the resonance frequency while the piezoelectric transducer varies its position on the sample. The forces between the surface and the tip (e.g. Van der Waals interactions) cause the resonance frequency to shift as the tip gets closer or more distance, due to the irregularities of the sample. The feedback control then regulates the piezoelectric transducer to maintain always the same distance between the surface and the tip, causing the probe tip to change its height in conformity with the sample morphology. A

laser reflected on the tip onto a photoelectrode detector catches these variations, generating an image of the surface analysed.

In this thesis, AFM (XE15-AFM from Park systems, located at IREC) in tapping mode was used to study the roughness of the epitaxial LSM_y samples (Chapter **3**), the grain size of LSM polycrystalline thin films with different thickness (Chapter **4**) and to investigate the surface of BICUVOX and LSF thin films (Appendix **A** and **B** respectively).

2.3.1.7 Raman spectroscopy

Raman spectroscopy is a technique based on the observation of vibrational, rotational and other low-frequency modes obtained by inelastic scattering of a monochromatic light. It can be used for phase identification on crystalline samples and thin films. The main components of a Raman spectroscopy set-up consist in a monochromatic light source, an optical microscopy to focus the laser on the surface's sample and a monochromator, which analyses the reflected light and generates the spectroscopy signal.

In this thesis, Raman spectroscopy was used for identifying the phase of the Mn_3O_4 thin films deposited for the combinatorial LSM_y analysis (Chapter **3**) and the phase of BICUVOX thin films deposited at different pressure (Appendix **A**). The Raman used was a HORIBA Scientific iHR320 spectrometer equipped with a HORIBA syncerity CCD and a laser at $\lambda = 532$ nm (green) located at IREC.

2.3.2 Optical properties and XANES

2.3.2.1 Ellipsometry

Ellipsometry is an optical spectroscopy technique based on the measure of the variation of polarization of a light beam reflected on a thin film sample. It is a non-destructive technique that can be used to measure many structural and optical characteristics of a thin film, such as its thickness and optical constants.[44]

The schematic setup of the operation principle of ellipsometry is shown in **Figure 2.8**. First, a white light typically coming from a Xenon lamp is linearly polarized by a polarizer. A linear polarization of an electromagnetic wave takes place when the two spatial components of the electric field ($E_{p,in}$ and $E_{s,in}$, perpendicular to the light beam) are in-phase between each other, resulting in an oscillation of the electric field along one direction. Then, the polarized light is reflected by the sample, giving rise to a change of components of the electric filed ($E_{p,out}$ and $E_{s,out}$) that modifies the polarization from linear to elliptical. The angle of light incidence is set close to the Brewster angle in order to maximize the difference between the reflected electric field

components ($E_{p,out}$ and $E_{s,out}$) and, consequently, between the Fresnel coefficients (r_p and r_s), defined as:

$$r_p = \frac{E_{p,out}}{E_{p,in}} \quad , \quad r_s = \frac{E_{s,out}}{E_{s,in}} \qquad \text{Eq. 2.3}$$

The light beam is then forced to pass through a modulator and an analyser, which restore the linear polarization and allow the measure of the complex reflectance ($\rho = \frac{r_p}{r_s}$) by the detector. Finally, a monocromator placed before the detector separates the different light wavelengths, generating the spectroscopy measure.

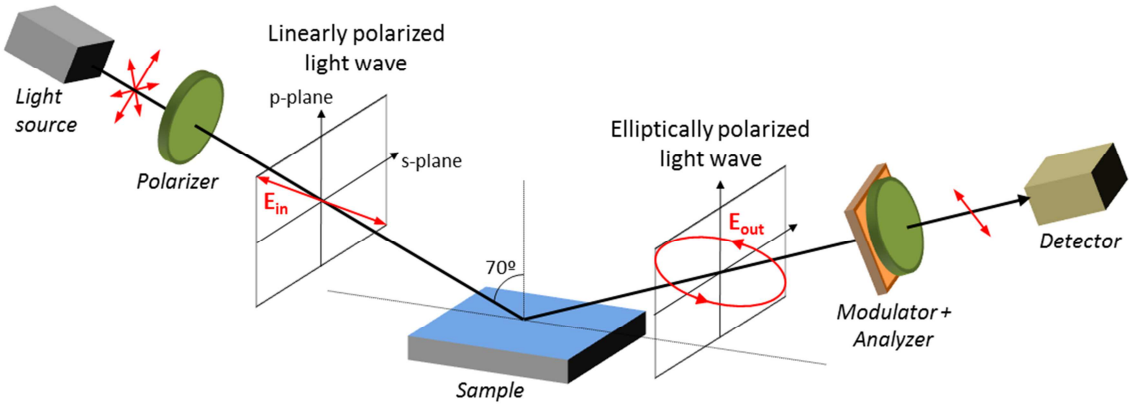

Figure 2.8 Typical scheme of the ellipsometry set up and operation principle.

2.3.2.1.1 Ellipsometry principles

The variation of light polarization produced by the reflection of the light on the sample can be described by the angles ψ and Δ, which represent respectively the relative variation of amplitude and phase between the r_p and r_s components, as:

$$\rho = \frac{r_p}{r_s} = \tan(\psi)\, e^{i\Delta} \qquad \text{Eq. 2.4}$$

In this sense, an ellipsometry measurement originates two spectra of ψ and Δ as a function of the incoming photon energy. As an example, **Figure 2.9** shows the results obtained for B-site deficient LSM thin films (Mn/(La+Sr) = 0.85, hereby $LSM_{0.85}$) deposited on Sapphire (0001) and measured at 473 K by an ellipsometry from Horiba UVISEL at IREC. Considering a bulk semi-infinite sample (one interface: air-substrate), the following relation can be found between the complex dielectric constant of the material ($\bar{\varepsilon} = \varepsilon_1 + i\varepsilon_2$) and the complex reflectivity:

$$\bar{\varepsilon} = \bar{\varepsilon}_a \sin^2(\Phi)\left[1 + \tan^2(\Phi)\left(\frac{1-\rho}{1+\rho}\right)^2\right] \qquad \text{Eq. 2.5}$$

Where $\bar{\varepsilon}_a$ is the dielectric constant of the air and Φ the incident angle. The complex dielectric constant is related to the optical constants of the material by:

$$\bar{\varepsilon} = (n + ik)^2 \qquad \text{Eq. 2.6}$$

Where *n* is the refractive index and *k* the extinction coefficient.

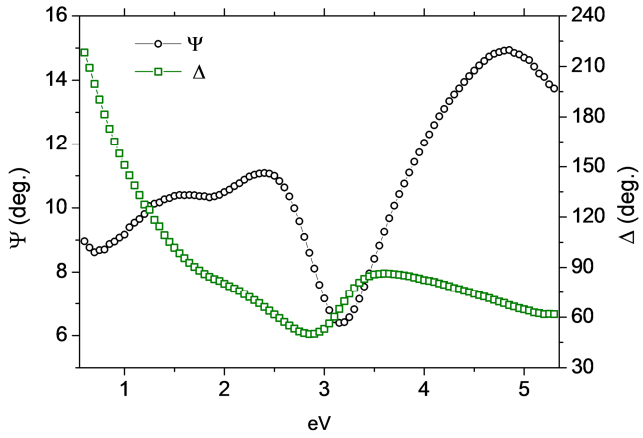

Figure 2.9 Raw spectra measured in an $LSM_{0.85}$ thin film deposited on sapphire (0001). The data are recorded at 473 K in air at IREC

From the fitting of the measured spectra with Eq. **2.5** it is possible to derive *n* and *k* of the bulk semi-infinite material. Different models are available to describe the dielectric properties of oxides. For semiconductors perovskites, the dielectric properties of the thin films can be simulated as a series of Lorentzian oscillators:[45–47]

$$\bar{\varepsilon} = \varepsilon_0 + \sum_{j=1}^{n} \frac{f_j \omega_{0,j}^2}{\omega_{0,j}^2 - \omega^2 + i\gamma_j \omega} \qquad \text{Eq. 2.7}$$

Where ε_0 is the high frequency dielectric costant, ω is the light angular frequency and ω_0, γ_j, f_j are respectively the resonance frequency, the broadening and the amplitude of the j^{th} oscillator. Although very general, this equation was found to provide a good representation of the optical behaviour of the materials analysed. From the extinction coefficient of the material, the absorption coefficient (α) was calculated as:

$$\alpha = \frac{4\pi k}{\lambda} \qquad \text{Eq. 2.8}$$

Where λ is the light wavelength. Also, the real part of the optical conductivity (σ) can be calculated as:

$$\sigma_{opt} = \frac{4\pi nk}{\lambda Z_0} = \frac{\alpha n}{Z_0} \qquad \text{Eq. 2.9}$$

With $Z_0 = \sqrt{\mu_0/\varepsilon_0} = 377\ \Omega$ being the impedance of free space. Nevertheless, the ellipsometry measurements of thin films also carry information of other features (i.e. film roughness, film thickness, optical constants of the substrate and the film), meaning that, to extract the properties of the layer, it is necessary to first model the whole systems under analysis. The result of a multilayer system can be considered as the total amount of reflected light created by the sum of all the reflections generated at every

interface (e.g. film-air and film-substrate). This phenomenon also gives rise to the characteristic oscillations observed in the spectra of semi-transparent layers, which are due to the constructive or destructive interference between the series of light reflections and depends on the layer thickness.

In this thesis, Ellipsometry measurements were carried out in a UVISEL plus equipment from Horiba scientific, with spectral range 0.6 – 5.3 eV (see **Figure 2.10**). The spectra were collected in air varying the temperature using the heating stage of the Linkam probe station (between RT and 473 K). The spectra were collected with a light incidence angle of 70º and with the modulator and analyser set at 0º and 45º respectively. Prior to the measurements, the system was calibrated using a Si (001) thermally oxidized substrate. Ellipsometry results are presented in Chapter **3** and Chapter **6**.

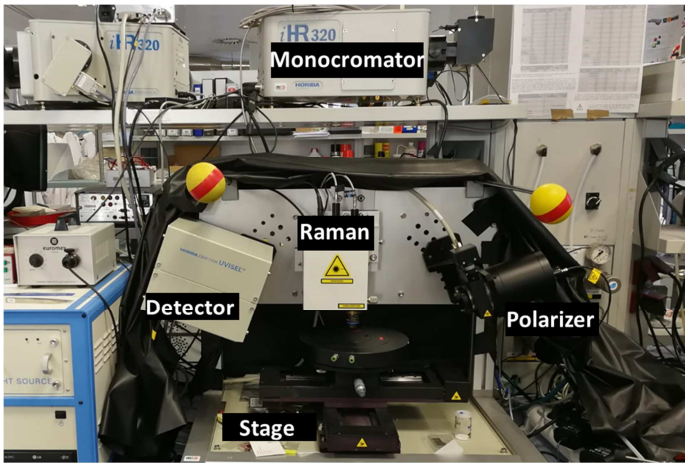

Figure 2.10 Ellipsometry and Raman system from Horiba UVISEL located at IREC.

2.3.2.1.2 Modelling Ellipsometry spectra

The optical constants and thickness of the thin films was obtained by modelling and fitting the ellipsometry spectra with the DeltaPsi2 software from Horiba. In the following, the fitting procedure used to extract the optical properties of the thin films is described for an exemplifying B-site deficient $LSM_{0.85}$ thin film deposited on Sapphire (0001). **Figure 2.11a** shows the experimental light intensities components I_s and I_c obtained for this sample, measured at 473 K. For the fitting of the the thin film optical properties, it is generally recommended to use light intensity components I_s and I_c rather than ψ and Δ. This is because the system actually measures the light intensity and then converts it into ψ and Δ depending on the modulator and analyser set up. This way, a higher sensitivity of the fitting is expected. The model used for the fitting is shown in the inset of **Figure 2.11a** and consists of a three layer model, *viz.* the substrate, the thin film under study and an additional top layer formed by 50% of void and 50% of the same material of the underneath film. This top layer is intended to describe the film roughness and/or possible differences in the optical properties of the surface and is typically a few nm thick. In order to exclude the substrate from the fitting procedure, the

spectrum of a sapphire (0001) single crystal was previously measured and its optical constants extracted. One side polished substrates were generally used, since these can be modelled as a semi-infinite medium (no reflections are generated in the non-polished backside surface).

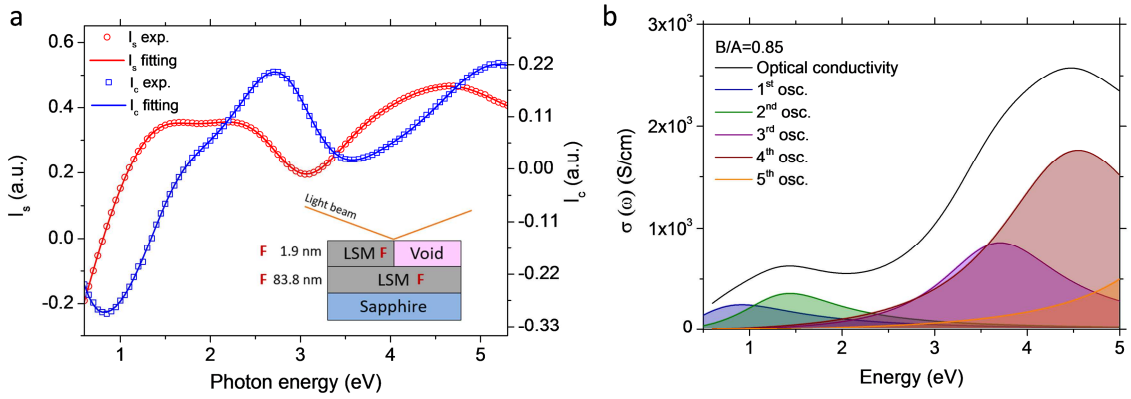

Figure 2.11 a, raw ellipsometry data and fitting of a B-site deficient $LSM_{0.85}$ thin films deposited on Sapphire (0001) and measured at 473 K. The inset of **a** shows the model used for the fitting. **b**, optical conductivity extracted of the $LSM_{0.85}$ layer extracted from the fitting shown in **a**. The optical conductivity contributions of the single Lorentzian oscillators are also shown in **b**.

The fitting was then performed by leaving as free parameters: (i.) a certain number of optical oscillators for describing the optical constants of the thin film, (ii.) the thickness of the layer and (iii.) the thickness of the roughness layer. For instance, in the example of shown in **Figure 2.11a**, an excellent fitting characterized by a $\chi^2 = 0.025$ was obtained. The thickness extracted was also confirmed by SEM cross section measurements. In this way, the optical properties of the thin film can be extracted. As an example, the total optical conductivity and the single optical contributions obtained for the B-site deficient $LSM_{0.85}$ thin films measured at 473 K is shown in **Figure 2.11b**. This procedure was applied to all the thin films analysed in this work: LSM_y thin films in chapter **3** and **4**, the LSMC thin films in Chapter **6** and the $La_{0.8}Sr_{0.2}FeO_{3-\delta}$ (LSF) thin films in Appendix **B**.

2.3.2.1.3 *In-situ* ellipsometry measurments

For measuring the evolution of optical properties in thin films at high temperature and in different atmosphere, a partial home-made set-up was developed (see **Figure 2.12**). The system is composed of a high temperature linkam for heating the sample and providing the electrical connections and a home-made plastic cover, which was produced by 3D printing at IREC. The main characteristic of the cover is that it was designed to accommodate two transparent windows tilted 70º respect to the sample normal vector, which is the exact same angle of the incident and reflected light beam (see **Figure 2.12b**). In this way, the light is expected to be fully transmitted and not to modify its polarization. This was also confirmed by assuring that the spectra measured with and without cover were identical. The pO_2 in the chamber was varied by using a

ZIROX sensor placed before the gas inlet and confirmed by a second ZIROX sensor located after the gas outlet. The final set-up allows measuring the electrical resistivity and the optical properties of a thin film under controlled atmosphere and temperature.

In this thesis, *in situ* ellipsometry study of $La_{0.8}Sr_{0.2}FeO_{3-\delta}$ (LSF) thin films were carried out at 673 K as a function of the pO_2 in the chamber (1 - 3~10^{-4} bar). The results of this study are shown in Appendix **B**.

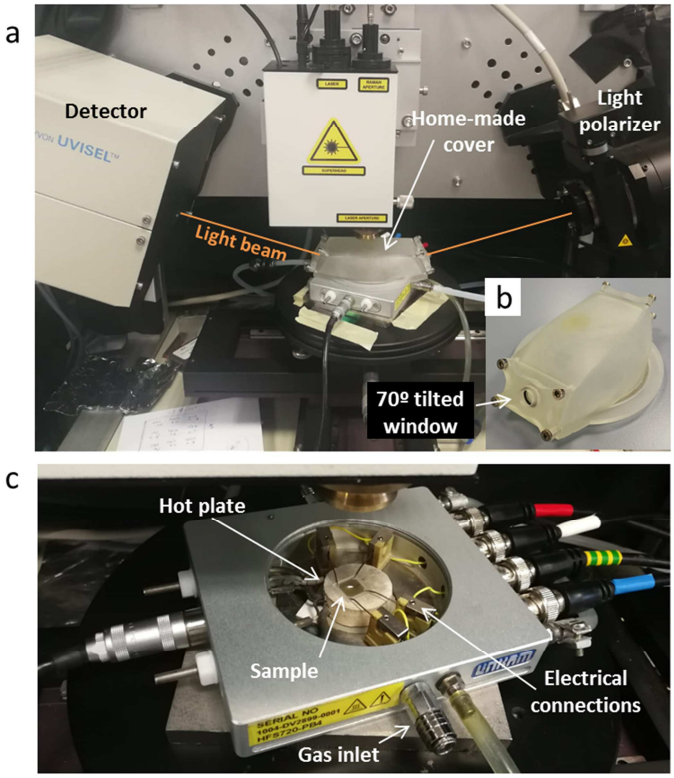

Figure 2.12 Experimental set up used for the *in-situ* investigation of the optical properties of LSF thin films under controlled atmosphere and temperature. The overall configuration of the set-up is shown in **a** while in **b** a photograph of the cover is reported. **c**, picture of one sample illuminated by the light beam.

2.3.2.2 X-ray Absorption Near Edge Structure (XANES)

X-ray Absorption Near Edge Structure (XANES) is a technique used for the direct analysis of the oxidation state, coordination chemistry and atomic distances of a specific element in a material.[48] XANES is based on the adsorption of X-rays causing the excitation of a core electron of an atom to an empty state below the ionization threshold or to the continuum state. The energy necessary to promote an electron from its binding state towards the continuum is called edge. Each element possesses different edges depending on the electron core shell excited (i.e. K edge for the 1s electrons, L edge for the 2p and 2s electrons, M edge for the 3s, 3p and 3d electrons). The edges of an element are related to the electrostatic attraction of a binding electron to the nucleus, meaning that each element possesses unique features that can be used to study its chemical and electronic properties. Moreover, the edge also depends on the formal

oxidation state of the atom but not on its crystalline structure. This means that by XANES it is possible to measure the oxidation state of an element by comparing it to standard compounds in which the oxidation state is known.

XANES measurements are generally performed at synchrotrons, since they require an intense and tuneable source of soft X-rays. When the energy of the incoming X-ray beam is close to an edge of one element a sudden increase of absorption takes place. This can be measured directly, by recording the intensity transmitted by the sample, or indirectly, by measuring the fluorescent emission taking place when the core hole is filled by energetic electrons. For X-ray energies higher than the edge, the promotion of core electrons to the continuum generates photoelectrons waves that interacts with the surroundings atoms and give rise to interference patterns in the spectra. This region is called extended X-ray absorption fine-structure spectroscopy (XANES) and can provide information about the chemical and structural environment around the absorbing species.

In this thesis, systematic Mn K-edge XANES measurements were performed on ID12 Synchrotron beamline at the ESRF (Grenoble, France) to estimate the Mn valence changes in the LSM_y thin films (Chapter **3**). The spectra were collected in the electron yield and fluorescence mode in a nearly constant beam current of 200 mA, under vacuum and at T = 298 K. Two silicon photodiodes detectors were used, one in back-scattering geometry and a second diode mounted at 20° with respect to the incident beam to collect the fluorescence. The spectra were recorded in the energy range 6530 - 6628 eV, every 0.15 eV. **Figure 2.13** shows the XANES spectra obtained for an LSM_y thin film and its corresponding 1st derivative. For each composition analysed, at least two different spectra were acquired to confirm the reliability of the measurement. The formal valence of Mn was estimated from the white line by calculating the inflection point energy, given by the maximum of the 1st derivative.

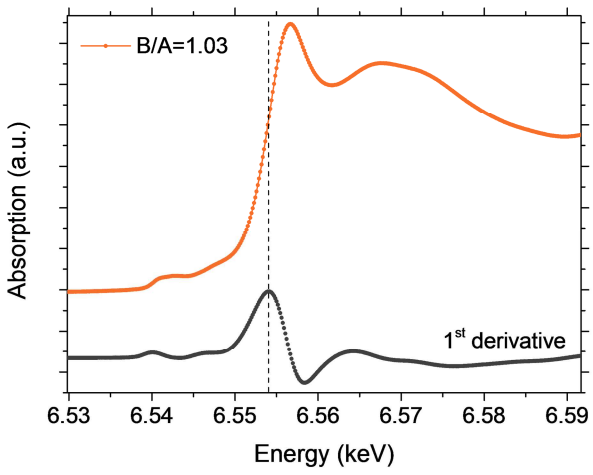

Figure 2.13 XANES spectra of one characteristic sample along with its 1st derivative. The dashed line indicates the inflection point of the spectra, which was used to study the change of Mn valence varying B/A ratio in LSM_y thin films (see Chapter **3**).

2.4 Functional properties characterization techniques

2.4.1 In-plane electrical measurements

The in-plane electrical resistivity of the thin films deposited was studied by two different types of configuration: Van Der Pauw and in-plane four probe geometry with finger contact electrodes (see **Figure 2.14**).

Van Der Pauw method is a special type of four probe configuration largely used in the characterization of thin films resistivity and Hall coefficient.[49] The great advantage in using this method comes from the possibility of measuring the resistivity of a sample with arbitrary shape. Nevertheless, some conditions must be still fulfilled: (i.) the film must be homogenous in composition and thickness; (ii.) The electrical contacts must be at least one order of magnitude smaller than the sample (ideally point contact should be used); (iii.) the thickness of the thin film must be far smaller than the lateral sizes. The configuration used in the Van Der Pauw is shown in **Figure 2.14a**. The measurements were performed by placing 4 contacts at the edges of the sample (A, B, C, D in the figure). If a current is applied between A and B contacts (I_{AB}), a certain voltage will be measured between the D and C contacts (V_{DC}), resulting on a resistance R_O defined by the basic expression $R_O = V_{DC}/I_{AB}$. The sheet resistance of the sample can be measured by alternatively changing the polarity and the contacts side, resulting in two different resistances R_v and R_O along the two in-plane directions in the sample, which for symmetry reasons read as:

$$R_v = \frac{V_{AD}}{I_{BC}} = \frac{V_{DA}}{I_{CB}} = \frac{V_{BC}}{I_{AD}} = \frac{V_{BC}}{I_{AD}} \qquad \text{Eq 2.10}$$

$$R_O = \frac{V_{AB}}{I_{DC}} = \frac{V_{BA}}{I_{CD}} = \frac{V_{DC}}{I_{AB}} = \frac{V_{CD}}{I_{BA}} \qquad \text{Eq 2.11}$$

According to Van Der Pauw method, the sheet resistance (R_S) can be calculated following the expression:

$$e^{-\frac{\pi R_v}{R_S}} + e^{-\frac{\pi R_O}{R_S}} = 1 \qquad \text{Eq 2.12}$$

In a perfectly square homogenous sample R_v and R_O are identical and equation **2.12** can be analytical solved. Nevertheless, it is common to find small differences between R_v and R_O, which make the calculation of R_S more challenging. An easy way to take in account this differences is to insert in equation **2.12** the average of R_v and R_O and then correct the result using a dimensionless factor f, which depends on the ratio R_v/R_O.[50] The solution then follows:

$$R_S = \frac{\pi}{\ln(2)} \left(\frac{R_O + R_v}{2}\right) f\left(\frac{R_v}{R_O}\right) \qquad \text{Eq 2.13}$$

Finally, the resistivity of the thin film (ρ) is obtained by multiplying R_S by the thin film thickness.

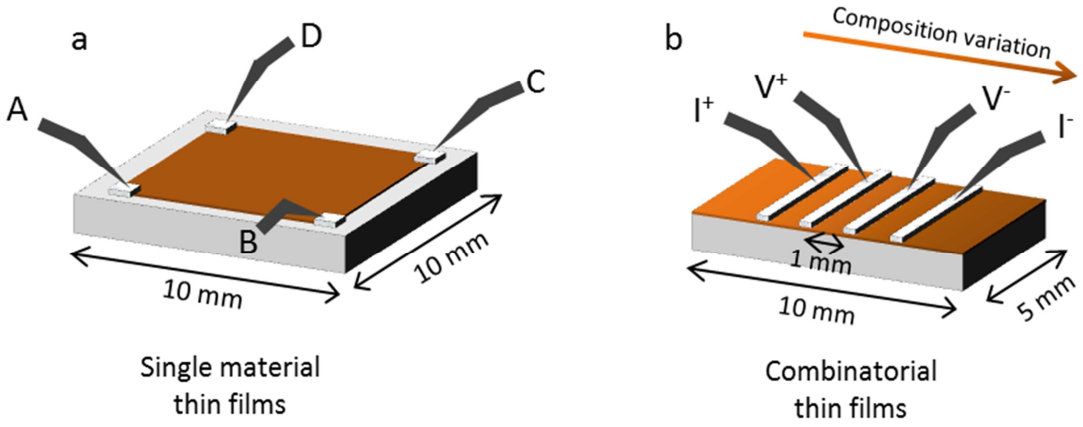

Figure 2.14 Schematic representation of the method used for the thin films electrical characterization. **a**, Van Der Pauw method, used in case of homogenous composition thin films and **b**, in plane 4 probe technique used for combinatorial samples.

Unfortunately, it is not possible to use Van Der Pauw method when measuring a thin film with inhomogeneous thickness and/or composition. This is the case of the combinatorial thin films deposited in this work (LSM_y and LSMC layers), where the composition continuously varies between the plume centers. Therefore, for these films an in-plane four probe geometry with fingers contact electrodes was used (see **Figure 2.14b**). The composition variation was designed to take place just along the 1 cm side (the chips are aligned between the two plume centers). The contact electrodes were designed to be of rectangular shape and reaching both sides of the cut chips. Current was applied between the two outer electrodes and voltage was measured between the two central ones. The distance between the two central electrodes was set to be 1 mm. Based on this measuring configuration, no lateral effects are expected and it is ensured that the current lines are linear between the two central voltage electrodes. The resistance of the thin films (R_f) was analyzed in a linear regime and was obtained by linear fitting of the IV curves. The resistivity of the thin films (ρ) can be obtained by:

$$\rho = R_f \frac{L \cdot d}{t} \qquad \text{Eq 2.14}$$

Where L is the side of the contact electrodes, d is the distance between the two voltage electrodes and t is the film thickness.

In this thesis, the Van Der Pauw method was used to measure the resistivity of parent compound thin films (LSM in chapter **4**, LSC in chapter **6** and LSF in Appendix **B**) on different substrates (1 cm x 1 cm Sapphire (0001), heterostructures of 50 nm Yttria-stabilized Zirconia (YSZ) / 300 nm Si_3N_4 / 100 nm SiO_2 grown on Si (100) substrates, 1 cm x 1 cm $NdGaO_3$ (110) substrates). Instead, in-plane four probe geometry with finger contact electrodes was preferred in the combinatorial thin films (LSM_y in chapter **4** and LSMC in chapter **6**). The substrates used for the combinatorial measurements were: (i.) YSZ/Si 4" wafers, (ii.) 1 cm x 0.5 cm Sapphire (0001) substrates, (iii.) 1 cm x 0.5 cm $NdGaO_3$ (110) substrates. The 4" wafers were cut into specimens of 1 cm x 0.5 cm after

the deposition, following a straight line between the two plume centers. This way, samples with composition variation taking place along the 1 cm lateral size (parallel to the current flow) were obtained, while the composition along the 5 mm side (perpendicular to the current flow) was kept constant. The Co or Mn content variation taking place between the two voltage electrodes was considered in the calculation of the measurement error.

The electrical measurements in this thesis were performed varying the temperature (both above and below RT) and the oxygen partial pressure (pO_2). The low temperature measurements were conducted in a temperature-controlled Linkam probe station (THMS350) cooled by liquid nitrogen between 83 K and 523 K. The experiments were conducted in vacuum (0.1 mbar) to avoid humidity condensation on the sample. The high temperature measurements were performed in a temperature-controlled Linkam probe station (THMS600) between 273 K and 873 K in synthetic air (see **Figure 2.15a**). The high temperature pO_2 experiments were made in a Probostat stage (NorECs) placed in a tubular furnace in order to control the temperature. The pO_2 inside the Probostat stage was controlled with a ZIROX oxygen pump and monitored by a lambda-sensor located next to the analyzed sample (see **Figure 2.15b**). For the electrical measurements a Keithley 2400 was used.

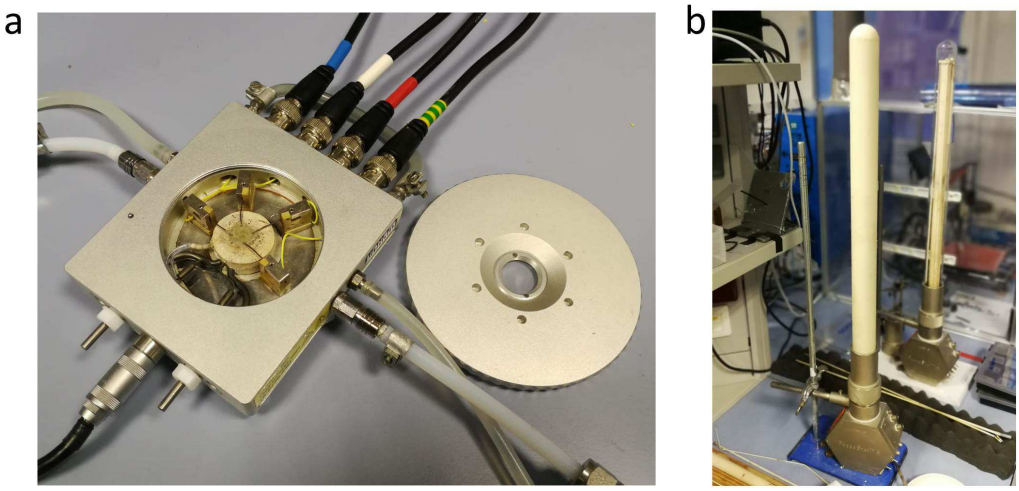

Figure 2.15 Linkam (**a**) and Probostat (**b**) stages used for the measurements of electrical and electrochemical properties of the thin films.

2.4.2 Electrochemical measurements

The electrochemical properties of the thin films were studied by Electrochemical Impedance Spectroscopy (EIS). Impedance spectroscopy is a powerful technique used to study many different phenomena, such as mechanism of electrochemical reactions, dielectric and transport properties of materials, corrosions and many others.[51] Among all these applications, EIS was intensively applied to the study of SOFC electrochemical properties, due to its ability to separate the contribution of each component to the total resistance of the cell.[52]

EIS is a transient technique based on the application of an AC voltage to a system in a certain frequency range. In general, electrochemical cells are characterized by non-linear phenomena, meaning that the relation current-voltage is highly non-linear. Nevertheless, it is possible to operate in a regime of pseudo linearity by applying small signals, which allows treating the problem with linear mathematics. In EIS the value of voltage applied has a sinusoidal form that can be written as:

$$V(t) = V_0 \cdot e^{i\omega t} \qquad \text{Eq. 2.15}$$

Where V_0 is the voltage amplitude, ω the variable angular frequency and t the time. An electrochemical system stimulated by a transient voltage will give rise to transient current, characterized by a shift θ of the phase and amplitude I_0, that is:

$$I(t) = I_0 \cdot e^{i\omega t + \theta} \qquad \text{Eq. 2.16}$$

Similarly to the definition of ohmic resistance, the impedance is defined as the ratio between E(t) and I(t) :

$$Z(\omega) = \frac{E(t)}{I(t)} = |Z| \cdot e^{(-i\theta)} \qquad \text{Eq. 2.17}$$

It is also possible to write the impedance in terms of real and imaginary components:

$$Z(\omega) = |Z|\cos\theta - i|Z|sin\theta = Z'(\omega) - iZ''(\omega) \qquad \text{Eq. 2.18}$$

There are different ways to plot the impedance. The representation in vectors form, in which Z' is the real part and Z'' the imaginary part, of the complete impedance plane is known as Nyquist diagram (see **Figure 2.16a**).

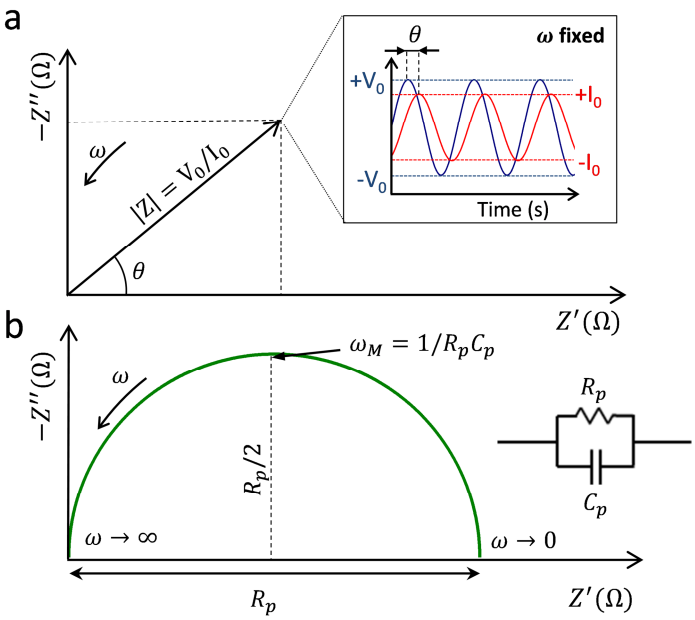

Figure 2.16 a, Vector representation of the impedance showing the relation between voltage-current angular shift ($\boldsymbol{\theta}$) and signal amplitude ($\boldsymbol{V_0, I_0}$) for a fixed $\boldsymbol{\omega}$. **b**, Nyquist representation of the impedance spectra of a RC element. The main relationships between the circuit parameters and the curve are shown.

The impedance spectroscopy measurement is obtained by varying the frequency of the signal ($f = \frac{\omega}{2\pi}$) in a large range (several orders of magnitude) while recording the impedance. In an electrochemical system, each phenomena is characterized by a specific relaxation time (τ_M), equal to the time required for reaching the equilibrium after the application of the perturbation signal. Therefore, by varying the signal frequency, the EIS allows to recognize and separate these contributions from the total cell resistance. The simplest model to describe an electrochemical system is based on a linear combination of RC elements, where resistance (R) and capacitance (C) are connected in parallel. **Figure 2.16b** shows the characteristic shape of the impedance of a RC element, plotted in the Nyquist plot. The diameter of the semicircle is equal to the ohmic resistance of the element and the maximum of the Z'' takes place for the angular frequency:

$$\omega_M = \frac{1}{RC} = \frac{2\pi}{\tau_M} \qquad \text{Eq. 2.19}$$

Which represents the relaxation time τ_M of the corresponding electrochemical process. If the relaxation times of n consequential phenomena are separated enough, n semicircles will appear in the Nyquist plot, each characterized by a diameter equal to the resistance of the RC element. However, in real systems the electrochemical processes are not characterized by a single relaxation times, but rather by a distribution of τ_M, which give rise to an apparent depression of the semicircles in Nyquist plot. In this case, a Constant Phase Element (CPE) is commonly used in parallel to the resistance instead of a capacitance, allowing a better fitting of the EIS measurements. This mathematical element is characterized by an impedance $Z_{CPE} = 1/(Q(j\omega)^p)$, where Q is a pseudo-capacitance and p the dispersion element with value $0 < p < 1$. The relaxation time of the R-CPE element is equal to:

$$\omega_M = \left(\frac{1}{RQ}\right)^{1/p} \qquad \text{Eq. 2.20}$$

By using a series of R-CPE elements it is possible to easily fit any electrochemical measurement. Nevertheless, one must be extremely cautious in the interpretation of the results, since an R-CPE does not have a single physical meaning but represents a mathematical element. For this reason, it is always preferred to use equivalent circuits that have been derived from a solid physical theory, where each element can be assigned to a specific phenomenon.

In this thesis, EIS was used to characterize the oxygen mass transport properties of LSM_y thin films with different Mn content (see Chapter **5**). The thin films were deposited on Yttria Stabilized Zirconia (YSZ) (001) single crystals to allow the across plane measurements of oxygen phenomena. The substrate YSZ (001) used had two dimensions: (i.) 1 cm x 1 cm and (ii.) 0.3 cm x 0.3 cm. The former was used for the characterization of the single deposited LSM thin films, while the latter for the LSM_y combinatorial thin films. The measurements were performed both in symmetrical

configuration (LSM deposited on both sides of the substrate) and by applying porous Ag paste on the backside of the YSZ chip as reference electrode. Ag paste was confirmed to have a negligible contribution in the polarization impedance of the LSM_y/YSZ/Ag paste system by measuring a symmetrical Ag/YSZ/Ag cell. Porous gold paste was applied on the LSM_y layers to increase electron percolation and effectively measure the entire thin film surface. Gold mesh and gold wires were used for the electrical connections. The gold was chosen because of its poor oxygen reduction properties.[53,54] In the combinatorial samples, the Mn content variation taking place inside the 0.3 cm x 0.3 cm single crystal was considered in the calculation of the measurement error.

The EIS measurements were performed in a ProboStat stage (NorECs). The temperature was varied between 823 and 973 K using a tubular oven. Ceramic Al_2O_3 supports produced by the 3D printer located at IREC were used to facilitate the cell arrangement set-up. The pO_2 inside the Probostat stage was controlled with a ZIROX oxygen pump and confirmed by a lambda-sensor located next to the analyzed sample. The impedance spectroscopy was measure with a Novocontrol system (Alpha-A High performance frequency analyzer), varying the frequency in the range 10^6 – $5 \cdot 10^{-2}$ Hz. Voltage amplitude of 0.05 V was applied in the experiments. The experimental set-up system is shown in **Figure 2.17**.The impedances were fitted by ZView software using a physically-meaningful electrical model (see Chapter **6**).

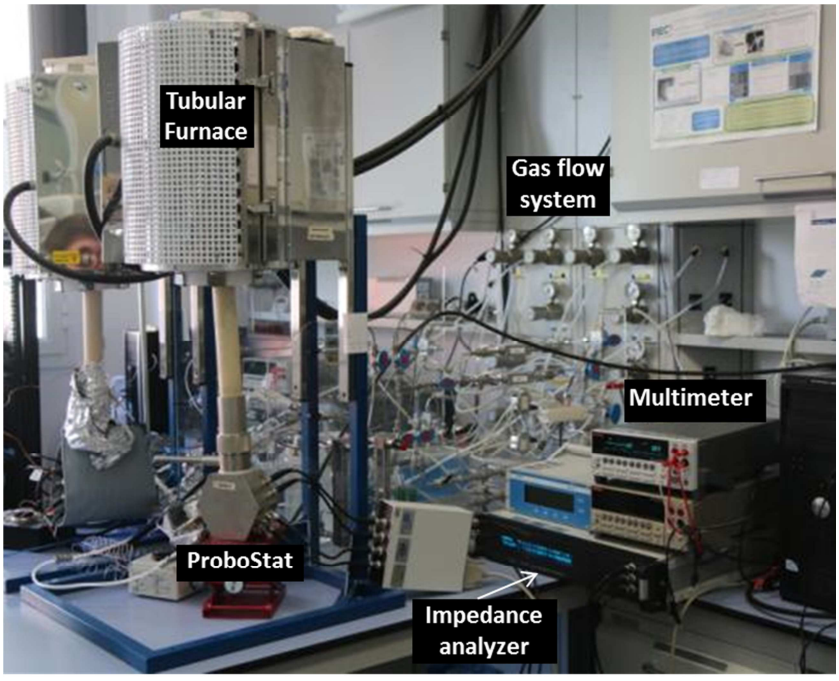

Figure 2.17 Image of the experimental set-up system used for the electrochemical and electrical characterization of the thin films.

2.4.3 Oxygen isotope exchange depth profile technique coupled with secondary ion mass spectrometry (IEDP-SIMS)

Isotope Exchange Depth Profiling using Secondary Ion Mass Spectroscopy (IEDP-SIMS) is a direct method used to determine the oxygen kinetic parameters where oxygen mass transport takes place under zero electrochemical driving force.[55] These oxygen mass transport parameters are described by the oxygen diffusion (D^*) and the surface exchange parameter (k^*). The technique can be divided into two parts: (i.) oxygen isotope exchange and (ii.) Time of Flight - Secondary Ion Mass Spectroscopy (ToF – SIMS).

In the oxygen isotope exchange, the sample is first subjected to a long term annealing in pure oxygen with natural $^{18}O/^{16}O$ ratio in order to equilibrate the sample. Then, the specimen is annealed for a certain time (t_{ex}) under controlled conditions (temperature and oxygen partial pressure) in an ^{18}O enriched atmosphere (55.3 % to 93.9 % of ^{18}O). This step forces the incorporation and diffusion of ^{18}O inside the sample. At a certain time t_{ex}, the process is intentionally blocked by rapidly cooling down the chamber. After the isotope exchange, the sample is analysed by ToF – SIMS. This technique involves the bombardment of the sample surface by highly energetic negative primary ions that give rise to an ejection of secondary ions of the material. The ions ejected (atoms, clusters and molecular fragments) are then collected in a detector that measures the number of arrival species and their ToF. Since the ToF is proportional to the mass of the ions, it is possible to measure the concentration of ^{18}O isotope ejected from the sample surface. Increasing the sputtering time, deeper regions of the thin film are exposed to the ion source (sample gets drilled), thus allowing building the oxygen concentration profiles by simply analysing the secondary ions emitted as a function of time.

In this thesis, TOF.SIMS[5] machine from ION-TOF is used to investigate the oxygen mass transport properties of LSMC combinatorial thin film (see Chapter **6**). The experiments were carried out at 873 – 973 K. Silicon wafer substrates were employed to avoid oxygen diffusion intake from the backside during the exchange process, therefore limiting the incorporation of oxygen to the top surface area. These experiments were performed by Dr. Monica Burriel at Imperial College in London (UK).

2.5 Finite Element Modelling (FEM)

Finite Element Modelling (FEM) is a mathematical method to numerically solve partial differential equations (PDE). It is based on the discretization of the variables in finite elements of arbitrary size, which allows to solve complex multidimensional problems without analytical solution.[56] One example of PDE equation is the convection-diffusion equation, with general form:

$$\frac{\partial c(x,y,z,t)}{\partial t} + \nabla \cdot \boldsymbol{J} = g(c,x,y,z,t) \qquad \text{Eq. 2.21}$$

Where $c(x,y,z,t)$ is the concentration of a specie, $g(c,x,y,z,t)$ is a source element, such as a fixed concentration on a certain boundary, and $\boldsymbol{J}$ is the diffusion flux, described as:

$$\boldsymbol{J} = -D(x,y,z) \cdot \nabla c(x,y,z,t) \qquad \text{Eq. 2.22}$$

Where $D(x,y,z)$ is the diffusion coefficient. Some analytical solutions of equation **2.21** are available for simplified problems, for example in 1D systems where the diffusion coefficient is independent of the spatial coordinate.[57] Nevertheless, since a general analytical solution does not always exist, mathematical models offer an alternative way to deal with complex problems. In this sense, FEM is one of the most commonly used methods for the solution of PDEs in complex geometries. The FEM method is based on the discretization of a continuous domain into a finite one, which can be then solved with numerical methods. The main assumption behind FEM is that it is possible to describe any variable by a linear combination of a basis function (Ψ_i), each defined on an arbitrary small domain Ω_i. For example, the concentration c of equation **2.21** can be written by:

$$c \approx c_h = \sum_{i=1}^{n} c_i \Psi_i \qquad \text{Eq. 2.23}$$

Where c_i is the concentration coefficient of each domain, which denotes the unknown variable to approximate c. As an example, Ψ_i in a 1-D problem may be defined as a function equal to 1 in the i^{th} node and 0 to the other ones. Thus, by discretizing the spatial coordinates in sufficiently small elements, any function can be approximated. When solving PDEs with FEM method, the equation must be written in an integral form, called also weak formulation.[56] In this form, the equations are translated from an infinite dimensional function space into a finite dimensional function space. Then, by using the discretization of equation **2.23**, the equations are finally converted in a matrix formulation, which can be solved by numerical methods. For solving time-dependent problems, the most common approach is to use a discretization method independent on the FEM model.[56] As an example, finite difference methods can be employed to study the time evolution of a system.

In this thesis, FEM was used to model the oxygen concentration profiles obtained by IEDP-SIMS for LSMC polycrystalline thin films (Chapter **6**). FEM simulations were

performed by COMSOL Multiphysics using the *Transport of diluted species* module in 3D configuration. The geometry of the model consisted of a bilayer, YSZ underneath and LSMC on the top (see **Figure 2.18a**). The LSMC top layer was designed as a columnar grain divided into four equal subgrains ($d_g/4$) by a cross of δ_{gb}=1 nm wide that corresponds to grain boundaries in the film. Instead, the YSZ bottom layer was modelled as an undivided columnar grain. The thickness of the two materials and the dimensions of the grains were varied in accordance to the values measured in LSMC thin films (see Chapter **6**). The equation of diffusion (equation **2.21**) was then considered for all the solid domains. In the LSMC layer, two different diffusion coefficients were set in the GB and grain bulk domain (D^*_{gb} and D^*_b respectively). The diffusivity of YSZ layer was fixed at $D^*_{YSZ} = 3 \cdot 10^{-8} cm^2 s^{-1}$, since it can be considered an oxygen sink in the range of temperatures and thicknesses under study.[58]

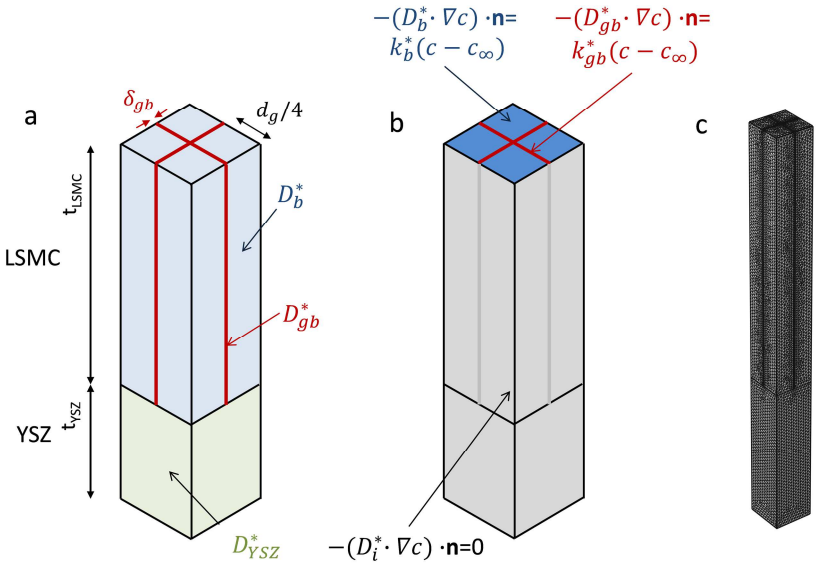

Figure 2.18 a, Sketch of the columnar repeating unit cell designed for simulating the oxygen diffusion profiles obtained by IEDP-SIMS. Different diffusion coefficients were set in GBs and grain of LSMC layer and in the YSZ film. **b**, Boundary conditions considered in the model. **c**, example of meshing of the unit cell.

The boundary conditions considered are shown in **Figure 2.18b**. On the top surface of the LSMC layer, convection type boundary condition was imposed with two different coefficients for GB and grain bulk (k^*_{gb} and k^*_b respectively). All the other surfaces were set as adiabatic (diffusion flux equal to zero). Free tetrahedral elements were used for the meshing of the bilayer (see **Figure 2.18c**). A mesh refinement was performed near the GB to better describe the heterogenous properties of LSMC thin films. Finally, the solution was computed in time dependent mode, setting the solution time equal to the exchange time of the isotope exchange experiments.

References

1. Lee, S. *et al.* Strain Tuning and Strong Enhancement of Ionic Conductivity in $SrZrO_3$-RE_2O_3 (RE = Sm, Eu, Gd, Dy, and Er) Nanocomposite Films. *Adv. Funct. Mater.* **25,** 4328–4333 (2015).
2. Navickas, E. *et al.* Fast oxygen exchange and diffusion kinetics of grain boundaries in Sr-doped $LaMnO_3$ thin films. *Phys. Chem. Chem. Phys.* **17,** 7659–7669 (2015).
3. Saranya, A. M. *et al.* Engineering Mixed Ionic Electronic Conduction in $La_{0.8}Sr_{0.2}MnO_{3+\delta}$ Nanostructures through Fast Grain Boundary Oxygen Diffusivity. *Adv. Energy Mater.* **5,** 1500377 (2015).
4. Ji, H.-I. *et al.* Enhanced oxygen diffusion in epitaxial lanthanum–strontium–cobaltite thin film cathodes for micro solid oxidefuel cells. *Energy Environ. Sci.* **6,** 116–120 (2013).
5. Roddatis, V. *et al.* Tailoring the Oxygen Evolution Activity and Stability Using Defect Chemistry. *Catalysts* **7,** 139 (2017).
6. Stoerzinger, K. A. *et al.* Highly Active Epitaxial $La_{1-x}Sr_xMnO_3$ Surfaces for the Oxygen Reduction Reaction: Role of Charge Transfer. *J. Phys. Chem. Lett.* **6,** 1435–1440 (2015).
7. Kan, D. *et al.* Overpotential-Induced Introduction of Oxygen Vacancy in $La_{0.67}Sr_{0.33}MnO_3$ Surface and Its Impact on Oxygen Reduction Reaction Catalytic Activity in Alkaline Solution. *J. Phys. Chem. C* **120,** 6006–6010 (2016).
8. Petrie, J. R., Jeen, H., Barron, S. C., Meyer, T. L. & Lee, H. N. Enhancing Perovskite Electrocatalysis through Strain Tuning of the Oxygen Deficiency. *J. Am. Chem. Soc.* **138,** 7252–7255 (2016).
9. Schweiger, S., Kubicek, M., Messerschmitt, F., Murer, C. & Rupp, J. L. M. A Microdot Multilayer Oxide Device: Let Us Tune the Strain-Ionic Transport Interaction. *ACS Nano* **8,** 5032–5048 (2014).
10. Schweiger, S., Pfenninger, R., Bowman, W. J., Aschauer, U. & Rupp, J. L. M. Designing Strained Interface Heterostructures for Memristive Devices. *Adv. Mater.* **29,** 1605049 (2017).
11. Baiutti, F. *et al.* High-temperature superconductivity in space-charge regions of lanthanum cuprate induced by two-dimensional doping. *Nat. Commun.* **6,** 1–8 (2015).
12. Eason, R. *Pulsed Laser Deposition of Thin Films*. (Wiley Interscience, 2007). doi:10.1557/JMR.1997.0359
13. Baiutti, F., Wrobel, F., Christiani, G. & Logvenov, G. Oxide molecular beam epitaxy of complex oxide heterointerfaces. *Met. Oxide-Based Thin Film Struct.* 53–78 (2018). doi:10.1016/B978-0-12-811166-6.00003-0
14. Smith, H. M. & Turner, A. F. Vacuum Deposited Thin Films Using a Ruby Laser. *Appl. Opt.* **4,** 147 (1965).
15. Venkatesan, T. Pulsed laser deposition—invention or discovery? *J. Phys. D. Appl. Phys.* **47,** 34001 (2014).
16. Jisrawi, N. *et al.* Preparation of Y□Ba□Cu oxide superconductor thin films using pulsed laser evaporation from high T c bulk material. *Appl. Phys. Lett.* **51,** 619–621 (2002).
17. Schou, J. Physical aspects of the pulsed laser deposition technique: The stoichiometric transfer of material from target to film. *Appl. Surf. Sci.* **255,** 5191–5198 (2009).
18. Johansson, J., De Groot, D. G., Rector, J. H., Huijbregtse, J. & Dam, B. Mechanism of

incongruent ablation of $SrTiO_3$. *J. Appl. Phys.* **83,** 3386–3389 (2002).

19. Ojeda-G-P, A., Döbeli, M. & Lippert, T. Influence of Plume Properties on Thin Film Composition in Pulsed Laser Deposition. *Adv. Mater. Interfaces* **5,** 1–16 (2018).

20. Wicklein, S. *et al.* Pulsed laser ablation of complex oxides: The role of congruent ablation and preferential scattering for the film stoichiometry. *Appl. Phys. Lett.* **101,** (2012).

21. Sambri, A. *et al.* Effects of oxygen background pressure on the stoichiometry of a $LaGaO_3$ laser ablation plume investigated by time and spectrally resolved two-dimensional imaging. *J. Appl. Phys.* **119,** (2016).

22. Amoruso, S., Sambri, A., Vitiello, M. & Wang, X. Propagation of $LaMnO_3$ laser ablation plume in oxygen gas. *Appl. Surf. Sci.* **252,** 4712–4716 (2006).

23. Sambri, A. *et al.* Plasma dynamics and cations off-stoichiometry in $LaAlO_3$ films grown in high pressures regimes. *J. Appl. Phys.* **120,** (2016).

24. Sambri, A., Amoruso, S., Wang, X., Granozio, F. M. & Bruzzese, R. Plume propagation dynamics of complex oxides in oxygen. *J. Appl. Phys.* **104,** (2008).

25. Amoruso, S., Toftmann, B. & Schou, J. Thermalization of a UV laser ablation plume in a background gas: From a directed to a diffusionlike flow. *Phys. Rev. E - Stat. Physics, Plasmas, Fluids, Relat. Interdiscip. Top.* **69,** 6 (2004).

26. Irissou, E., Le Drogoff, B., Chaker, M. & Guay, D. Correlation between plasma expansion dynamics and gold-thin film structure during pulsed-laser deposition. *Appl. Phys. Lett.* **80,** 1716–1718 (2002).

27. Bindhu, C. V., Tillack, M. S., Harilal, S. S., Gaeris, A. C. & Najmabadi, F. Internal structure and expansion dynamics of laser ablation plumes into ambient gases. *J. Appl. Phys.* **93,** 2380–2388 (2003).

28. Chen, J. *et al.* Plasma interactions determine the composition in pulsed laser deposited thin films. *Appl. Phys. Lett.* **105,** 114104 (2014).

29. Schneider, C. W., Wokaun, A., Lippert, T., Döbeli, M. & Ojeda-G-P, A. The importance of pressure and mass ratios when depositing multi-element oxide thin films by pulsed laser deposition. *Appl. Surf. Sci.* **389,** 126–134 (2016).

30. Chen, J. *et al.* Tracing the origin of oxygen for $La_{0.6}Sr_{0.4}MnO_3$ thin film growth by pulsed laser deposition. *J. Phys. D. Appl. Phys.* **49,** 45201 (2016).

31. Petrov, I., Barna, P. B., Hultman, L. & Greene, J. E. Microstructural evolution during film growth. *J. Vac. Sci. Technol. A Vacuum, Surfaces, Film.* **21,** S117–S128 (2003).

32. Xu, C. *et al.* Impact of the interplay between nonstoichiometry and kinetic energy of the plume species on the growth mode of $SrTiO_3$ thin films. *J. Phys. D. Appl. Phys.* **47,** (2014).

33. Thornton, J. A. Influence of substrate temperature and deposition rate on structure of thick sputtered Cu coatings. *J. Vac. Sci. Technol.* **12,** 830–835 (1975).

34. Infortuna, A., Harvey, A. S. & Gauckler, L. J. Microstructures of CGO and YSZ thin films by pulsed laser deposition. *Adv. Funct. Mater.* **18,** 127–135 (2008).

35. Greer, J. A. History and current status of commercial pulsed laser deposition equipment. *J. Phys. D. Appl. Phys.* **47,** 34005 (2014).

36. Christen, H. M., Silliman, S. D. & Harshavardhan, K. S. Continuous compositional-spread technique based on pulsed-laser deposition and applied to the growth of epitaxial films. *Rev. Sci. Instrum.* **72,** 2673–2678 (2001).

37. Christen, H. M. & Eres, G. Recent advances in pulsed-laser deposition of complex oxides. *J. Phys. Condens. Matter* **20,** 264005 (2008).

38. Noh, M., Thiel, J. & Johnson, D. C. Synthesis of Crystalline Superlattices by Controlled Crystallization of Modulated Reactants. *Science (80-.).* **270,** 1181–1184 (1995).

39. Noh, M., Johnson, C. D., Hornbostel, M. D., Thiel, J. & Johnson, D. C. Control of reaction pathway and the nanostructure of final products through the design of modulated elemental reactants. *Chem. Mater.* **8,** 1625–1635 (1996).

40. Fister, L. & Johnson, D. C. Controlling Solid-State Reaction Mechanisms Using Diffusion Length in Ultrathin-Film Superlattice Composites. *J. Am. Chem. Soc.* **114,** 4639–4644 (1992).

41. Williams, D. B. & Carter, C. B. *Transmission Electron Microscopy*. (Springer, US, 2009).

42. Egerton, R. F. *Electron Energy-Loss Spectroscopy in the Electron Microscope*. (Springer, 2011).

43. Kolasinski, K. W. *Surface science: foundations of Catalysis and Nanscience*. (John Wiley & Sons, Ltd, 2008).

44. Tompkins, H. G. & Irene, E. A. *Handbook of ellipsometry*. (William Andrew, inc, 2005). doi:10.1016/B978-0-12-405889-7.01001-7

45. Scafetta, M. D., Xie, Y. J., Torres, M., Spanier, J. E. & May, S. J. Optical absorption in epitaxial $La_{1-x}Sr_xFeO_3$ thin films. *Appl. Phys. Lett.* **102,** 81904 (2013).

46. Mildner, S., Hoffmann, J., Blöchl, P. E., Techert, S. & Jooss, C. Temperature- and doping-dependent optical absorption in the small-polaron system $Pr_{1-x}Ca_xMnO_3$. *Phys. Rev. B* **92,** 35145 (2015).

47. Nomerovannaya, L. V., Makhnev, A. A. & Rumyantsev, A. Y. Evolution of the optical properties of single-crystal $La_{1-x}Sr_xMnO_3$. *Phys. Solid State* **41,** 1322--1326 (1999).

48. Newville, M. Fundamentals of XAFS. *Rev. Mineral. Geochemistry* **78,** 33–74 (2014).

49. Van Der Pauw, L. J. A methode of measuring specific resistivity and Hall effect of discs of arbitrary shape. *Philips Res. reports* **13,** (1958).

50. Chan, W. K. On the calculation of the geometric factor in a van der Pauw sheet resistance measurement. *Rev. Sci. Instrum.* **71,** 3964 (2000).

51. Barsoukov, E. & MacDonald, J. R. *Impedance spectroscopy theory, experiment, and applications*. (Jhon Wiley & Sons, Inc., 2005).

52. Huang, Q. A., Hui, R., Wang, B. & Zhang, J. A review of AC impedance modeling and validation in SOFC diagnosis. *Electrochim. Acta* **52,** 8144–8164 (2007).

53. Aydin, H., Korte, C. & Janek, J. 18O-tracer diffusion along nanoscaled Sc_2O_3/yttria stabilized zirconia (YSZ) multilayers: On the influence of strain. *Sci. Technol. Adv. Mater.* **14,** (2013).

54. Boukamp, B. A., Hildenbrand, N., Bouwmeester, H. J. M. & Blank, D. H. A. Impedance of thin film cathodes: Thickness and current collector dependence. *Solid State Ionics* **283,** 81–90 (2015).

55. Kilner, J. A., Skinner, S. J. & Brongersma, H. H. The isotope exchange depth profiling (IEDP) technique using SIMS and LEIS. *J. Solid State Electrochem.* **15,** 861–876 (2011).

56. Larson, M. G. & Bengzon, F. *The Finite Element Method: Theory, Implementation, and Applications*. (Springer-Verlag Berlin Heidelberg, 2013).

57. Crank, J. *The mathematics of diffusion*. (Oxford science, 1956).

58. Kilo, M., Argirusis, C., Borchardt, G. & Jackson, R. A. Oxygen diffusion in yttria stabilised zirconia—experimental results and molecular dynamics calculations. *Phys. Chem. Chem. Phys.* **5,** 2219–2224 (2003).

3.Atomistic Picture of Bulk and Grain Boundaries in $La_{0.8}Sr_{0.2}Mn_yO_{3\pm\delta}$ Thin Films

3.1 Introduction

Grain boundaries (GBs) in oxides are well known for displaying a highly insulating behaviour for both electronic and oxygen ion conduction. Although the GB core usually presents more reducible behaviour than the bulk, the oxygen vacancies accumulated in this region do not give rise to a preferential pathway for oxygen diffusion.[1] The sluggish oxygen ion diffusion in these structural defects is due to different phenomena, such as low vacancies mobility and creation of a space charge region in lightly doped $SrTiO_3$,[2,3] or the association of dopant-oxygen vacancy defects in doped ceria.[4] Nevertheless, it was discovered that GBs in $La_{0.8}Sr_{0.2}MnO_{3\pm\delta}$ (LSM) thin films are responsible for a substantial enhancement of oxygen diffusion and oxygen reduction reactions (ORR).[5–7] This substantial difference between LSM and other oxides is at the centre of an important debate within the scientific community, since the comprehension of the phenomena might open new horizons to take advantage of GB peculiarities in several families of solid-state electrochemical devices.

In this chapter, the composition and structure of GBs in polycrystalline LSM thin films is deeply analysed. The LSM thin films were deposited by Pulsed Laser Deposition (PLD) under a set conditions previously optimized for obtaining fully-dense polycrystalline thin films, suitable for the analysis of the grain and grain boundaries oxygen mass transport properties.[5] The compositional analysis of these films revealed a severe Mn deficiency, mainly due to the plasma-background interaction in the deposition (section **3.2**). On top of that, TEM-EELS analysis of the GB composition revealed that both a cationic and anionic redistribution takes place in the GBs, involving an increase of La and Sr and a decrease of Mn and O. This unusual behaviour suggested an interesting connection between the Mn-deficiency in the bulk and a GB compensation mechanism involving cationic modifications. For this reason, the effect of the overall cationic composition on the GB local-non-stoichiometry was investigated (section **3.3**). Taking advantage of the capabilities of the large-area PLD (LA-PLD), thin films with different Mn content were produced by a combinatorial deposition approach. After analysing the bulk chemical and structural properties, focus is placed on the control of GB composition by modifying the overall cationic content in the films. As it will be shown later in this chapter, increasing the bulk Mn concentration leads to a sudden change of the GB equilibrium, switching from Mn deficient (La-rich) to Mn rich (La deficient) compositions. Finally, a discussion on the compensation and equilibrium mechanisms of bulk and GBs in LSM films with different overall Mn content is presented (section **3.4**).

3.1 Mn-deficient LSM thin films

3.2.1 Deposition of $LSM_{0.85}$ thin films

In this thesis, polycrystalline and epitaxial thin films of LSM were deposited by Large-Area Pulsed Laser Deposition (LA-PLD). The polycrystalline films were grown on different substrates, selected for avoiding unwanted interferences during the different characterization experiments (details for each specific case will be discussed later) and for preventing a preferential orientation in the LSM thin films (being the substrates lattice parameter very different from the LSM one). In particular, LSM films were deposited on: (i) heterostructures of 50 nm Yttria-stabilized Zirconia (YSZ) / 300 nm Si_3N_4 / 100 nm SiO_2 grown on Si (100) substrates, (ii) Sapphire (0001) and (iii) yttria-stabilized zirconia (100) substrates (YSZ). The initial deposition conditions were directly derived from previous works at IREC, in order to study the GBs of the very same thin films.[5,7] For this reason, the layers were deposited with an energy fluence of ~1 J cm^{-2} per pulse at a frequency of 10 Hz. The substrate was kept at 973 K in an oxygen pressure of 0.026 mbar during the deposition and the substrate-target distance was set to 95 mm. Additionally, also epitaxial thin films were grown under the same conditions of the polycrystalline layers on $NdGaO_3$ $(110)_o$ substrates (hereby NGO). In this case, the NGO substrate was selected because its lattice parameter is similar to the LSM one (just a slight compressive strain of ~0.6 % is expected).[8–10] **Figure 3.1** shows a schematic representation of the LSM thin films deposited on the different substrates. More information on the deposition conditions can be found in Chapter **2**.

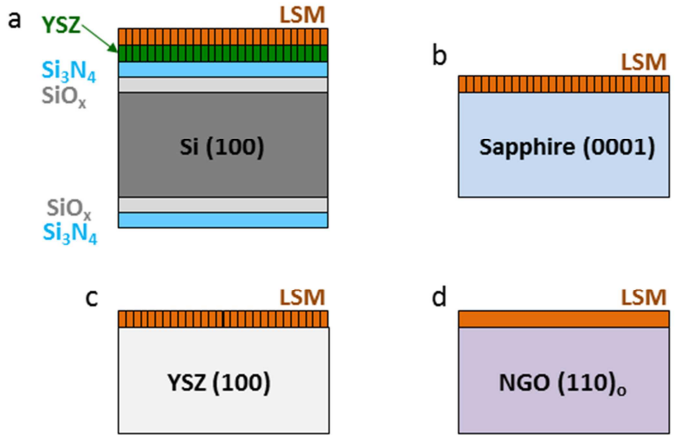

Figure 3.1 Schematic representation of the LSM thin films deposited on YSZ / Si_3N_4 / SiO_2 / Si (100) (**a**), Sapphire (0001) (**b**), YSZ (100) (**c**) and NGO (110) substrate (**d**).

The cationic composition of the LSM thin films was first investigated by wavelength dispersive spectroscopy (WDS) and Energy Dispersive X-ray Analysis (EDS). The atomic ratio (Mn)/(La+Sr) (B/A ratio) was estimated to be 0.85 ± 0.04, while the Sr/(La+Sr) (A-site) ratio was found to be equal to 0.20 ± 0.01. Since the nominal composition of the commercial target is $La_{0.8}Sr_{0.2}MnO_{3+\delta}$, the large Mn deficiency

found in the thin films implies a non-stoichiometric transfer during the laser ablation deposition. It is interesting to note that the cationic thin film off-stoichiometry just involve the Mn atoms, as a correct relative transfer of La/Sr was obtained. It is well known that the two most relevant phenomena that can lead to a variation of the cationic content in the PLD deposited thin films are (i) a not congruent laser ablation of the target species and (ii) the plasma-background interactions in the deposition chamber (see Chapter **2** for a detailed description of PLD phenomena).[11,12] The former is mainly governed by the laser fluence, while the latter is controlled by the deposition oxygen pressure and the substrate to target distance. In the case of manganites, it was demonstrated that, at intermediate pressure (0.001 – 0.1 mbar), a preferential scattering of the lighter Mn atoms in the plasma plumes favours the transfer of the heavier Sr and La species, giving rise to highly B-site deficient thin films.[13] This phenomenon is particularly important when the atomic species present a large difference in atomic weight.[*] Considering that our LSM thin films were deposited in this pressure range (0.026 mbar) and that the large substrate-target distance used in our LA-PLD increases the scattering events of the ablated species, it is plausible that the plasma-background interactions are at the origin of the off-stoichiometry measured in the LSM thin films.

3.2.2 Structure and bulk properties of $LSM_{0.85}$ thin films

Due to the large off-stoichiometry measured, it is particularly important to study the structure and the phase of the Mn deficient LSM thin films (hereby $LSM_{0.85}$). **Figure 3.2** shows the XRD of the $LSM_{0.85}$ layers deposited on different substrates. The films present a polycrystalline structure without any preferential orientation. No long-range secondary phases were detected in any of the thin films, meaning that despite the Mn deficiency, a single-phase perovskite structure was obtained. This is in agreement with the extension of solubility limits of B-site vacancies in the perovskite structure when decreasing the temperature.[14] As an example, Van Roosmalen *et al.*[15] found a single phase up to a value of B/A ≈ 0.82 at 1100 K in LMO, suggesting that the $LSM_{0.85}$ thin films growth at 973 K fall into the single perovskite solubility limits.

[*]As an exemplifying case of study, Annex **A** shows the effect of the deposition distance and pressure on the cationic content in the solid electrolyte $Bi_4V_{1.8}Cu_{0.2}O_{10.7}$, in which, due to the relative weight difference of bismuth and vanadium, the plasma scattering effect dominates the thin film composition.

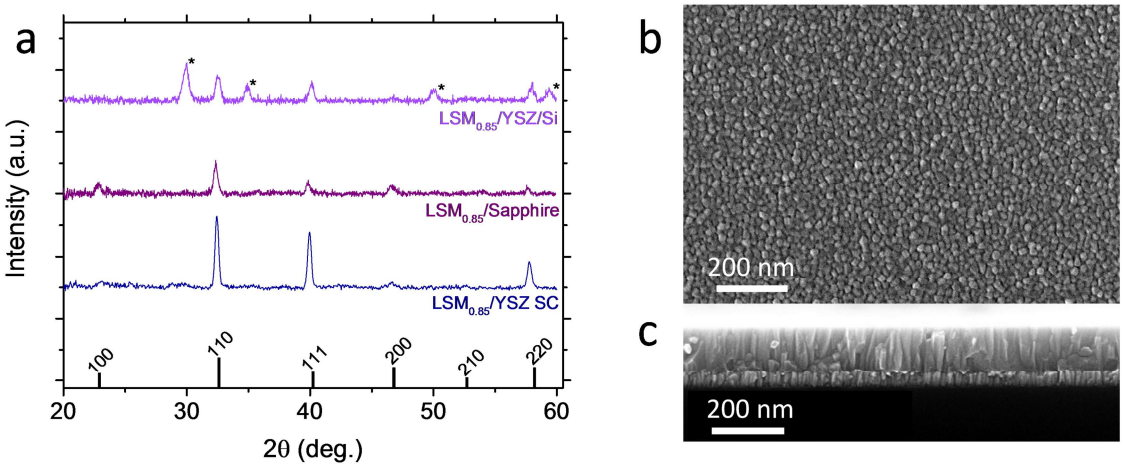

Figure 3.2. a, XRD of Mn-deficient $LSM_{0.85}$ thin films deposited on YSZ / Si_3N_4 / SiO_2 / Si (100), Sapphire (0001) and YSZ (100) substrates. The bulk LSM reference in pseudo-cubic notation (see note p. 87) is included for comparison. The peaks corresponding to the YSZ thin film in the LSM/YSZ/Si_3N_4/SiO_2/Si heterostructure are highlighted with asterisks. **b** and **c,** SEM images of the planar view and cross section, respectively, of a characteristic $LSM_{0.85}$ thin film deposited on YSZ/Si_3N_4/SiO_2/Si.

Top view and cross section SEM pictures (**Figure 3.2b** and **c**, respectively) show that the $LSM_{0.85}$ layers are fully dense, with well-defined nanometric columnar grains of tens of nanometres in diameter. HR-TEM cross section picture confirms the columnar structure of the grains, which grow perpendicular to the substrate (**Figure 3.3**). Also, the TEM pictures confirm the absence of secondary phases in the layers, reinforcing the XRD results. Overall, the structural characterization demonstrates the high quality of the $LSM_{0.85}$ polycrystalline layers and their suitability for the study of the GBs structure and composition.

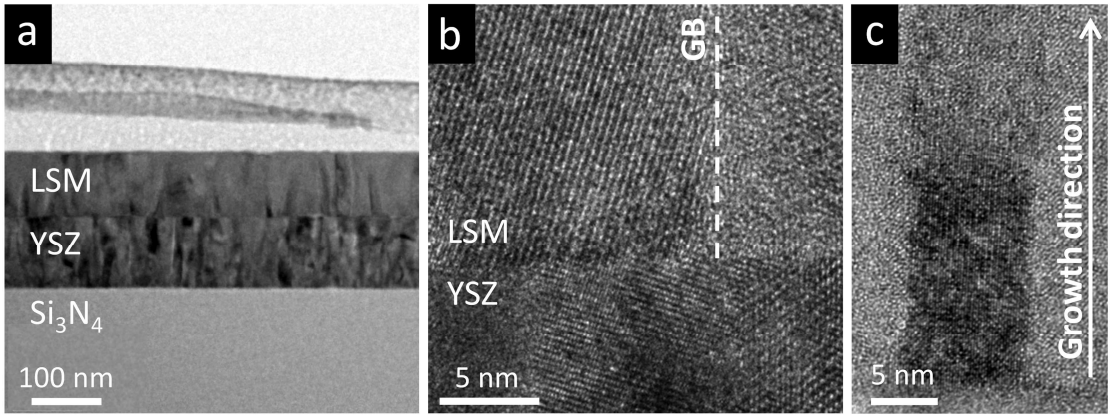

Figure 3.3. a, TEM cross section of the $LSM_{0.85}$/YSZ/Si_3N_4/SiO_2/Si thin films. **b**, HRTEM image of YSZ/LSM interface showing one GB (highlighted by a white dashed line). **c**, HRTEM of one grain (~10 nm of diameter) showing the characteristic columnar structure perpendicular to the substrate.

Moreover, in order to study the functional properties of Mn-deficient LSM thin films in the absence of GBs and, eventually, to distinguish the bulk and GB contribution in the polycrystalline samples (Chapters **4** and **5**), epitaxial thin films of $LSM_{0.85}$ were additionally grown under the same conditions of the polycrystalline layers on NGO $(110)_o$.

The θ-2θ XRD scan of the $LSM_{0.85}$ layers on NGO is presented in **Figure 3.4a**. The film presents a unique orientation, corresponding to the $(00l)_{pc}$ (where pc stands for pseudo-cubic†), in accordance with literature.[8,9] The high resolution XRD of the $LSM_{0.85}$/NGO structure around the $(002)_{pc}$ peak (**Figure 3.4b**) reveals a highly oriented thin film with finite-size oscillations, demonstrating the long-range homogeneity of the film. A thickness of 60 nm is extracted from the fitting of the oscillations, consistent with the thickness measured by ellipsometry. The phi-scan around the 220 peak (inset of **Figure 3.4b**) and the reciprocal space maps around the $\bar{3}03$ and the 033 asymmetrical peaks (**Figure 3.4c** and **d**) show that the film is coherently strained by the substrate, being the two in-plane reciprocal space coordinates of the substrate (Q_x and Q_y) equal to the ones of the film. Therefore, a "cube on cube" growth of the film on the substrate is expected[9] (schematically shown in **Figure 3.4e**).

†The pseudo-cubic notation can be used to describe crystals that owe lower levels of symmetry (i.e. rhombohedral or orthorhombic) with a cubic structure. The unit cell is called "pseudo" cubic because the tetragonal distortions of the original structure generate small differences in the lattice parameters (a, b, c) of the cell and/or the corners' angle. This notation is commonly used when analyzing thin films by XRD, where the small amount of material makes the identification of small tetragonal distortions complicated. In the case of NGO, which possesses a orthorhombic structure (o), the $(110)_o$ plane directly corresponds to the $(001)_{pc}$ in pseudo-cubic notation, and the relation between the lattice parameters are: $a_{pc} = \frac{1}{2}c_o$ and $b_{pc} = c_{pc} = \frac{1}{2}\sqrt{a_o^2 + b_o^2}$. Although the small differences in modulus between a_{pc} and b_{pc} could generate a slight distortion in the thin films, the angle between them is 90º, making the NGO $(110)_o$ substrates suitable for the epitaxial growth of thin films.[9]

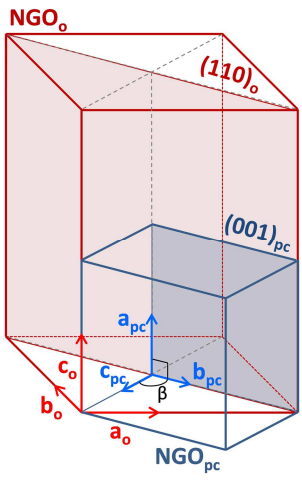

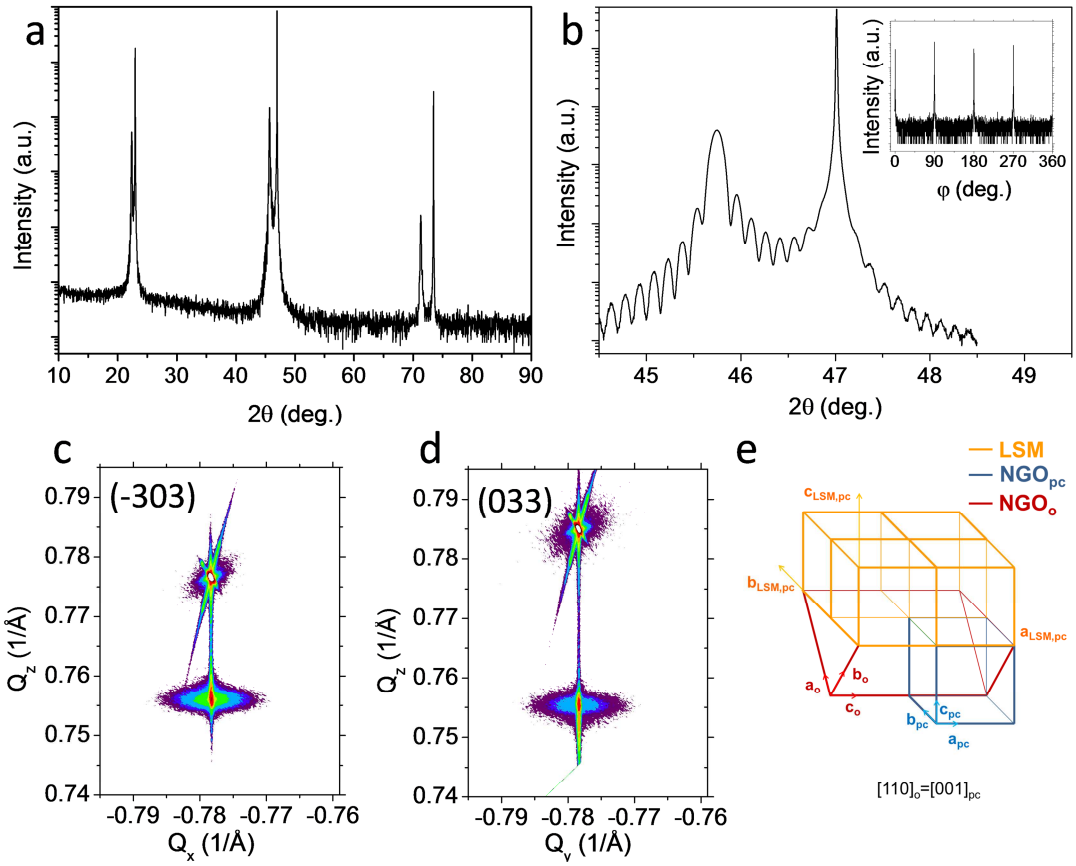

Figure 3.4. a, XRD of the $LSM_{0.85}$ thin film grown on NGO $(110)_O$ substrate. **b**, high resolution XRD around the 200 peaks showing finite-size oscillations originating from the long-range homogeneity of the film. The inset shows the φ scan around the 220 peak. Reciprocal space maps of $\bar{3}$**03** and **033** in plane reflection showing that the film is coherently strained by the substrate (**c** and **d** respectively). **e**, scheme of the epitaxial relation between pseudo-cubic LSM and orthorhombic/pseudocubic NGO $(110)_o$.

X-ray Absorption Near-Edge Structure (XANES) was then carried out around the Mn K-edge in a polycrystalline and epitaxial $LSM_{0.85}$ thin film (deposited on sapphire and on NGO respectively) to asses possible differences in the Mn valence of the two layers (**Figure 3.5**). The Mn K-edge, which involves a transition from Mn 1s to Mn 4p states, has been demonstrated to display an energy shift depending on the Mn valence in many different compounds, including perovskites.[16,17] In particular, the K-edge energy increases almost linearly with the Mn valence in LSM, shifting approximately 1 eV per 0.27 valence change.[18,19] The position of the white line was extracted by calculating the inflection point energy, given by the maximum of the first derivative (more information can be found in the Chapter **2**). It is important to note that this technique is not able to separate grain and grain boundary contributions, therefore the results described next can be mainly ascribed to the bulk $LSM_{0.85}$, since it represents approximately the 90 vol.% of the polycrystalline films. **Figure 3.5** shows that the two spectra are nearly identical, and the extracted Mn valence difference is less than 3%. Therefore, the epitaxial $LSM_{0.85}$ film is expected to behave mostly like the grain interior of polycrystalline $LSM_{0.85}$ and is taken as a reference to ensure that the effects observed are associated to

the GBs. Indeed, the polycrystalline and epitaxial $LSM_{0.85}$ thin films present the same bulk cationic composition, Mn oxidation state and, consequently, oxygen content.

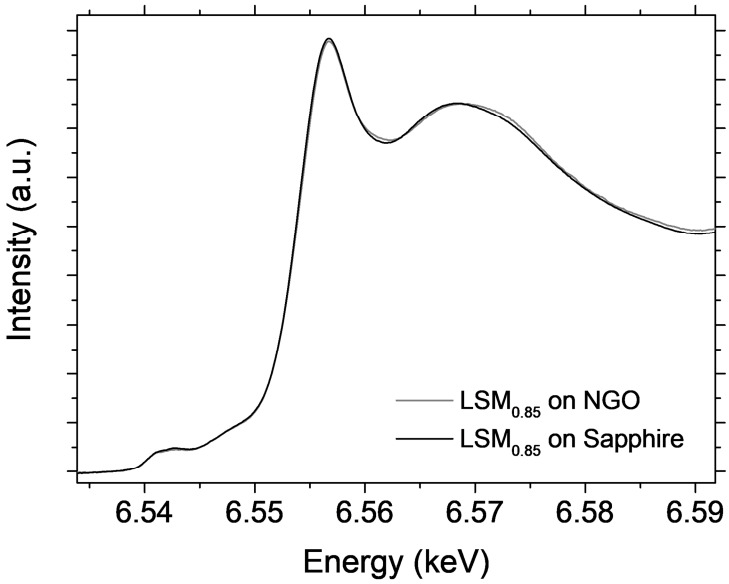

Figure 3.5. Normalized XANES spectra at the Mn K-edge for the Mn deficent LSM thin films deposited on sapphire (0001) and NGO $(110)_o$. The K-edge energy differs for less than 0.1 eV between the two films.

3.2.3 Grain boundary investigation of Mn-deficient LSM thin films

3.2.3.1 The grain boundary structure

The GBs' atomic structure in the $LSM_{0.85}$ thin films deposited on $YSZ/Si_3N_4/SiO_2/Si$ heterostructure was analysed by cross-section HR-TEM. **Figure 3.6a** shows a high resolution HRTEM image of two columnar LSM grains. The corresponding fast Fourier transform (FFT) was indexed to the orthorhombic space group 62 (Pnma) (**Figure 3.6b**). **Figure 3.6c** shows the Fourier filtered image of the red dotted square depicted in **Figure 3.6a**. No secondary phases were detected either in the bulk or in the GB core, in line with the comments of section **3.2.1**. Still, a high concentration of fringe-like features was visible at the GB, recurring all along the observed zone with a periodicity of ~1nm and propagating for some nanometers inside the grains. Zooming in the GB interface, **Figure 3.6d**, allows identifying the origin of the fringes as atomic disorder associated to the formation of a dense array of edge dislocations, consisting of a missing (02-2) plane one out every four. This large dislocation density derives from the lattice misorientation of the different grains, which drives a plastic deformation to mitigate elastic effects. Nevertheless, dislocations are known to impose an elastic deformation in their surroundings which can propagate for different nanometers,[4,20] as visible in **Figure 3.6d**. Moreover, due to the closeness and periodicity of dislocations, the strain fields can overlap, determining a fully strained region in the vicinity of the grain boundary.[21]

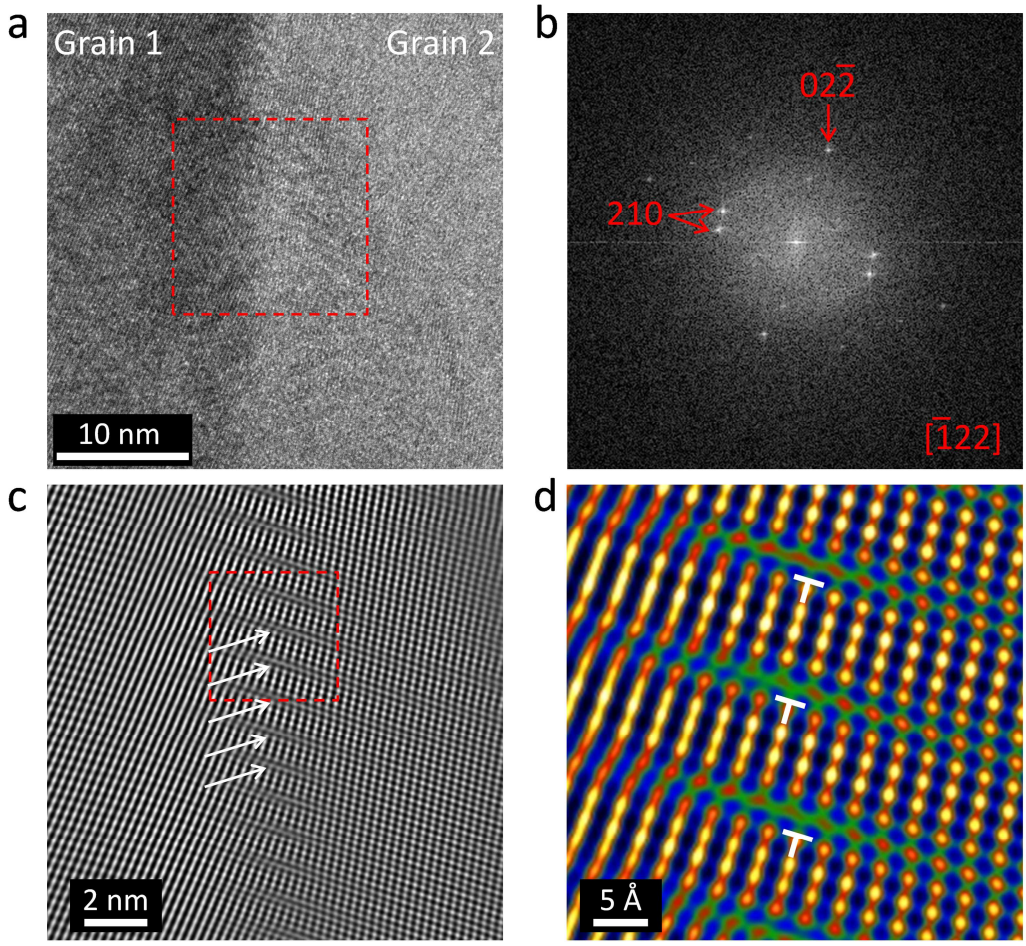

Figure 3.6. a, HRTEM image containing a grain boundary separating two $LSM_{0.85}$ columnar grains. Fast Fourier transform (**b**) and Fourier filtered image (**c**) of the area highleghted with a red dashed square in **a**. The white arrows in **c** are intended to highlight the dislocation pattern. **d**, coloured enlargement of the red dotted square shown in **c**, in which 3 dislocations are highlighted by white "T" symbols.

It is important to comment here that not all the grain boundaries analysed displayed visible dislocations. As an example, **Figure 3.7a** shows the HRTEM of another GB studied. From corresponding FFT, both grains were once again indexed to the orthorhombic space group 62 (Pnma). The Fourier filtered image (**Figure 3.7a**) revealed no dislocations at the interface. Nevertheless, these may still be present in the GB core but not visible in this specific orientation (for instance if the dislocation line is parallel to the electron beam).

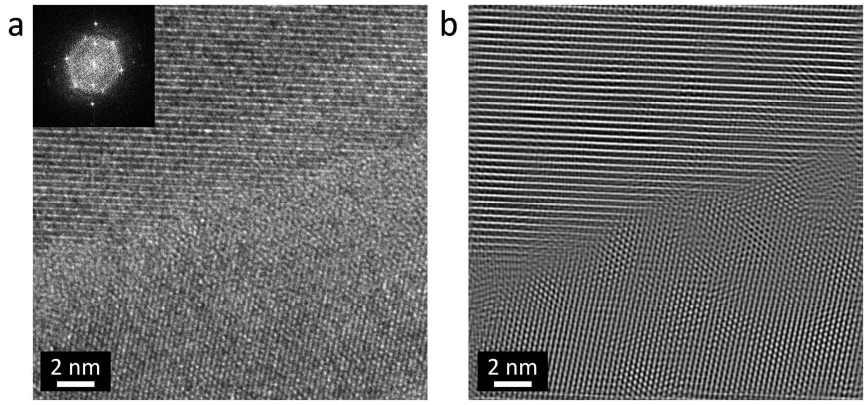

Figure 3.7. a, HRTEM image of a $LSM_{0.85}$ grain boundary. The inset of **a** shows the corresponding FFT. **b**, Fourier filtered image of the image shown in **a**.

3.2.3.2 The grain boundary local-nonstoichiometry

The chemical composition of these GBs was analysed by high angle annular dark-field (HAADF) and electron energy-loss spectroscopy (EELS). In order to properly derive the quantification of all the elements in the $LSM_{0.85}$ thin films, the EELS spectra were measured over a large energy window, mainly because of the low energy onset of the Sr M edge (**Figure 3.8**). The elemental quantification was performed by integration of the different edges (O K edge, Mn L edges, La M edges and Sr M edge).

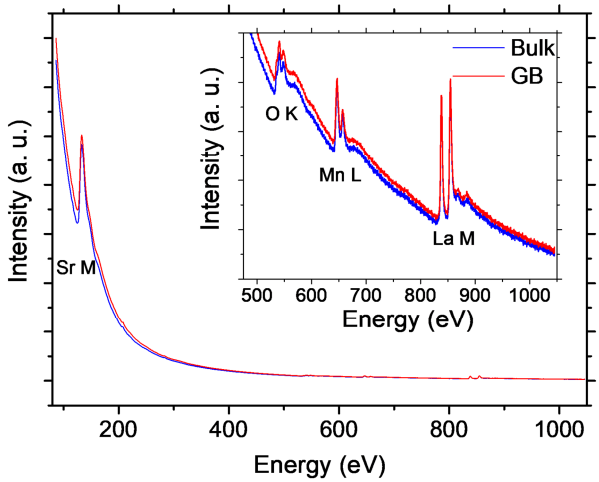

Figure 3.8. EELS spectra of the grain interior and grain boundary region obtained over a large energy window to measure the Sr M edge (133 eV). The inset shows a magnification of the region showing the O K edge (532 eV), Mn L edges (640-651 eV) and La M edges (832-849 eV).

Figure 3.9a shows the high angle annular field (HAADF) image of a GB (indicated by black triangles in the figure). A zone of lighter contrast is clearly visible at the interface between the two grains, offering a first hint of a different chemical composition. **Figure 3.9b** shows the normalized elemental concentration obtained along the white arrow shown in **Figure 3.9a.** An evident rearrangement of the elements occurs at the GB. Specifically, a clear increase of concentrations of the A-site cations is observed (Sr and

La), accompanied by a simultaneous decrease of the B-site Mn concentration. Also, the O content appears to decrease in the GB region, revealing the oxygen deficient character of $LSM_{0.85}$ grain boundaries. Interestingly, the relative increase of Sr and La is similar, meaning that the doping ratio Sr/(La+Sr) keeps nearly constant across the GBs.

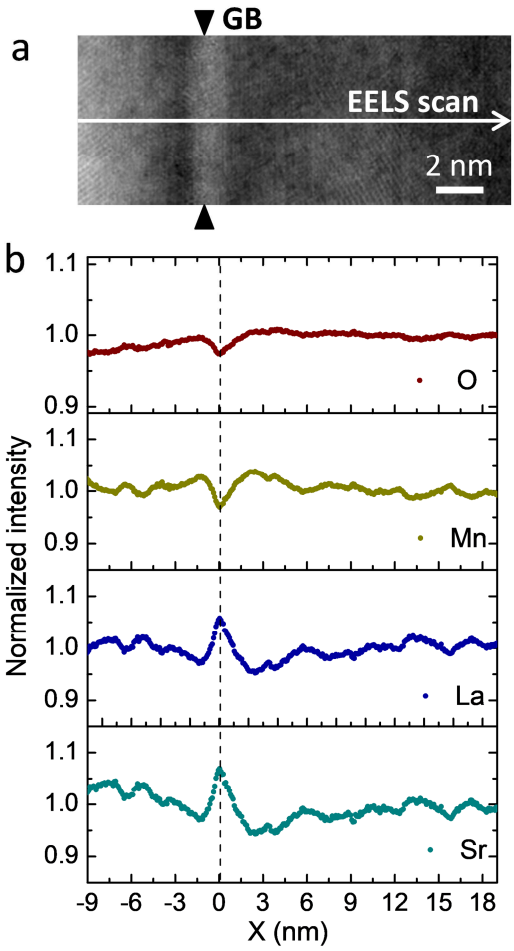

Figure 3.9. a, HAADF image of the GB, showing a different contrast at the interface. **b**, chemical composition obtained from the EELS scan across the GB (white arrow in a). Integrated intensity signals were normalized to the grain (bulk) values for each element.

The analysis was repeated for different GBs with a smaller energy window (excluding the Sr M edge) in order to increase the sensitivity of the measurement and to confirm the cation local-nonstoichiometric described in **Figure 3.9**. **Figure 3.10** shows the compositional map of La and Mn measured in two adjacent $LSM_{0.85}$ grains near the YSZ interface. In both GBs, an increase of La together with a decrease of Mn concentration is detected, similiar to **Figure 3.9**. This figure endorses qualitatively the homogeneity of the GB local nonstoichiometry in $LSM_{0.85}$ thin films. Nevertheless, we cannot exclude from the current study that the extent of the off-stoichiometry is higher in some specific orientations.[22]

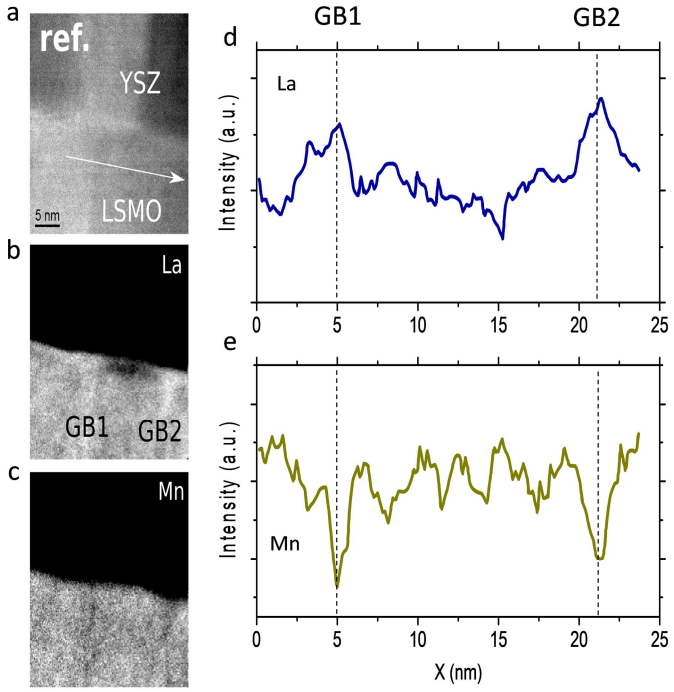

Figure 3.10. a, HAADF figure of two grains near the interface with YSZ film. EELS compositional maps of La (**b**) and Mn (**c**) concentrations. Compositional variation of La (**d**) and Mn (**e**) along the white arrow drawn in (a).

Additionally, the variation of Mn oxidation state has been derived from the Mn L_{32} ratio in the EELS spectra (**Figure 3.11a**). It is well known that a variation of Mn valence originates a shift in the Mn L edge energy as well as a change in the L_{32} ratio intensity.[23] Nevertheless, despite the stoichiometry deviation, a constant Mn L_{32} ratio of *ca.* 2.5 (corresponding to a Mn oxidation state of ~3.4)[23] was measured across the GB (**Figure 3.11b**).

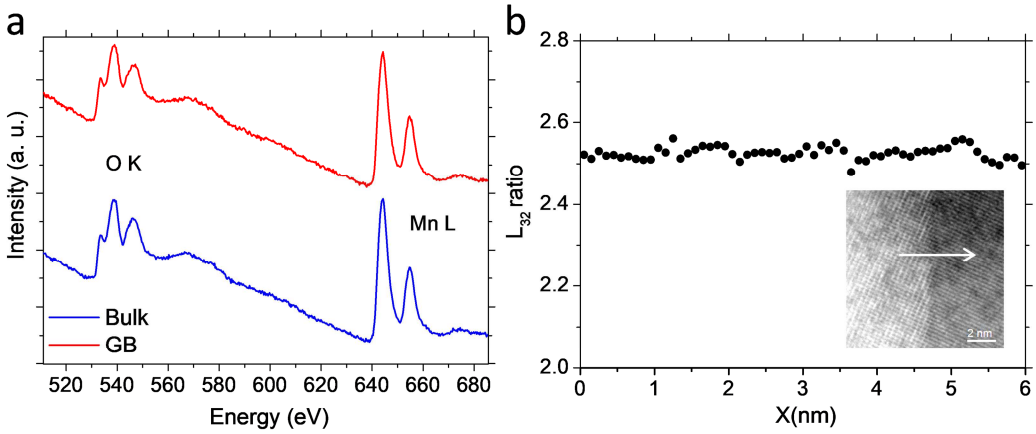

Figure 3.11. a, EELS of grain and grain boundary regions obtained over a small energy window in order to detect variance of oxidation state. **b**, Mn L_{32} ratio across a grain boundary showing a constant profile and indicating no Mn valence change. The inset shows the HADDF of a grain boundary analysed.

To better localize the origin of cationic variations, EELS measurements along a GB have been performed, see **Figure 3.12**. Here, a clear array of atomic fringes is visible in Bright Field HRTEM mode (**Figure 3.12a-c**), similarly to the pattern observed in **Figure 3.9**. The EELS analysis presented in **Figure 3.12d** shows that the increase of La and reduction of Mn is not homogenous but occurs at specific sites. The periodicity of the cation local nonstoichiometry well matches with the dislocation pattern observed (emphasized by red arrows in **Figure 3.12b**), suggesting that these strained regions are strongly related with the local variation of the stoichiometry.

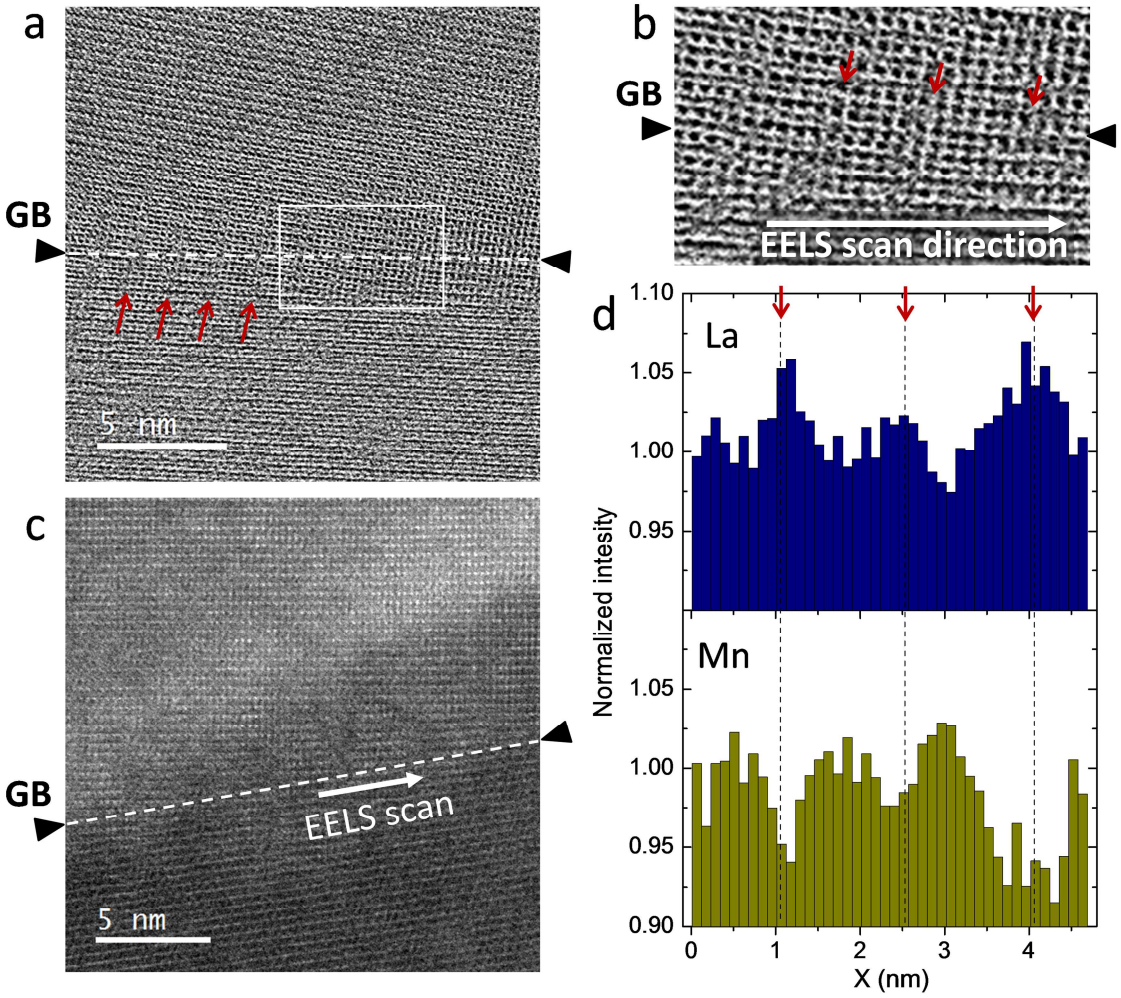

Figure 3.12. Bright Field HRTEM (**a** and **b**) and STEM-HAADF (**c**) figures of a GB showing atomic fringes at the interface (indicated by red arrows) that match with the dislocations pattern observed in **Figure 3.9**. **b**, Enlargment of the white rectangle drawn in **a**. **d**, La and Mn variation extracted from EELS scan along the GB (white arrow in **c**). An increase of La coupled to decrease of Mn concentration is observed at specific locations that corresponds well with the fringe pattern observed, indicating that the chemical variations occurs in the vicinity of the dislocations.

3.3 Engineering of grain boundary local non-stoichiometry

The analysis of the $LSM_{0.85}$ thin films revealed that the GBs are characterized by significant changes of both the anionic and the cationic concentration. The decrease of B-site Mn content in the GB of Mn-deficient thin films suggests a possible connection between the cation chemical potential in the grain bulk (i.e. cationic concentration in the thin film) and the GB chemical equilibrium. In other words, the change of cation concentration at the GB seems to be somehow connected with the large off-stoichiometry of the $LSM_{0.85}$ thin films. In this section, the possibility of influencing the elemental concentration in the GBs by varying the overall cation concentration in the thin films is investigated.

3.3.1 Deposition of LSM_y thin films by combinatorial PLD

Combinatorial Pulsed Laser Deposition (C-PLD) was used to grow $La_{0.8}Sr_{0.2}Mn_yO_{3\pm\delta}$ (LSM_y) with variable content of Mn (y = 0.85 – 1.1). C-PLD is a technique based on the coupled deposition of two parent compounds on a large area substrate (see Chapter **2** for more information).[24–27] The two parent compounds used were $La_{0.8}Sr_{0.2}MnO_{3\pm\delta}$ (LSM) and Mn_3O_4, which were deposited under the same conditions employed in the growth of the $LSM_{0.85}$ thin films (see **section 3.2.1**). The aim of the study is to generate a thin film with continuous map of compositions $La_{0.8}Sr_{0.2}Mn_yO_{3\pm\delta}$ (LSM_y), starting from a Mn-deficient layer and progressively adding Mn by C-PLD (y = 0.85 – 1.1). Although other approaches are available to vary the cation composition in thin films, such as changing the deposition conditions,[13] these are also known to severely influence the thin film microstructure.[28] By means of C-PLD, we were able to study the effect of cationic composition without strongly affecting the layer morphology. This last aspect is particularly important here, since the goal is to study of the functional properties of the GBs (Chapters **4** and **5**).

First, single parent compounds plumes were deposited on 4” Si (100) wafers to measure the plume profiles and the material growth rate. In the case of Mn_3O_4 plume, a homogenous 20 nm layer of YSZ was deposited prior to the parent compound in order to avoid the reaction between the Si substrate and the Mn_3O_4 film and therefore allow a proper analysis of the oxide film. **Figure 3.13a** and **b** show respectively the thickness of $LSM_{0.85}$ and Mn_3O_4 plumes, measured by ellipsometry along the central axis. The experimental points were fitted with a Pseudo-Voigt curve and the deposition rate (pulses/nm) of each material as a function of the distance to the plume centre was obtained.

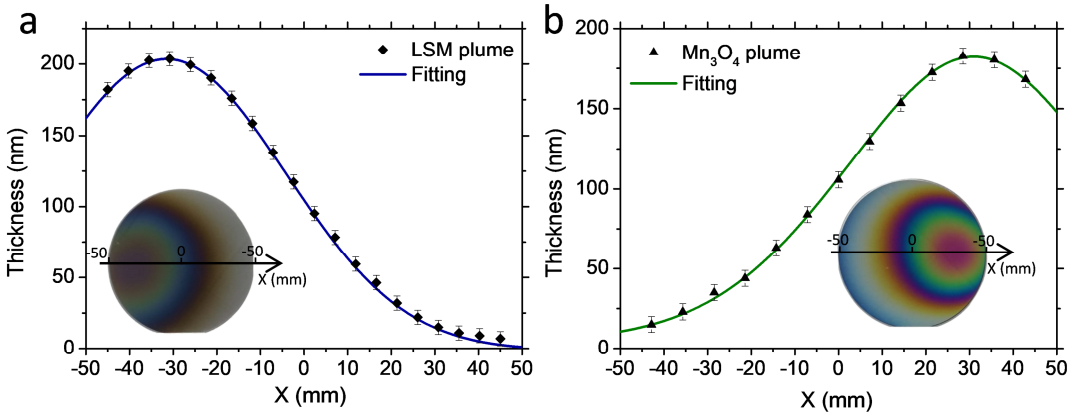

Figure 3.13. Thickness measured by ellipsometry for LSM (**a**) and Mn_3O_4 (**b**) plumes. The curves were fitted using a Pseudo-Voigt function.

The Mn_3O_4 thin film plume was then analysed by SEM (**Figure 3.14a**), revealing a well-ordered dense structure. The phase of the layer was obtained by Raman spectroscopy. This technique was demonstrated to be very sensitive to the different structure of the Mn_xO_y compound.[29] **Figure 3.14b** shows that single phase Mn_3O_4 thin films were obtained on different substrates (YSZ/Si and Sapphire).[29]

The LSM plume deposited on Si was analysed by EDS in order to study the composition as a function of the plume centre distance. A constant value of Mn/(La+Sr) = 0.85 ± 0.04 was measured independently on the wafer position.

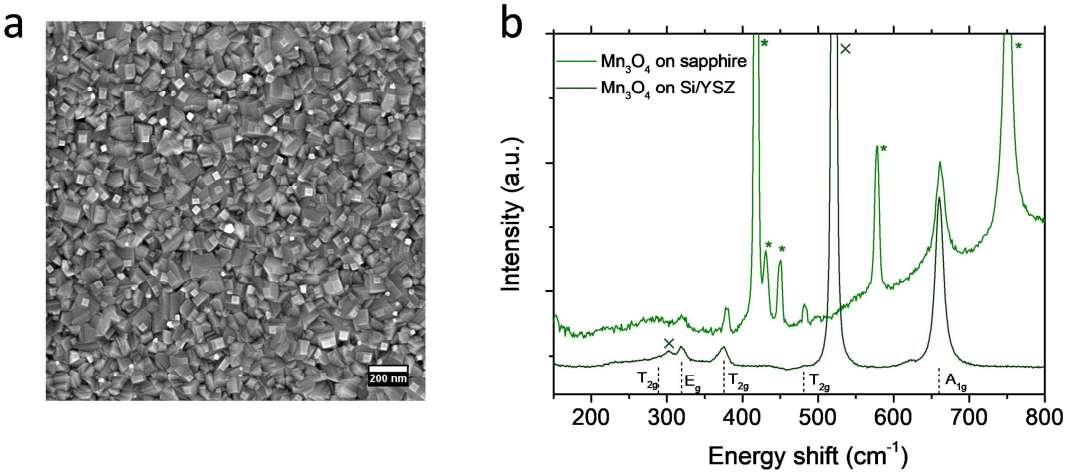

Figure 3.14 a, SEM top view of the Mn_3O_4 parent compound deposited on YSZ/Si. **b**, Raman spectra of the Mn_3O_4 deposited on sapphire (light green) and YSZ/Si (dark green). Both samples present the characteristic bands of the Mn_3O_4 phase.[29] In the graph, green asterisks and crosses show the sapphire and Si peaks respectively.

After the parent compounds individual characterization, a combinatorial LSM_y sample was produced on a 4" YSZ/Si wafer to determine the compositional variation along the plumes' intersection axis. A thickness of 1 nm and 0.25 nm per cycle for LSM and

Mn_3O_4, respectively, were selected to ensure a proper cation interdiffusion between the two layers.[30,31] **Figure 3.15a** shows the thickness profile measured by ellipsometry along the plumes centres for the combinatorial LSM_y. The experimental points were fitted by a superimposition of the two parent compound plumes previously characterized (**Figure 3.13**), leaving as free parameters only the plume maximum thickness and the position of centres. The fitting is in good agreement with the experimental data.

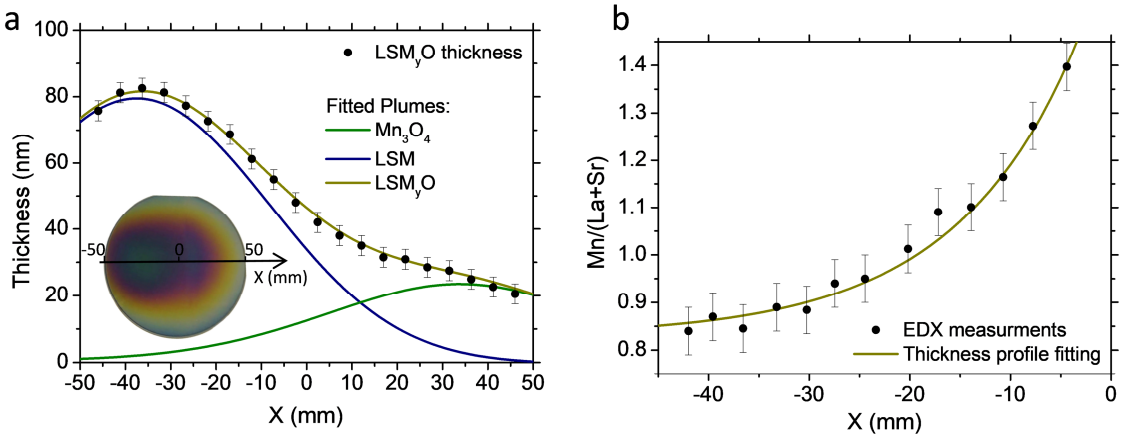

Figure 3.15 a, Thickness of the LSM_y combinatorial sample measured by ellipsometry and fitted by the superimposition of the parent compounds plumes. **b**. B/A ratio measured by EDS and calculated by equation 3.2 using the plumes thickness obtained in **a**.

Once the thickness profiles and the exact position of the parent compounds plumes are known, the compositional variation of the atomic ratio Mn/(La+Sr) between the maxima can be calculated as:

$$\frac{Mn}{La+Sr} = \frac{\text{moles } Mn_{LSM} + \text{moles } Mn_{Mn_3O_4}}{\text{moles } La_{LSM} + \text{moles } Sr_{LSM}} \qquad \textit{Eq. 3.1}$$

Transforming the equation:

$$\frac{Mn}{La+Sr} = \frac{0.85 \cdot \rho_{LSM} \cdot t_{LSM} / M(LSM) + 3 \cdot \rho_{Mn_3O_4} \cdot t_{Mn_3O_4} / M(Mn_3O_4)}{(0.8+0.2) \cdot \rho_{LSM} \cdot t_{LSM} / M(LSM)} \qquad \textit{Eq. 3.2}$$

Where ρ is the density, M the molar mass, t the thickness. In other words, the compositional variation can be described as a function of the single plume thicknesses, considering a constant B/A ratio equal to 0.85 and that the phase of the manganese oxide film deposited is Mn_3O_4 (3 atoms of Mn for each molecule of Mn_3O_4). The result is shown in **Figure 3.15b**, along with the B/A ratio measured by EDS. The plume fitting procedure yielded to a similar profile than the experimental one. The plume B/A ratio smoothly varies from 0.85 to 1.2 in almost 4.5 cm. This procedure also offered the opportunity of quantifying the compositional error in the different characterization techniques. Indeed, knowing the position and dimensions of the portion of combinatorial sample studied, one can calculate the uncertainty in the composition with

equation 3.2 (error bars in **Figure 3.15b**). This method will be used for the B/A error propagation in the experimental techniques used in this chapter as well as the electrical and electrochemical experiments (Chapter **4** and **5**, respectively).

Similarly to the Mn-deficient films detailed in section **3.2**, different substrates were used for the deposition of the combinatorial LSM_y films, aiming to avoid unwanted effects on the electrical and electrochemical experiments detailed in next chapters. This includes: (i.) Si (100) 4-inch wafer passivated with 100 nm YSZ; (ii.) 5 mm x 10 mm Sapphire (0001) single crystal substrates; (iii.) 5mm x 10mm NGO $(110)_o$ substrates (for electrical characterization of both polycrystalline and epitaxial films, respectively, in chapter **4**) and (iv.) 3x3 mm YSZ (001) single crystal substrates (for out of plane electrochemical experiments, in chapter **5**). When using pre-cut smaller substrates (i.e. sapphire, NGO and YSZ), these were attached with Silver paste to a 4-inch Si wafer forming a line between the two plume centres, allowing a gradual increase of B/A=Mn/(La+Sr) ratio.

3.3.2 Characterization of LSM_y thin films

This section presents the quality analysis of the deposited LSM_y layers, necessary for assessing their suitability for the study of the thin film functional properties (presented in chapters **4** and **5**). First, the phase and the microstructure of the thin films was investigated in order to prove the correct interdiffusion of the two parent compounds during the C-PLD deposition. Also, since large Mn deficiencies are achieved in this work, the Mn valence and electronic structure of the bulk were determined.

3.3.2.1 Structural analysis

A microstructural study of the LSM_y thin films was performed in order to check the microstructure and phase evolution. The surface of the LSM_y samples were first studied by scanning electron microscopy (SEM). **Figure 3.16a**, **b** and **c** show the top-view of the LSM_y thin films deposited on YSZ/Si for different B/A ratio equal to 0.92, 0.97 and 1.05, respectively. No substantial evolution of the grain size is observed, meaning that the fraction of the GB area remains nearly constant. This point is required especially for the electrochemical analysis (chapter **4**), because a modification of the grain size can give rise to changes in the overall oxygen mass transport properties[32]. TEM cross sections of the combinatorial LSM_y (**Figure 3.16d-f**) show that a dense polycrystalline columnar structure was obtained for all the compositions analysed.

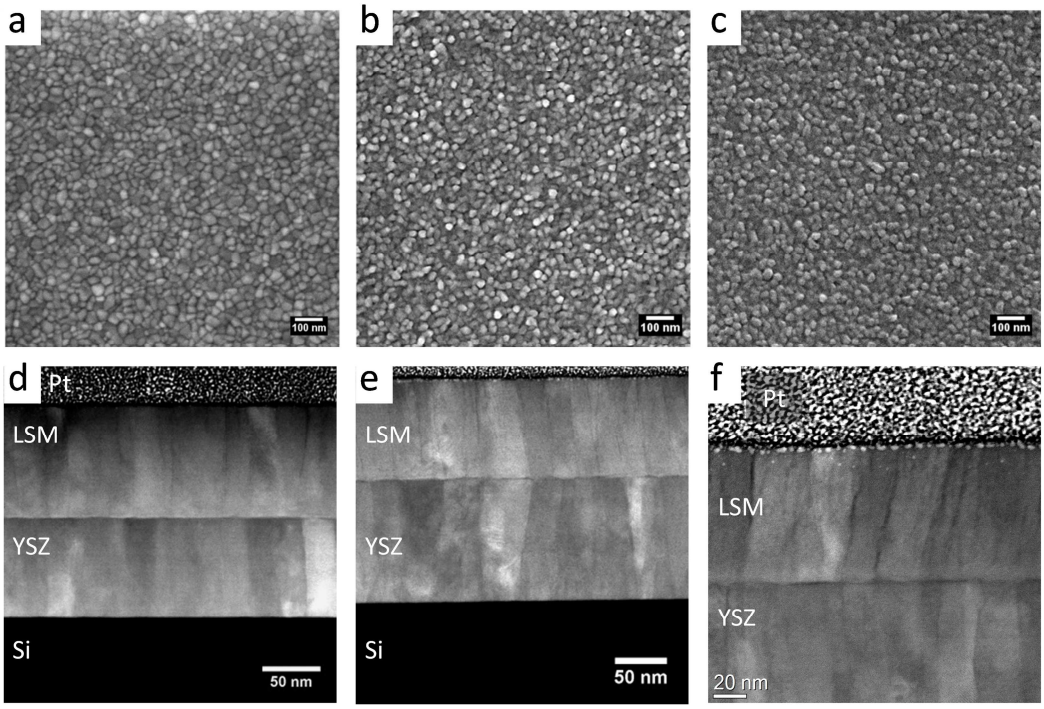

Figure 3.16 SEM top view of LSM_y samples deposited on YSZ/Si for B/A = 0.92 (**a**), B/A = 0.97 (**b**) and B/A = 1.05 (**c**). No significant microstructural evolution is observed. Cross section TEM images of LSM_y samples for B/A = 0.94 (**d**), B/A = 0.98 (**e**), B/A = 1.05 (**f**). The polycrystalline LSM_y/YSZ bilayers on top of the Si wafers are visible in all the cross sections.

The θ-2θ XRD patterns of the LSM_y samples deposited on YSZ/Si (**Figure 3.17a**), on Sapphire (**Figure 3.17b**) and on YSZ (100) single crystals (**Figure 3.17c**) revealed a single-phase deposition independent of the Mn content up to B/A = 1.2 ± 0.04 on all the substrates.

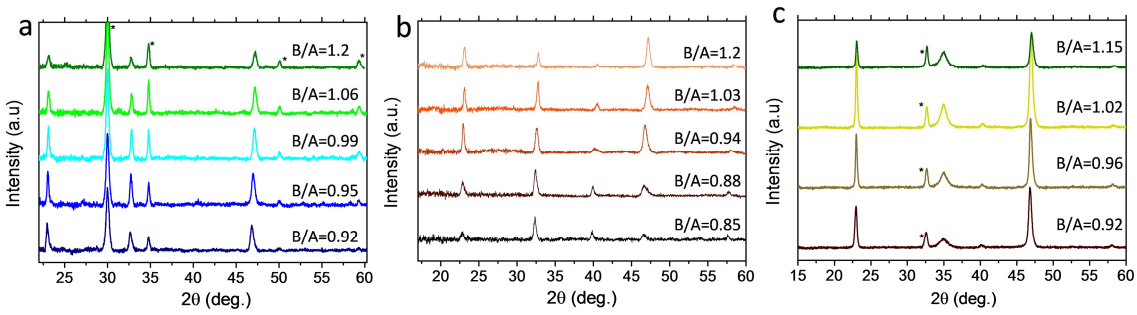

Figure 3.17 XRD of LSM_y samples deposited on YSZ/Si (**a**) and on Sapphire (**b**) for different B/A ratio. Black asterisks marks the diffraction peaks of the YSZ thin films (**a**) and of the YSZ single crystals (**c**).

Again, a complementary set of epitaxial thin films with variable Mn content were deposited on NGO $(110)_o$, in order to properly compare the grain and grain boundary properties of the films. **Figure 3.18a** shows the XRD obtained for three different films with composition spanning from Mn deficient (B/A = 0.88± 0.02) to Mn rich (B/A = 1.10 ± 0.03). The films show no secondary phases and a preferential orientation growth

$(001)_{pc}$, similarly to what was obtained for the $LSM_{0.85}$ thin films (**section 3.2.1**). The thickness of the films, measured by ellipsometry, is between 70 and 100 nm. The AFM images of the films (**Figure 3.18b-d**) show an atomic smooth surface with similar roughness (rms < 0.4 nm).

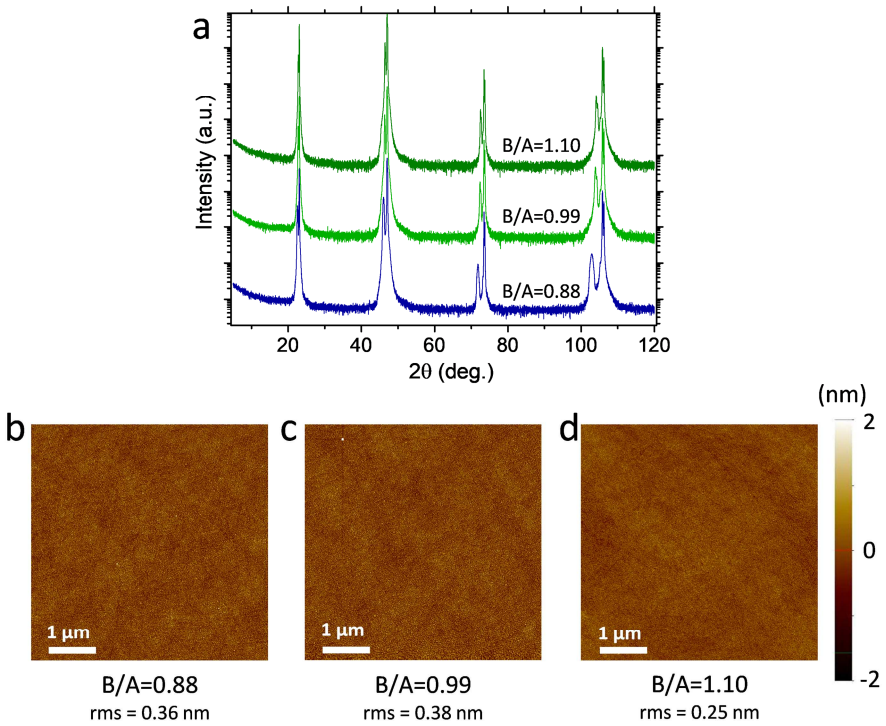

Figure 3.18 a, XRD of epitaxial LSM_y films deposited on NGO with different B/A ratios and respective AFM images of the surfaces (**b-d**).

Figure 3.19a shows the XRD pattern around the 200 peak for the LSM_y epitaxial films. A clear shift to higher angle takes place increasing the Mn content, corresponding to a decrease of out of plane lattice parameter (c_{pc}). **Figure 3.19b** displays the evolution of c_{pc} as a function of B/A ratio, calculated for the epitaxial and polycrystalline samples. A significant linear expansion of the unit cell is observed in the Mn deficient part, while a minor shrinkage is detected increasing the Mn content above B/A = 1. This behavior is similar to the one found in other perovskites.[33–35] The LSM_y films deposited on Sapphire and YSZ/Si show comparable c_{pc}, implying that the substrate is not affecting the stress state in the polycrystalline layers. Moreover, polycrystalline and epitaxial films present the same trend upon Mn substitution but the lattice parameter of the latter is constantly shifted to higher values. This difference in the absolute value of c_{pc} between the polycrystalline and epitaxial thin films could be due to the compressive in plane stress imposed by the NGO substrate (-0.70% and -0.47% on a_{pc} and b_{pc} respectively), which causes a slight expansion of the out of plane lattice parameter. The origin of the change of unit cell volume will be discussed in **section 3.4.1**. All in all, the C-PLD revealed to be a successful approach to obtain fully dense and single phase LSM_y thin films suitable for the analysis of the evolution of GBs properties.

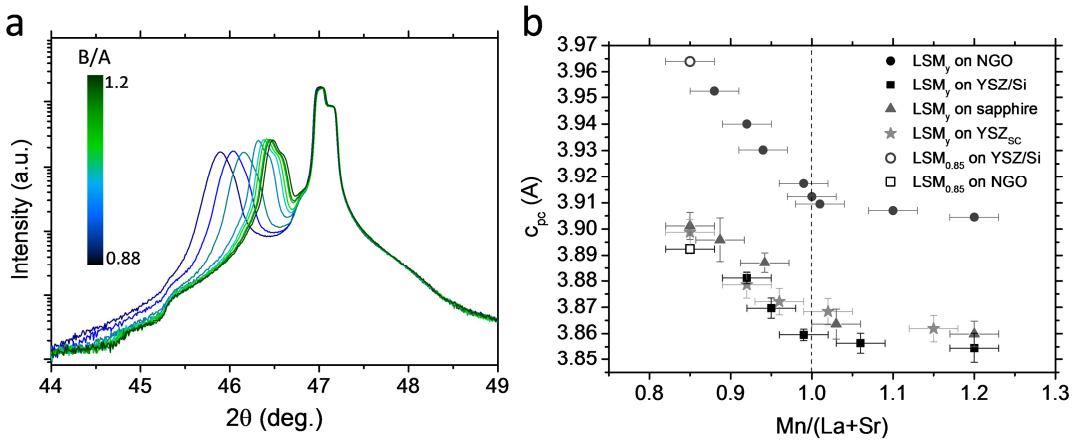

Figure 3.19 a, XRD around the 200 peak showing the evolution for increasing B/A ratio in epitaxial LSM_y films. **b**, Out of plane lattice parameter obtained for the epitaxial and polycrystalline samples as a function of the B/A ratio. c_{pc} of the $LSM_{0.85}$ samples on NGO (empty dot) and on YSZ/Si (empty square) are taken from the XRD analysis presented in Section **3.2**.

In the next, this chapter and Chapter **3** and **4**, the LSM_y thin films will be only analysed for the range of compositions between B/A = 0.85 - 1.1. This is mainly due to two reasons: (i) B/A = 1.1 is the limit of solubility of La vacancies in the perovskite phase as measured for LMO;[14,15] (ii) for B/A > 1.1 the slope of the compositional variation rapidly increases as a function of wafer position (see **Figure 3.15b**). This makes the analysis of a single cationic composition challenging and brings associated an increasing error of the B/A ratio estimation in the different experimental techniques.

3.3.2.2 Optical and XANES characterization

X-ray Absorption Near-Edge Structure (XANES) and ellipsometry were carried out on the LSM_y film series in order to investigate the effect of varying the B/A ratio on the Mn electronic structure. In order to equilibrate the oxygen stoichiometry of the samples, the thin films were annealed for 6 hours in air at 923 K prior to these experiments. As mentioned before, these two techniques are not able to separate grain and grain boundary contributions, therefore the results described in the next can be mainly ascribed to the bulk LSM_y, since it represents approximately the 90 vol.% of the polycrystalline films. **Figure 3.20a** shows the Mn K-edge XANES spectra of the polycrystalline LSM_y thin films deposited on sapphire for different B/A ratios. Here we focus on the absorption edge region, particularly on the white line positioned at *ca.* 6554 eV. Its position for each spectrum was extracted by calculating the inflection point energy, given by the maximum of the first derivative (see Chapter **2** for detailed information). As commented in **chapter 3.2.1**, this feature was demonstrated to increase its energy almost linearly with the Mn valence in LSM (approx. 1 eV per 0.27 valence change).[18,19] In the LSM_y samples, no significant changes were measured in the Mn deficient films and only a minor increase of ~ 0.1 eV (corresponding to a relative increase of just 3% in $[Mn^{4+}]$[18,19,36]) was observed in the La-rich compositions (**Figure**

3.20b). Therefore, the change of Mn concentration did not cause substantial variation of Mn valence in the grain bulk of the thin films.

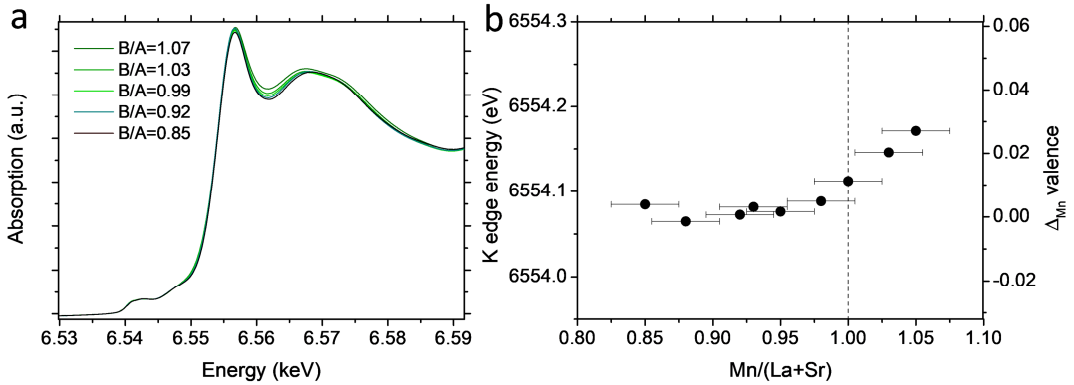

Figure 3.20 a, normalized XANES spectra at the Mn K-edge for various B/A ratios. **b**, variation of the calculated inflection points energy with the cationic composition in LSM_y films. The corresponding relative change of Mn valence is also shown in the right axis.[18,19]

The electronic bulk properties of LSM_y thin films were then investigated by ellipsometry. As discussed in detail Chapter **2,** the raw data were fitted by five Lorentzian oscillators in order to extract the optical constants of the materials.[37–39] The spectra were acquired at 473 K in order to ensure that all the samples are in the same paramagnetic state and ruling out the large low energy optical modifications originated near the metal-insulator transition, where a Drude-like optical absorption takes place.[40] This point is particularly important for allowing a proper comparison among the thin films, since, as will be shown in further detail in chapter **4**, the bulk metal-insulator transition temperature varies with the Mn content. **Figure 21a** shows the evolution of the optical conductivity (σ(ω)) with the Mn content in the films (B/A = 0.85 – 1.03) at 473 K. A significant growth in the σ(ω) intensity takes place in the low energy transitions (0 – 3 eV) for B/A ratio up to the unity, while just small variations are measured in the high energy part (3 – 5 eV). Moreover, the peak maximum in the low energy region tends to shift towards lower energies as the Mn content in the film increases. Although a comprehensive theory of optical transitions in manganites is still missing, it is commonly accepted that in the paramagnetic state the low energy components originate from intra-band Mn 3d transitions.[38–43] In order to emphasize the variation of the low energy transitions, the high energy contributions have been subtracted to the optical conductivity spectra (**Figure 21b**). Here, it becomes clear that two different features can be distinguished in this low energy region, with oscillator maxima at *ca.* 0.9 eV (oscillator 1) and *ca.* 1.5 eV (oscillator 2), respectively. In agreement with literature, we assigned the latter to an intra-atomic transition $Mn^{3+}(e_g^1) \rightarrow Mn^{3+}(e_g^2)$ gap, allowed by Jahn–Teller (J-T) distortions and the strong hybridization between O 2p and Mn 3d states.[38–40] Oscillator 1 has been instead assigned to an inter-atomic polaron hopping between different Mn sites: $Mn^{3+}(e_g^1) \rightarrow Mn^{4+}(e_g)$.[38,41,44] Indeed, in this insulating state of LSM, the electron transport is generally interpreted as small polaron hopping conduction, with the charge carriers

localized by strong electron-phonon coupling, such as J-T distortions.[45–49] These two transitions are schematically represented in **Figure 21d**.

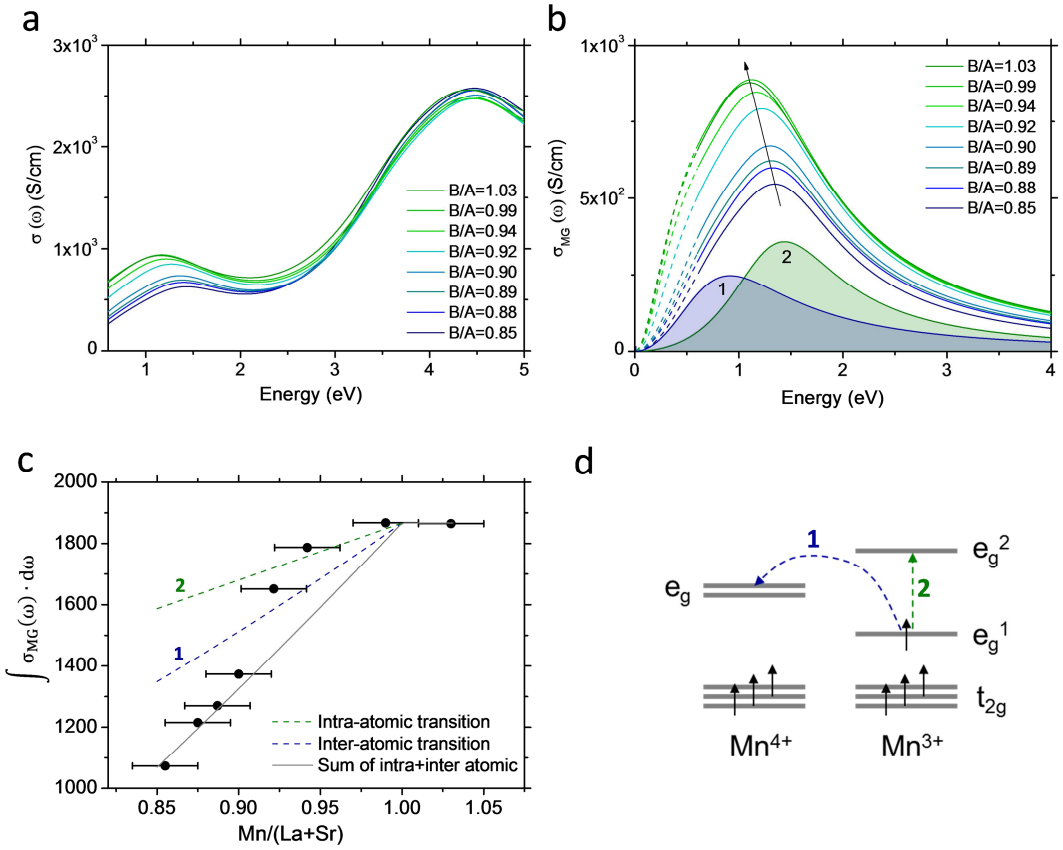

Figure 21 a, Evolution of the optical conductivity as a function of the photon energy for different Mn content (B/A = 0.85 – 1.03) at 473 K. **b**, Low energy optical conductivity contributions extracted from **a.** The deconvolution of the two transitions 1 and 2 is reported for the B/A = 0.85 film. **c**, spectral weight of the low energy contributions presented in **b**. as a function of the B/A ratio. The lines show the theoretical slope that the transition 1 and 2 should experience varying the Mn content. **d**, sketch of the inter-atomic polaron and the intra-atomic J-T transitions.

Since no change in Mn oxidation state was detected for B/A < 1, the modifications of the optical properties in the low energy region within the film series may be interpreted as a total variation of the optical active centres, i.e. the nominal variation of Mn content in the films. In order to confirm this hypothesis, we calculated the spectral weight (SW) of the two low energy components (**Figure 21b**), as: $SW_{MG} = \int \sigma_{MG}(\omega) \cdot d\omega$. In **Figure 21c**, the variation of SW_{MG} with the B/A ratio for the different LSM_y films have been represented. In this figure, we also report the theoretical variation of spectral weight expected for each single transition (sketched in **Figure 21d**), *viz.* the intra-atomic transition 2 ($SW_2 \propto [Mn_{Mn}^{x}] \propto [Mn]$) and the inter-atomic transition 1 ($SW_1 \propto [Mn_{Mn}^{\bullet}] \cdot [Mn_{Mn}^{x}] \propto [Mn] \cdot [Mn] = [Mn]^2$), as well as the sum of the two contributions.[38,41] As can be observed, the measured SW_{MG} agrees well with the predicted trend (sum of both contributions) for low Mn content (B/A < 0.9), while it appears to approach the J-T intra-atomic transition curve as B/A approaches unity. Such deviation can be attributed to the fact that for high Mn contents, the first transition

moves at the edge of our detection limits (0.6 eV), as can be seen in **Figure 21b**, which could produce errors in the fit of this component. In chapter **4**, the applicability of the small polaron theory to the electronic transport is further analysed, confirming this hypothesis. All things considered, these results show that the optical conductivity can be fully described considering only the variation of the total Mn concentration, confirming the constant $[Mn^{4+}]$ observed by XANES.

3.3.3 Grain boundary composition in LSM_y thin films

Analogously to the study of Mn-deficient LSM films, HAADF and EELS analysis of the LSM_y layers were carried out by TEM. Here, a clear impact of the change in the bulk stoichiometry on the local cation composition at the grain boundary level was observed, **Figure 3.22**. The analysis reflects that the GBs suddenly pass from a Mn-deficient (La-rich) state to a Mn-rich (La-deficient) one with the overall Mn content, presumably changing the defect chemistry and giving rise to two different types of GBs, with opposite cation depletion. The first interface is hereby named GB_{def}, while the second one GB_{rich}.

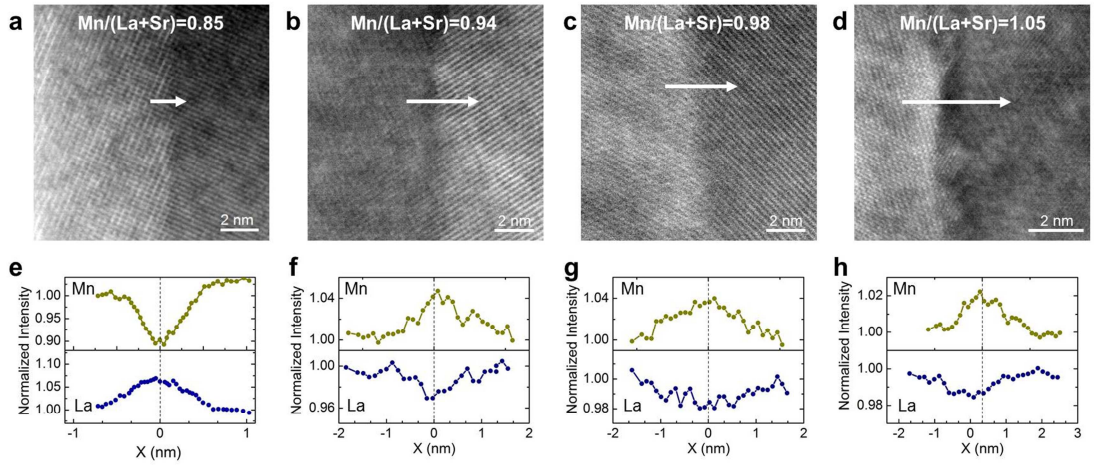

Figure 3.22 a-d Annular dark field images of grain boundaries in samples with different B/A ratio and **e-h** corresponding La and Mn variation extracted from EELS scans. A sudden decrease of La and a progressive increase of Mn are obtained in the GBs changing the overall Mn content in the thin films.

Figure 3.23a and **b** quantitatively compare the cationic composition[‡] in the different GBs analysed. The compositional variations were obtained normalizing the EELS scans to the nominal concentration in the grain bulk. The figure shows that the Mn-deficient GB (B/A = 0.85) presents the highest cationic change, while in the Mn rich GBs the

[‡]It is important to stress that the quantitative analysis of GB composition in polycrystalline thin films can be susceptible to a non-negligible error. This is because slight differences in the GB angles with respect to the TEM incident beam can partially mask the compositional changes. The tilt of the GB angle can therefore explain differences in the ionic composition when comparing different GBs from a sample with similar overall cation content, such as the interfaces for B/A = 0.85 analysed here and the ones of **Figure 3.9**.

absolute change tends to decrease while increasing the B/A ratio. The qualitative trends presented in this work were fully consistent in the entire set of GBs analyzed for each composition.

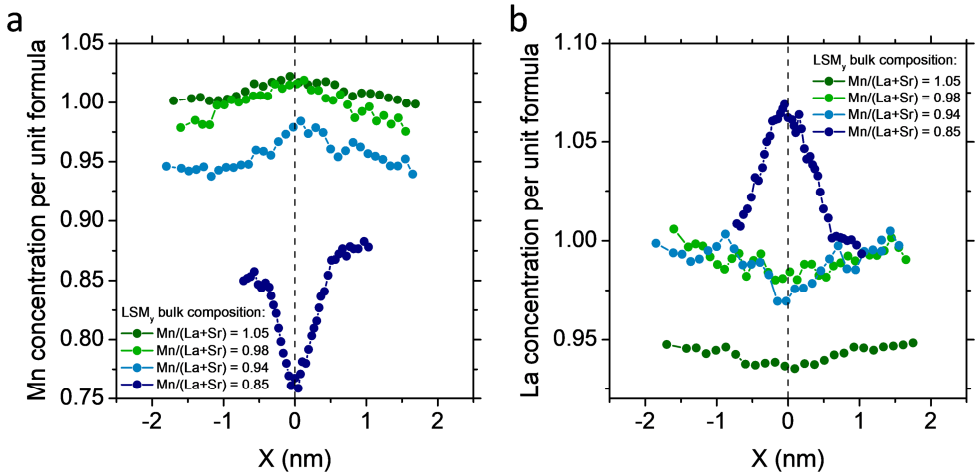

Figure 3.23 Quantitative compositional variation of Mn (**a**) and La (**b**) obtained by EELS in the GBs of LSM$_y$ samples deposited on YSZ/Si for B/A=0.85, B/A=0.94, B/A=0.98 and B/A=1.05.

Figure 3.24 shows the variation of oxygen content obtained by EELS scan across three GBs with different Mn content. Notably oxygen deficiency was found in all the GBs, independently on the Mn content, meaning that in LSM polycrystalline films the GBs are always far more reducible than the bulk.

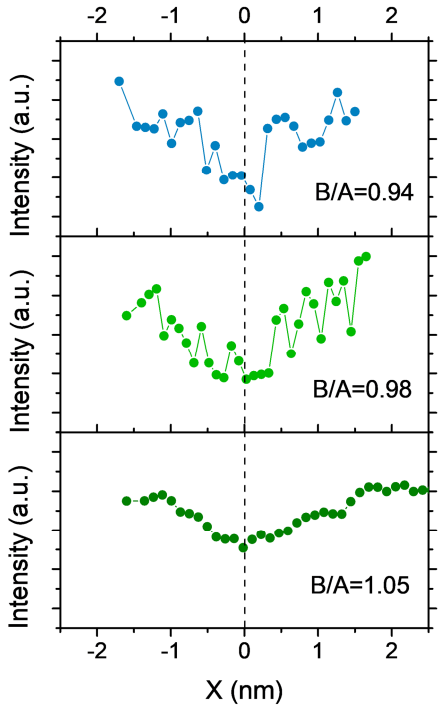

Figure 3.24 Compositional variation of O obtained by EELS in three GBs of LSMy samples deposited on YSZ/Si for B/A=0.94, B/A=0.98 and B/A=1.05. The GBs analysed are the very same of **Figure 3.22**.

3.4 Discussion

3.4.1 Bulk compensation mechanism

The discussion on the bulk defect chemistry for different cationic ratios is particularly important since large Mn deficiencies are explored in this study. In this sense, a change in the B/A ratio is expected to create negative cation vacancies in LSM ($V_{Mn}^{'''}$or $V_{La}^{'''}$) that need to be compensated by positive defects ($V_O^{\cdot\cdot}$ and/or $Mn_{Mn}^{\bullet}$). Nevertheless, according to the XANES and ellipsometry results, the bulk electro-neutrality in the Mn-deficient LSM_y films cannot be attributed to a change in the Mn valence state. The most probable compensation mechanism would therefore be the formation of positive defects, such as oxygen vacancies, usually present in a very low concentration in stoichiometric LSM.[49,50] However, the total charge compensation by oxygen vacancies (with equilibrium $[V_O^{\cdot\cdot}] = 3/2 \cdot [V_{Mn}^{'''}]$) would result in a great oxygen deficiency and a much higher increase of bulk oxygen diffusion than the one observed in previous works[5,7] (see also chapter **4**).

Alternatively, we propose a different mechanism in which the cation vacancies are mainly compensated by the formation of neutral anti-site defects (La_{Mn}^{x}). Although this mechanism is not commonly observed in bulk perovskites, similar anti-site defects have been recently reported by Qiao *et al.* in Cr deficient epitaxial $LaCrO_3$ films.[33] In the frame of this work, Density Functional Theory (DFT) simulations were carried out for LSM in order to validate this hypothesis (collaboration with Prof. Chroneos and coworkers).[51] The results showed that the formation energy of La_{Mn}^{x} strongly decreases in the presence of oxygen vacancies, i.e. the formation of the anti-site defects is favourable under the reducing PLD growing conditions. This compensation mechanism is also in good agreement with the increase of the out-of-plane lattice parameter measured in our films (see **Figure 3.19**), since, being the La ionic radius bigger than the Mn one, La_{Mn}^{x} are expected to produce a significant lattice expansion.[33,52]

Additionally, La_{Mn}^{x} anti-sites defect can partially reduce the total negative charge created by the cationic defect, even if they do not hold a formal positive charge. This consideration is based after the model of Nakamura *et al.*, first proposed for La-deficient $LaMnO_3$ for justifying the changes in Mn^{4+} concentration independent to the nominal concentration of $V_{La}^{'''}$.[53] Here, their model is adapted for the Mn-deficient LSM, considering that only the La atoms form anti-site defects. Naming the concentration of Mn vacancies per unit formula as Δ, the creation of anti-site La_{Mn}^{x} defects means that Δ_2 La atoms enter into the B site, leaving Δ_2 vacancies in the A site. The creation of Δ_2 anti-sites give rise to $\Delta_1 = \Delta - \Delta_2$ vacancies in the B site. Therefore, we can reformulate the unit formula as:

$$La_{0.8}Sr_{0.2}Mn_{1-\Delta}O_{3+\delta} = \{La_{0.8-\Delta_2}Sr_{0.2}V_{\Delta_2}\}\{Mn_{1-\Delta}La_{\Delta_2}V_{\Delta_1}\}O_{3+\delta} \qquad \textit{Eq. 3.3}$$

In this way, a certain concentration of cation vacancies is formed on both the A (V_{Δ_2}) and B (V_{Δ_1}) sites. As previously discussed in the Chapter **1**, the meaning of over-stoichiometry ($+\delta$) in LSM does not imply the presence of interstitial oxygens but rather of the existence of cationic vacancies on both the A and B sites according to the Schottky equilibrium.[50] This means that we can reformulate the unit formula as:

$$\{La_{0.8-\Delta_2}Sr_{0.2}V_{\Delta_2}\}\{Mn_{1-\Delta}La_{\Delta_2}V_{\Delta_1}\}O_{3+\delta} =$$

$$(1-\Delta_2)\left\{La_{\frac{0.8-\Delta_2}{1-\Delta_2}}Sr_{\frac{0.2}{1-\Delta_2}}\right\}\left\{Mn_{\frac{1-\Delta}{1-\Delta_2}}La_{\frac{\Delta_2}{1-\Delta_2}}V_{\frac{\Delta_1-\Delta_2}{1-\Delta_2}}\right\}O_{3+\frac{\delta+3\Delta_2}{1-\Delta_2}} \approx$$

$$(1-\Delta_2)\{La_{0.8}Sr_{0.2}\}\left\{Mn_{\frac{1-\Delta}{1-\Delta_2}}La_{\frac{\Delta_2}{1-\Delta_2}}V_{\frac{\Delta_1-\Delta_2}{1-\Delta_2}}\right\}O_{3+\frac{\delta+3\Delta_2}{1-\Delta_2}} \qquad \textit{Eq. 3.4}$$

Therefore, the excess of oxygen is now $\delta' = (\delta + 3\Delta_2)/(1-\Delta_2)$. In the oxygen plateau (i.e. the thermodynamic state with $\delta' = 0$ and no Schottky-generated further cationic vacancies), the concentration of Mn vacancies is therefore:

$$[V''''_{Mn}] = \frac{\Delta_1-\Delta_2}{1-\Delta_2} + \frac{\delta'}{3} = \frac{\Delta_1-\Delta_2}{1-\Delta_2} = \frac{\Delta-2\Delta_2}{1-\Delta_2} \approx \Delta - 2\Delta_2 \qquad \textit{Eq. 3.5}$$

As an example, in a sample with B/A composition = 0.9, considering Δ_2 (La^x_{Mn}) equal to 0.04, the nominal Mn vacancy concentration per unit formula is not 0.10 but almost 0.02, implying that a significantly lower amount of negative charge needs to be compensated by positive defects (i.e. oxygen vacancies).

All in all, it appears that Mn-deficient LSM thin films (B/A < 1) present a bulk defect chemistry dominated by the formation of random La^x_{Mn} anti-site defects, which radically decreases the need of positive defects to reach charge neutrality. Since no change of Mn valence were detected varying the Mn content, the presence of a small amount of V''_O is foreseen as the most probable charge compensation mechanism. As a counterpart, for moderately Mn rich samples (B/A > 1), the presence of La vacancies (V'''_{La}) may be mainly compensated by the formation of the likely occurring Mn^x_{La} anti-site defects accompanied by a small increase of Mn^{4+} (see **Figure 3.20**).

3.4.2 Grain boundary compensation mechanisms

Two main conclusions arise from the investigation of compositional variation in the LSM_y grain boundaries: (i) constant increase of oxygen vacancies concentration (compared to the bulk) and (ii) different cationic reorganization depending on the bulk B/A ratio. The first observation goes in line with the oxygen deficiency found in many other oxides at the grain boundary core, and is thought to be the main mechanism of lattice relaxation at interfaces.[54–57] Indeed, lattice strain and atomic disorder have been proved to provide a mean of vacancy formation energy modification in different materials,[3,21] including LSM.[58,59] Therefore, it seems reasonable to think that the grain

boundary core in LSM is more reduced than the bulk, giving rise to a positive charge in the interface.[1] It is well known that the typical mechanism of charge compensation in grain boundaries is the creation of a space charge region, in which mobile species (electrons/holes and oxygen vacancies) vary their concentration in the GB surroundings (up to several nm, as shown in Chapter **1**).[1,60] In the particular case of LSM, due to the high concentration of charge carriers (Mn^{4+}, mainly originated by the A-site divalent substitution), one would expect a limited extension of the space charge region and a core charge easily screened by the change of Mn oxidation state[60,61]. However, we did not observe any change of oxidation state (**Figure 3.11**) but instead a large cation rearrangement. Although an enrichment of divalent dopant (i.e. Sr'_{La}) in the GB core has been reported before,[4,62] the redistribution of other cationic species is far less common. Specifically, for low bulk Mn chemical potential (highly Mn deficient thin films) the GBs (GB_{def}) are characterized by an additional depletion of Mn, while La and Sr increase. When the overall Mn chemical potential rises (rising bulk Mn content), the interfaces completely change the cationic distribution, turning to La deficient regions with progressive increase of Mn (GB_{rich}) (**Figure 3.22**).

In GB_{def}, it appears that oxygen and cations vacancies are linked by the formation of associated defects. In a recent work, Lee *et al.* found by DFT calculations that cation vacancies, both V'''_{La} and V'''_{Mn}, are attracted to oxygen vacancies forming associated defects that should be considered together in the calculation of the defect chemistry equilibrium.[31] In the GBs, where a great amount of oxygen vacancies is found, these would attract the negative defects from the bulk, forming associated defects of the type $V_O^{\cdot\cdot} - V'''_{Mn}$. Through this mechanism, cation vacancies can provide a way to partially compensate the positive charge of the GBs introduced by the generalized oxygen deficiency (GB_{def} in **Figure 3.25**).

Nevertheless, a mechanism just based on electroneutrality still does not explain the observed increase of Lanthanum in the GB_{def}. Its rise, and the availability of V'''_{Mn}, suggests a second mechanism based on the formation of antisite defects, $La^{\times}_{Mn}$, similar to that described for the bulk Mn-deficient LSM. As mentioned earlier, recent Density Functional Theory (DFT) simulations carried out for LSM[51] showed that the formation energy of $La^{\times}_{Mn}$ defects is lowered in the presence of oxygen vacancies $V_O^{\cdot\cdot}$ and, moreover, in the vicinity of the smaller Sr cations (Sr'_{La}). Notably, no significant variation was observed in the simulations when applying strain in the presence of Sr doping atoms and/or oxygen vacancies. This suggest that strain is not the main driver for the formation of the oversized $La^{\times}_{Mn}$, although for the difference in cationic radius between Mn^{3+} (0.0645) and La (0.136 nm) this antisite defect could have provided a mean of relaxation of the tensile strain. Rather, it appears more probable that the presence of strain generates an increase of $V_O^{\cdot\cdot}$, which in turn diminishes the formation energy of $La^{\times}_{Mn}$, leading to the complex association of defects suggested.

Therefore, an analogous mechanism to that proposed for the Mn deficient bulk can explain the rise of La in GB_{def}, although here significantly enhanced due to the higher

concentration of $V_O^{\cdot\cdot}$. Also, the difference with the bulk is that, there, the defects are randomly distributed and due to the low concentration of oxygen vacancies, probably present in small amount. In the GB_{def} instead, the high presence of $V_O^{\cdot\cdot}$ can stabilize a higher concentration of anti-sites $La_{Mn}^{\times}$, clustered in the GB vicinity.

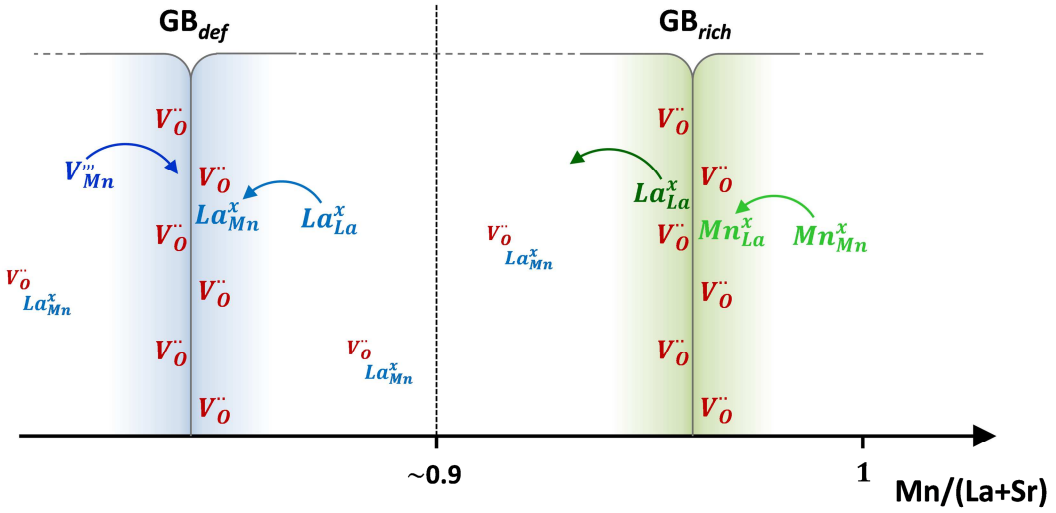

Figure 3.25. Sketch of the composition and mechanism proposed for the two GB's type found in LSM_y thin films.

Increasing the overall Mn concentration, the GBs composition change, giving rise to an accumulation of Mn and a decrease of La (GB_{rich}) but maintaining the oxygen deficiency character. The origin of this change is somehow more uncertain. One possible explanation could be that, analogously to GB_{def}, the positive GB oxygen vacancies are now compensated by lanthanum vacancies ($V_{La}^{'''}$) and the formation of antisite defects $Mn_{La}^{\times}$, naturally occurring in bulk stoichiometric LSM.[63] However, the switch of GB mechanism takes place in thin films that are still largely Mn deficient (B/A ~ 0.9), that is when the bulk should be still plenty of $V_{Mn}^{'''}$ ready to associate with the GB's $V_O^{\cdot\cdot}$, while just a small amount of $V_{La}^{'''}$ should be present. Another possibility to consider is that the increase of Mn observed in the GBs could be the result of the combinatorial procedure adopted in this work. In this sense, the Mn coming to the Mn_3O_4 plume could first migrate into the Mn-deficient GBs, forcing a different type of equilibrium and pushing out the La atoms (**Figure 3.25**). In any case, as will be further discussed in Chapter **4**, the electrical measurements presented there suggest that the Mn atoms are forming anti-site defects $Mn_{La}^{\times}$, occupying La sites and giving rise to a decrease of La concentration. More work is however needed in order to fully understand the bulk-GB electrochemomechanical interactions that lead to this complex behaviour.

All in all, it was demonstrated that, through the change of Mn chemical potential (overall Mn concentration in the thin films), it is possible to engineer the GB composition of polycrystalline LSM thin films. It is to be noted that, local cation non-stoichiometry in manganites was also observed in other type of structural defects and

interfaces, *e.g.* dislocations in epitaxial $La_{0.7}Sr_{0.3}MnO_3$ on $LaAlO_3$[64,65] or purely strained $La_{0.7}Sr_{0.3}MnO_3/SrTiO_3$ hetero-interfaces[66–68]. This suggests that the compensation mechanism observed in this work can be extrapolated to other strained and oxygen deficient interfaces. The natural presence of cationic vacancies in manganites, even in the nominally stoichiometric material,[69] is surely the main driver of this unusual elemental rearrangement. The GB engineering shown in this chapter could be therefore extended to other interfaces and, more interestingly, to other perovskites, opening the way for new strategies to control the transport properties of materials by tuning the local non-stoichiometry.

3.5 Conclusions

In this chapter, the GB and bulk composition and structure of LSM_y thin films were deeply analysed. First, Mn-deficient polycrystalline $LSM_{0.85}$ thin films have been deposited and structurally characterized. TEM-EELS analysis of the GBs revealed that a profound atomic reorganization takes place in these interfaces under the lattice distortions and strain created by dislocations. In detail, these GBs are characterized by a Mn and O depletion along with a La and Sr enrichment. The reduction of Mn and O content suggests a compensation mechanism based on the creation of associated defects of the type $V_O^{\cdot\cdot} - V_{Mn}^{'''}$. Instead, the increase of La concentration found, which cannot be explained by charge compensation, points at the formation of antisite $La_{Mn}^{\times}$ defects, as supported by theoretical calculations.

Afterwards, the influence of the overall bulk cationic content on the GB composition was studied. By combinatorial LA-PLD approach, a set of thin films with a continuous evolution of Mn concentration (B/A = 0.85 - 1.2) has been deposited. The structural analysis revealed that single phase polycrystalline and epitaxial LSM_y thin films were successfully grown on different substrates. The optical and XANES study of the grain bulk showed that the oxidation state of the Mn does not vary for B/A < 1, while, in the same compositional range, a continuous increase of lattice parameter was measured by XRD analysis. This behaviour suggests a bulk charge compensation mechanism based on the creation of antisite defects $La_{Mn}^{\times}$ along with the creation of positive $V_O^{\cdot\cdot}$ to equilibrate the negative cation vacancies. Furthermore, TEM-EELS analysis of the GBs showed that nearly at B/A =0.9 the cationic composition of the GB switches, passing from a Mn poor (La rich) to a Mn rich (La poor) environment, while maintaining its oxygen deficient character. This clearly shows that the GB composition can be altered by tuning the overall cationic concentration in the bulk, providing a way for engineering GBs and, as will be showed in Chapter **4** and **5**, the overall functional properties of LSM_y thin films.

References

1. Chiabrera, F., Garbayo, I. & Tarancón, A. in *Metal Oxide-Based Thin Film Structures* 409–439 (Elsevier, 2018). doi:10.1016/B978-0-12-811166-6.00017-0
2. Waldow, S. P. & De Souza, R. A. Computational Study of Oxygen Diffusion along a [100] Dislocations in the Perovskite Oxide $SrTiO_3$. *ACS Appl. Mater. Interfaces* **8,** 12246–12256 (2016).
3. Marrocchelli, D., Sun, L. & Yildiz, B. Dislocations in $SrTiO_3$: Easy to Reduce but Not so Fast for Oxygen Transport. *J. Am. Chem. Soc.* **137,** 4735–4748 (2015).
4. Sun, L., Marrocchelli, D. & Yildiz, B. Edge dislocation slows down oxide ion diffusion in doped CeO_2 by segregation of charged defects. *Nat. Commun.* **6,** 6294 (2015).
5. Saranya, A. M. *et al.* Engineering Mixed Ionic Electronic Conduction in $La_{0.8}Sr_{0.2}MnO_{3+\delta}$ Nanostructures through Fast Grain Boundary Oxygen Diffusivity. *Adv. Energy Mater.* **5,** 1500377 (2015).
6. Navickas, E. *et al.* Fast oxygen exchange and diffusion kinetics of grain boundaries in Sr-doped $LaMnO_3$ thin films. *Phys. Chem. Chem. Phys.* **17,** 7659–7669 (2015).
7. Saranya, A. M. *et al.* Unveiling the Outstanding Oxygen Mass Transport Properties of Mn-Rich Perovskites in Grain Boundary-Dominated $La_{0.8}Sr_{0.2}(Mn_{1-x}Co_x)_{0.85}O_{3\pm\delta}$ Nanostructures. *Chem. Mater.* **30,** 5621–5629 (2018).
8. Stankevic, V. *et al.* Uniaxial stress influence on electrical conductivity of thin epitaxial lanthanum-strontium manganite films. *Thin Solid Films* **540,** 194–201 (2013).
9. Boschker, H. *et al.* Strong uniaxial in-plane magnetic anisotropy of (001)- and (011)-oriented $La_{0.67}Sr_{0.33}MnO_3$ thin films on $NdGaO_3$ substrates. *Phys. Rev. B* **79,** 1–6 (2009).
10. Adamo, C. *et al.* Effect of biaxial strain on the electrical and magnetic properties of (001) $La_{0.7}Sr_{0.3}MnO_3$ thin films. *Appl. Phys. Lett.* **95,** 112504 (2009).
11. Wicklein, S. *et al.* Pulsed laser ablation of complex oxides: The role of congruent ablation and preferential scattering for the film stoichiometry. *Appl. Phys. Lett.* **101,** (2012).
12. Ojeda-G-P, A., Döbeli, M. & Lippert, T. Influence of Plume Properties on Thin Film Composition in Pulsed Laser Deposition. *Adv. Mater. Interfaces* **5,** 1–16 (2018).
13. Chen, J. *et al.* Plasma interactions determine the composition in pulsed laser deposited thin films. *Appl. Phys. Lett.* **105,** 114104 (2014).
14. Palcut, M., Wiik, K. & Grande, T. Cation self-diffusion and nonstoichiometry of lanthanum manganite studied by diffusion couple measurements. *J. Phys. Chem. C* **111,** 813–822 (2007).
15. van Roosmalen, J. A. M., van Vlaanderen, P., Cordfunke, E. H. P., Ijdo, W. L. & Ijdo, D. J. W. Phases in the perovskite-type $LaMnO_{3+\delta}$ Solid Solution and the La_2O_3-Mn_2O_3 Phase Diagram. *J. Solid State Chem.* **114,** 516–523 (1995).
16. De Vries, A. H., Hozoi, L. & Broer, R. Origin of the chemical shift in X-ray absorption near-edge spectroscopy at the Mn K-edge in manganese oxide compounds. *Int. J. Quantum Chem.* **91,** 57–61 (2002).
17. García, J., Subías, G., Cuartero, V. & Herrero-Martin, J. On the correlation between the X-ray absorption chemical shift and the formal valence state in mixed-valence manganites. *J. Synchrotron Radiat.* **17,** 386–392 (2010).
18. Subías, G., García, J., Proietti, M. & Blasco, J. X-ray-absorption near-edge spectroscopy

and circular magnetic x-ray dichroism at the Mn edge of magnetoresistive manganites. *Phys. Rev. B - Condens. Matter Mater. Phys.* **56,** 8183–8191 (1997).

19. Mastelaro, V. R., De Souza, D. P. F. & Mesquita, R. A. X-ray absorption spectroscopic studies of Mn atoms in $La_{0.67}Sr_{0.33}MnO_{3+\delta}$ compounds. *X-Ray Spectrom.* **31,** 154–157 (2002).

20. Hytch, M., Putaux, J.-L. & Penisson, J.-M. Measurement of the displacement field of dislocations to 0.03 A by electron microscopy. *Nature* **423,** 270–273 (2003).

21. Choi, S. Y. *et al.* Assessment of Strain-Generated Oxygen Vacancies Using $SrTiO_3$ Bicrystals. *Nano Lett.* **15,** 4129–4134 (2015).

22. Feng, B. *et al.* Atomic structures and oxygen dynamics of CeO_2 grain boundaries. *Sci. Rep.* **6,** 20288 (2016).

23. Varela, M. *et al.* Atomic-resolution imaging of oxidation states in manganites. *Phys. Rev. B - Condens. Matter Mater. Phys.* **79,** 1–14 (2009).

24. Christen, H. M. *et al.* A laser-deposition approach to compositional-spread discovery of materials on conventional sample sizes. *Meas. Sci. Technol.* **16,** 21–31 (2005).

25. Rossiny, J. C. H. *et al.* Combinatorial characterisation of mixed conducting perovskites. *Solid State Ionics* **179,** 1085–1089 (2008).

26. Greer, J. A. History and current status of commercial pulsed laser deposition equipment. *J. Phys. D. Appl. Phys.* **47,** 034005 (2014).

27. Christen, H. M. & Eres, G. Recent advances in pulsed-laser deposition of complex oxides. *J. Phys. Condens. Matter* **20,** 264005 (2008).

28. Infortuna, A., Harvey, A. S. S. & Gauckler, L. J. Microstructures of CGO and YSZ Thin Films by Pulsed Laser Deposition. *Adv. Funct. Mater.* **18,** 127–135 (2008).

29. Kim, M. *et al.* Pressure and field tuning the magnetostructural phases of Mn_3O_4: Raman scattering and x-ray diffraction studies. *Phys. Rev. B - Condens. Matter Mater. Phys.* **84,** 1–11 (2011).

30. Miyoshi, S. & Martin, M. B-Site cation diffusivity of Mn and Cr in perovskite-type $LaMnO_3$ with cation-deficit nonstoichiometry. *Phys. Chem. Chem. Phys.* **11,** 3063 (2009).

31. Lee, Y.-L. *et al.* Density-Functional-Theory Modeling of Cation Diffusion in Bulk $La_{1-x}Sr_xMnO_{3\pm\delta}$ (x=0.0-0.25) for solid-Oxide fuel-cell cathodes. *Phys. Rev. Appl.* **8,** 044001 (2017).

32. Usiskin, R. E., Maruyama, a S., Kucharczyk, b C. J., Takeuchib, a I. & Haile, S. M. Probing the reaction pathway in $(La_{0.8}Sr_{0.2})_{0.95}MnO_{3+\delta}$ using libraries of thin film microelectrodes. *J. Mater. Chem. A* **3,** 19330–19345 (2015).

33. Qiao, L. *et al.* The impacts of cation stoichiometry and substrate surface quality on nucleation, structure, defect formation, and intermixing in complex oxide heteroepitaxy-$LaCrO_3$ on $SrTiO_3$(001). *Adv. Funct. Mater.* **23,** 2953–2963 (2013).

34. Keeble, D. J. *et al.* Nonstoichiometry accommodation in $SrTiO_3$ thin films studied by positron annihilation and electron microscopy. *Phys. Rev. B* **87,** 195409 (2013).

35. Scafetta, M. D. & May, S. J. Effect of cation off-stoichiometry on optical absorption in epitaxial $LaFeO_3$ films. *Phys. Chem. Chem. Phys.* **19,** 10371–10376 (2017).

36. Maurin, I., Barboux, P., Lassailly, Y., Boilot, J. & Villain, F. Charge-carrier localization in the self-doped $La_{1-y}Mn_{1-y}O$ system. *J. Magn. Magn. Mater.* **211,** 139–144 (2000).

37. Scafetta, M. D., Xie, Y. J., Torres, M., Spanier, J. E. & May, S. J. Optical absorption in

epitaxial $La_{1-x}Sr_xFeO_3$ thin films. *Appl. Phys. Lett.* **102,** 081904 (2013).

38. Mildner, S., Hoffmann, J., Blöchl, P. E., Techert, S. & Jooss, C. Temperature- and doping-dependent optical absorption in the small-polaron system $Pr_{1-x}Ca_xMnO_3$. *Phys. Rev. B* **92,** 035145 (2015).

39. Nomerovannaya, L. V., Makhnev, A. A. & Rumyantsev, A. Y. Evolution of the optical properties of single-crystal $La_{1-x}Sr_xMnO_3$. *Phys. Solid State* **41,** 1322--1326 (1999).

40. Quijada, M. *et al.* Optical conductivity of manganites: Crossover from Jahn-Teller small polaron to coherent transport in the ferromagnetic state. *Phys. Rev. B* **58,** 16093–16102 (1998).

41. Jung, J., Kim, K., Noh, T., Choi, E. & Yu, J. Midgap states of $La_{1-x}Ca_xMnO_3$: Doping-dependent optical-conductivity studies. *Phys. Rev. B* **57,** 43–46 (1998).

42. Kovaleva, N. N. *et al.* Low-energy Mott-Hubbard excitations in $LaMnO_3$ probed by optical ellipsometry. *Phys. Rev. B - Condens. Matter Mater. Phys.* **81,** 1–13 (2010).

43. Jung, J. *et al.* Optical investigations of $La_{7/8}Sr_{1/8}MnO_3$. *Phys. Rev. B* **59,** 3793–3797 (1999).

44. Mostovshchikova, E. V. Optical evidence for lattice polarons in lightly doped lanthanum manganites in paramagnetic state. *Solid State Commun.* **150,** 1884–1887 (2010).

45. Varshney, D. & Dodiya, N. Electrical resistivity of the hole doped $La_{0.8}Sr_{0.2}MnO_3$ manganites: Role of electron-electron/phonon/ magnon interactions. *Mater. Chem. Phys.* **129,** 896–904 (2011).

46. Lanzara, A. *et al.* Crossover from Large to Small Polarons across the Metal-Insulator Transition in Manganites. *Phys. Rev. Lett.* **81,** 878–881 (1998).

47. Jaime, M. *et al.* Hall-Effect Sign Anomaly and Small-Polaron Conduction in $(La_{1-x}Gd_x)_{0.67}Ca_{0.33}MnO_3$. *Phys. Rev. Lett.* **38,** 951–954 (1997).

48. Ziese, M. & Srinitiwarawong, C. Polaronic effects on the resistivity of manganite thin films. *Phys. Rev. B* **58,** 11519–11525 (1998).

49. Pavone, M., Muñoz-García, A. B., Ritzmann, A. M. & Carter, E. A. First-principles study of lanthanum strontium manganite: Insights into electronic structure and oxygen vacancy formation. *J. Phys. Chem. C* **118,** 13346–13356 (2014).

50. Poulsen, F. Defect chemistry modelling of oxygen-stoichiometry, vacancy concentrations, and conductivity of $(La_{1-x}Sr_x)_yMnO_{3+\delta}$. *Solid State Ionics* **129,** 145–162 (2000).

51. Chiabrera, F. *et al.* Engineering Transport in Manganites by Tuning Local Non-Stoichiometry in Grain Boundaries. *Adv. Mater.* **31,** 1805360 (2019).

52. Fuchs, D. *et al.* Structural properties of slightly off-stoichiometric homoepitaxial $SrTixO_{3-\delta}$ thin films. *J. Appl. Phys.* **88,** 1844–1850 (2000).

53. Nakamura, K. The defect chemistry of $La_{1-d}MnO_{3+\delta}$. *J. Solid State Chem.* **173,** 299–308 (2003).

54. An, J. *et al.* Atomic scale verification of oxide-ion vacancy distribution near a single grain boundary in YSZ. *Sci. Rep.* **3,** 2680 (2013).

55. Hojo, H. *et al.* Atomic structure of a CeO_2 grain boundary: The role of oxygen vacancies. *Nano Lett.* **10,** 4668–4672 (2010).

56. Jia, C. L. & Urban, K. Atomic-Resolution Measurement of Oxygen Concentration in Oxide Materials. *Science (80-.).* **303,** 2001–2004 (2004).

57. Zhang, Z., Sigle, W. & Rühle, M. Atomic and electronic characterization of the a[100] dislocation core in $SrTiO_3$. *Phys. Rev. B* **66,** 094108 (2002).

58. Mayeshiba, T. & Morgan, D. Strain effects on oxygen vacancy formation energy in perovskites. *Solid State Ionics J.* **17,** 2715–2721 (2017).

59. Gan, L.-Y., Akande, S. O. & Schwingenschlögl, U. Anisotropic O vacancy formation and diffusion in $LaMnO_3$. *J. Mater. Chem. A* **2,** 19733–19737 (2014).

60. Gross, R. *et al.* On the nature of grain boundaries in the colossal magnetoresistance manganites. *J. Magn. Magn. Mater.* **211,** 150–159 (2000).

61. De Souza, R. A. The formation of equilibrium space-charge zone at grain boundaries in the perovskite oxide $SrTiO_3$. *Phys. Chem. Chem. Phys.* **11,** 9939–9969 (2009).

62. Lee, H. B., Prinz, F. B. & Cai, W. Atomistic simulations of grain boundary segregation in nanocrystalline yttria-stabilized zirconia and gadolinia-doped ceria solid oxide electrolytes. *Acta Mater.* **61,** 3872–3887 (2013).

63. Wolcyrz, M., Horyn, R., Bouree, F. & Bukowska, E. Structural defects in $LaMnO_3$ phase studied by neutron diffraction. *J. Alloys Compd.* **353,** 170–174 (2003).

64. Bagués, N. *et al.* The Misfit Dislocation Core Phase in Complex Oxide Heteroepitaxy. *Adv. Funct. Mater.* **28,** 1704437 (2018).

65. Song, K., Du, K. & Ye, H. Atomic structure and chemistry of a[100] dislocation cores in $La_{2/3}Sr_{1/3}MnO_3$ films. *Micron* **96,** 72–76 (2017).

66. Feng, Y. *et al.* Insulating phase at low temperature in ultrathin $La_{0.8}Sr_{0.2}MnO_3$ films. *Sci. Rep.* **6,** 22382 (2016).

67. Li, Z. *et al.* Interface and surface cation stoichiometry modified by oxygen vacancies in epitaxial manganite films. *Adv. Funct. Mater.* **22,** 4312–4321 (2012).

68. Estradé, S. *et al.* Effects of thickness on the cation segregation in epitaxial (001) and (110) $La_{2/3}Ca_{1/3}MnO_3$ thin films. *Appl. Phys. Lett.* **95,** 1–4 (2009).

69. Nowotny, J. & Rekas, M. Defect Chemistry of $(La,Sr)MnO_3$. *J. Am. Ceram. Soc.* **81,** 67–80 (1998).

4.The electrical properties of $La_{0.8}Sr_{0.2}Mn_yO_{3\pm\delta}$ grain boundaries

4.1 Introduction

Grain boundaries (GBs) in mixed valence manganites are known to represent a highly electrical insulating and magnetically disordered region.[1–3] Their presence in polycrystalline materials can give rise to a collection of unique properties compared to the bulk, such as a large magnetoresistance below Curie temperature[4] or the surge of different low temperature conduction mechanisms.[5,6] As a consequence, GBs can also have a large influence on the performance of numerous manganite-based devices, which can be either detrimental for the final application, such as in the case of magnetic cooling devices,[7] or highly beneficial, for example in spintronics applications or magnetic memories.[8–10] Although many efforts have been devoted to model the magnetic and electrical transport properties of polycrystalline manganites with nanometric grain size,[1,3,11–15] the origin of the poor electronic properties was generally addressed to structural defects and electron scattering but not fully investigated. The understanding of the origin of the peculiar properties associated to manganite GBs would represent an important step forward in the engineering of electronic and magnetic properties of polycrystalline materials.

In this chapter, we aim to address the conduction phenomena in the GBs of different $La_{0.8}Sr_{0.2}Mn_yO_{3\pm\delta}$ (LSM_y) thin films and to rationalize their electrical properties with the different type of local-nonstoichiometry found in the GBs (Chapter **3**). In the first part, the low temperature electrical conductivity of LSM_y thin films with different Mn content is considered (Section **4.2**). By confronting bulk epitaxial and polycrystalline thin films, it is shown how the GBs severely hinder the overall electrical properties. Moreover, the films characterized by GB_{def} (local decrease of Mn and O and increase of Sr and La) do not present the low temperature metal behaviour, because the lack of local Mn blocks the double exchange conduction mechanism. Then, in order to gain more insights into the GB electrical properties, the mechanisms of electronic conduction are considered (Section **4.3**). It is found that the small polaron hopping mechanism can perfectly describe the transport in the paramagnetic region, both for bulk and GBs. Meanwhile, at low temperature polycrystalline thin films with low Mn content better fits with a variable range hopping mechanism. The results obtained are discussed in light of the different GB ionic compositions described in Chapter **3**. Finally, the high temperature defect equilibrium is studied, analysing the evolution of in-plane conductivity for different oxygen partial pressure (pO_2) environments (Section **4.4**). The study reveals a surprisingly n-type behaviour in the polycrystalline thin films with B/A < 0.9, while for B/A > 0.9 the ordinary p-type trend is restored.

4.2 Tuning the electrical transport in LSM_y thin films

In order to assess the impact of the GBs on the transport properties of the LSM_y films, we evaluated the in-plane electrical conductivity for the whole series of compositions deposited (see Chapter **3**). The layers were analyzed in an in-plane four-probe geometry, as shown in **Figure 4.1a** (see Chapter **2** for more information).

With the aim of identifying the contribution of GBs on the electrical properties of polycrystalline LSM_y films, two sets of equivalent polycrystalline and epitaxial samples with B/A ratios from 0.85 to 1.2 were deposited by Combinatorial PLD (C-PLD). For the deposition of polycrystalline samples, two substrates were used; sapphire (0001), known to be a good dielectric material, and a YSZ/Si_3N_4/SiO_2/Si substrate. In the latter, Si_3N_4/SiO_2 was intended to electrically passivate the silicon substrates with a stress-free dielectric bilayer, while the thin film of YSZ was deposited by PLD to avoid silicon diffusion to the LSM during the deposition.[16,17] Due to the nano-columnar structure of these polycrystalline thin films, the in-plane measurements are expected to be dominated by the GBs properties, since the current flow directly crosses a large number of grains (**Figure 4.1a**).

Meanwhile, epitaxial films were also grown on $NdGaO_3$ (110) (NGO) by C-PLD. These layers are expected to behave mostly like the grain interior of polycrystalline LSM_y, therefore taken as a reference to ensure that the effects observed in the corresponding polycrystalline films are indeed associated to the GBs and not to the corresponding changes in the bulk cation stoichiometry. Indeed, as shown in Chapter **3**, the polycrystalline and epitaxial LSM_y thin films present the same bulk cationic composition, Mn oxidation state and, consequently, oxygen content.

Additionally, Mn-deficient $LSM_{0.85}$ thin films were also deposited by PLD on the same three substrates (Sapphire, YSZ/Si_3N_4/SiO_2/Si and NGO). Since these films were found to behave exactly as the corresponding C-PLD layers with the same composition (B/A=0.85), in the following analysis no distinction is made between the deposition methods (*viz.* PLD and C-PLD).

Figure 4.1b shows the evolution of the thin films' resistivity as a function of temperature measured between 83 K and 573K. The figure presents the whole polycrystalline series deposited on sapphire and Si-based substrates (compositions marked with an asterisk in the legend). In addition, the epitaxial $LSM_{0.85}$ film on NGO (most Mn-deficient film) is shown for comparison. First, it is noted that the epitaxial $LSM_{0.85}$ thin film displays a metal-insulator (M-I) transition at *ca.* 200 K,[18,19] typical of

bulk mixed valence manganites.* Opposed to that, the polycrystalline counterpart (B/A = 0.85) presents one order of magnitude higher resistance, together with the suppression of the M-I transition. Remarkably, as shown in **Figure 4.1b**, progressively increasing the B/A ratio leads to a continuous decrease of the resistivity, recovering the low temperature M-I transition for Mn/(La+Sr) ~ 0.92. This means that for approximately B/A < 0.9, the polycrystalline layers maintain the insulating state for all the temperature range analysed, while for about B/A > 0.9, the typical low temperature metallic state is restored.

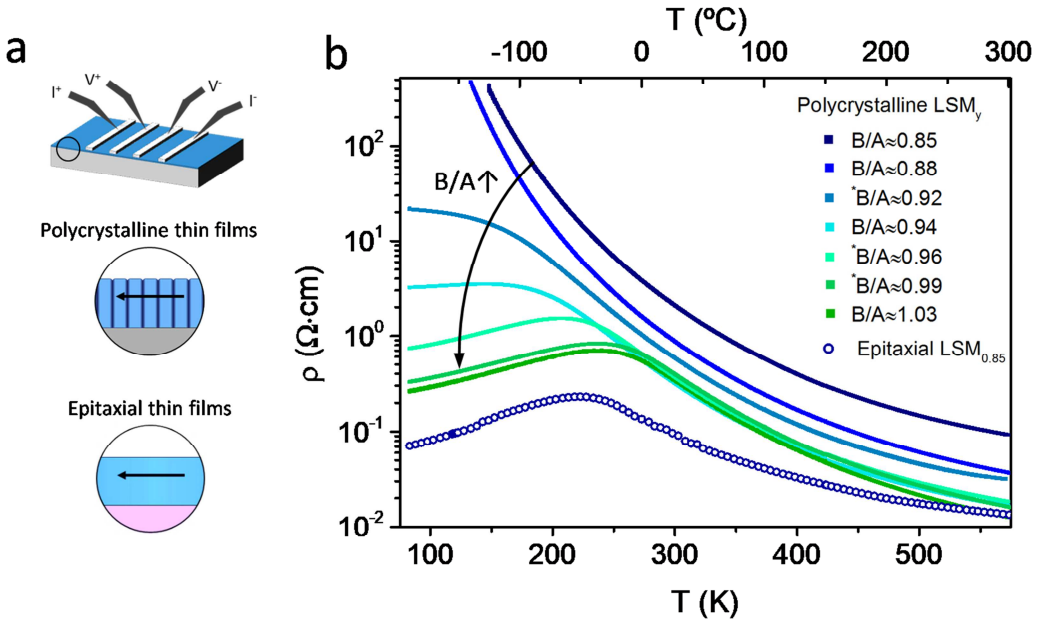

Figure 4.1 a, Sketch of the electrical measurement set up and of a cross-section of polycrystalline and epitaxial LSM thin films. **b**, in-plane electrical resistivity as a function of temperature measured for the polycrystalline LSM_y thin films deposited on sapphire and $YSZ/Si_3N_4/SiO_2/Si$ (indicated in the legend with an *). Epitaxial $LSM_{0.85}$ thin film on NGO is included for comparison.

* The electron transport behaviour in mixed valence manganites is generally characterized by two different regimes. Above the Curie temperature (T_C), the holes, generated by the Sr substitution, are strongly localized by electron-phonon coupling phenomena such as Jahn-Teller (JT), giving rise to an insulating regime.[5,28] Below T_C, the electronic spin configuration changes from paramagnetic to ferromagnetic.[18] In the latter, the alignment of the spins permits the double-exchange interaction between two neighbouring Mn ions, giving rise to a metallic conduction.[55] It is possible to visualize this phenomenon as a tunnelling of the e_g electron of a Mn^{3+} ion to a neighbour vacant site (Mn^{4+}) through the oxygen O2p orbital, see figure. Even though to fully explain the M-I transitions one should also consider the influence of JT polarons,[56] the double exchange mechanism is considered the most important phenomenon for the metallic-type conduction in manganites.[18,19,57]

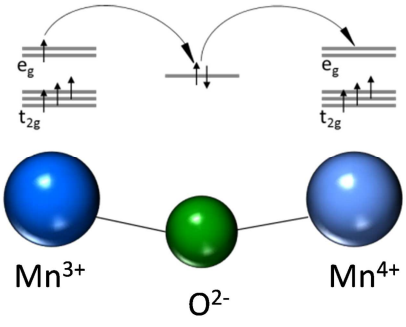

In order to demonstrate the impact of GBs in the electrical transport of LSM_y polycrystalline thin films, the effect of varying the B/A ratio on bulk electrical properties was also considered. For this reason, the resistivity of three epitaxial thin films with composition B/A = 0.85, B/A = 1.03, B/A = 1.2 was measured, see **Figure 4.2**. As it can be observed in the figure, all these layers present the expected M-I transition regardless of the composition. Also, a constant shift of the metallic state towards higher temperature is measured increasing the Mn content. Since no change of Mn valence was observed along the thin films series (see Chapter **3**), this behaviour is believed to be related to the interruption of the network of Mn-O-Mn bonds. This was reported to hinder the double exchange mechanism shifting the insulator-metal transition to lower temperature or even completely preventing it.[20–24] Nevertheless, even in the most deficient epitaxial layer measured ($LSM_{0.85}$) the M-I transition currently takes place, mainly due to the random position of these atomic vacancies and to the absence of extended structural defects, which are able to preserve the long range electronic order and to permit the electron percolation. Furthermore, the bulk changes observed are expected to play a second role on the conductivity of the whole series of polycrystalline thin films, since the resistivity measured in the epitaxial layers is orders of magnitude lower than the corresponding polycrystalline one. These observations suggest that the GB contribution is always dominating the macroscopic electronic transport in the polycrystalline thin films.

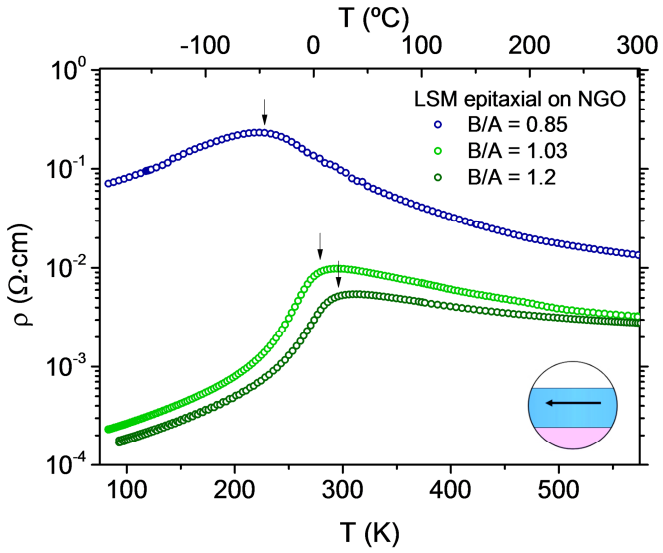

Figure 4.2 In-plane electrical resistivity as a function of temperature measured for the epitaxial LSM_y deposited on NGO. The arrows indicate the M-I transition.

Therefore, the lack of metallic state observed in the highly Mn deficient polycrystalline thin films (B/A < 0.9), as well as its recovery for B/A > 0.9, is certainly ascribed to the presence and the nature of the GBs in the different samples. It is important to note that no changes in the electrical resistivity were observed after annealing at temperatures as high as 923 K for 5 hours (measured in the Mn-deficient films, see **Figure 4.3**), suggesting a strong equilibrium of the GB local composition observed.

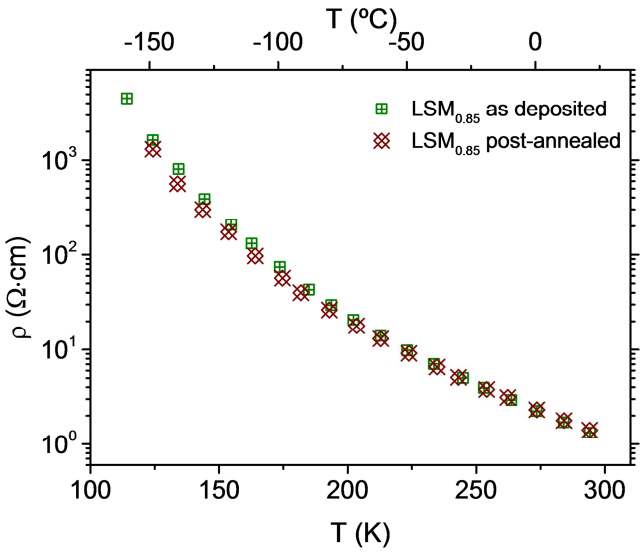

Figure 4.3 Electrical resistivity as a function of temperature of Mn-deficient polycrystalline $LSM_{0.85}$ thin films as deposited and annealed at 650ºC for 5 hours.

Remarkably, the TEM analysis shown in **Chapter 3.4** revealed, for these two ranges, two different types of GBs with opposite cationic depletion, which can perfectly explain the change of electronic behaviour observed, as follows:

i. For B/A < 0.9 (GB_{def}), the GBs present a simultaneous depletion of O and Mn that is expected to strongly impede the double exchange mechanism due to the interruption of the Mn-O-Mn chains. This type of local-nonstoichiometry therefore results in highly insulating GBs, which blocks the in-plane electron percolation and hinders the metallic behaviour.

ii. The recovery of the M-I transition for B/A > 0.9 (GB_{rich}) correlates with the change of GB composition observed by increasing the overall B/A ratio. In these films, characterized by an enrichment of Mn and a depletion of O and La at the GBs, the decrease of La is not supposed to affect the electronic transport, while the progressive increase of Mn helps to restore the metallic long-range order, gradually improving the metallic behaviour. Although we observed a decrease of O concentration in GB_{rich}, this does not appear to significantly hinder the M-I transition, contrary to what is usually found in literature.[25,26] Nevertheless, one must note that in bulk materials the oxygen deficiency is always associated to a decrease of Mn^{4+} concentration, which is critical for the appearance of the metallic state.[22] In our case, we did not observe any change of Mn oxidation state in all the GBs analysed, suggesting that, when the oxygen deficiency is compensated by other mechanisms (e.g. La vacancies), the depletion of O has a lower impact into the electronic transport.

All in all, these results show that, by tuning the overall Mn content in polycrystalline LSM thin films, it is possible to engineer the electronic transport properties, and that this behaviour is ascribable to the radical change of the GB local nonstoichiometric composition described in Chapter **3**.

4.3 Mechanisms of electronic conduction in LSM_y grain boundaries

In this section, the mechanism of electron transport was investigated in order to gain more insights into the effect of the GBs on the electronic conduction. As in the previous chapter, polycrystalline thin films with variable Mn content were studied and confronted with epitaxial layers to distinguish the bulk and GB contributions.

4.3.1 High temperature regime

The high temperature (423 – 873 K) electronic conductivity was measured in all the thin films in an in-plane four probes geometry (see Chapter **2**). The results are displayed in **Figure 4.4** in an Arrhenius-like representation. One can note that, similarly to **Figure 4.1**, the polycrystalline thin films present lower conductivity with respect to the epitaxial ones of similar composition, while an increase in conductivity is observed when increasing the Mn content, for both types of films. Nevertheless, all the films show a linear behaviour in the ln(σT) vs 1/T plot, suggesting that the high temperature electronic transport is characterized by adiabatic small polaron hopping conduction, regardless of the film's microstructure and composition. Indeed, it is generally believed that, in the high temperature paramagnetic insulating state of LSM, the charge carriers are localized in the Mn site by strong electron-phonon coupling, such as JT distortions, giving rise to a small polaron hopping conduction mechanism.[6,27–30] According to this model, the polarons can move to the Nearest Neighbour Hopping (NNH) site with the assistance of phonons, leading to the following expression of conductivity in the case of adiabatic limit:[31]

$$\sigma(T) = \frac{\sigma_0}{T} \cdot \exp\left(\frac{E_a}{k_b T}\right) \qquad \text{Eq 4.1}$$

Where E_a refers to the activation energy of the hopping mechanism, k_b is the Boltzmann constant and σ_0 is the pre-exponential factor.

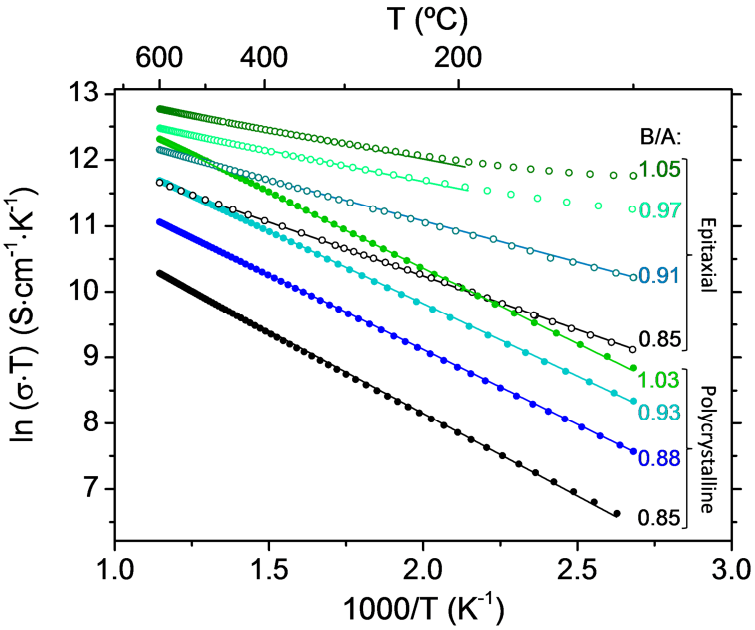

Figure 4.4 In-plane electronic conductivity as a function of temperature for the epitaxial and polycrystalline LSM_y thin films, plotted according to the adiabatic small polaron model.

By fitting the conductivity values with Equation 1, E_a and σ_0 have been calculated and represented in **Figure 4.5a** and **b**, respectively. First, the bulk activation energy of the epitaxial samples is lower than that of the polycrystalline ones. Moreover, the epitaxial samples present a progressive decrease of the activation energy while increasing the B/A ratio, whereas in the polycrystalline ones E_a keeps almost constant. This can be clearly associated to the presence of structural and chemical defects in both types of GBs (GB_{def} and GB_{rich}) that cause the localization and trapping of charge carriers, breaking the conduction paths and increasing the polaron energy barrier. Also, the decrease of E_a in the epitaxial samples is consistent with the decrease observed in the out-of-plane lattice parameter (see **Figure 3.18** in Chapter **3**), which represents a reduction of the tetragonal distortion of the cell and diminishes the polaron barrier.[32–34]

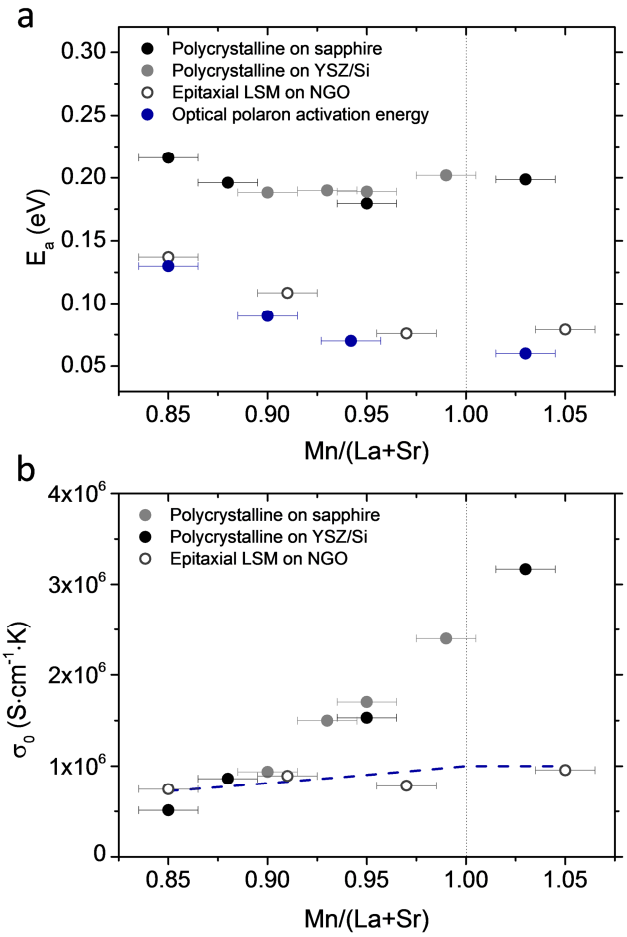

Figure 4.5 Energy of activation ($\mathbf{E_a}$) (**a**) and pre-exponential factor ($\boldsymbol{\sigma_0}$) (**b**) derived from the small polaron fitting. The polycrystalline samples measured on two different substrates give rise to similar results. The blue dots in (**a**) represents the thermal polaron activation energy extracted from optical measurements. The blue dashed line in (**b**) indicates the theoretical trend expected from the decrease of Mn hopping sites and no change in Mn valence ($\boldsymbol{\sigma_0 \propto [Mn]^2}$).

In order to confirm the validity of the polaron model, the activation energy of the epitaxial samples has been also confronted with the bulk optical polaron transition energy obtained by ellipsometry in Chapter **3**. Indeed, in the adiabatic polaron regime, the thermal activation energy is related to the maximum energy of the optical transition ($\hbar\omega_{max}$) by

$$E_a = \frac{1}{4}\hbar\omega_{max} - J \qquad \text{Eq. 4.2}$$

where J is the electron transfer energy[†]. The results are plotted in **Figure 4.5a** considering a literature value of J = 0.09 eV (dark blue dots).[35] Noteworthy, the values obtained perfectly matches with the thermal bulk epitaxial values for all the B/A ratios, also displaying the same trend with the Mn content. This clearly proves that the polaron model provides a good description of the high temperature electrical mechanism in LSM_y thin films.

Further insights into the singular properties of the GBs come from the study of the pre-exponential factor evolution, see **Figure 4.5b**. This figure shows that, in the presence of GBs, the film presents a surprising increment of σ_0, surpassing that of the epitaxial layers for B/A≈0.9 and steadily growing in the whole range of compositions studied (up to B/A=1.03). In order to understand this behaviour, it is necessary to consider the meaning of the pre-exponential factor. Worledge *et al.*[36] derived the formal expression of σ_0 starting from the Emin and Holstein model[31] and considering the on-site coulombic repulsions as:

$$\sigma_0 = \frac{e^2 \nu}{a k_b} \cdot [Mn^{4+}] \cdot [Mn^{3+}] \qquad \text{Eq. 4.3}$$

Where e, ν, a are the electron charge, the polaron attempt frequency and the site-to-site hopping distance, respectively. This model implies that the polaron (Mn^{4+}) needs a vacant site (Mn^{3+}) in the immediate vicinity for being able to successfully move. In the grain bulk, since negligible manganese valence changes were measured, the pre-exponential directly increases with the Mn content, $\sigma_0 \propto [Mn^{4+}] \cdot [Mn^{3+}] \propto [Mn]^2$. Thus, a decrease of the Mn concentration generates fewer sites for the polarons to hop, resulting in lower values of conductivity. As a matter of fact, the pre-exponential factor of the epitaxial LSM_y films perfectly follows this theoretical trend (blue dashed line in **Figure 4.5b**), reinforcing the proposed defect model for the bulk material (see Chapter **3**). Hence, the surprising increment of σ_0 as a function of Mn measured in the polycrystalline samples clearly appears to be originated by the GBs.

For B/A < 0.9, the pre-exponential factor is slightly smaller than that of the bulk, what can be associated to the Mn deficient character of GB_{def} for this composition (see

[†]In the small polaron adiabatic model developed by Holstein,[31] the thermal activation energy is related to the polaron formation energy (E_p) by $E_a = \frac{1}{2}E_p - J$, where J is the transfer energy originated by the resonance of the electron jumping forward and backwards in equilibrium and decreasing the energy barrier. According to Franck-Condon principle,[58] the photon energy required for the optical transition of one polaron from one position to another is $\hbar\omega_{max} = 4E_p$, where $\hbar\omega_{max}$ represents the energy of the maximum in the optical conductivity. Therefore, the thermal and optical transition energy are linked by: $E_a = \frac{1}{4}\hbar\omega_{max} - J$. In the footnote figure this energy relation between two arbitrary coordination states is depicted.

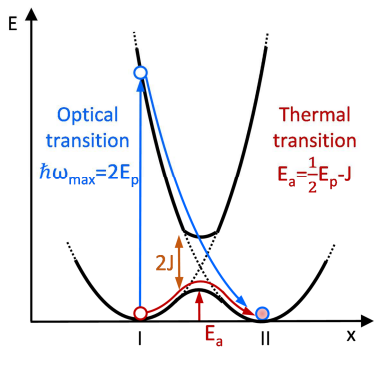

Figure 4.6, left). Indeed, the decreases of Mn concentration, generates fewer active sites for the polarons to hop, resulting in a decrease of σ_0. For B/A > 0.9, the presence GB_{rich} in the films implies the availability of new Mn sites at the GBs that promotes the polaronic transport, entailing the large increment of σ_0. The higher value of σ_0 in the stoichiometric polycrystalline LSM respect to the epitaxial films suggests that the increase of Mn concentration observed in Chapter **3** is related to the creation of anti-sites Mn_{La}^{x} at the interface, which were demonstrated to offer an additional pathway for electronic conduction.[37]

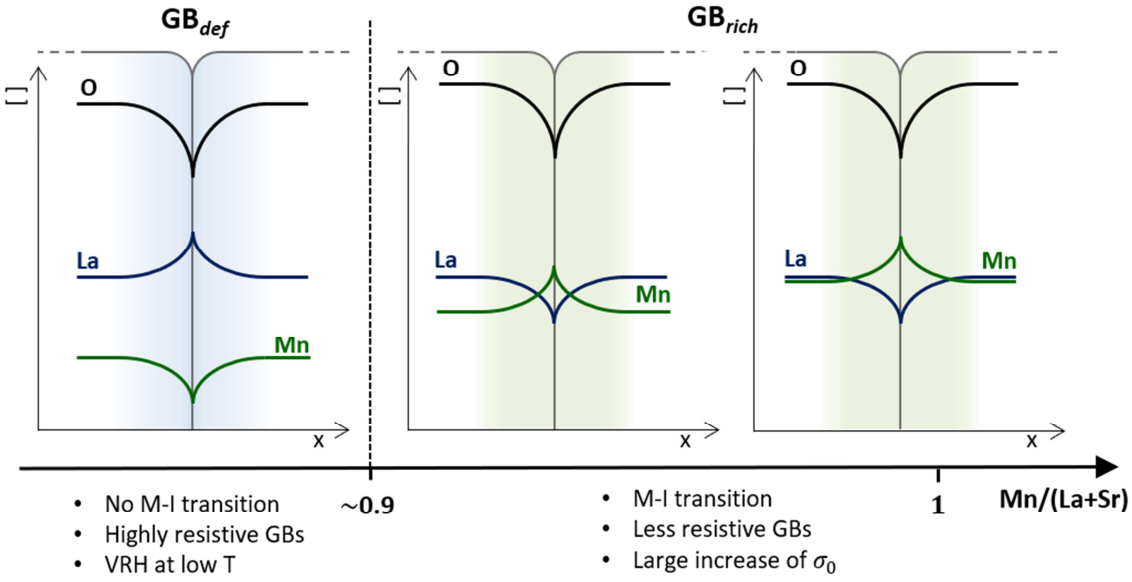

Figure 4.6 Sketch of the evolution of the ionic concentration in the GBs for increasing overall B/A ratio, as derived from the TEM analysis of Chapter 3.

4.3.1 Low temperature regime

Complementary to the high temperature conductivity presented in the previous section, in this section the electrical mechanism in the whole range of temperatures is now considered (T = 83 – 873K). **Figure 4.7a** shows a representation of the conductivity of specific compositions of epitaxial and polycrystalline thin films according to the NNH small polaron conduction model in this range. According to this figure, nearly stoichiometric (B/A = 1.03) polycrystalline layers, as well as epitaxial thin films (both Mn-deficient, B/A = 0.85 and slightly Mn-rich, B/A=1.05), appear to experience the NNH model for the whole temperature range down to the M-I transition, highlighted with a black arrow. Opposite, as commented in **Chapter 4.2**, the polycrystalline Mn deficient sample (B/A = 0.85) does not present the M-I transition and maintains an insulating state down to low temperatures (see **Figure 4.1**). This film only shows a good agreement with the NNH model in the high temperature range (T > 473 K), while decreasing the temperature it seems to experience a deviation from the expected behaviour.

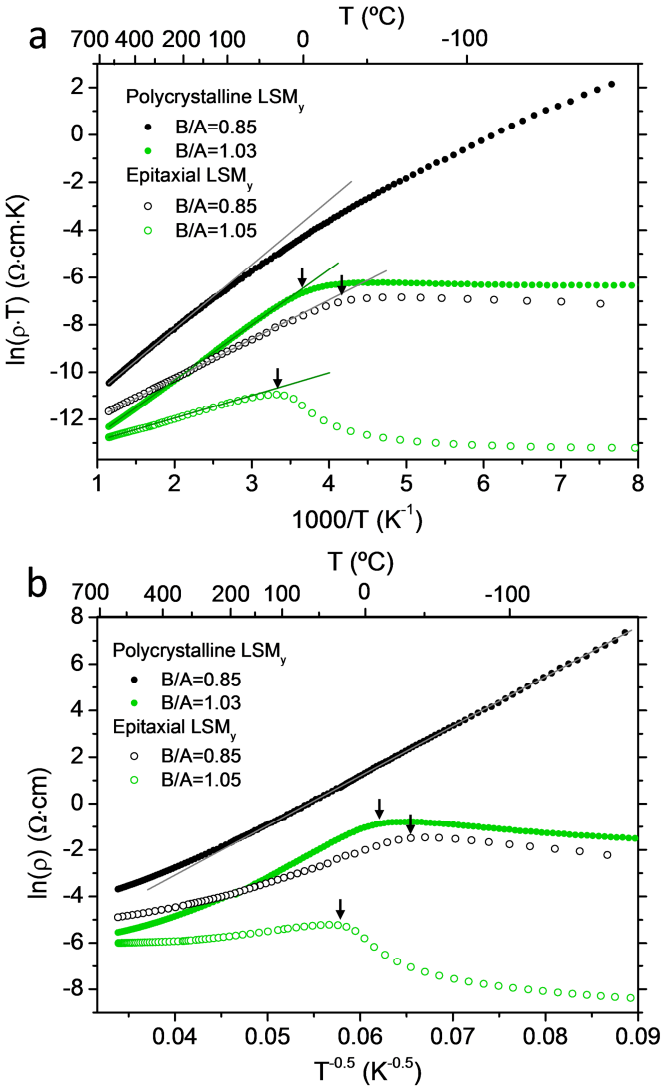

Figure 4.7 In plane electronic resistivity plotted according to the adiabatic small polaron model (**a**) and to the SE-VRH model (**c**) for a wide set of temperatures. In the polycrystalline sample with B/A = 0.85, the first well describes the conductivity for T > 473 K, while for T < 473 K the second shows a better fitting.

In detail, the thin film goes through an apparent decrease of energy of activation, suggesting of the typical performance of a Variable Range Hopping (VRH) conduction mechanism. This model was first developed by Mott for disordered semiconductors,[38] where the probability of finding an available site with a proper energy level decreases with temperature, determining a temperature-dependent hopping length. In other words, the electron does not always move to the nearest neighbour position but prefers to tunnel to farer sites that minimize the polaron energy difference. In manganites, VRH conduction was observed in semi-disordered systems, such as polycrystalline manganite thin films,[5,6] disordered B-doped bulk manganites[39,40] and ultrathin epitaxial thin films.[41] The general expression of the VRH mechanism is:

$$\sigma(T) = \sigma_p \cdot \exp\left(-\frac{T_0}{T}\right)^p \qquad \text{Eq. 4.4}$$

With T_0 being the characteristic temperature and p the exponent term that equals to ¼ in the case of a Mott (M) regime[38] and ½ for a Shklovskii–Efros (SE) mechanism.[42] The SE-VRH mechanism is generally determined by coulombic repulsion of the charge carriers but, more in general, is characteristic of a material with parabolic density of states at the Fermi level, while the Mott VRH mechanism by a constant one.[39,40,43] For Mn-deficient polycrystalline LSM films, we found a good consistency with the SE-VRH model, see **Figure 4.7b**. By fitting the curve with equation 4.4, a value of T_0 equal to $4.5 \cdot 10^4$ is extracted, in agreement with previous works on manganites.[39,40,43,44]

The appearance of VRH conduction in the films with GB_{def} is clearly not intrinsic but due to the localized defects in the GBs, since the epitaxial film with the same composition shows a better agreement with the NNH adiabatic model in the whole temperature range above the occurrence of the M-I transition. From a mechanistic point of view, the Mn deficiency and the presence of oxygen vacancies at the interface in GB_{def} naturally hinder the metallic behaviour and, instead, give rise to the VRH mechanism, in which polarons need to jump towards distant sites across the GB. It is important to note that the VRH observed could not be associated to a Coulombic blockade, in which the electric transport is dominated by the tunnelling of charges across distant metallic grains,[45,46] also found in polycrystalline manganites but at far lower temperatures (below 10 K).[47,48] Indeed, even if the two conduction mechanism lead to the same dependence with the temperature (Eq. 4.4), the average range hopping extracted from the fitting is on the order of some lattice parameter[‡] and not of the LSM grain size, indicating that the tunneling is happening across the GB and not across distant grains.[49] Finally, the appearance of the SE-VRH instead of the M-VRH could indicate that the charged defects in the GBs, such as $V_O^{\bullet\bullet}$, promote coulombic repulsion with the polarons.[39,40,43]

[‡]In the SE-VRH model the characteristic temperature is equal to $T_0 = \frac{\beta e^2}{k_b 4\pi\epsilon_r\epsilon_0\xi}$, where e is the electron charge, k_b the Boltzmann constant, ξ the localization radius of hopping carrier, ϵ_r the dielectric constant, ϵ_0 the vacuum dielectric and β a constant (for 3D transport equal to 2.8). Considering a value of ϵ_r equal to 4 (see [40] for a discussion on the validity of the continuum approximation of the dielectric properties), a localization radius of 0.26 nm is extracted from the fitted T_0, in agreement with other results obtained in manganites.[39,40,43,44] The hopping average length can be therefore calculated as: $r_{hop} = \xi \cdot \left(\frac{T_0}{T}\right)^{1/2}$, yielding at 100 K to r_{hop}~1.5 nm. This value indicates that the polaron hopping length is about the size of the GB.

4.4 Electrical conductivity as a function of pO_2 in LSM_y

4.4.1 The impact of Mn content on the pO_2 dependence

At this stage, it is clear that GBs in LSM_y films are responsible of significant changes in the electrical properties of the films (E_a, σ_0 and suppression of M-I transition), which can be explained by the different GB ionic compositions found varying the B/A ratio. In order to get deeper insights into the defect chemistry of LSM_y GBs, we analysed the high temperature oxygen partial pressure (pO_2) dependence of the in-plane electronic conductivity. All these experiments were conducted at 923 K for ensuring a fast equilibration with the atmosphere while preventing grain growth in the polycrystalline films.

The pO_2 dependence of the electrical conductivity for polycrystalline thin films with different compositions is shown in **Figure 4.8a**. First, it is possible to note the large difference in absolute value measured in the various films, whose origin was commented in the previous chapter. Also, a rather small change varying the oxygen partial pressure is observed. In order to emphasize the relative changes originated by the pO_2, the conductivities were normalized to the value measured at 50 ppm for each composition (**Figure 4.8b**). Results obtained for an epitaxial film with nominal composition B/A = 0.85 are also included for comparison. Interestingly, while the Mn-deficient epitaxial sample displays the typical p-type behaviour expected for the bulk defect model (calculated for 923 K, see Appendix **C** for further details), for the polycrystalline samples p-type and n-type like dependences are observed for B/A > 0.9 (GB_{rich}) and B/A < 0.9 (GB_{def}), respectively.

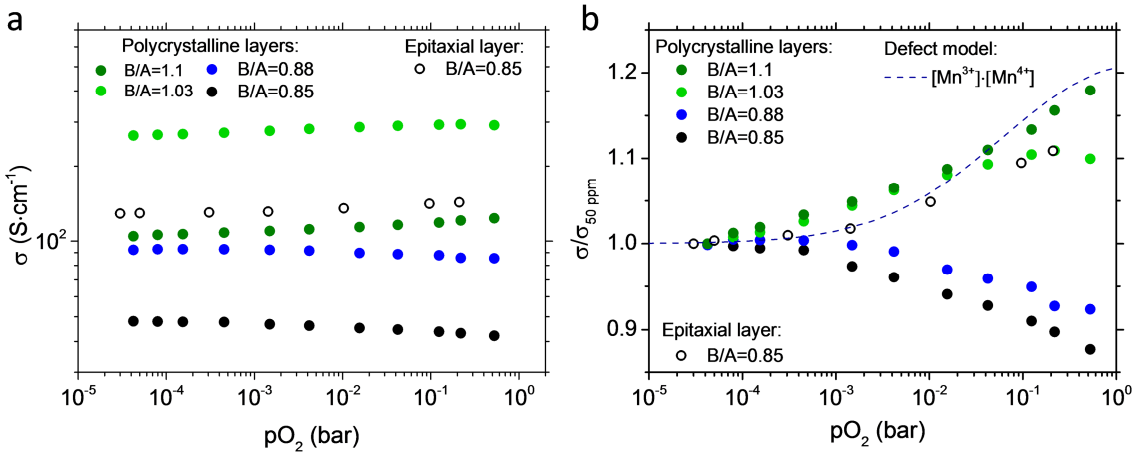

Figure 4.8 Absolute (**a**) and relative (**b**) in-plane electronic conductivity of the polycrystalline LSM_y films as a function of the pO_2 measured at 923 K. In **b**, the values are normalized to the low pO_2 (50 ppm) conductivity value for each film. The epitaxial film with B/A = 0.85 is reported for comparison (open symbols). The blue dashed line show the trend expected from the bulk random defect chemistry calculated at 923 K (see Appendix **C**).

Here, it is important to note that oxidation-reduction studies of Mn-deficient polycrystalline samples, shown in **Figure 4.9**, proved the reversibility of the unusual n-type like response, discarding any type of stabilization issues in this analysis.

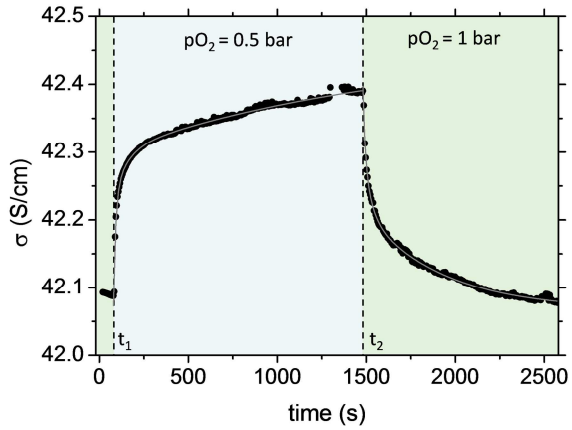

Figure 4.9 Time response of the conductivity for reduction and oxidation steps at 923 K in the polycrystalline thin films with B/A = 0.85. The vertical dotted lines indicate the times at which the oxygen content in the atmosphere was changed (t_1 and t_2).

In order to highlight the role of GBs in the n-type behaviour observed, complementary measurements on an $LSM_{0.85}$ sample with lower GB density have been performed. This layer was grown under the same deposition conditions of the thinner $LSM_{0.85}$ films (therefore yielding to the same cationic composition) but intentionally thicker (400 nm), leading to an increase of the average grain size from *ca.* 30 nm to *ca.* 60 nm (see AFM measurements in **Figure 4.10a** and **b**). In this sample, due to the lower density of GBs, the relative importance of the grain bulk is enhanced, as demonstrated by the overall increase of conductivity (~42 S/cm in the thin layer vs ~97 S/cm in the thick films at 923 K). Moreover, the oxidation-reduction equilibration of electronic conductivity between pO_2=0.5 bar and pO_2=1 bar (**Figure 4.10c**) clearly stressed two different contributions, namely, a fast one with the unusual n-type like and a slower one, showing the expected p-type conduction. Confronting the evolution measured in $LSM_{0.85}$ films with small (**Figure 4.9**) and bigger grains (**Figure 4.10c**), it seems reasonable to assign the n-type fast contribution to the GB_{def} and the slow p-type to the bulk (also measured in the $LSM_{0.85}$ epitaxial layer). Therefore, this experiment strongly suggests that the n-type behaviour found in LSM_y thin films for B/A < 0.9 (**Figure 4.8**) is due to the high concentration of GB_{def} found in this samples.

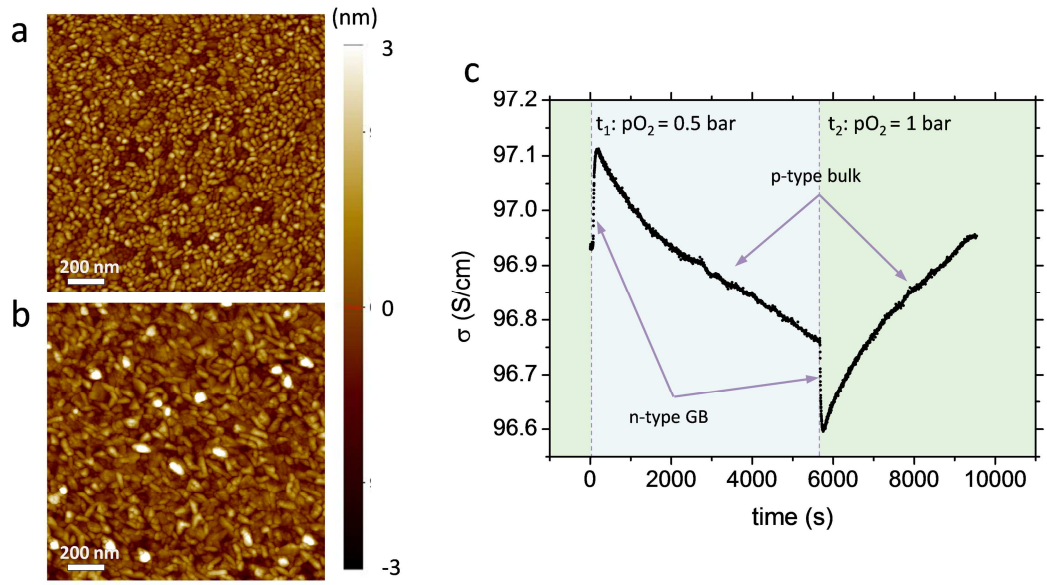

Figure 4.10 *AFM measurements of the surface of 100 nm and 400 nm thick samples ((**a**) and (**b**) respectively), with the same composition B/A = 0.85. The average grain size almost double increasing the film thickness (from ca. 30 nm to ca. 60 nm).* ***c****, equilibration of the electronic resistivity for the reduction (starting at t_1) and oxidation step (starting at t_2) between 100% O_2 and 50% O_2 for the 400 nm thick sample.*

4.4.2 Discussion on GB defect chemistry

In order to discuss the different behavior found as a function of pO_2, it is necessary to consider the defect chemistry of bulk LSM. As described in Chapter **1**, the defect model developed for LSM includes different mechanisms, which become more or less relevant depending on the oxygen partial pressure range.[50,51] In the high pressure pO_2 regime (i.e. the one investigated in the previous section), the most important equilibrium phenomenon involves the creation of cationic vacancies, with equilibrium:

$$6Mn_{Mn}^{x} + {}^{3}/_{2}\, O_2 \leftrightarrow V_{La}''' + V_{Mn}''' + 6Mn_{Mn}^{\bullet} + 3O_o^x \qquad \text{Eq. 4.5}$$

This means that, increasing the oxygen partial pressure, new cation vacancies are created and equilibrated by the increase of $[Mn^{4+}]$. Therefore, the electronic conduction is expected to display p-type behaviour, with the conductivity varying as $\sigma \propto [Mn^{4+}] \cdot [Mn^{3+}]$ (in the polaron model, see equation **4.3**). This theoretical tendency was calculated from the random model presented in Appendix **C**, after extrapolating the literature high temperature equilibrium constants to 923 K.[51] As shown in **Figure 4.8b**, this simple defect model well reproduces the variation of conductivity measured in the epitaxial films with B/A = 0.85 and in the polycrystalline thin films characterized by the presence of GB_{rich} (B/A = 1.03, B/A = 1.1). Thus, in agreement with the previous sections, the increase of Mn in GB_{rich} does not severely affect the electrical properties of these interfaces, resulting in a bulk-like p-type oxygen dependence of the electronic

conductivity. Contrary, the n-type behaviour observed in Mn-deficient polycrystalline thin films cannot be explained by the Equation **4.5**. The agreement between the defect chemistry model and the results obtained for the *bulk* epitaxial Mn-deficient thin films proves that GB_{def} are responsible for the unusual n-type behaviour observed. In the following, the possible origins of this pO_2 dependence in GB_{def} films are discussed.

The most straightforward hypothesis suggests for thi n-type behaviour the appearance of Mn^{2+} in the GB core, which would give rise to a n-type conduction even in oxidizing conditions.[50] However, the TEM-EELS analysis in Chapter **3** contradicts this hypothesis since we did not observe any local change of oxidation state in GB_{def}. A second hypothesis suggests be the creation of a negative space charge layer caused by the positive oxygen vacancies in the GB core, which could originate an enrichment of negative elements (Mn^{2+}) in the GB surroundings.[52] Additionally, the presence of negative cation defects, which are also actively involved in the oxidation mechanism, could also play a role in defining the space charge properties.[53] Nevertheless, due to the high carrier concentration of the bulk and the small band-gap of LSM, the expected width of the space charge layer is extremely small, in principle ruling out this option.[1,54] Finally, a third mechanism based on trapping positive charge carriers created upon oxygen oxidation may explain the pO_2 trend observed. Indeed, an increase of Mn^{4+} necessarily implies a decrease of Mn^{3+} and, according to equation **4.3**, this could originate a decrease of the total conductivity (if Mn^{4+} is trapped). However, in the frame of this work we did not obtain any experimental evidence supporting (nor contradicting) this hypothesis. In any case, the appearance of this unusual pO_2 behaviour is undoubtedly related to the characteristic depletion of Mn in GB_{def} and could have direct implications especially on the electrochemical performance of the layers and their stability in redox conditions. In this sense, as it will be discussed in the following Chapter **5**, an odd weak pO_2 dependence of the oxygen diffusivity is also observed in Mn-deficient polycrystalline LSM layers, suggesting that a completely different equilibration mechanism from the bulk is taking place in GB_{def}.

4.5 Conclusions

In summary, in this chapter the electrical properties of epitaxial and dense polycrystalline thin films of $La_{0.8}Sr_{0.2}Mn_{1-y}O_{3\pm\delta}$ with B/A ratio ranging from 0.85 (Mn deficient) to 1.2 (La deficient films) have been studied. The comparison between epitaxial and polycrystalline LSM_y thin films allowed us to elucidate the unique features of the GBs.

In the bulk epitaxial thin films, the low temperature behaviour is characterized by a metallic-like conduction for any B/A ratio analysed. Although it was found that the presence of Mn vacancies lower the M-I transition, their random position and the absence of extended structural defects allow the preservation of the long range electronic order and permit the metallic electron percolation. In the high temperature paramagnetic state, the polaron hopping model well describes the electron transport, as confirmed by thermal and optical measurements. Additionally, increasing the B/A ratio a decrease of the activation energy was found, probably connected to the decrease of lattice out of plane parameter observed in the same range. The p-type behaviour measured as a function of pO_2 for the B/A = 0.85 is well explained by the bulk defect chemistry model presented in Chapter **1**.

In the polycrystalline samples, the electronic conductivity is dominated by the different types of GB compositions described in Chapter **3**, which largely impact the activation energy, the pre-exponential factor and even the conduction mechanism at low temperatures. In the thin films characterized by GB_{def} (B/A < 0.9), the lack of Mn and O blocks the double exchange mechanism, creating insulating interfaces and impeding the onset of the metal behaviour. Instead, a low temperature VRH mechanism takes place, in which polaron tunnels across the GBs for reaching distant Mn atoms. In the high temperature paramagnetic state, the local decrease of Mn concentration lowers the probability of finding a site for the polaron to hop, which reflects in a decrease of the pre-exponential factor respect to the corresponding bulk value. Remarkably, n-type behaviour is found in the high temperature pO_2 experiments, indicating that the complex defect distribution found in GB_{def} strongly affects the equilibration mechanism. In the thin films characterized by GB_{rich} (B/A > 0.9), the local enrichment of Mn gradually restores the low temperature metallic behaviour and causes an overall increase of electronic conductivity in all the temperature range. Also, in the paramagnetic state the increase of Mn atoms originate an interesting increase of pre-exponential factor, which has been explained by the increase of Mn sites in GB_{rich} available for the polaron hopping. Finally, a p-type pO_2 trend was measured in these films, similar to the one expected from the defect chemistry model.

Overall, the results demonstrate the possibility of actively engineering the electrical properties of LSM_y polycrystalline thin films by modifying the GB cationic composition.

References

1. Gross, R. *et al.* On the nature of grain boundaries in the colossal magnetoresistance manganites. *J. Magn. Magn. Mater.* **211,** 150–159 (2000).
2. Kar, S., Sarkar, J., Ghosh, B. & Raychaudhuri, A. Spatially resolved study of electronic transport through grain boundaries in nanostructured films of $La_{0.67}Sr_{0.33}MnO_3$. *Phys. Rev. B* **74,** 85412 (2006).
3. Gupta, A. *et al.* Grain-boundary effects on the magnetoresistance properties of perovskite manganite films. *Phys. Rev. B* **54,** R15629–R15632 (1996).
4. Mathur, N. D. *et al.* Large low-field magnetoresistance in $La_{0.7}Ca_{0.3}MnO_3$ induced by artificial grain boundaries. *Nature* **387,** 266–268 (1997).
5. Prasad, R. *et al.* Comparative study of transport properties of compressively strained epitaxial and polycrystalline $La_{0.88}Sr_{0.12}MnO_3$ thin film. *Phys. Status Solidi Basic Res.* **246,** 1662–1673 (2009).
6. Ziese, M. & Srinitiwarawong, C. Polaronic effects on the resistivity of manganite thin films. *Phys. Rev. B* **58,** 11519–11525 (1998).
7. Phan, M. H. & Yu, S. C. Review of the magnetocaloric effect in manganite materials. *J. Magn. Magn. Mater.* **308,** 325–340 (2007).
8. Fina, I. *et al.* In-plane tunnelling field-effect transistor integrated on Silicon. *Sci. Rep.* **5,** 1–7 (2015).
9. Asamitsu, A., Tomioka, Y., Kuwahara, H. & Tokura, Y. Current switching of resistive states in magnetoresistive manganites. *Nature* **388,** 50–52 (1997).
10. Haghiri-Gosnet, A.-M. & Renard, J.-P. CMR manganites: physics, thin films and devices. *J. Phys. D. Appl. Phys.* **36,** R127–R150 (2003).
11. Narjis, A. *et al.* Low temperature electrical resistivity of polycrystalline $La_{0.67}Sr_{0.33}MnO_3$ thin films. *Mater. Sci. Semicond. Process.* **16,** 1257–1261 (2013).
12. Dey, P. & Nath, T. K. Effect of grain size modulation on the magneto- and electronic-transport properties of $La_{0.7}Ca_{0.3}Mn\ O_3$ nanoparticles: The role of spin-polarized tunneling at the enhanced grain surface. *Phys. Rev. B - Condens. Matter Mater. Phys.* **73,** 1–14 (2006).
13. López-Quintela, M. A., Hueso, L. E., Rivas, J. & Rivadulla, F. Intergranular magnetoresistance in nanomanganites. *Nanotechnology* **14,** 212–219 (2003).
14. Zhang, N., Ding, W., Zhong, W., Xing, D. & Du, Y. Tunnel-type giant magnetoresistance in the granular perovskite $La_{0.85}Sr_{0.15}MnO_3$. *Phys. Rev. B* **56,** 8138–8142 (1997).
15. Kameli, P., Salamati, H. & Aezami, A. Influence of grain size on magnetic and transport properties of polycrystalline $La_{0.8}Sr_{0.2}MnO_3$ manganites. *J. Alloys Compd.* **450,** 7–11 (2008).
16. Saranya, A. M. *et al.* Engineering Mixed Ionic Electronic Conduction in $La_{0.8}Sr_{0.2}MnO_{3+\delta}$ Nanostructures through Fast Grain Boundary Oxygen Diffusivity. *Adv. Energy Mater.* **5,** 1500377 (2015).
17. Saranya, A. M. *et al.* Unveiling the Outstanding Oxygen Mass Transport Properties of Mn-Rich Perovskites in Grain Boundary-Dominated $La_{0.8}Sr_{0.2}(Mn_{1-x}Co_x)_{0.85}O_{3\pm\delta}$ Nanostructures. *Chem. Mater.* **30,** 5621–5629 (2018).
18. Urushibara, A. *et al.* Insulator-metal transition and giant magnetoresistance in La_{1-}

$_x$Sr$_x$MnO$_3$. *Phys. Rev. B* **51,** 103–109 (1995).

19. Dabrowski, B. *et al.* Structure-properties phase diagram for $La_{1-x}Sr_xMnO_3$ (0.1<=x<=0.2). *Phys. Rev. B* **60,** 7006–7017 (1999).

20. Marozau, I. *et al.* Influence of La and Mn vacancies on the electronic and magnetic properties of $LaMnO_3$ thin films grown by pulsed laser deposition. *Phys. Rev. B* **89,** 174422 (2014).

21. Vergara, J. & Madurga, V. Effect of disorder produced by cationic vacancies at the B sites on the electronic properties of mixed valence manganites. *Phys. Rev. B* **60,** 1127–1135 (1999).

22. Malavasi, L. Role of defect chemistry in the properties of perovskite manganites. *J. Mater. Chem.* **18,** 3295 (2008).

23. Hébert, S. *et al.* Vacancies at Mn-site in Mn^{3+} rich manganites: a route to ferromagnetism but not to metallicity. *Solid State Commun.* **123,** 311–315 (2002).

24. Dezanneau, G., Sin, Ã. A., Roussel, H., Audier, M. & Vincent, H. Magnetic properties related to structure and complete composition analyses of nanocrystalline $La_{1-x}Mn_{1-y}O_3$ powders. *J. Solid State Chem.* **173,** 216–226 (2003).

25. Maeder, T. & Bednorz, J. . Influence of oxygen stoichiometry on electrical transport and magnetic properties of doped perovskite-type ferrate and manganate single crystals. *J. Eur. Ceram. Soc.* **19,** 1507–1510 (1999).

26. Baikov, Y. M., Nikulin, E. I., Melekh, B. T. & Egorov, V. M. Conductivity, Magnetoresistance, and Specific Heat of Oxygen-Deficient $La_{0.67}Sr_{0.33}MnO_{3-a}$ ($0 \leq a \leq 0.16$). *Phys. Solid State* **46,** 2086–2093 (2004).

27. Varshney, D. & Dodiya, N. Electrical resistivity of the hole doped $La_{0.8}Sr_{0.2}MnO_3$ manganites: Role of electron-electron/phonon/ magnon interactions. *Mater. Chem. Phys.* **129,** 896–904 (2011).

28. Lanzara, A. *et al.* Crossover from Large to Small Polarons across the Metal-Insulator Transition in Manganites. *Phys. Rev. Lett.* **81,** 878–881 (1998).

29. Jaime, M. *et al.* Hall-Effect Sign Anomaly and Small-Polaron Conduction in $(La_{1-x}Gd_x)_{0.67}Ca_{0.33}MnO_3$. *Phys. Rev. Lett.* **38,** 951–954 (1997).

30. Pavone, M., Muñoz-García, A. B., Ritzmann, A. M. & Carter, E. A. First-principles study of lanthanum strontium manganite: Insights into electronic structure and oxygen vacancy formation. *J. Phys. Chem. C* **118,** 13346–13356 (2014).

31. Emin, D. & Holstein, T. Studies of small-polaron motion IV. Adiabatic theory of the Hall effect. *Ann. Phys. (N. Y).* **53,** 439–520 (1969).

32. Yang, F., Kim, S. & Takamura, Y. Strain effect on the electrical conductivity of epitaxial $La_{0.67}Sr_{0.33}MnO_3$ thin films. *Scr. Mater.* **65,** 29–32 (2011).

33. Adamo, C. *et al.* Effect of biaxial strain on the electrical and magnetic properties of (001) $La_{0.7}Sr_{0.3}MnO_3$ thin films. *Appl. Phys. Lett.* **95,** 112504 (2009).

34. Mizusaki, J. *et al.* Electronic conductivity , Seebeck coefficient , defect and electronic structure of nonstoichiometric $La_{1-x}Sr_xMnO_3$. *Solid State Ionics* **132,** 167–180 (2000).

35. Mildner, S., Hoffmann, J., Blöchl, P. E., Techert, S. & Jooss, C. Temperature- and doping-dependent optical absorption in the small-polaron system $Pr_{1-x}Ca_xMnO_3$. *Phys. Rev. B* **92,** 35145 (2015).

36. Worledge, D. C., Mie, L. & Geballe, T. H. On-site Coulomb repulsion in the small polaron system $La_{1-x}Ca_xMnO_3$. *Phys. Rev. B* **57,** 267–271 (1998).

37. Aruta, C. *et al.* Off-stoichiometry effect on orbital order in A-site manganites probed by x-ray absorption spectroscopy. *Phys. Rev. B - Condens. Matter Mater. Phys.* **86,** 1–8 (2012).

38. Mott, N. F. & Davis, E. A. *Electronic Processes in Non-crystalline Materials*. (Oxford University Press, 1971). doi:10.1016/0040-6090(72)90068-5

39. Laiho, R. *et al.* Variable-range hopping conductivity in $La_{1-x}Ca_xMn_{1-y}Fe_yO_3$: evidence of a complex gap in density of states near the Fermi level. *Journal of Physics: Condensed Matter* **14,** 8043–8055 (2002).

40. Laiho, R., Lisunov, K. G., Lähderanta, E., Stamov, V. N. & Zakhvalinskii, V. S. Variable-range hopping conductivity in $La_{1-x}Ca_xMnO_3$. *J. Phys. Condens. Matter* **13,** 1233 (2001).

41. Feng, Y. *et al.* Insulating phase at low temperature in ultrathin $La_{0.8}Sr_{0.2}MnO_3$ films. *Sci. Rep.* **6,** 22382 (2016).

42. Efros, A. L. & Shklovskii, B. I. Coulomb gap and low temperature conductivity of disordered systems. *J. Phys. C Solid State Phys.* **8,** L49–L51 (1975).

43. Laiho, R. *et al.* Lattice distortions, magnetoresistance and hopping conductivity in $LaMnO_{3+d}$. *J. Phys. Condens. Matter* **17,** 105–118 (2005).

44. Laiho, R. *et al.* Mechanisms of hopping conductivity in weakly doped $La_{1-x}Ba_xMnO_3$. *J. Phys. Condens. Matter* **17,** 3429–3444 (2005).

45. Sheng, P., Abeles, B. & Arie, Y. Hopping Conductivity in Granular Metals. *Phys. Rev. Lett.* **31,** 44–47 (1973).

46. Sheng, P. & Klafter, J. Hopping conductivity in granular disordered systems. *Phys. Rev. B* **21,** 2583–2586 (1983).

47. Balcells, L., Fontcuberta, J., Martínez, B. & Obradors, X. High-field magnetoresistance at interfaces in manganese perovskites. *Phys. Rev. B* **58,** R14697–R14700 (1998).

48. Balcells, L., Martínez, B., Sandiumenge, F. & Fontcuberta, J. Low-temperature magnetotransport in nanometric half-metallic ferromagnetic perovskites. *J. Phys. Condens. Matter* **12,** 3013–3018 (2000).

49. Sheng, P., Abeles, B. & Arie, Y. Hopping conductivity in granular systems. *Phys. Rev. Lett.* **31,** 159–162 (1973).

50. Poulsen, F. Defect chemistry modelling of oxygen-stoichiometry, vacancy concentrations, and conductivity of $(La_{1-x}Sr_x)_yMnO_{3+\delta}$. *Solid State Ionics* **129,** 145–162 (2000).

51. Nowotny, J. & Rekas, M. Defect Chemistry of $(La,Sr)MnO_3$. *J. Am. Ceram. Soc.* **81,** 67–80 (1998).

52. Chiabrera, F., Garbayo, I. & Tarancón, A. in *Metal Oxide-Based Thin Film Structures* 409–439 (Elsevier, 2018). doi:10.1016/B978-0-12-811166-6.00017-0

53. Preis, W. & Sitte, W. Modelling of grain boundary resistivities of n-conducting BaTiO3ceramics. *Solid State Ionics* **177,** 2549–2553 (2006).

54. Polfus, J. M., Yildiz, B. & Tuller, H. L. Origin of Fast Oxide Ion Diffusion along Grain Boundaries in Sr-doped $LaMnO_3$. *Phys. Chem. Chem. Phys.* **20,** 19142–19150 (2018).

55. Zener, C. Interaction between the d-Shells in the Transition Metals. II. Ferromagnetic Compounds of Manganese with Perovskite Structure. *Phys. Rev.* **82,** 403–405 (1951).

56. Millis, A. J., Littlewood, P. B. & Shraiman, B. I. Double Exchange Alone Does Not Explain the Resistivity of $La_{1-x}Sr_xMnO_3$. *Phys. Rev. Lett.* **74,** 5144–7 (1995).

57. To, J. & Goodenough, J. B. $LaMnO_{3+\delta}$ Revisited. *J. Solid State Chem.* **128,** 117–128 (1997).

58. Austin, I. G. & Mott, N. F. Polarons in crystalline and non-crystalline materials. *Adv. Phys.* **50,** 757–812 (2001).

5. Oxygen mass transport properties of $La_{0.8}Sr_{0.2}Mn_yO_{3\pm\delta}$ grain boundaries

5.1 Introduction

Sr-doped lanthanum manganite (LSM) is one of the most studied materials for solid oxide fuel cell cathodes because of its high electronic conductivity, good high temperature mechanical compatibility with Yttria-Stabilized Zirconia (YSZ) and low fabrication cost.[1–6] However, LSM is known to be a poor oxygen conductor, leading to a limited active surface of the cathode and high polarization losses.[2,5,6] Nevertheless, it was recently discovered that polycrystalline LSM thin films shows a substantial enhancement of oxygen diffusion and oxygen reduction reactions (ORR) respect to the bulk counterpart, which was correlated to the high concentration of GBs that boosts oxygen traansport phenomena.[7–9] In this case, the observed improvement of oxygen mass transport properties is able to completely change the nature of the material converting the mainly electronic LSM into a good mixed ionic-electronic conductor (MIEC). This behaviour is definitely unusual, since in oxides, GBs are known to severely hinder the oxygen diffusion, either due to the low vacancies mobility and creation of a space charge region (e.g. in lightly doped $SrTiO_3$),[10,11] or to the association of dopant-oxygen vacancy defects (e.g. in doped ceria).[12] This substantial difference between LSM and other oxides is at the centre of debate within the solid state ionic community, since the comprehension of the phenomena might open new horizons to take advantage of GB peculiarities in several families of solid-state electrochemical devices.

In this chapter, we aim to analyse the oxygen mass transport phenomena in the GBs of different LSM_y polycrystalline thin films and to rationalize their electrochemical properties with the different types of local-nonstoichiometry found in the GBs as a function of the absolute Mn content in the films (see Chapter **3**). In order to do so, electrochemical impedance spectroscopy (EIS) analysis was systematically performed on LSM_y thin films with different Mn content as a function of temperature. The obtained spectra were fitted by a physically-meaningful model to extract the main oxygen mass transport properties (i.e. oxygen diffusion D^* and surface exchange coefficient k^q). By confronting these values with the ones in literature, the impact of GBs on oxygen transport was clearly stressed. Also, these parameters are observed to strongly vary as a function of B/A content, both in terms of absolute values and activation energies. In order to gain more insights into the mechanism of ORR and in the defect chemistry of the GBs, the evolution of EIS with oxygen partial pressure was considered. Finally, the results are discussed considering the effect of B/A ratio on electrochemical properties. It is suggested that the availability of oxygen vacancies in the GBs governs the oxygen mass transport properties for all the composition range analysed. Nevertheless, for B/A < 0.9 decreasing the Mn content causes a rapid increase of both k^q and D^*, while for B/A > 0.9 D^* displays a constant behaviour while k^q progressively increase while Mn is inserted in the structure. The origin of this behaviour is linked to a combined effect of GBs and the presence of surface oxygen vacancies.

5.2 The effect of GBs in the electrochemical properties of LSM_y thin films

5.2.1 Electrochemical impedance spectroscopy study

In this chapter, electrochemical impedance spectroscopy (EIS) was extensively used for characterizing the oxygen mass transport properties of LSM_y thin films. First, combinatorial PLD was employed to deposit LSM_y layers with variable Mn content on 3 mm x 3 mm YSZ (100) single crystals (YSZ_{SC}). The small dimensions of the crystals permitted to minimize the intrinsic compositional variation inside each sample due to the fabrication procedure, which was considered for the calculation of the B/A error (see figures legends). LSM_y thin films presented a polycrystalline structure with nanometric grain size for the entire compositional range analysed (B/A = 0.85 - 1.1). More details on the deposition method and thin film characterization can be found in Chapter **2** and **3**.

The scheme of the set-up used for the EIS measurements is shown in **Figure 5.1a**. The use of a pure oxygen conductor as substrate was intended to interrupt the electronic pathway and allow the measurement of the ionic phenomena. Silver paste was used as counter back electrodes and was measured to give a negligible effect in the overall electrochemical polarization resistance due to its high electrochemical properties.[13] Porous gold paste was applied on the LSM_y thin films for ensuring a fast in plane electronic conduction. Moreover, since gold is known to be mostly inactive for ORR reactions,[14,15] the oxygen incorporation phenomena of LSM_y are not influenced by the presence of this metal on top. This way, the high temperature polarization impedance is expected to provide a direct measurement of the LSM_y oxygen mass transport properties. Also, due the fully-dense structure of the thin films and to the extremely unfavourable triple phase boundary pathway compared to the bulk one (3PB : 2PB ratio $\sim 10^{-3}$ μm^{-1}), the ORR and incorporation are likely taking place on the LSM surface, which acts like a MIEC.[3,13,16] It is interesting to note that, while in the in-plane electrical measurements of Chapter **4** the GBs were oriented perpendicular to the current flow, in this out of plane EIS configuration the columnar-like shape of the grains offers a direct pathway for oxygen incorporation and diffusion along the GBs, permitting the direct study of the oxygen mass transport properties of these interfaces.

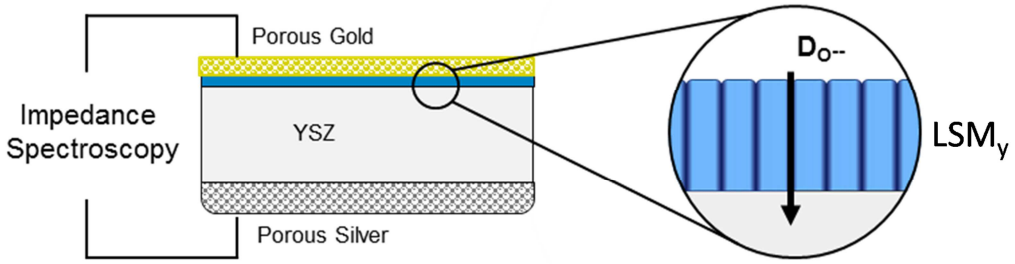

Figure 5.1 a, Scheme of the system used for the electrochemical measurements.

The thin films were studied in synthetic air as a function of B/A ratio and temperature, between 976 K – 898 K. The effect of varying the temperature on the oxygen electrochemical properties of the thin films is shown in **Figure 5.2** for one particular sample with B/A = 0.89 ± 0.02, where the Nyquist (**Figure 5.2a** and **b**) and Bode (**Figure 5.2c**) representation of the impedance spectra are depicted. First, in the magnification of Nyquist plot (**Figure 5.2b**), it is possible to observe a shift on the high frequency axis intercept with the temperature, physically corresponding to a thermally activated pure resistive contribution ($\tilde{R}_{\text{series}}$). Second, in both representations one can note that the polarization impedance (middle-to-low frequencies) is composed by two distinct phenomena, which, as in the case of the $\tilde{R}_{\text{series}}$, appear to be strongly dependent on the temperature. Indeed, the total polarization resistance of this film ($\tilde{R}_{\text{pol}}$) is observed to vary almost 1 order of magnitude between 976 K and 898 K.

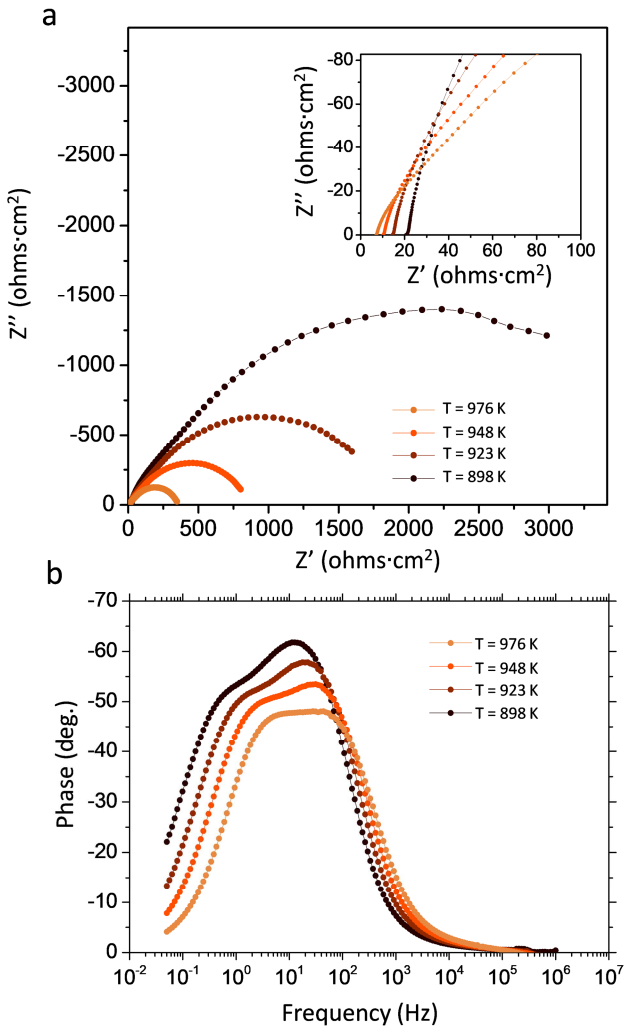

Figure 5.2 Nyquist (**a**) and Bode plots (**c**) of the impedance spectra obtained for the B/A = 0.89 ± 0.02 LSM_y sample in synthetic air at different temperatures. The inset in **a** shows a magnification of the high frequency region of the Nyquist plot.

Complementary to **Figure 5.2**, **Figure 5.3** shows the evolution of the impedances measured at 923 K for a selection of films with variable Mn content. The Nyquist

(**Figure 5.3a**) and Bode (**Figure 5.3c**) representation evidence significant changes as a result of the B/A variation, both in the total polarization resistance and in the shape of the impedances. Nevertheless, the interpretation of the phenomena is not straightforward, since the spectra are characterized by a non-monotonic trend of $\tilde{R}_{pol}$ and by a different evolution of the two impedance contributions. On the other side, the magnification of the high frequency part of the Nyquist plot (**Figure 5.3b**) reveals that the $\tilde{R}_{series}$ is independent of the total B/A ratio.

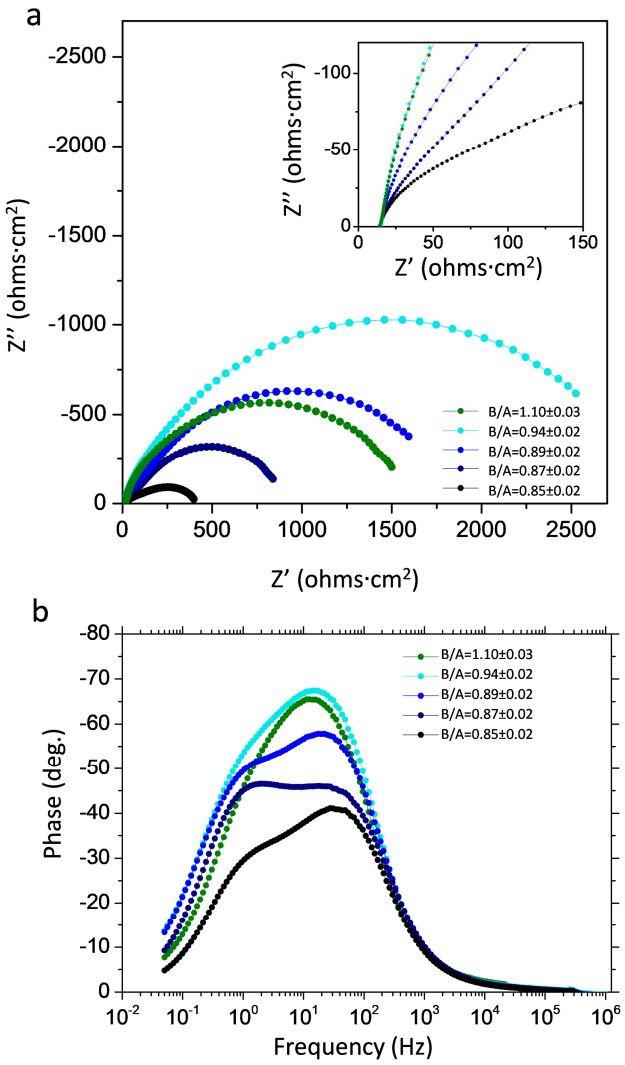

Figure 5.3. **a**, Nyquist and **c**, Bode plots of the impedance spectra obtained at 923 K in synthetic air for LSM_y films with different B/A ratio. The inset in **a** shows a magnification of the high frequency region of the Nyquist plot. A clear evolution of the polarization resistance is observed, while the series resistance stays constant.

The first useful conclusion that can be drafted is on the $\tilde{R}_{series}$ contribution. On one side, the Arrhenius representation of $\tilde{R}_{series}$ as a function of temperature reveals an activation energy of 1.13 eV for all the compositions measured, comparable with the one found in literature for YSZ single crystals in the same temperature range, see **Figure 5.4**.[17,18] Moreover, similar $\tilde{R}_{series}$ were obtained in symmetrical Ag paste / YSZ_{SC} / Ag paste

measurements. Taken this into consideration, it can be concluded that $\tilde{R}_{series}$ is dominated by the oxygen ionic transport resistance of the YSZ_{SC} substrate.

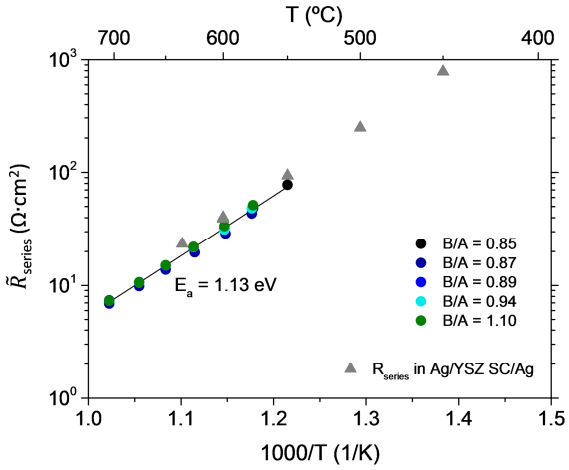

Figure 5.4 Temperature dependence of the specific series resistance obtained from the EIS spectra of a selection of B/A ratios analysed, compared to the values obtained in an $Ag/YSZ_{SC}/Ag$ symmetrical cell.

Then, focusing on the mid-to-low frequency part of the spectra, it is clear that thermal energy and Mn content have a severe impact on the impedance of the LSM_y thin films. However, from a simple analysis of the bare EIS spectra, it was not possible to draft any definitive conclusion on the effect of varying Mn content on the oxygen mass transport properties in LSM_y thin films, stressing the necessity of a physical equivalent model able to interpret and quantify the different electrochemical contributions. The following section focuses on the analysis of polarization resistance in the LSM_y films series through modelling of the EIS results.

5.2.2 Modelling the equivalent circuit in dense MIEC electrodes

In order to reproduce the EIS behaviour of dense MIEC thin films deposited on a pure ionic conductor electrolyte, the equivalent circuit derived by Jamnik and Maier is adopted.[19] The importance of this model stems from the fact that it was directly derived from the mass transport equations taking into account electrical and chemical parameters in a unified way. In other words, the equivalent circuit reproduces the exact physical response of an AC signal and its components can be used to derive the oxygen mass transport properties of MIEC thin films. This model was demonstrated to successfully describe the impedance spectra of LSM thin films[3,13] and other MIEC dense layers.[20–23]

5.2.2.1 Description of the equivalent circuit

The sketch of the oxygen electrochemical reactions and transport phenomena taking place across dense LSM thin films in response to an AC signal are shown in **Figure 5.5**, along with the corresponding electrical equivalent circuit. As it can be noted, it is

possible to divide the figure in four sections, from left to right: (i) heterogenous interface air/LSM, (ii) bulk transport inside the LSM, (iii) interface LSM/YSZ and (iv) pure ionic transport in YSZ substrate. At the LSM surface, a ZARC element (R_s and Q_s in parallel) describes the reaction of ORR and oxygen incorporation. A CPE was preferred to a simple capacitance to better catch the heterogeneity of the incorporation reactions on the LSM surface, similarly to the model adopted by Usiskin *et al.*[13]

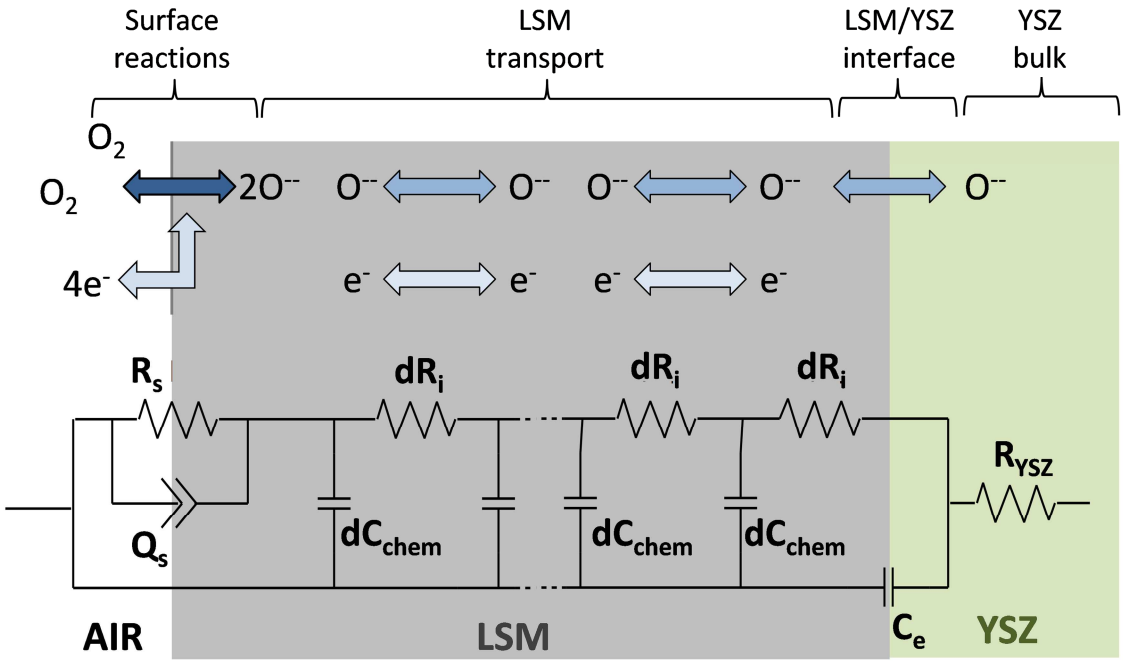

Figure 5.5 Scheme of the oxygen transport and reaction processes taking place in dense MIEC LSM thin films on pure ionic conductor YSZ upon an AC voltage impulse and corresponding equivalent circuit. The figure is adapted from the circuit employed by Fleig *et al.*[3]

The transport inside the LSM thin film is characterized by a transmission line with two parallel pathways, *viz.* the oxygen ion and the electronic transport line. The former is described by a series of infinitesimal resistance dR_i, representing the movement of oxygen vacancies inside the film. Instead, no voltage drops are considered in the electronic trail, since electrons are expected to be far more mobile than ionic defects. The two pathways are connected by a series of infinitesimal capacitances (dC_{chem}), which characterise the chemical capacitance of the material. This element describes the ability of a material to change the j carrier concentration c_j on a certain variation of the chemical potential μ_j and is defined as:[24]

$$C_{chem,j} = V(z_j e)^2 \left(\frac{\partial c_j}{\partial \mu_j}\right) \qquad \text{Eq. 5.1}$$

Where V is the volume of the material, z_j the formal charge number and e the electron charge. The chemical capacitance is a measure of the chemical energy stored in the material and is directly linked to the defect chemistry of the oxides.[22,23] Overall, this

part of the equivalent circuit describes the solution of the diffusion and conservation equations.[25]

At LSM/YSZ interface the electronic pathway stops, since the YSZ behaves as a pure oxygen ion conductor. Therefore, a capacitance (C_e) is placed at the end of the electronic rail. It is important to note that this capacitance is also in parallel with the dielectric capacitance of the whole cell (not drawn in **Figure 5.5**). No drops of voltage are considered across this interface for the ionic transport. Finally, the oxygen ion conduction in the YSZ is described by a resistance (R_{YSZ}), which, as discussed in the previous section, is the main responsible for the series resistance observed in the impedance spectra.

5.2.2.2 Impedance spectra fitting

The MIEC equivalent circuit was then used to fit the impedance spectra measured for the LSM_y thin films with ZView®. As an example, **Figure 5.6** shows the high quality of a typical fitting of the measured impedance spectra by using this model, which yielded to the set of parameters collected in **Table 5.1**. The accurate fitting validates the proposed equivalent circuit, meaning that the electrochemical oxygen reduction reactions (ORR) take place mostly at the LSM surface and are followed in series by the oxygen diffusion through the cathode thin film until reaching the YSZ electrolyte. Considering the fitted polarization resistances, the surface resistance (R_s, corresponding to the low frequency arc) was always higher that the ionic one (R_i, intermediate frequency arc), meaning that the surface reactions dominate the overall polarization resistance. Nevertheless, the contribution of the ionic transport was perfectly distinguishable in all the samples measured, implying that the oxygen diffusion caused a non-negligible contribution. All the impedance spectra measured for the LSM_y samples well agrees with the MIEC equivalent circuit.

Table 5.1 Fitted parameters of the impedance spectra measured at 650 ºC in synthetic air for the B/A = 0.89 ± 0.02 thin film.

$R_{ysz}/10$ ($\Omega \cdot cm^2$)	$R_s/10^3$ ($\Omega \cdot cm^2$)	$R_i/10^2$ ($\Omega \cdot cm^2$)	$C_e/10^{-5}$ (F/cm^2)	$Q_s/10^{-4}$ (F/cm^2)	n_s	$C_{chem}/10^{-4}$ (F/cm^2)
1.50 ± 0.02	1.45 ± 0.02	3.70 ± 0.01	5.55 ± 0.05	3.40 ± 0.03	0.74 ± 0.01	1.60 ± 0.05

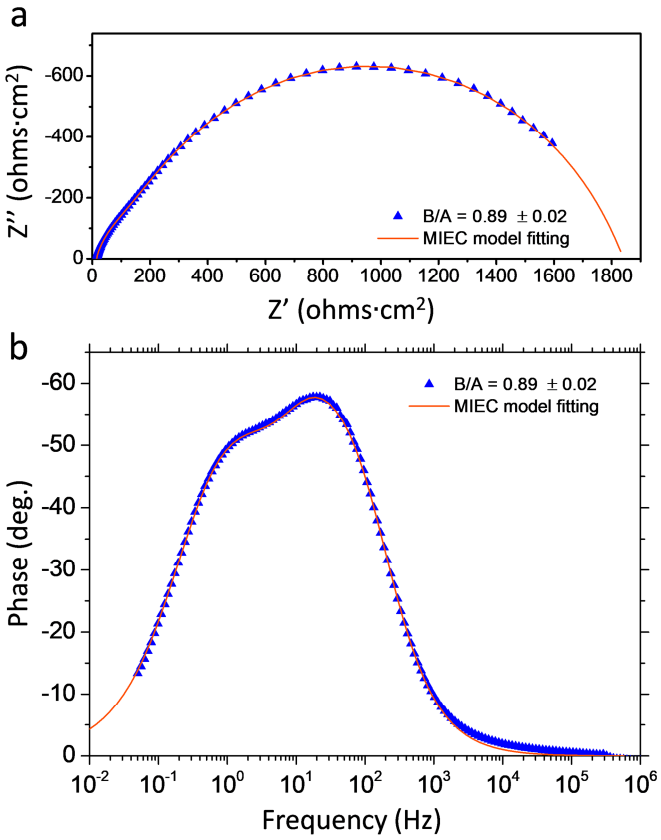

Figure 5.6 a, Nyquist and **b**. Bode plots of the impedance spectra measured at 650 ºC in synthetic air for the B/A = 0.89 ± 0.02 sample along with the obtained results of the MIEC equivalent model fitting.

5.2.3 Oxygen mass transport properties in LSM_y thin films

The parameters obtained by impedance fitting can be used to extract the two main oxygen mass transport parameters, namely the overall surface exchange coefficient k^q and the oxygen diffusion D^q. As derived from the Nernst-Einstein equation, the diffusion coefficient is linked to the ionic resistance by:

$$D^q = \frac{L}{R_i \cdot A} \cdot \frac{k_b T}{c_{O2} z_i^2 e^2} = \sigma_{ion} \cdot \frac{k_b T}{c_{O2} z_i^2 e^2} \qquad \text{Eq. 5.2}$$

Where L and A are respectively the thickness and the surface area of the LSM, k_b is the Boltzmann constant and c_{O2} is the concentration of oxygen in the LSM lattice. The coefficient D^q can be confronted with the diffusion coefficient D^* obtained in the oxygen tracer experiments considering a correlation factor of f=0.69.[26,27] The surface exchange coefficient is given by:

$$k^q = \frac{1}{R_s \cdot A} \cdot \frac{k_b T}{z_i^2 e^2 c_{O2}} \qquad \text{Eq. 5.3}$$

A direct comparison between k^q and k^* (being k^* the oxygen self-diffusion exchange coefficient) is still possible, although some differences could rise from the use of a catalytically active current collector.[26] For this reason, gold paste and gold cables were

used in the measurements (being gold known to be mostly inactive for ORR reactions).[28]

The evolution with the temperature of the oxygen diffusion (D^*) and of the surface exchange coefficient (k^q) calculated for a selection of B/A ratios are shown in **Figure 5.7a** and **b**, respectively. For comparison, these figures also include previously reported literature parameters for both bulk and grain boundary LSM. Only LSM thin films deposited by PLD were considered, except for the reference values measured by De Souza and co-workers for LSM bulk diffusion.[2,29] The values extracted from Saranya *et al.*[30] have been recalculated in the frame of this work by a FEM fitting of the oxygen profiles measured using Isotope Exchange Depth Profiling coupled to Secondary Ion Mass Spectroscopy (IEDP-SIMS) (see Chapter **2** for a description of the FEM model).

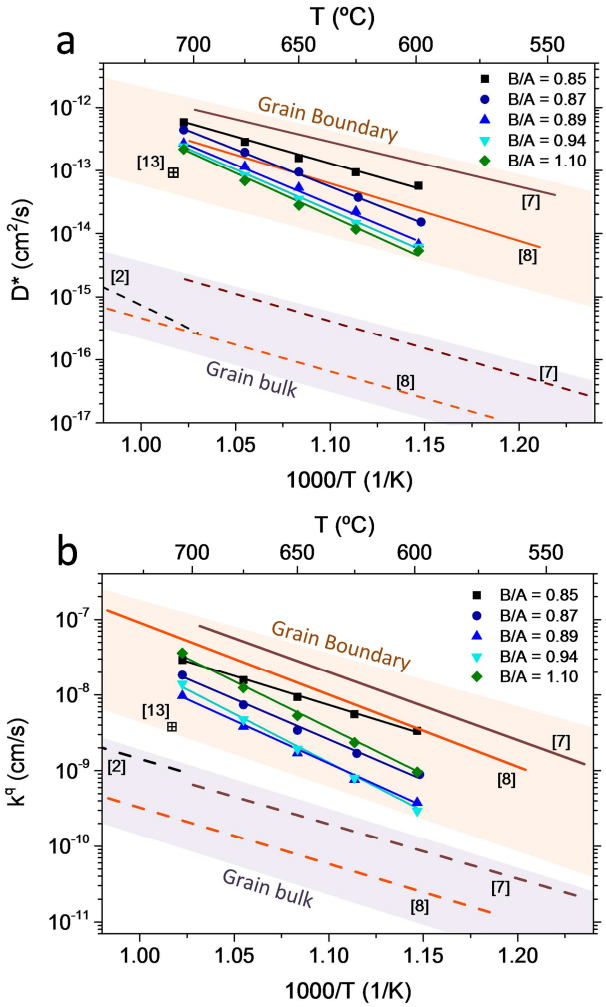

Figure 5.7 Temperature dependence of the ionic diffusion coefficient (**a**) and the surface exchange coefficient (**b**) calculated for a selection of films with different B/A ratios. Values of D^* and k^q from Ref. [30] are recalculated in the frame of this thesis with FEM fitting of the oxygen exchange profiles measured by Saranya *et al.* (brown lines: dashed bulk, solid grain boundary). Other literature values: Navickas *et al.*[8] (orange lines, dashed bulk, solid grain boundary), De Souza *et al.*[2] (black dashed for bulk) and Usiskin *et al.*[13]

First, a substantial increase of the diffusivity (above two orders of magnitude) with respect to the reported bulk values is observed for all the B/A ratios. Moreover, the values obtained are comparable to the literature GB diffusion, confirming the existence of an oxygen fast diffusion pathway along these interfaces, independently of the Mn/(La+Sr) ratio. Similar considerations hold also for the surface exchange coefficient, although in this case the difference between bulk and GB is reduced. Nevertheless, the beneficial effect of GBs on the ORR and incorporation is verified.

On top of that, clear changes in both D^* and k^q are observed varying the overall Mn content in the thin films. In order to highlight this effect, the diffusion and surface exchange coefficients measured at 923 K are plotted as a function of the B/A ratio in **Figure 5.8**, along with the bulk and GB literature values. It is important to note that the diffusion and surface exchange parameters obtained in this study represent an averaged value between the grain and grain boundary, since EIS is unable to distinguish the two contributions taking place in parallel. This points out that in order to permit a reasonable confrontation with the coefficients extracted in SIMS experiments[2,8,30] (in which grain and grain boundary coefficients were separated) one has to average D^* and k^q with the effective area that grain and GB regions occupy. Being the structure of these thin films dense and columnar, it is straightforward to calculate the overall D^* and k^q that these films would display in an electrochemical experiment. The dimensions of grain and grain boundary used for the calculation are the ones used for the SIMS oxygen concentration fitting in the different works.[2,8,30] Remarkably, these averaged parameters nicely matches with the ones measured in this work, confirming the dominant role of GB in the EIS measurements.

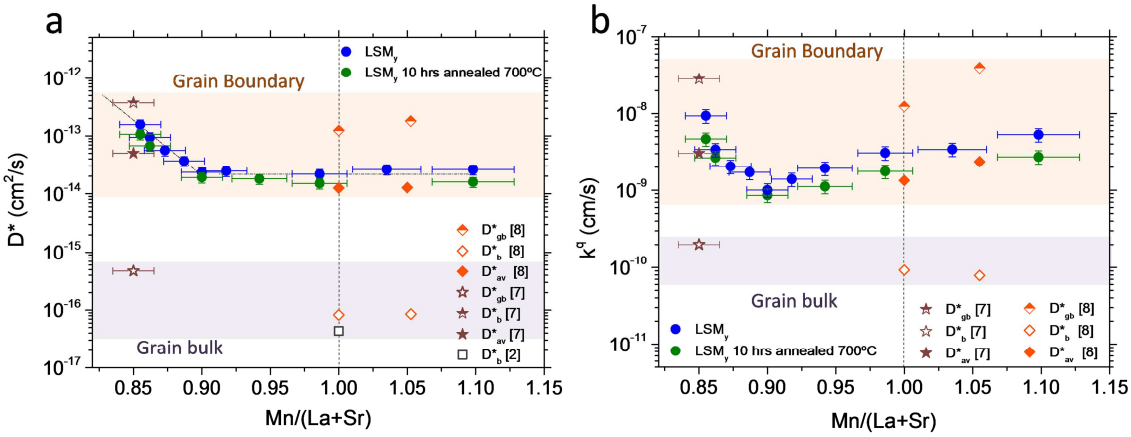

Figure 5.8 Oxygen diffusion (**a**) and surface exchange coefficient (**b**), extracted from the impedance at 650ºC in air for different B/A ratio. Bulk, GB and averaged coefficients measured in SIMS experiments by Saranya *et al.*[7], Navickas *et al.*[8] (films deposited at 700ºC) and De Souza *et al.*[2] are reported for comparison. Stoichiometry of films from reference [7] were measured within the frame of this work.

Figure 5.8 also stresses the impact of the overall Mn composition on the oxygen mass transport properties. Indeed, it is possible to observe that Mn-deficient layers with B/A < 0.9 present an additional increase up to one order of magnitude in the diffusivity

(**Figure 5.8a**), while for B/A > 0.9, no substantial change is observed. Regarding the surface exchange (**Figure 5.8b**), a steep increase is observed for B/A < 0.9 (analogous to D^*), while a gradual monotonically rise is measured for B/A > 0.9. On one side, these results may be behind some of the discrepancies observed by different authors in the past,[7,8] while on the other they demonstrate the possibility of tuning the oxygen mass transport properties by controlling the Mn content in the thin films. In order to investigate the origin of the observed differences in D^* and k^q, the activation energy of the two processes has been calculated, see **Figure 5.9**. First, it is possible to note that diffusion and surface reactions appear to be strictly related. Indeed, not only they present a similar trend but also comparable absolute energy values, suggesting a close relationship between the two processes. The increase of both D^* and k^q observed in **Figure 5.8** for B/A < 0.9 is clearly related to a decrease of activation energy observed in the same range. Instead, for B/A > 0.9 a roughly flat behaviour is observed for the diffusion, while for the surface ORR a more scattered trend is visible. The origin of the enhancement of the oxygen mass transport properties, as well as the impact of the different types of GBs observed in Chapter **3** will be discussed in section **5.4**.

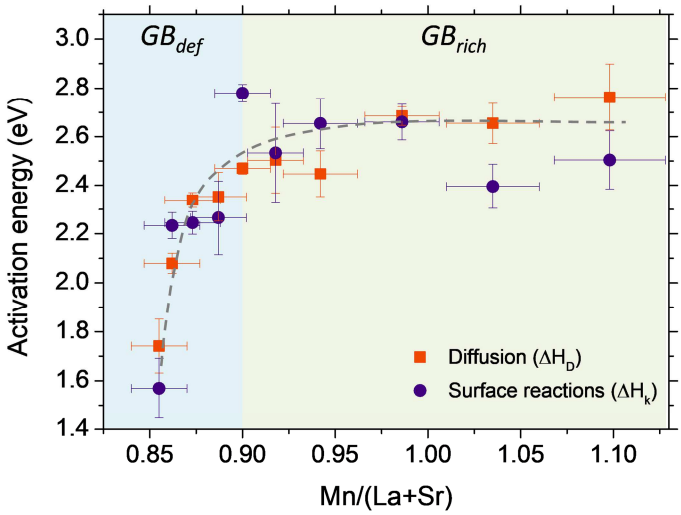

Figure 5.9 Activation energy of diffusion and surface reactions phenomena as a function of the B/A ratio in the LSM_y thin films.

5.2.4 Chemical capacitance in LSM_y thin films

Complementary to the analysis of the oxygen mass transport parameters, in this section the chemical capacitance extracted from the equivalent circuit of **Figure 5.5** is considered. The chemical capacitance is a direct measure of the defect chemistry of the material, since it represents the capability of varying the concentration of defects in response to a change of chemical potential.[3] Indeed, in literature are present some remarkable works in which the defect chemistry of a thin film oxide is derived by the measure of the chemical capacitance as a function of the oxygen partial pressure.[22,23] Motivated by these studies, we investigated the possibility of obtaining insights into the defects concentration of the GBs by studying the evolution of the chemical capacitance

as a function of Mn content, see **Figure 5.10a**. In the figure, the capacitance was normalized to the volume of the films, since C_{chem} is by definition an extensive property of the material.

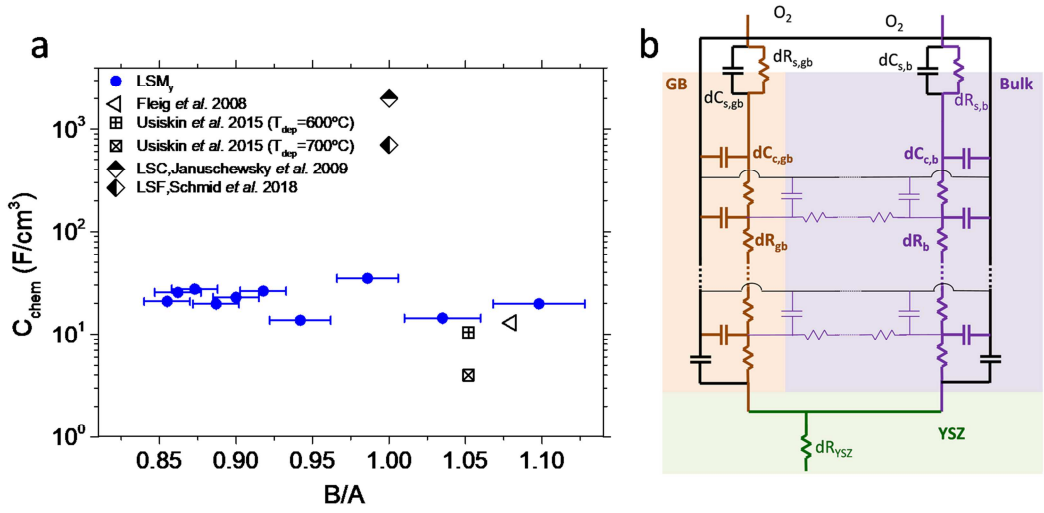

Figure 5.10 a, Chemical volumetric capacitance extracted from the impedance at 650 ºC in air for different B/A ratios. Values measured in literature for LSM,[3,13] LSF[23] and LSC[31] are reported for comparison. **b**, Sketch of a possible equivalent circuit that consider the GB and bulk parallel pathways as well as diffusion between them.

Despite the large differences observed in the oxygen mass transport properties, no significant changes were observed in C_{chem} varying the B/A ratio. Moreover, the values obtained are comparable with the ones measured in previous works for LSM thin film presenting lower values of oxygen diffusivity.[3,8] The reason could be that, although the oxygen transport takes place mostly in the grain boundaries, the chemical response of the bulk is still accessible with the EIS measurements (see **Figure 5.10b**). Indeed, since the electronic pathway extends also to the grain, the chemical capacitance will correspond to the response of the bulk to the chemical potential gradient induced by the diffusion through the grain boundary. This example points out the limitation of adopting a homogeneous equivalent model when studying heterogeneous systems.

Also, it should be noted that, due to the complex defect chemistry of LSM (see Appendix **C**), the chemical capacitance is not a direct measure of the oxygen concentration, as it was found in other oxides. Indeed, if the oxygen vacancy formation is compensated just by a reduction of holes concentration ($O_O^x + 2h^{\cdot} \leftrightarrow \frac{1}{2}O_2 + V_O^{\cdot\cdot}$), the chemical capacitance, calculated by **Eq. 5.1**, reads as:[32]

$$C_{chem} = \frac{e^2}{k_b T}\left(\frac{1}{4c_v} + \frac{1}{c_h}\right)^{-1} \approx \frac{4e^2}{k_b T} c_v \qquad \text{Eq. 5.4}$$

The last approximation holds if the concentration of holes (c_h) is far higher than the oxygen vacancy one (c_v). Nevertheless, in LSM the oxygen equilibrium involves also a change of cationic species,[33] resulting in a not straightforward expression because of the

large number of defect species participating in the equilibrium.[22] In conclusion, further work is needed in order to derive a correct expression that can link the chemical capacitance to the defect chemistry of LSM.

5.3 Electrochemical properties as a function of pO_2 in Mn-deficient LSM thin films

In order to gain more insights into the mechanism of oxygen mass transport properties in GBs, the electrochemical properties of LSM thin films have been studied as a function of the oxygen partial pressure (pO_2). For this study, LSM thin films with the lowest Mn content have been targeted because of their superior oxygen diffusion and surface ORR properties (see section **5.2**). For this analysis, 100 nm and 200 nm -thick films were symmetrically deposited on both sides of YSZ_{SC} (100) double-side polished substrates (1 cm x 1 cm) by LA-PLD under the same conditions described before (see Chapters **2** and **3**). The characterization of the films unveiled a fully dense polycrystalline structure, consistent with the observations of Chapter **3**. Composition analysis revealed a cationic composition of B/A = 0.82 ± 0.03, slightly lower than the one measured for other thin films grown under the same conditions. Porous gold paste was applied on both LSM electrodes to promote current collection, being gold known to be mostly inactive for ORR reactions.[28] EIS measurements were then conducted between 600ºC to 700ºC, after stabilization at the lowest oxygen partial pressure for 12 hours. **Figure 5.11** shows the evolution of the electrochemical impedance for three selected oxygen partial pressures ranging from 10^{-1} to 10^{-5} bar at 948 K. A clear evolution of the polarization impedance is visible in both Nyquist and Bode plots.

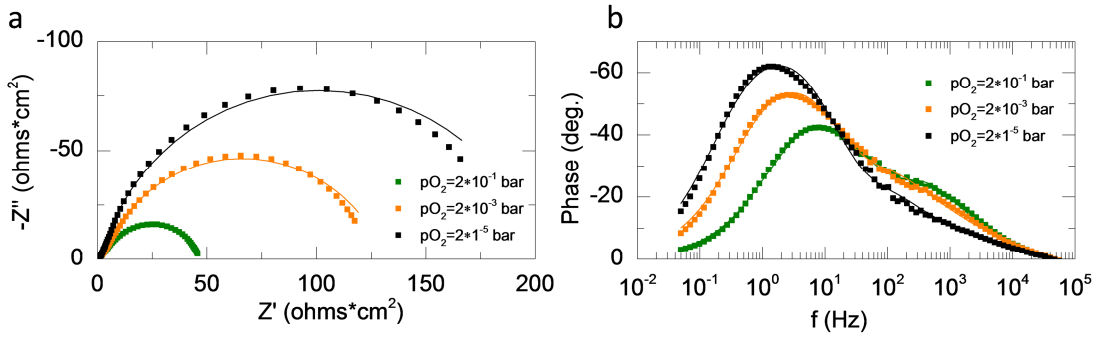

Figure 5.11 Nyquist (**a**) and Bode (**b**) representations of the impedance spectra measured in a 200 nm $LSM_{0.82}$ sample at different oxygen partial pressure and 948 K.

In order to quantitatively extract the dependence of the main transport parameters with pO_2, the fitting of the impedance spectra obtained at different pO_2 is carried out by employing the model presented in section **5.2.2**. **Figure 5.12** shows the change in oxygen diffusion for the LSM thin films with variable thickness as a function of the oxygen partial pressure at different temperatures. For comparison, **Figure 5.12** also includes data extracted from literature for bulk[3] and similar LSM layers.[13] As previously pointed out in section **5.2**, diffusion values several orders of magnitude higher than bulk references have been obtained in this study, also for different partial pressures, meaning that the EIS measurements are mainly governed by the GBs. Still, it should be noted that these samples presented values of diffusivity higher than the ones measured in the combinatorial analyses of the previous section (but still in line with the enhancement of

oxygen mass transport observed for B/A < 0.9). Moreover, the diffusion presents an approximately flat behavior varying the pO_2, with a calculated slope of the log-log plot m=-0.05 in the entire set of measurements. This evolution is significantly different to the one measured for Mn-rich LSM thin films by Fleig *et al.*,[3] suggesting different equilibrium mechanisms in the GBs of the Mn deficient layers prepared here.

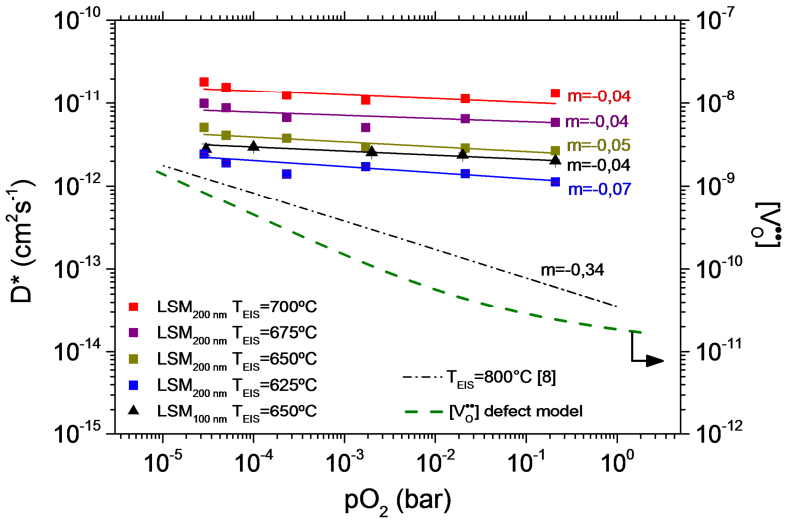

Figure 5.12 Partial pressure dependence of the ionic diffusion of the 200nm-thick $LSM_{0.82}$ sample at 625°C, 650°C, 675°C and 700°C and of the 100nm-thick sample at 650°C. Diffusion coefficient extrapolated from the conductivity measured for Mn-rich LSM thin films in literature is included for comparison.[3,13] The green dashed line shows the evolution of the oxygen vacancy concentration calculated by the defect model equilibrium at 650 ºC (see Appendix **C**).

In addition to the oxygen diffusivity, the behavior of the oxygen surface exchange coefficient k^q as a function of pO_2 was extracted from the impedance fitting, see **Figure 5.13**. The data exhibits a slope m ($k^q \propto pO_2^m$) equal to 0.17 at 700°C. By lowering the temperature, the slope continuously decreases. There is a strong discrepancy of these results with the slope values of m=0.49 usually found in the literature for the bulk material at 800°C [3]. In principle, the evolution of k^q with the pO_2 is strictly correlated with the nature of the oxygen involved in the rate-determining step (*rds*) of the oxygen incorporation on the MIEC surface. According to the literature, values of m higher than 0.5 are related to one or more molecular species (such as O_2^- or O_2^{2-}) while a slope of 0.5 is found for atomic species controlling the *rds* (O^-).[34] High vacancy and electron concentrations contribute to lower the slope, due to their general negative dependence,[35] leading to a value of $m \approx 0.25$ for a *rds* based on charge transfer mechanisms.[28,36] Even lower values of slope are ascribable to a nonlinear correlation between the oxygen surface coverage and the pO_2, since charged species at the surface can generate a potential step that decreases the partial pressure dependence of k^q.[37] This behavior is more evident at low temperatures, due to the higher oxygen chemisorption barrier. Therefore, the hereby observed unusually low P_{O2} dependence for LSM surface exchange coefficient is in good agreement with the possibility of a rate determining step involving monoatomic oxygen species (O^-).

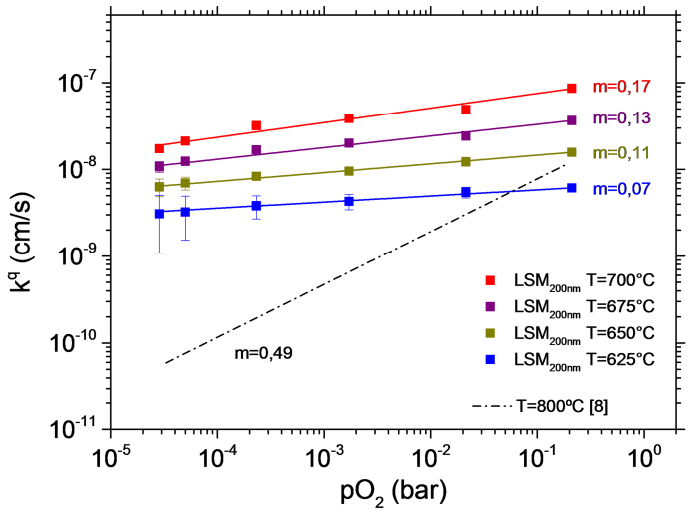

Figure 5.13 Partial pressure dependence of the surface exchange coefficient of a 200 nm-thick $LSM_{0.85}$ sample at 625°C, 650°C, 675°C and 700°C. Surface exchange extrapolated from Mn-rich thin films is included.[3]

5.4 Discussion

5.4.1 Diffusion in LSM_y GBs

Overall, the results obtained in this chapter support the theory that the GBs represent a preferential pathway for oxygen diffusion in polycrystalline LSM_y thin films for the entire compositional range analysed. In order to discuss the origin of this enhancement, it is convenient to recall the definition of oxygen diffusion in the case of oxygen vacancies as mobile dilute defects:[38]

$$D^* = f n_v D_v \qquad \text{Eq. 5.5}$$

Where f is the correlation factor, n_v the site fraction of oxygen vacancies ($n_v = [V_O^{\cdot\cdot}]/[O_O^x]$) and D_v the vacancy diffusion coefficient. This means that, in MIEC oxides, D^* is directly proportional to the concentration of oxygen vacancies, which, as shown in Chapter **1**, is controlled by the reduction equilibrium constant. Therefore, from **Eq. 5.5** it directly follows that the thermal activation energy of oxygen diffusion (ΔH_D) is composed by the sum of oxygen vacancy migration enthalpy (ΔH_m) and vacancy formation enthalpy (ΔH_f), as:

$$D^* = D_o \exp\left(\frac{\Delta H_D}{k_b T}\right) = D_o \exp\left(\frac{\Delta H_m + \Delta H_f}{k_b T}\right) \qquad \text{Eq. 5.6}$$

Where D_o is a pre-exponential factor taking into account the entropy terms and other material constants.

In light of the TEM observation (see Chapter **3**), it appears that the origin of the high oxygen diffusion in LSM GBs relies in the presence of oxygen vacancies near the interface, resulting in a preferential pathway for oxide-ion movement respect to the oxygen vacancy poor grain bulk. Although these defects are not usually mobile in the GB core of most of oxides,[10–12] one has to consider that in bulk LSM the total concentration of $V_O^{\cdot\cdot}$ is extremely low, suggesting that, even if less mobile, the $V_O^{\cdot\cdot}$ observed by TEM can still produce a substantial increase of diffusivity. Indeed, this observation was recently confirmed by Polfus *et al.*, who investigated by DFT the chemical composition and ionic diffusion of stoichiometric LSM GBs.[39] They found that in the GB core ΔH_f is lower than in the bulk, which leads to the generation of more $V_O^{\cdot\cdot}$ and an enhancement of the oxygen diffusion. Nevertheless, in their simulations no variations of cationic species near the interface were considered, contrary to our experimental observations (see Chapter **3**). In fact, the change of behaviour of oxygen mass transport properties measured for B/A ~ 0.9 (see **Figure 5.8a**) suggests that the different local nonstoichiometry observed (GB_{def} for B/A < 0.9 and GB_{rich} for B/A > 0.9) definitely plays a role influencing the electrochemical properties. According to this, and similarly to the study of in-plane electronic transport (see Chapter **4**),[9] two different compositional ranges with different defect chemistries can be discussed for LSM_y films.

In the samples characterized by GB_{def} (B/A < 0.9), the decrease of activation energy of oxygen diffusivity (**Figure 5.9**) suggests that the number of $V_O^{\cdot\cdot}$ stabilized in this type of interface is enhanced, as compared to GB_{rich}. Indeed, considering the definition of activation energy (**Eq. 5.6**) it should be noted that a change of activation energy necessarily means a change of either ΔH_m or ΔH_f. On one side, the vacancy migration enthalpy is not expected to be affected by the changes observed in the GBs, because, as commented before, the opposite behavior is usually found in the presence of charge defects (such as $V_{Mn}^{'''}$) .[10–12,40] Moreover, Polfus *et al.*[39] calculated that ΔH_m in these interfaces presents a value of almost 0.6 eV, which is lower than the total change of activation energy measured when decreasing B/A (~1 eV). Therefore, the observed trend suggests that the vacancy formation energy is dominating, being the lowest in the most Mn deficient sample (B/A = 0.85) and rapidly increasing when Mn is inserted in the structure. A constant value of ~2.6 eV is obtained when the local nonstoichiometry of the GB switches from GB_{def} to GB_{rich}.

Additionally, according to **Eq. 5.5**, the bulk oxygen diffusivity is expected to vary with the pO_2, since a change of oxygen chemical potential should modify the point defects equilibrium of the oxide, eventually leading to a large variation of the oxygen stoichiometry (depending on the defect chemistry of the material).[41] In particular, hyper-stoichiometric perovskite materials such as LSM should present a large increase of diffusivity by decreasing the pO_2 due to an increase of the oxygen vacancies concentration.[2,3] To better visualize this phenomenon, **Figure 5.12** also displays the variation of oxygen vacancy concentration calculated according to the defect model presented in Appendix **C** for T=650ºC. The observed change is consistent with the results obtained by Fleig *et al.* for Mn rich thin films,[3] but opposite to the behavior observed here for Mn-deficient LSM thin films. The low dependence found indicates that a high concentration of oxygen vacancies is already present in air in the GBs and that the change in pO_2 is not able to modify the equilibrium. This observation endorses the idea that the increase of availability of oxygen vacancies in the GBs is at the origin of the enhancement of oxygen diffusion. Moreover, together with the n-type behavior measured for Mn-deficient thin films in Chapter **4**, this observation suggests that a completely different equilibration mechanism is taking place in GB_{def}, as compared to the bulk. This behavior is clearly related to the complex local non-stoichiometry observed in these GBs in Chapter **3**, although the exact mechanism is still unknown.

Opposed to that, the samples characterized by GB_{rich} (B/A > 0.9) do not present any effect of bulk Mn content in the oxygen diffusion (see **Figure 5.8a**). Nevertheless, these interfaces still present an oxygen vacancy concentration higher than in the grain bulk, resulting in a remarkable increase of oxygen diffusivity having the origin on the reducing nature of the GBs. Despite the gradual accumulation of Mn occurring in GB_{rich} between B/A = 0.9 - 1.1, the diffusivity activation energy keeps constant, meaning that no sensitive modification of ΔH_m or ΔH_f takes place in this range.

5.4.2 ORR and incorporation in LSM_y GBs

Finally, in line with the obtained results, a reasonable ORR mechanism for LSM_y polycrystalline thin films is presented here. For this analysis, the work by Maier and co-workers is first considered.[42] In that study, they analysed the most favourable pathways for oxygen incorporation in bulk LSM by DFT calculations. They found that, for high pO_2, the vacancy approach to an absorbed O^- is the rate limiting step, leading to an overall activation energy comparable to the surface oxygen diffusion and a pO_2 dependence of $m<0.5$. According to this mechanism, the surface exchange reaction rate $\mathcal{R}$ is given by the following proportionality:

$$\mathcal{R} \propto k^q \propto c_v \cdot D_v \cdot \theta(O^-) \qquad \text{Eq. 5.7}$$

where c_v is the concentration of vacancies, D_v is the vacancy diffusion and $\theta(O^-)$ is the adsorbate coverage. Due to the high values of D_v even in bulk LSM ($\sim 10^{-7} cm^2/s$ at 700 ºC)[38] and a similar expected adsorbate coverage, the reaction rate will be mainly dependent on the change in the amount of available vacancies at the bulk surfaces.

In the samples characterized by GB_{def} (B/A < 0.9), we found a concordance between the activation energy of oxygen diffusion and of surface ORR (**Figure 5.9**), as well as a scarce partial pressure dependence (**Figure 5.13**). Both points match well with the mechanism proposed by Maier and co-workers for bulk materials.[42] Therefore, assuming this *rds*, it is likely that the enhancement of k^q measured here is due to the high concentration of mobile vacancies present in the grain boundaries, which would act as a sink for the oxygen adsorbed on the surface. This also goes in line with the progressive decrease of activation energy of k^q measured for B/A < 0.9, since in this region lowering Mn concentration generates a reduction of the vacancy formation energy and a consequent increase of GB oxygen vacancies. Hence, this mechanism seems to be perfectly transferable to the case of interface-dominated LSM thin films, see GB_{def} in **Figure 5.14**. In air, the oxygen will be rapidly adsorbed and dissociated near the grain boundary and then a vacancy will diffuse reaching the atomic O^- and finally incorporating it into the lattice. As it will be shown in Chapter **6**, this conclusion is endorsed by the study of Co substitution in $La_{0.8}Sr_{0.2}(Mn_{1-y}Co_y)_{0.85}O_{3\pm\delta}$ thin films.

In the samples characterized by GB_{rich} (B/A > 0.9), a progressive rise of k^q observed for an increase of B/A ratio (**Figure 5.8b**), although a non-clear trend was detected in the activation energy (**Figure 5.9b**). Moreover, the constant oxygen diffusion measured in this range suggest that GB_{rich} is not at the origin of this ORR enhancement but it is more likely due to an evolution of the surface upon Mn insertion. Indeed, one may observe that in the mechanism of **Figure 5.14,** the grain bulk surface may still play a role in the surface incorporation reactions, as long as it presents a concentration of oxygen vacancies high enough to allow fast surface oxygen diffusion. This effect seems to be more probable in Mn rich thin films, since it was found that MnO_2 termination layers presents 5 orders of magnitude more oxygen vacancies respect to (La,Sr)O ones (and

also to bulk LSM).[43] Therefore, we speculate that the increase of k^q measured for B/A > 0.9 may be due to a progressive enrichment of Mn in the surface that leads to an increase of oxygen vacancy concentration and, as consequence of Eq. **5.7**, an enhancement of the surface reaction rates (see GB_{rich} in **Figure 5.14**).

It is important to note that we cannot rule out a positive influence of the combinatorial approach in the presence of Mn terminated surfaces, especially for B/A > 1. Indeed, addition of simple metal oxides on MIEC perovskite surface is known to play an important role in the ORR properties.[44] For this reason, we performed in some of the samples a long-term annealing at 700 ºC for promoting a stabilization of the surface, before measuring again the electrochemical properties. As shown in **Figure 5.8**, we effectively noticed a worsening of the surface exchange coefficient, especially in the Mn-rich part, while the diffusion did not significantly vary. Nevertheless, we still observe a small improvement of k^q for B/A > 0.92 as well as a good match with results obtained in literature.[8]

Overall, the results suggest that the increase of ORR rates in LSM is strongly linked to the possibility of increasing the availability of oxygen vacancies, either by accumulation in the GBs or by surface modification.

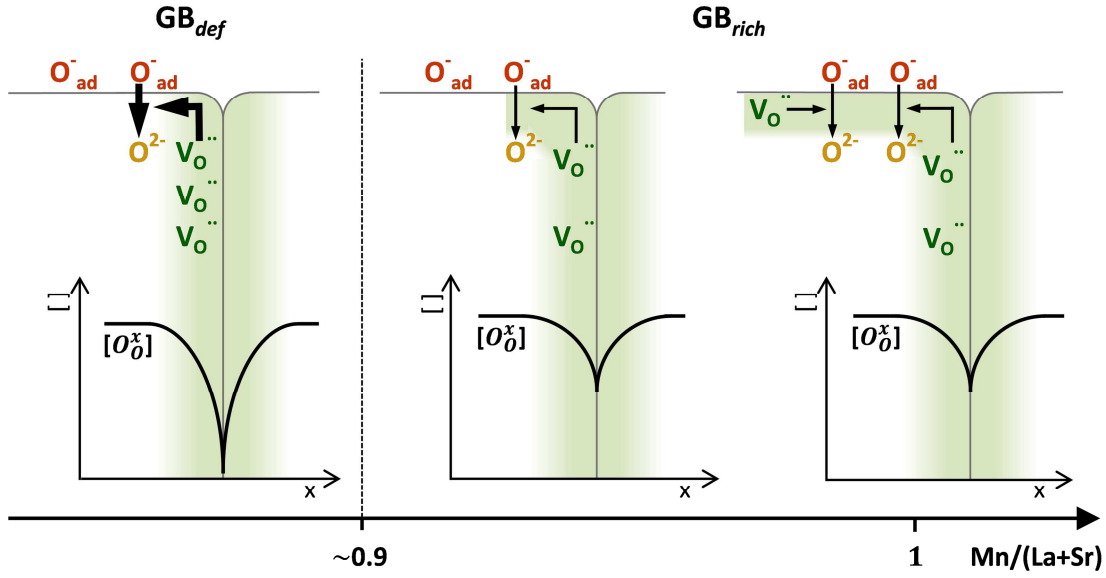

Figure 5.14 Sketch of the most probable ORR mechanism taking place near the GBs for different Mn contents. In GB_{def} the high concentration of oxygen vacancies in the GB assure fast oxygen incorporation. Passing from GB_{def} to GB_{rich} causes a decrease of GB oxygen vacancies, which reflects in a decrease of incorporation rate. Keeping increasing the Mn content, even if no further changes comes from the GBs, the surface becomes more active for ORR, leading to a gradual increase of k.

5.5 Conclusions

In this chapter, the high temperature oxygen electrochemical properties of dense polycrystalline thin films of $La_{0.8}Sr_{0.2}Mn_{1-y}O_{3\pm\delta}$ with B/A ratio ranging from 0.85 (Mn deficient) to 1.1 (La deficient films) have been studied by EIS. The oxygen mass transport properties (D^* and k^q) have been extracted from the impedance spectra using a physically-meaningful equivalent circuit fitting. The results show that the GBs dominate the electrochemical properties, leading to an enhancement of D^* and k^q respect to the bulk values for any B/A ratio measured. Moreover, varying the Mn content in polycrystalline LSM_y thin films has a notable impact on both diffusion and ORR phenomena. Two different behaviours were found to take place in the two GB types observed in Chapter **3.**

In the thin films characterized by GB_{def} (B/A < 0.9), D^* and k^q were found to steeply increase when decreasing the Mn content. The origin of this change was found to be a simultaneous decrease of both activation energies, indicating a strong interdependence between the two phenomena. Moreover, the diffusion coefficient was found to be nearly constant with the pO_2, suggesting that a high concentration of oxygen vacancies is already present in air and not easily modifiable by change in the oxygen chemical potential. These observations, together with the GB oxygen deficiency observed by TEM in Chapter **3**, support the hypothesis that the accumulation of oxygen vacancies is at the origin of both the large improvements of D^* and k^q. In this sense, an oxygen incorporation model has been proposed. According to it, the GBs act as a sink providing $V_O^{\cdot\cdot}$ to the surface where the reduction of oxygen adsorbate species takes place. Finally, this analysis shows the possibility of further increasing the GB oxygen diffusivity (and therefore the oxygen vacancy concentration) by decreasing the overall Mn content, probably interrelated to the local decrease in Mn content in GB_{def} and subsequent presence of negative defects such as Mn vacancies ($V_{Mn}^{''''}$) to compensate the high concentration of $V_O^{\cdot\cdot}$ (see Chapter **3**).

In the thin films characterized by GB_{def} (B/A > 0.9), while D^* was observed to be independent of B/A, a gradual increase of k^q was measured rising the Mn content up to B/A = 1.1. The flat behaviour of oxygen diffusion indicate that no further variation of GB oxygen vacancy concentration takes place in this range, despite the evolution observed in the cationic species (progressive increase of Mn and decrease of La, see Chapter **3**). This also suggests that the increase of k^q is related to an evolution of the thin films surface upon the Mn insertion, rather than a direct effect of the GB composition.

Overall, the results demonstrate the possibility of actively engineering the electrochemical properties of LSM_y polycrystalline thin films by modifying their cationic composition.

References

1. Adler, S. B. Factors governing oxygen reduction in solid oxide fuel cell cathodes. *Chem. Rev.* **104,** 4791–4843 (2004).
2. De Souza, R. A. De, Kilner, J. A. & Walker, J. F. A SIMS study of oxygen tracer diffusion and surface exchange in $La_{0.8}Sr_{0.2}MnO_{3+\delta}$. *Mater. Lett.* **43,** 43–52 (2000).
3. Fleig, J., Kim, H.-R., Jamnik, J. & Maier, J. Oxygen Reduction Kinetics of Lanthanum Manganite (LSM) Model Cathodes: Partial Pressure Dependence and Rate-Limiting Steps. *Fuel Cells* **8,** 330–337 (2008).
4. Poulsen, F. Defect chemistry modelling of oxygen-stoichiometry, vacancy concentrations, and conductivity of $(La_{1-x}Sr_x)_yMnO_{3+\delta}$. *Solid State Ionics* **129,** 145–162 (2000).
5. Hammouche, A., Siebert, E., Hammou, A. & Kleitz, M. Electrocatalytic Properties and Nonstoichiometry of the High Temperature Air Electrode $La_{1-x}Sr_xMnO_3$. *J. Electrochem. Soc.* **138,** 1212 (1991).
6. Siebert, E., Hammouche, A. & Kleitz, M. Impedance spectroscopy analysis of $La_{1-x}Sr_xMnO_3$-yttria-stabilized zirconia electrode kinetics. *Electrochim. Acta* **40,** 1741–1753 (1995).
7. Saranya, A. M. *et al.* Engineering Mixed Ionic Electronic Conduction in $La_{0.8}Sr_{0.2}MnO_{3+\delta}$ Nanostructures through Fast Grain Boundary Oxygen Diffusivity. *Adv. Energy Mater.* **5,** 1500377 (2015).
8. Navickas, E. *et al.* Fast oxygen exchange and diffusion kinetics of grain boundaries in Sr-doped $LaMnO_3$ thin films. *Phys. Chem. Chem. Phys.* **17,** 7659–7669 (2015).
9. Saranya, A. M. A. M. *et al.* Unveiling the Outstanding Oxygen Mass Transport Properties of Mn-Rich Perovskites in Grain Boundary-Dominated $La_{0.8}Sr_{0.2}(Mn_{1-x}Co_x)_{0.85}O_{3\pm\delta}$ Nanostructures. *Chem. Mater.* **30,** 5621–5629 (2018).
10. Waldow, S. P. & De Souza, R. A. Computational Study of Oxygen Diffusion along a [100] Dislocations in the Perovskite Oxide $SrTiO_3$. *ACS Appl. Mater. Interfaces* **8,** 12246–12256 (2016).
11. Marrocchelli, D., Sun, L. & Yildiz, B. Dislocations in $SrTiO_3$: Easy to Reduce but Not so Fast for Oxygen Transport. *J. Am. Chem. Soc.* **137,** 4735–4748 (2015).
12. Sun, L., Marrocchelli, D. & Yildiz, B. Edge dislocation slows down oxide ion diffusion in doped CeO_2 by segregation of charged defects. *Nat. Commun.* **6,** 6294 (2015).
13. Usiskin, R. E., Maruyama, a S., Kucharczyk, b C. J., Takeuchib, a I. & Haile, S. M. Probing the reaction pathway in $(La_{0.8}Sr_{0.2})_{0.95}MnO_{3+\delta}$ using libraries of thin film microelectrodes. *J. Mater. Chem. A* **3,** 19330–19345 (2015).
14. Aydin, H., Korte, C. & Janek, J. 18O-tracer diffusion along nanoscaled Sc_2O_3/yttria stabilized zirconia (YSZ) multilayers: On the influence of strain. *Sci. Technol. Adv. Mater.* **14,** (2013).
15. Boukamp, B. A., Hildenbrand, N., Bouwmeester, H. J. M. & Blank, D. H. A. Impedance of thin film cathodes: Thickness and current collector dependence. *Solid State Ionics* **283,** 81–90 (2015).
16. Chueh, W. C. & Haile, S. M. Electrochemistry of mixed oxygen ion and electron conducting electrodes in solid electrolyte cells. *Annu Rev Chem Biomol Eng* **3,** 313–341 (2012).
17. Gerstl, M. *et al.* The separation of grain and grain boundary impedance in thin yttria

stabilized zirconia (YSZ) layers. *Solid State Ionics* **185,** 32–41 (2011).

18. Ahamer, C., Opitz, A. K., Rupp, G. M. & Fleig, J. Revisiting the Temperature Dependent Ionic Conductivity of Yttria Stabilized Zirconia (YSZ). *J. Electrochem. Soc.* **164,** F790–F803 (2017).

19. Jamnik, J. & Maier, J. Generalised equivalent circuits for mass and charge transport: chemical capacitance and its implications. *Phys. Chem. Chem. Phys.* **3,** 1668–1678 (2001).

20. Lai, W. & Haile, S. M. Impedance Spectroscopy as a Tool for Chemical and Electrochemical Analysis of Mixed Conductors: A Case Study of Ceria. *J. Am. Ceram. Soc.* **88,** 2979–2997 (2005).

21. Boukamp, B. A., Hildenbrand, N., Bouwmeester, H. J. M. & Blank, D. H. A. Impedance of thin film cathodes: Thickness and current collector dependence. *Solid State Ionics* **283,** 81–90 (2015).

22. Chen, D., Bishop, S. R. & Tuller, H. L. Non-stoichiometry in Oxide Thin Films: A Chemical Capacitance Study of the Praseodymium-Cerium Oxide System. *Adv. Funct. Mater.* **23,** 2168–2174 (2013).

23. Schmid, A., Rupp, G. M. & Fleig, J. Voltage and partial pressure dependent defect chemistry in (La,Sr)$FeO_{3-\delta}$ thin films investigated by chemical capacitance measurements. *Phys. Chem. Chem. Phys.* **20,** 12016–12026 (2018).

24. Jamnik, J. & Maier, J. Treatment of the Impedance of Mixed Conductors Equivalent Circuit Model and Explicit Approximate Solutions. *J. Electrochem. Soc.* **146,** 4183 (1999).

25. Bisquert, J., Garcia-Belmonte, G., Fabregat-Santiago, F. & Bueno, P. R. Theoretical models for ac impedance of finite diffusion layers exhibiting low frequency dispersion. *J. Electroanal. Chem.* **475,** 152–163 (1999).

26. Maier, J. On the correlation of macroscopic and microscopic rate constants in solid state chemistry. *Solid State Ionics* **112,** 197–228 (1998).

27. Ishigaki, T., Yamauchi, S., Kishio, K., Mizusaki, J. & Fueki, K. Diffusion of oxide ion vacancies in perovskite-type oxides. *J. Solid State Chem.* **73,** 179–187 (1988).

28. Chueh, W. C., Lai, W. & Haile, S. M. Electrochemical behavior of ceria with selected metal electrodes. *Solid State Ionics* **179,** 1036–1041 (2008).

29. De Souza, R. A. & Kilner, J. a. Oxygen transport in $La_{1-x}Sr_xMn_{1-y}Co_yO_{3\pm\delta}$ perovskites: Part II. Oxygen surface exchange. *Solid State Ionics* **126,** 153–161 (1999).

30. Saranya, A. M. *et al.* Engineering Mixed Ionic Electronic Conduction in $La_{0.8}Sr_{0.2}MnO_{3+\delta}$ Nanostructures through Fast Grain Boundary Oxygen Diffusivity. *Adv. Energy Mater.* **5,** 1500377 (2015).

31. Januschewsky, J., Ahrens, M., Opitz, A., Kubel, F. & Fleig, J. Optimized $La_{0.6}Sr_{0.4}CoO_{3-\delta}$ thin-film electrodes with extremely fast oxygen-reduction kinetics. *Adv. Funct. Mater.* **19,** 3151–3156 (2009).

32. Fleig, J. *et al.* The Chemical Capacitance as a Fingerprint of Defect Chemistry in Mixed Conducting Oxides. *Acta Chim. Slov.* 509–518 (2016). doi:10.17344/acsi.2016.2302

33. Nowotny, J. & Rekas, M. Defect Chemistry of (La,Sr)MnO_3. *J. Am. Ceram. Soc.* **81,** 67–80 (1998).

34. Wang, L., Merkle, R., Mastrikov, Y. a., Kotomin, E. a. & Maier, J. Oxygen exchange kinetics on solid oxide fuel cell cathode materials—general trends and their mechanistic interpretation. *J. Mater. Res.* **27,** 2000–2008 (2012).

35. De Souza, R. a. A universal empirical expression for the isotope surface exchange coefficients (k*) of acceptor-doped perovskite and fluorite oxides. *Phys. Chem. Chem. Phys.* **8,** 890–897 (2006).

36. Jung, W. & Tuller, H. L. A New Model Describing Solid Oxide Fuel Cell Cathode Kinetics: Model Thin Film SrTi1-xFexO3-δ Mixed Conducting Oxides–a Case Study. *Adv. Energy Mater.* **1,** 1184–1191 (2011).

37. Fleig, J., Merkle, R. & Maier, J. The p(O2) dependence of oxygen surface coverage and exchange current density of mixed conducting oxide electrodes: model considerations. *Phys. Chem. Chem. Phys.* **9,** 2713–2723 (2007).

38. De Souza, R. & Kilner, J. a. Oxygen transport in $La_{1-x}Sr_xMn_{1-y}Co_yO_{3\pm\delta}$ perovskites Part I. Oxygen tracer diffusion. *Solid State Ionics* **106,** 175–187 (1998).

39. Polfus, J. M., Yildiz, B. & Tuller, H. L. Origin of Fast Oxide Ion Diffusion along Grain Boundaries in Sr-doped $LaMnO_3$. *Phys. Chem. Chem. Phys.* **20,** 19142–19150 (2018).

40. Arora, G. & Aidhy, D. Segregation and Binding Energetics at Grain Boundaries in Fluorite Oxides. *J. Mater. Chem. A* 4026–4035 (2017). doi:10.1039/C6TA09895A

41. Yokokawa, H. *Perovskite Oxide for Solid Oxide Fuel Cells*. *Perovskite Oxide for Solid Oxide Fuel Cells* (Springer US, 2009). doi:10.1007/978-0-387-77708-5

42. Mastrikov, Y. A., Merkle, R., Heifets, E., Kotomin, E. A. & Maier, J. Pathways for oxygen incorporation in mixed conducting perovskites: A DFT-based Mechanistic analysis for (La, Sr)$MnO_{3-\delta}$. *J. Phys. Chem. C* **114,** 3017–3027 (2010).

43. Mastrikov, Y. a., Merkle, R., Kotomin, E. A., Kuklja, M. M. & Maier, J. Surface termination effects on oxygen reduction reaction rate at fuel cell cathodes. *J. Mater. Chem. A* (2018). doi:10.1039/C8TA02058B

44. Mutoro, E., Crumlin, E. J., Biegalski, M. D., Christen, H. M. & Shao-Horn, Y. Enhanced oxygen reduction activity on surface-decorated perovskite thin films for solid oxide fuel cells. *Energy Environ. Sci.* **4,** 3689 (2011).

6. The effect of Co substitution on $La_{0.8}Sr_{0.2}(Mn_{1-y}Co_y)_{0.85}O_{3\pm\delta}$ functional properties

6.1 Introduction

In the previous chapters, the great enhancement of oxygen mass transport properties in LSM_y grain boundaries (GBs) was attributed to a local oxygen deficiency near these interfaces, which provides a direct pathway for oxygen diffusion and incorporation. Moreover, it was shown that, by tuning the overall cationic content in the thin films, it is possible to further modify the concentration of vacancies in the GBs, giving rise to the best electrochemical performances for the most Mn deficient thin films. Nevertheless, a generalization of the enhancement of mass transport properties of MIEC oxides at the grain boundary level is far from being fully established since, as commented before, the opposite behaviour is usually found in other complex oxides.[1–4] In order to evaluate whether the GB engineering approach is limited to LSM, it is of particular interest to understand if the enhancement occurring in materials with low ionic conductivity is also happening in materials showing reasonably good mass transport properties at the bulk level. This can be rationally done by studying the effect of a high density of grain boundaries in the mass transport properties of a material system with tuneable oxygen diffusivity and surface exchange. In this direction, it is well known that the substitution of Mn by Co in the $La_{0.8}Sr_{0.2}Mn_{1-y}Co_yO_{3\pm\delta}$ (LSMC) perovskite promotes significant changes in the oxygen mass transport properties converting a mainly electronic conductor, such as the oxygen hyper-stoichiometric LSM, into a reasonably good MIEC, such as the oxygen deficient perovskite $La_{0.8}Sr_{0.2}CoO_{3-\delta}$ (LSC).[5,6] Nevertheless, it is unknown how the GBs behaves in this system, whether they still represent a preferential pathway for oxygen, such as in the LSM case,[7,8] or they hinder the oxygen diffusion, such in the case of $SrTiO_3$.[1,2]

In order to answer this interesting question, a thin film binary system $La_{0.8}Sr_{0.2}(Mn_{1-y}Co_y)_{0.85}O_{3\pm\delta}$ ($y \approx 0$ to 1) was grown by using combinatorial Pulsed Laser Deposition (C-PLD), on top of a 4" Si-based wafer. After proving the high quality of the films, with fully dense and columnar-type nanostructures as required for accurate oxygen diffusion characterization, we show the evolution of the mass transport properties as a function of the cobalt contenct, directly measured by O^{18} Isotope Exchange Depth Profiling coupled to Time of Flight Secondary Ion Mass Spectroscopy (IEDP-ToF-SIMS). The relevant bulk and grain boundary oxygen diffusion and surface exchange coefficients (D^*, k^*) were quantified by numerical simulations of the obtained diffusion profiles, for different temperatures and cobalt contents. By comparing both sets of mass transport coefficients, we clearly prove an independent behaviour of the grain boundary transport properties and the bulk ones. The electronic conduction properties of the LSMC family were also measured, revealing the impact of GBs especially in the Mn-rich LSMC compounds. Finally, by comparing the results obtained here and in the previous chapters, the crucial role of the Mn sub-lattice coupled with the presence of a high amount of oxygen vacancies at the grain boundary level is exposed.

6.2 Deposition and structural properties of LSMC thin films

In order to study the transport properties in nanostructured $La_{0.8}Sr_{0.2}(Mn_{1-y}Co_y)_{0.85}O_{3\pm\delta}$ (y = 0 - 0.8), a real continuous compositional-spread LSMC system was deposited in thin film form by combinatorial Pulsed Laser Deposition (C-PLD).[9–17] The employed combinatorial PLD approach is based on the superposition of large-area films of two parent compounds, i.e. LSM and LSC, centred at opposite sides of a 4" wafer substrate (see more details of the C-PLD deposition method in Chapter **2**). The different thickness of the LSM and LSC layers along the wafer defines the relative Co:Mn content, namely the composition of the final LSMC layer at each position. This *in-situ* synthesis of the LSMC compound by inter-diffusion of Mn and Co cations was achieved by depositing very thin individual alternate LSM and LSC layers at high substrate temperatures (T = 700ºC).[18–20]

The characterization of the compositional variation between the parent compound plumes was carried out with the same approach adopted in the case of LSM_y combinatorial films (see Chapter **3.3**). First, a detailed analysis of the shape of the parent compound patterns and their overlapping as a function of plumes' thicknesses and relative distance (d) was carried out in a previous work.* The analysis revealed the optimized conditions in order to obtain a reasonable thickness of the LSCM layer (from 80 to 175 nm) and a low Co-content gradient. Then, the final LSMC combinatorial sample covering the whole range of compositions ($La_{0.8}Sr_{0.2}(Mn_{1-y}Co_y)_{0.85}O_{3\pm\delta}$; $y \approx 0$ to 1) was grown on a 4-inch (100)-oriented Si wafer covered with a 100-nm thick yttria-stabilized zirconia (YSZ) layer (**Figure 6.1a**). The thickness distribution along the central axis of the LSMC combinatorial sample was studied by Scanning Electron Microscopy (SEM) and ellipsometry, showing good agreement with the thickness distribution predicted from the parent layer superposition study (**Figure 6.1b**). Additionally, the composition distribution along the central axis was studied by Energy Dispersive Spectroscopy (EDS) and Wavelength Dispersive Spectroscopy (WDS), see **Figure 6.1c**. The atomic percentage of Mn and Co cations follows a Gaussian distribution along the central axis (similarly to the thickness) showing a good agreement with the predicted values. A constant value of B/A = 0.85 ± 0.03 is obtained independently on the wafer position, mainly due to the plasma-background interactions at intermediate deposition pressures (consistent with the results discussed in Chapter **3.2** for LSM thin films).[21,22] Instead, the atomic percentage of A-site cations (La and Sr) was measured to be close to the nominal percentage of 80:20 for La:Sr in any position of the wafer.

*The compositional and structural measurements of LSMC combinatorial thin films (XRD, SEM, EDS, WDS, AFM) were carried out by Dr. Saranya A. M. in the framework of her thesis. The results have been included in this thesis for completeness.[55]

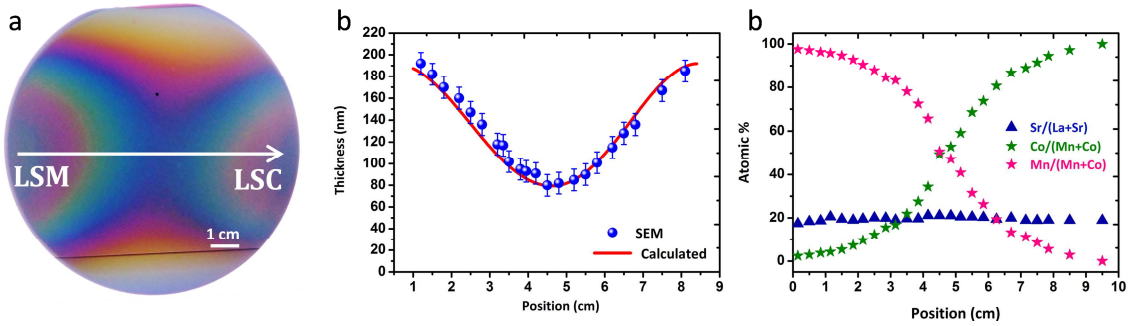

Figure 6.1a, top-view image of the as-prepared LSMC pseudo-binary system at wafer level. Thickness (**b**) and composition (**c**) along the central axis of the combinatorial sample obtained by SEM and WDS techniques, respectively. The calculated thickness in (**b**) refers to the superposition of the thickness profiles obtained for the individual parent compound layers (LSM and LSC plumes).

A comprehensive structural and microstructural characterization of the combinatorial sample was carried out by various experimental techniques. The series of XRD patterns acquired along the central axis of the LSMC combinatorial sample (corresponding to a predicted increment of the Co concentration from y = 0.03 to y = 0.94) show single phase deposition of polycrystalline YSZ and LSMC layers (**Figure 6.2a**). A shift of the perovskite peaks to higher angles was observed by increasing the Co doping concentration, in agreement with the shrinkage of the unit cell volume due to a continuous decrease of the lattice parameter as a function of the Co-content from approximately a_{pc}=3.90 Å to 3.84 Å (where a_{pc} refers to the pseudo-cubic lattice), see **Figure 6.2b**.[23–25] This decrease is generally ascribed to the smaller average ionic radius of Co^{3+} (0.61 Å) compared to Mn^{3+} (0.645 Å). A change in peak intensity is observed when increasing the Co concentration (increase of the l00 reflections and decrease of the 111 and 211 reflections). This variation might be related to a preferential orientation appearing when increasing the Co content.

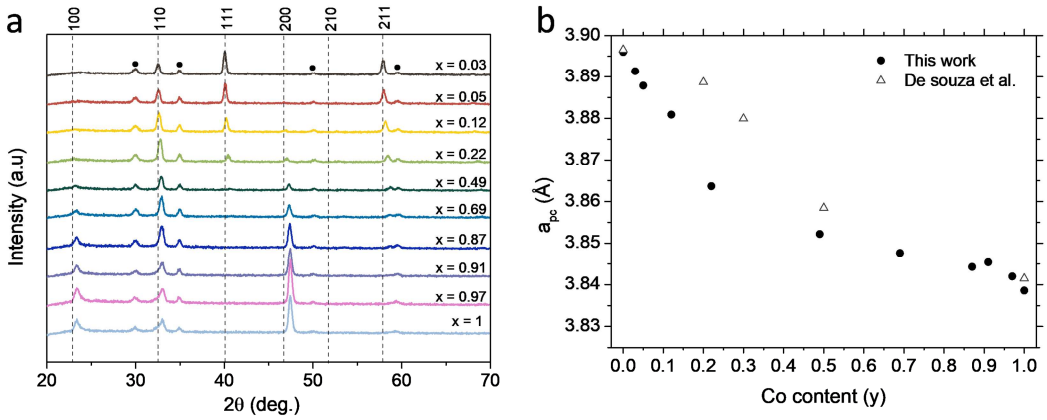

Figure 6.2 a, XRD patterns of the LSMC system as a function of the Co-content. The vertical dashed lines corresponds to the position of the pseudo-cubic diffraction peaks of bulk LSM ($a_{pc,LSM}$ = 3.89 Å). **b**, Pseudo-cubic lattice parameter for the LSMC system obtained by XRD. Values from De Souza et al.[5,6] for bulk LSMC samples are presented for comparison.

Cross-section and top view SEM (**Figure 6.3**) demonstrate a full dense columnar-type microstructure with grain sizes in the nanoscale (20 – 50 nm) for the LSMC film. Low-magnification SEM surface images (**Figure 6.4**) show the formation of cracks for Co-rich compositions with y > 0.8, limiting the current diffusion study to the range of compositions with y < 0.8.

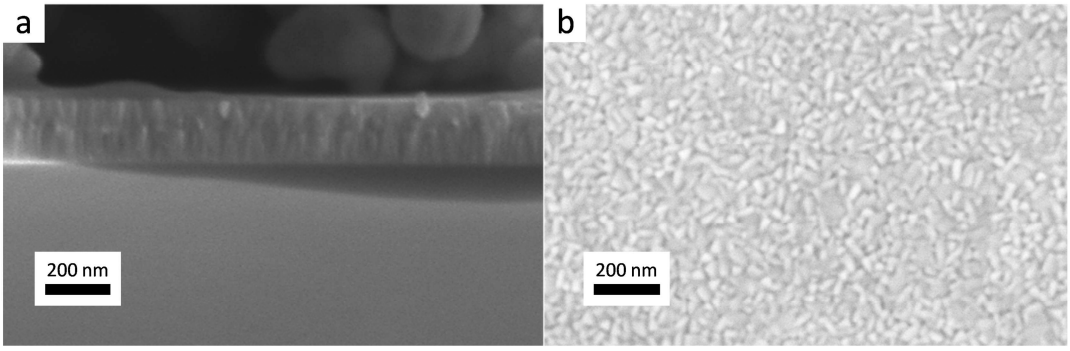

Figure 6.3 Typical cross-section (**a**) and top-view (**b**) SEM images of the LSMC layer (~50% Co). The cross-section shows a columnar-like structure for the YSZ and LSMC layers.

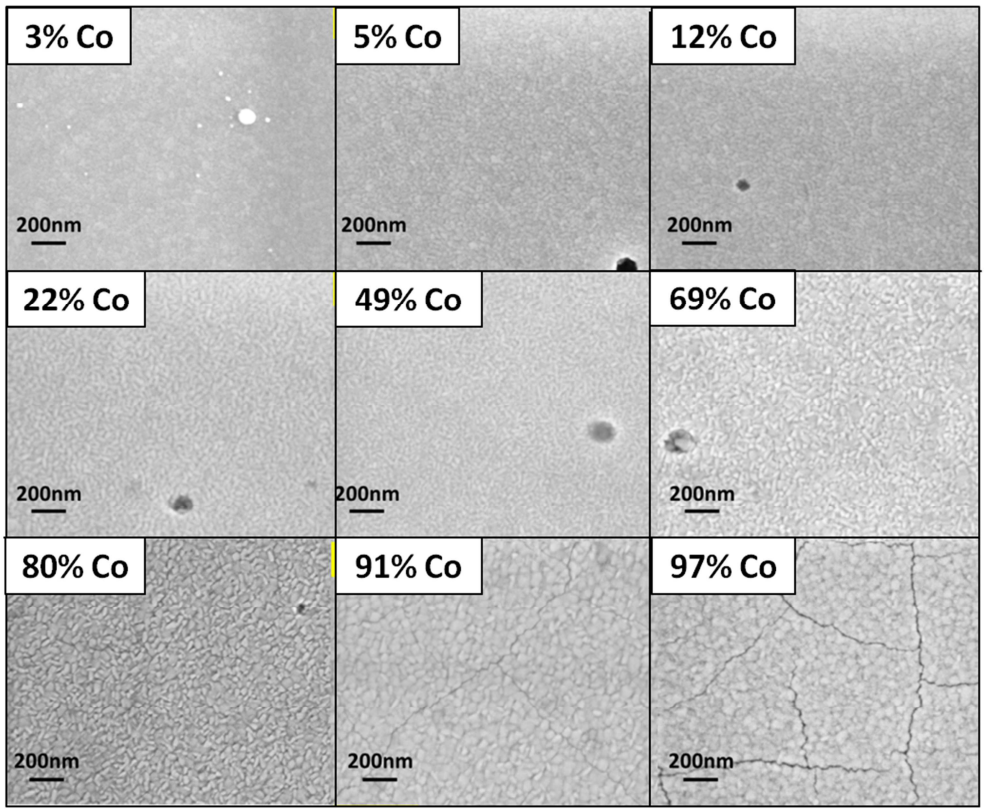

Figure 6.4 SEM top-view images of the LSMC layer for different Co contents. Above y = 0.80, the layer present crack formation.

The grain size in the LSMC combinatorial sample was measured by SEM and confirmed by atomic force microscope (AFM). A morphological evolution was observed in the Co-rich part of LSMC thin films, consisting of a variation of grain size from 20 to 50 nm and surface roughness from 1.5 to 2.7 nm (see **Figure 6.5**).

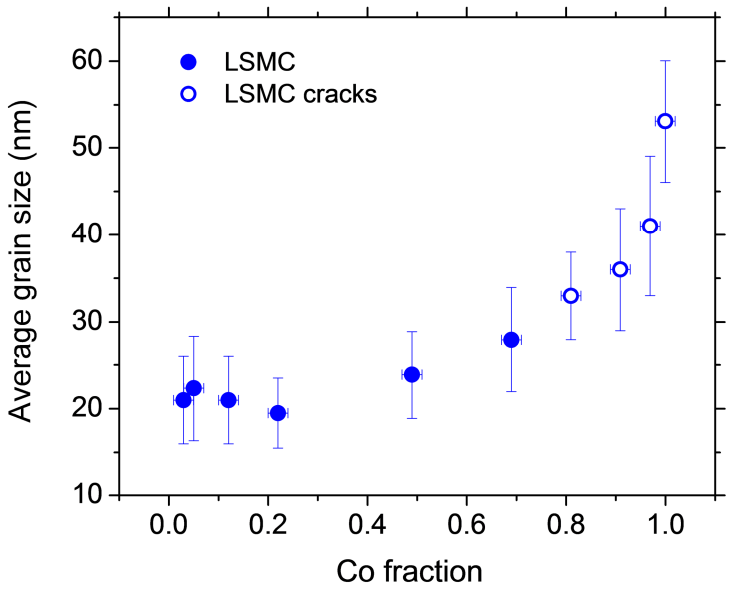

Figure 6.5. Average grain size estimated from SEM and AFM images plotted against the Co fraction.

Overall, the thin film morphology and microstructure in the range y = 0 – 0.8 was found to be suitable for the study of bulk and GBs functional properties in the LSMC system as a function of Co content.

6.3 Oxygen mass transport properties of LSMC thin films

6.3.1 IEDP-SIMS measurements

The oxygen transport in LSMC thin films was examined by mapping the combinatorial sample using IEDP-ToF-SIMS.[26,27] The parameters acquired from IEDP-SIMS are typically the oxygen self-diffusion coefficient (D^*) and the oxygen surface exchange coefficient (k^*). In order to determine these oxygen transport parameters for the LSMC system, IEDP-ToF-SIMS experiments were carried out at 600 and 700 ºC. The sputter-time was converted into depth using thickness values of the films measured by SEM. The ^{18}O and ^{16}O secondary ions measured allowed calculating the ^{18}O isotopic fraction as a function of the distance to the top surface, $C'(x)$, corrected for the background isotope fraction (C'_{bckg}) and normalized to the ^{18}O concentration of the exchange gas (C'_g)[†] (see Chapter **2** for more information).

The obtained set of normalized isotopic fraction profiles for the whole range of compositions studied for 700 ºC and 600ºC are presented in **Figure 6.6a** and **b**, respectively. Since similar exchange times (1250 - 1500 s) were employed for all experiments, higher isotopic concentrations and flatter diffusion profiles are roughly correlated to better oxygen mass transport properties. Accordingly, it is clear from **Figure 6.6** that increasing the cobalt content and temperature leads to an enhancement of the oxygen diffusion and exchange. In fact, at 700 °C the samples with high Co fractions above 0.6 were fully saturated in ^{18}O isotope. Because of that, the samples corresponding to the Co-rich range (between y =0.6 and 0.8) were analysed at a lower temperature of 600 ºC.s

[†] IEDP-SIMS experiments were carried out at Imperial College London (UK) by Dr. M. Burriel and Dr. A. Cavallaro.

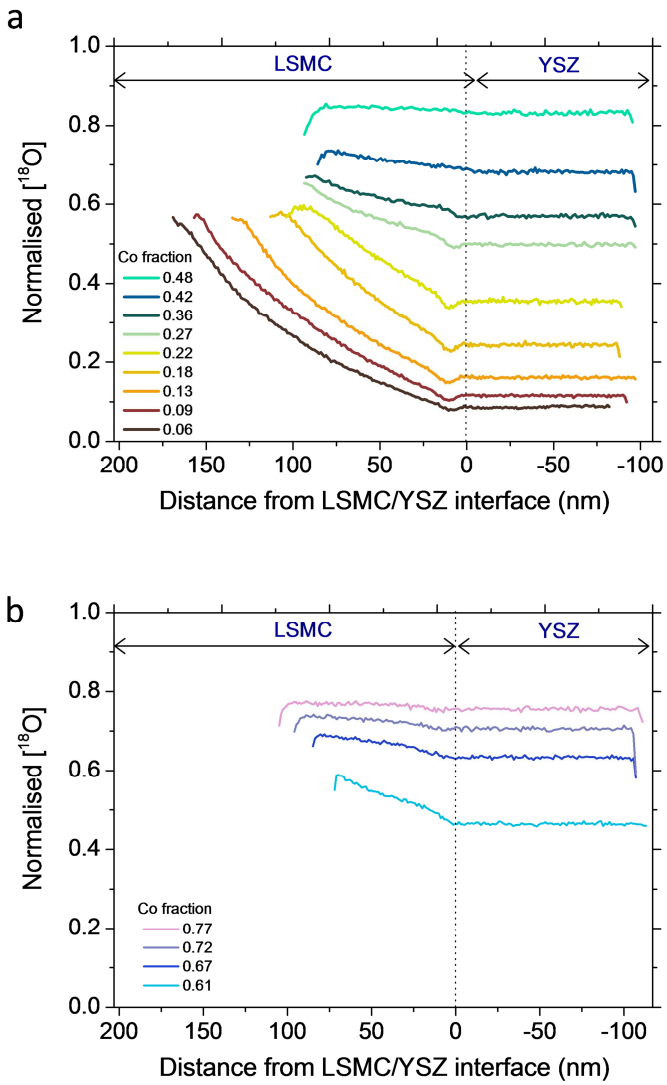

Figure 6.6 Normalized ^{18}O isotopic fraction depth profile obtained in LSMC/YSZ bilayers deposited on silicon substrates as obtained by IEDP-ToF-SIMS measurement. The x-axis represents the distance from the LSMC/YSZ interface. Note that thickness of the LSMC film changes with the Co fraction, derived from the C-PLD deposition procedure. Isotope exchange temperatures of (**a**) 700 °C and (**b**) 600 °C are represented for different cobalt fractions.

Similarly to what was previously reported by Saranya *et al.* for LSM thin films,[8] the shape of the oxygen diffusion profiles indicates that LSMC is not a homogeneous medium. Indeed, especially in the Mn-rich compositions, the concentration profiles present deep-penetrating diffusion tails and a step at the LSMC/YSZ interface which are not compatible with the profiles expected for a simple two slabs diffusion (see **Figure 6.7a** and **c** for the characteristic concentration distributions simulated for homogenous layers). A higher isotopic concentration in the YSZ thin films without accumulation in the LSMC layer suggests the existence of two different pathways for oxygen diffusion, one fast and narrow and the other slow and wide. To illustrate this, a 2D FEM model of a bilayer presenting this heterogenous distribution of diffusivities in the top layer was considered (see **Figure 6.7b** and **d**). As it can be observed in the figure, this simple model is already able to catch the characteristic features of the LSMC diffusion profiles.

For low exchange times (t_1) two different slopes are visible in **Figure 6.7d**, corresponding to the oxygen diffusion processes of the fast and slow pathways, while increasing the exchange time, the two slopes tends to merge. Also, the experimental step observed at the YSZ interface is clearly reproduced here. It is important to note that this depletion in oxygen concentration cannot be associated to an interface additional resistance, which, on the contrary, would originate an accumulation of concentration species.

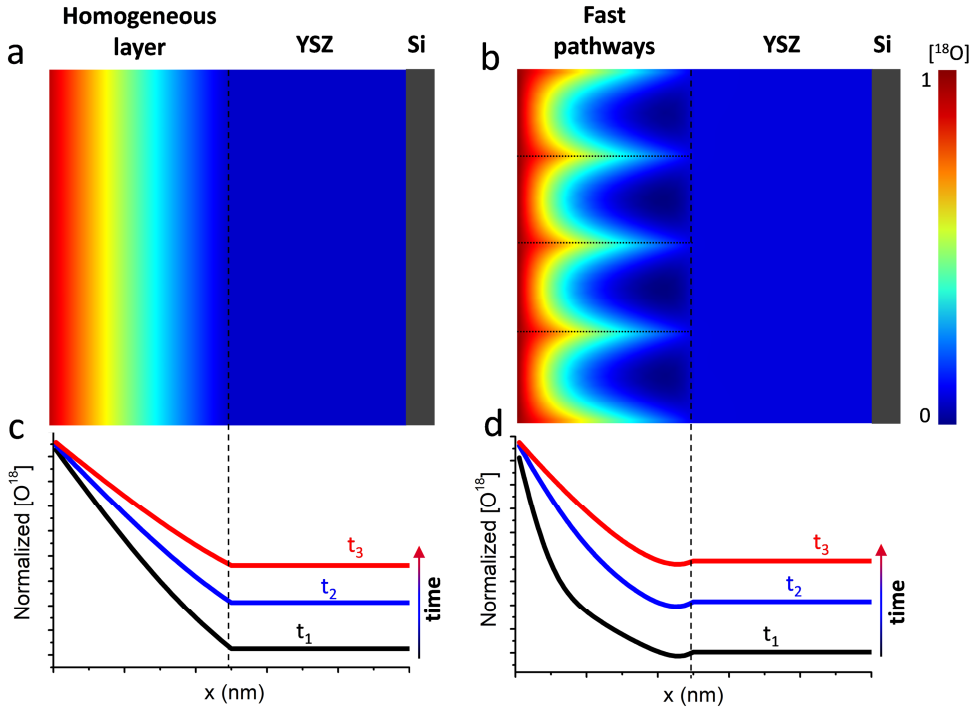

Figure 6.7 Examples of simulations of oxygen diffusion distributions for a homogenous layer (**a** and **c**) and a heterogeneous layer with fast narrow pathways in parallel to thick slow ones (**b** and **d**). In both configurations, the YSZ is considered as an oxygen sink and the Si interface as oxygen blocking. The effect of increasing exchange time ($t_1<t_2<t_3$) on the oxygen averaged profiles is shown in **c** and **d** for the homogenous and fast pathway case, respectively.

Due to the columnar structure of the thin films, these fast pathways are probably originated by the GBs, already suggesting that their superior oxygen diffusivity can be extended from LSM[8,7] to LSMC thin films. Nevertheless, since analytical solutions are not available for diffusion in such a heterogeneous bilayer thin film, numerical FEM modelling was used to fit the oxygen isotope diffusion profiles of the LSMC/YSZ bilayer and to extract the oxygen transport parameters along the bulk and grain boundaries of the LSMC film.

6.3.2 3-D FEM model of bulk and GB contributions

A 3D FEM model was developed to fit the oxygen profiles of LSMC/YSZ films. The geometry of the FEM model consisted of a columnar cell made of four-half grains separated by 1 nm thick GB (see Chapter **2** for further information about the model).

The average grain size values and thickness measured by SEM and AFM were used for the construction of the different geometries for the different compositions. The free parameters in the fitting were the bulk and GB diffusion and surface exchange coefficient (*i.e.* D_b^*, D_{gb}^* and k_b^*, k_{gb}^*). The use of two surface coefficients was necessary to properly reproduce the curves, similarly to the LSM case.[7,8] The YSZ diffusion coefficient was fixed to the literature value since it can be considered an oxygen sink in the range of temperatures and thicknesses under study ($D^* = 3 \cdot 10^{-8} cm^2 s^{-1}$).[28] Previously reported values of the bulk coefficients for the whole range of cobalt content[5,6] were employed as a starting point for the fitting. For the grain boundary, manually adjusted values of diffusion and exchange coefficients (D_{gb}^* and k_{gb}^*) were used to approach to the experimental profiles. Then, a matrix of solutions was simulated varying all the parameters to find the best fitting, which was evaluated by the total sum of errors. As an example, the oxygen isotope profile simulated for a LSMC/YSZ bilayer with 6% Co (y = 0.06) is given in **Figure 6.8a**. The simulated profile is in good agreement with the experimental one, confirming that the FEM model could fit the different regions of the experimental measure. In this figure, the best fitted solution obtained by FEM model of homogenous LSMC/YSZ bilayer is also shown. The comparison between this solution and the experimental values clearly prove that fast diffusion GBs are necessary to reproduce the oxygen profile. In this sense, the 3D isotopic concentration maps generated by simulation after fitting the mass transport parameters clearly support the existence of an oxygen diffusion highway through the LSMC GBs from the top surface to the YSZ (see inset in **Figure 6.8b**).

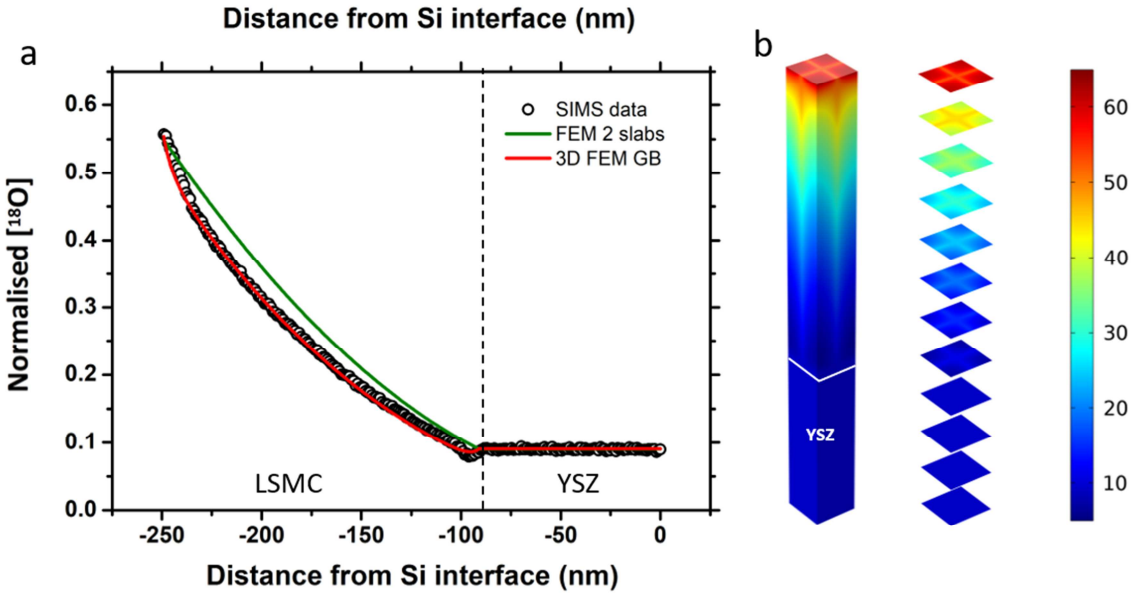

Figure 6.8 a, experimental and simulated oxygen isotope concentration profiles corresponding to the sample with 6% Co. The red line shows the 3D FEM GB model while the green line represents the best fitting obtained with a 2-slabs homogenous model. **b**, 3D image and cross sections of the oxygen isotope (^{18}O) concentration distribution map obtained by FEM for the same sample.

A sensitivity analysis has also been conducted in order to check the strength of the fitted parameters. **Figure 6.9** summarizes the effect of changing each mass transport parameter in the simulations, for an exemplifying sample of 6% Co. As it can be observed, changes in D^*_{gb} strongly affect the slope of the oxygen profile. k^*_{gb} plays a key role in obtaining the oxygen concentration in the YSZ buffer layer. A clear minimum is obtained when calculating the sum of errors; see the inset in the figures. As expected, D^*_b and k^*_b have a less influence in the total fitting error. Nevertheless, the oxygen profile shows some characteristic features (such as the increase near the surface or the lower concentration near the LSMC-YSZ interface) associated to these two parameters that help in obtaining a good fitting and determine a minimum in the total error.

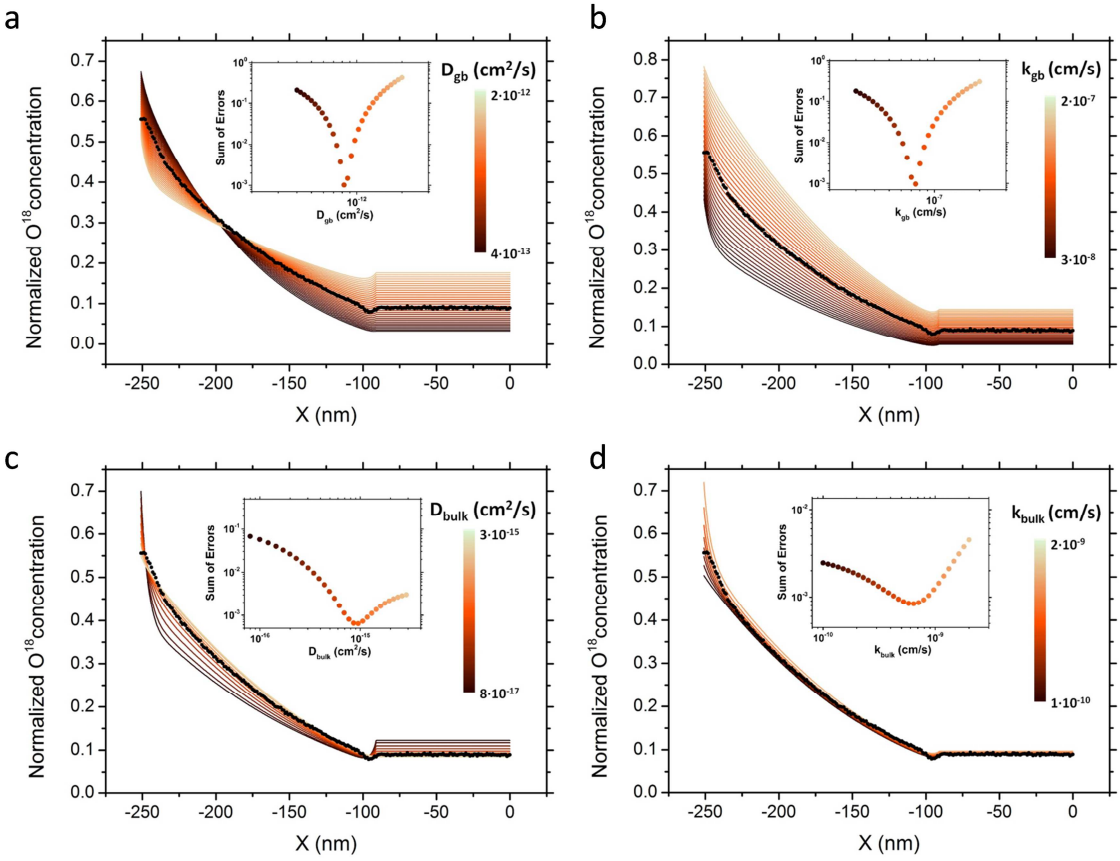

Figure 6.9 Sensitivity analysis of the simulated profiles corresponding to the sample with 6% Co. The four plots represent four sets of fittings varying $\mathbf{D^*_{gb}}$, $\mathbf{k^*_{gb}}$, $\mathbf{D^*_b}$ and $\mathbf{k^*_b}$ (**a**, **b**, **c**, **d** respectively). The insets present the sum of errors as a function of the parameter changed in each case.

Furthermore, an analysis of the grain size effect on the fitting was also carried out. This was necessary in order to assess the model inaccuracies associated to the grain size error found in the films (see **Figure 6.5**). The model was able to reproduce the profile of oxygen concentration for the whole range of grain size considered (see **Figure 6.10**). The variation obtained in the 6% Co case for D^*_{gb}, k^*_{gb}, D^*_b *and* k^*_b are collected in **Table 6.1**. As can be observed, k^*_{gb} and D^*_{gb} increases for increasing the grain size.

Also D_b^* follows the same trend, since for bigger grains higher bulk diffusion would be needed to fill the grain interior. Such analysis has been used in order to calculate the error on the obtained D^* and k^* values (error bars in **Figure 6.12a** and **b**), based on the grain size distribution obtained from both AFM and SEM analysis.

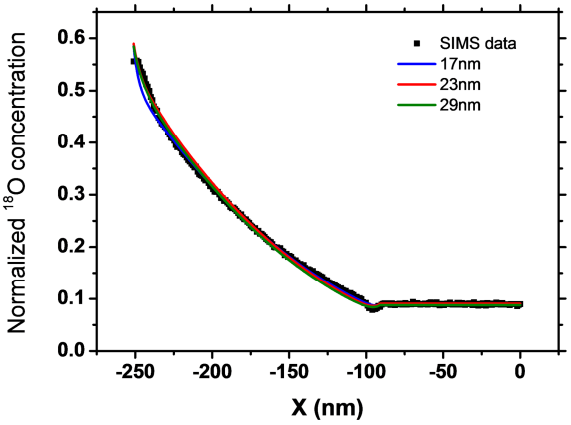

Figure 6.10 Simulated profiles of a LSMC film with 6% Co content, for three different grain sizes d = 17, 23, 29 nm, compared to the isotopic diffusion profile obtained by SIMS.

Table 6.1 Fitted values for $\mathbf{D^*_{gb}}$, $\mathbf{k^*_{gb}}$, $\mathbf{D^*_b}$ and $\mathbf{k^*_b}$ as a function of grain size, for a LSMC film with 6% Co content.

	Grain size		
	17 nm	***23 nm***	*29 nm*
$\mathbf{D^*_{gb}}$ [cm^2/s]	$6.80\cdot10^{-13}$	$\mathbf{8.50\cdot10^{-13}}$	$1.00\cdot10^{-12}$
$\mathbf{D^*_b}$ [cm^2/s]	$7.00\cdot10^{-16}$	$\mathbf{8.80\cdot10^{-16}}$	$1.30\cdot10^{-15}$
$\mathbf{k^*_{gb}}$ [cm/s]	$5.30\cdot10^{-8}$	$\mathbf{7.20\cdot10^{-8}}$	$9.06\cdot10^{-8}$
$\mathbf{k^*_b}$ [cm/s]	$6.50\cdot10^{-10}$	$\mathbf{6.00\cdot10^{-10}}$	$6.06\cdot10^{-10}$

The complete set of oxygen tracer diffusivities and surface exchange coefficients for bulk and GBs of the nanostructured LSMC was simulated and fitted. It is interesting to mention that increasing the Co content makes the effect of the grain boundary less evident due to a homogenization of the isotopic concentration caused by an increase of the bulk diffusivity, which allows lateral diffusion from the GB into the bulk (**Figure 6.11**). For this reason, for Co fractions higher than 0.4 the fitting with a 2-slabs model was also performed. Moreover, it is interesting to note that for high Co content (Co > 0.4) an apparent accumulation of oxygen starts to occur at the LSMC/YSZ interface, which cannot be fitted by the model described before. It is speculated that this effect may be due to an additional interface resistance related with cobalt accumulation in the interface, as found by Kubicek *et al.* in $La_{0.6}Sr_{0.4}CoO_{3-\delta}$ thin films deposited by PLD on YSZ single crystals.[29] In this work, this small additional contribution was not considered.

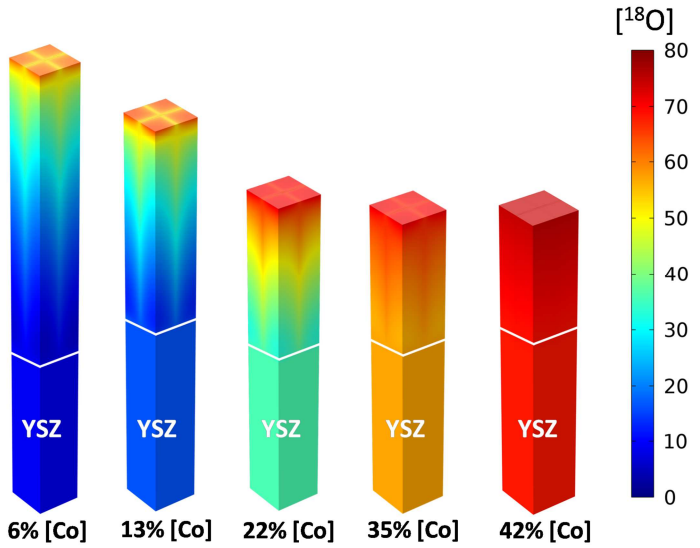

Figure 6.11 3D images of the oxygen isotope (^{18}O) concentration distribution maps obtained by FEM for the whole range of Co content fitted at T=700ºC.

6.3.3 Oxygen mass transport parameters of LSMC thin films

The set of oxygen mass transport coefficients obtained by FEM analysis as a function of the cobalt content and temperature is shown in **Figure 6.12a** and **b**. The values obtained for the bulk coefficients (D_b^* and k_b^*) are consistent with literature values[5,6] (also included in **Figure 6.12a** and **b** for comparison). On the other hand, for the whole range of cobalt under study, the GB coefficients are orders of magnitude larger than the bulk ones indicating the presence of high diffusion pathways and excellent oxygen surface exchange. This enhancement represents a natural extension of the grain boundary effect previously observed for LSM (see Chapter **5**) to the LSMC family.[8,7]

Considering the diffusivity values, both D_b^* and D_{gb}^* increase with Co-content (**Figure 6.12a**). First, the origin of the rise in the bulk diffusivity, more noticeable for y > 0.2, is due to the already reported increase of the oxygen vacancy ($V_O^{\cdot\cdot}$) concentration in the transition from an oxygen hyper-stoichiometric material (LSM) to a sub-stoichiometric material (LSC, see Chapter **1**).[10,23,24] Increasing the cobalt content shows a smaller effect on the GB diffusivity up to y = 0.2, suggesting that the concentration of oxygen vacancies in these interfaces is not strongly affected by the presence of Co. Instead, for y > 0.2, a constant increase of GB diffusivity is observed, similarly to the bulk behaviour but with a smaller slope. This means that the Co starts to modify the GB equilibrium as well (which as shown in chapter **3** is dominated by cation vacancies in LSM), giving rise to a more facile oxygen transport. This could be due to a further increase of oxygen vacancies, such in the case of the bulk, or to an increase of oxygen mobility. Keeping rising the Co content, the bulk starts to influence the overall transport for y > 0.4, making the effect of the grain boundary less evident (see **Figure 6.11**). For this reason, the diffusivity values obtained by simple two slab theory (D_{eq}^*, k_{eq}^*) are

also shown in **Figure 6.12** for y > 0.4 (note that films in this range were measured at lower temperature, T = 600ºC).

Considering the surface exchange coefficient, **Figure 6.12b** shows that the increase of bulk k* as a function of the cobalt content is fully compatible with previously reported values in the literature.[5,6] Complementarily, a very large enhancement of the GB surface exchange coefficient is observed for the whole range of Co content, suggesting that GBs control the oxygen incorporation in this type of interface-dominated LSMC materials. Importantly, k^*_{gb} happens to be roughly constant along the whole set of compositions and presents values eventually slightly higher than those found in pure LSC for the entire LSMC family. This remarkable behaviour will be discussed in section **6.5**.

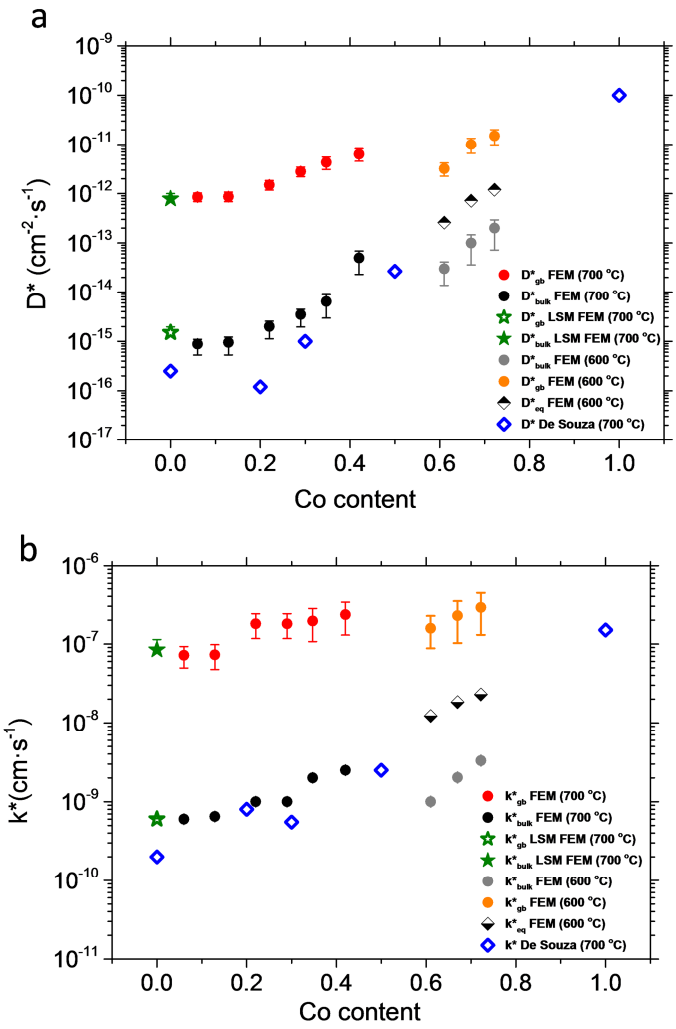

Figure 6.12 a, oxygen self-exchange diffusion and **b**, surface exchange coefficient along bulk and grain boundary extracted from simulation for T=600 °C and 700 °C. For y > 0.4 the results obtained by 2-slabs model are also reported (half-filled black diamonds). The values are compared with bulk literature values.[5,6] Error bars are calculated based on the grain size distribution observed in the films. Note that these are asymmetric because of the different effect on the fitting of either increasing or decreasing the grain size.

6.4 Electrical and optical characterization of LSMC thin films

6.4.1 Evolution of electrical properties along the LSMC system

To gain further insights into the GBs properties variation (composition, diffusion, surface exchange coefficient) with the Co content, the in-plane electronic conductivity of the combinatorial sample as a function of the temperature was studied. For doing so, the combinatorial sample was diced into individual 0.5 x 1 cm^2 chips with controlled composition and analyzed in an in-plane four probe geometry, similar to the LSM_y samples studied in Chapter **4** (see Chapter **2** for more information on the measurement configuration). The films were analyzed in the high temperature paramagnetic region (573-873 K) in synthetic air.

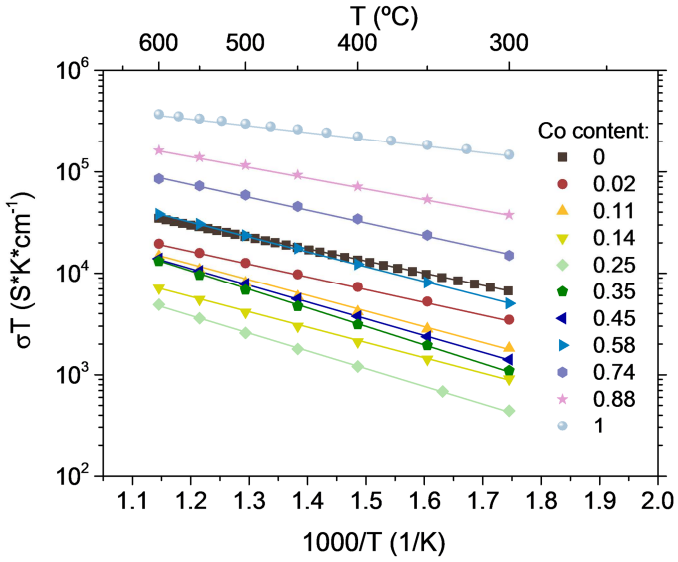

Figure 6.13 In-plane electrical conductivity as a function of the inverse of temperature for different Co content. The pure LSC measurements (y=1) refers to a sample deposited on sapphire (0001).

Figure 6.13 shows the evolution of the conductivity with the inverse temperature for the set of compositions. First, the adiabatic small polaron hopping model[‡] (see Chapter **4**) could be fitted for the whole range of Co content, as reported for bulk samples.[23,30,31] Parent compounds (LSM and LSC) showed the maximum values of conductivity with a minimum at an intermediate composition of y~0.25. For bulk LSMC, the substitution of Mn by Co in $La_{1-x}Sr_xMnO_{3+\delta}$ is known to progressively deteriorate the electrical

[‡] For the whole range of Co content, the conductivity obeys the small polaron behaviour, $\sigma = \frac{\sigma_0}{T}\exp(\frac{E_a \cdot k_b}{T})$, with E_a being the thermal activation energy of polaron motion and σ_0 the pre-exponential factor. $\sigma_0 = \frac{e^2 \nu}{a k_b} \cdot n_c \cdot C \cdot (1 - C)$, where n_c is the concentration of available lattice sites, C are the lattice sites occupied by charge carriers, e is the electron charge, a is the lattice constant, υ the vibrational frequency. In the LSMC, depending on the Co concentration, C may be dominated by Mn^{4+}, Co^{4+} or, for high Co concentration, Co^{2+}.[23,33,56]

conductivity, because the difference in cations size and electronegativity generate lattice distortions and increase of carrier localization effects.[31,32] Alternatively, it was also proposed by Gayathri *et al.*[31] that the Co substitution in $La_{0.7}Ca_{0.3}Mn_{1-y}Co_yO_{3\pm\delta}$ gradually reduces the concentration of Mn^{4+}, giving rise to an increase of Jahn Teller distortion and a deterioration of the electrical transport properties. On the other side, Mn substitution of Co in pure LSC also reduces the electronic conduction, due to the hole trapping effect of Mn cations.[33] This means that both Mn substitution in LSC and Co substitution in LSM are expected to hinder the bulk electrical transport properties. Indeed, an almost linear increase of polaron activation energy was found on both sides of the combinatorial compositional map (see **Figure 6.14a**), in good agreement with the existing literature for bulk LSMC, as presented in the same figure for direct comparison.[23] The position of the maximum (y ~ 0.35) is likely linked to the change of electronic conduction from the Mn to the Co sub-lattice. Indeed, this value is related, in solid solutions, to the activation of the conduction pathway through the dopant-cation sub-lattice for compositions above the percolation threshold, *e.g.* y ~ 0.31 in simple cubic lattices. This consideration is also supported by the sudden increase of pre-exponential factor for y ~ 0.35 (**Figure 6.14b**), indicating an increase of charge carries probably due to a higher disproportion mechanism of Co ($2Co_{Co}^{x} \leftrightarrow Co_{Co}' + Co_{Co}^{\bullet}$) with respect to Mn (the conduction in Co-rich LSMC could be n or p type depending on the Mn and oxygen vacancy concentration[33]).

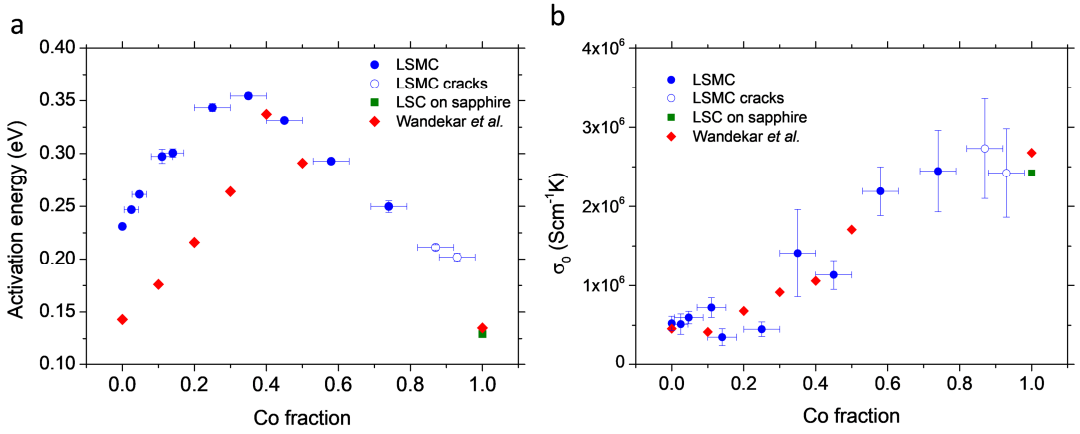

Figure 6.14 Activation energy (**a**) and pre-exponential factor $\boldsymbol{\sigma_0}$ (**b**) as a function of Co content derived from the fitting of conductivity measurements according to the small polaron hopping mechanism. The open symbols refer to samples with visible cracks that could affect the conduction mechanism. The green squares with composition y=1 refer to a LSC sample deposited on sapphire single crystal. Data from LSMC bulk sample from the literature are reported for comparison.[23]

Additionally, it is important to discuss the GBs effect in the electronic conductivity of LSMC thin films. First, it is recalled that all the LSMC thin films analysed in this chapter present a B/A ratio equal to 0.85, meaning that when Co fraction is close to zero, the GBs are expected to be compositionally analogous to the GB_{def} observed in Chapter **3** (increase of La and Sr and decrease of Mn and O). As deeply analysed in Chapter **4**, LSM thin films characterized by GB_{def} present an insulating behaviour, mainly due to

the accumulation of Mn vacancies and structural defects that break the Mn-O-Mn sub-lattice and increase the polaron hopping barrier. This behaviour is consistent with the higher hopping activation energy observed for polycrystalline LSM parent compound respect to the bulk literature reference, see **Figure 6.14a**.[23] Also, in **Figure 6.14a** two behaviour can be observed. When the Mn is dominating the polaron transport ($y < 0.35$), the energy of activation rapidly increases upon the Co substitution and keeps constantly higher than the bulk reference up to $y \sim 0.3$. This means that in this region the GBs dominate the electronic transport, hindering the overall conductivity. Nevertheless, it is interesting to note that for bulk and polycrystalline thin films the maximum value of activation energy is roughly the same ($E_a \sim 0.36$ eV), mainly due to a steep rise between $y = 0.3 - 0.4$ in the bulk values. Also, the measured overall trend with the Co content is fully compatible with the bulk one, suggesting that the mechanisms that cause the increase of polaron localization and activation energy are similar in the two cases. Instead, when the Co is dominating the polaron transport ($y > 0.35$), polycrystalline LSMC thin films and bulk reference activation energy display an analogous behaviour, both in terms of trend and of overall value.

A complete satisfactory explanation for this behaviour is still lacking at the moment. Considering that the LSM parent compound is characterized by GB_{def}, the Co actively participates to the GB equilibrium, progressively occupying the Mn vacant sites. The presence of Co in the GBs would originate a similar detrimental effect to the one observed in the bulk but enhanced by the accumulation of chemical and structural defects. Considering that no substantial evolution is observed in the pre-exponential factor for $y < 0.3$ (**Figure 6.14b**), it seems that the Co is not modifying the oxidation state of the Mn in the GBs (see Eq. **4.3**, Chapter **4**). The observation of a constant σ_0 is also consistent with the hypothesis that Co is occupying the Mn vacancies of the GBs, which are already not available as active sites for the polaron hopping (as discussed in Chapter **4**). Therefore, it is believed that the increase of activation energy in this region is due to an increase of polaron barrier derived from the difference of electronegativity between the two cations, which promote electron localization.[32] At $y = 0.35$, the Co sub-lattice pathway starts to be active, leading to a progressive decrease in activation energy and an increase of available charges. In this region, the impact of the GBs is less relevant for electronic transport, which may be due to a change of GB equilibration mechanism. More work is needed to fully address this aspect.

6.4.2 Evolution of optical properties along the LSMC system

The optical properties of LSMC thin films were then investigated by ellipsometry. A series of spectra was acquired at room temperature along the centres of the two parent compounds plumes in the combinatorial sample, allowing the study the optical evolution as a function of Co content. The raw data were fitted by a series of Lorentzian oscillators in order to extract the optical constants of the materials, see Chapter **2** for details.[34–36] For the LSC parent compound, an additional Drude element was necessary

to better reproduce the optical properties at low energy. As commented in Chapter **3**, ellipsometry is not able to separate grain and grain boundary contributions, therefore the results described next can be mainly ascribed to the bulk LSMC, since it represents approximately the 90 vol.% of the polycrystalline films. The evolution of the absorption coefficient for a selection of films with different Co content is shown in **Figure 6.15a**. Only films with y = 0 - 0.74 are shown, since cracks start to appear on films above that range and these impeded a proper analysis of the spectra acquired. With the aim of offering a reference for a film with high Co content, the absorption measured on a 30 nm LSC thin film deposited on Sapphire (0001) was also included.

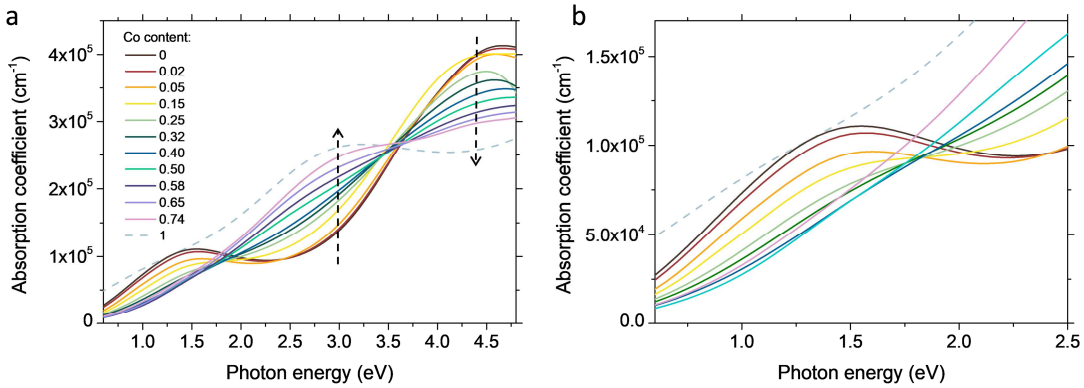

Figure 6.15 a, Absorption coefficient of LSMC thin films measured by ellipsometry as a function of Co content. The dashed line shows the absorption coefficient of a LSC thin film deposited on Sapphire (0001). The dashed arrows are intended to highlight the change of absorption in the visible and ultraviolet range. **b**, enlargement of the absorption coefficient in infrared and red region.

As expected, large modifications of the absorption coefficient take place while varying the composition of the thin films. In the visible and ultraviolet region (photon energy > 2 eV), two distinct processes can be identified when increasing the Co content, namely a continuous increase of absorption near 3 eV and a corresponding continuous decrease near 4.5 eV (see dashed arrows in **Figure 6.15a**). According to literature, the 3 eV and the 4.5 eV correspond to a characteristic transition of LSC and LSM respectively. Considering the LSM spectrum, the UV features are generally interpreted as electronic transitions between the Mn 3d - O 2p mixed states into minority $t_{2g}^{*}\downarrow$ and $e_{g}^{*}\downarrow$ states of Mn 3d character, lying well above the fermi level.[35–38] On the contrary, in the LSC parent compound, the prominent peak around 3 eV was assigned to either an intraband transition between hybridized t_{2g} - O 2p states to majority $e_{g}^{*}\uparrow$ states[39], or to mainly O 2p electrons jumping to minority $e_{g}^{*}\downarrow$ empty bands.[40] Whatever is the exact origin of these transitions, it is clear that they represent a fingerprint of the importance of Co and Mn on the overall electronic structure of LSMC thin films. Also, it is interesting to note that the gradual transfer of electrons from high to intermediate energy states is occurring with an almost isoabsorption point, see the nearly constant absorption at ~3.5 eV in **Figure 6.15a**. This suggests that, with increasing Co content, the transition at 3 eV grows at the expense of the 4.5 eV one. Therefore, it appears that the electronic structure of the LSMC thin films in the visible and ultraviolet range can be simply

described as a mixture of LSC and LSM and that no further intraband transitions are created.

In the red and infrared region (photon energy < 2) it is possible to observe a progressive decrease of the absorption peak with maximum at 1.5 eV (see **Figure 6.15b**). In LSM parent compound, this feature is originated by an intra-atomic transition originated by Jahn–Teller (J-T) e_g orbital splitting and an inter-atomic polaron hopping transfer (see Chapter **3** for more details). Therefore, the progressive decrease of the intensity of this peak is consistent with the decrease of Mn concentration in LSMC thin films. Unfortunately, since the Co substitution may affect also the Mn^{4+} concentration,[31] both J-T and polaron transitions may result in a non-trivial behaviour with the Co content, making challenging to separate their spectral weight from the other transitions.

It is interesting to note that the LSC thin film presents in the infrared region a significant absorption down to the detection limit of the ellipsometry (0.6 eV), which, if extrapolated to zero energy, results in a vanishing bandgap. This behaviour is typical of a metal, in agreement with the observation that LSC is characterized by a partially filled band near the fermi level.[41] Nevertheless, the LSMC thin films up to y = 0.75 display a non-vanishing bandgap, meaning that the Mn strongly influences the band structure near the fermi level, avoiding the metallic behaviour and originating a well-defined bandgap. Therefore, LSMC with y = 0.75 appears as a very interesting p-type oxide with high absorption in the visible range, which could have a direct application in oxide photovoltaics[42] or photoelectrochemical cells.[43,44]

6.4 Discussion

In this section, the evolution of the surface oxygen coefficients in the LSMC thin films series is discussed, in view of the results presented before. First, it is recalled that the k^*_{gb} shows mostly a flat behaviour varying the Co content, presenting values comparable with the bulk LSC for the complete set of compositions (see **Figure 6.12b**). Moreover, k^*_{gb} appears also not to be related to the electronic transport, which, as discussed in section **6.4.1**, undergoes through substantial modifications with the Co content. Indeed, a steep increase of polaron hopping activation energy was observed between y = 0 and y = 0.35, probably due to the accumulation of Co in the GBs, while only minor changes of k^*_{gb} were measured in the same range. Also, no apparent relationship is found between the k^*_{gb} and the transition of the electronic conduction from the Mn- to the Co-sub-lattice. This suggests that the availability of majority charge carriers is not affecting the oxygen incorporation in the LSMC grain boundaries.

For gaining more insights into the mechanism of oxygen incorporation in LSMC, the results obtained for diffusivity and surface coefficient of bulk and GB in LSMC thin films are collected in a $\log D^*$ *vs.* $\log k^*$ plot, see **Figure 6.16a**. In this figure, the values obtained in Chapter **5** for LSM_y by EIS as a function of temperature and Mn content are also depicted, as well as the values for $LSM_{0.85}$ thin films from Saranya *et al.*[8], recalculated in the frame of this work by FEM fitting of the IEDP-SIMS profiles and, finally, a variety of results obtained in literature for similar bulk perovskite materials.[6,45] Notably, despite the significant increase in mass transport properties of these GBs, all the obtained results are still in good agreement with the empirical law, firstly proposed by Kilner and co-workers,[6,46] which correlates D^* and k^* in a variety of MIEC perovskites along a line with gradient g_h = 0.5. Therefore, it appears that the superior properties of the GBs keep the trend reported for single phase perovskites despite the highly defective nature of these interfaces. This directly points at a similar oxygen incorporation mechanism occurring in the GBs and in the bulk material, although greatly enhanced in the former by the high oxygen vacancy concentration found there.

Nevertheless, it is possible to observe that even if the whole set of data approximately follows the 0.5 line, the slopes of the LSM_y and LSMC data sets (both for bulk and GBs) are different. This is clearly visible in **Figure 6.16b**, where a magnification of GB measurements for LSM_y and LSMC are depicted. This remark was first made by De Souza,[47] who observed that the empirical law holds for the MIEC family as a whole but not for the single components. In other words, even if values of slopes ranging between 0.5 – 1 can be found when fitting the single La-based perovskite series alone (as a function of temperature, composition…),[6] when considering them all together an average of g_h = 0.5 is revealed (this can be easily explained considering that the data sets are shifted relative to one another, see **Figure 6.16a**). In the particular case of this work, gradients between g_h = 0.36 and 1.17 have been obtained each individual set of films (*i.e.* different measurements of LSM_y and LSMC films), as shown in **Figure 6.16b**.

More in detail, a decrease of g_h is generally found when moving from LSM_y to LSMC thin films. In GB-dominated LSM_y films measured by different techniques (SIMS fitting, EIS) a value close to 1 is found, both as a function of temperature or B/A content. Instead, in the LSMC series, as a function of the Co content, a g_h lower than 0.5 is revealed. This difference implies that increasing the oxygen diffusivity has diverse impact on the surface exchange coefficient of LSM_y and LSMC GBs.

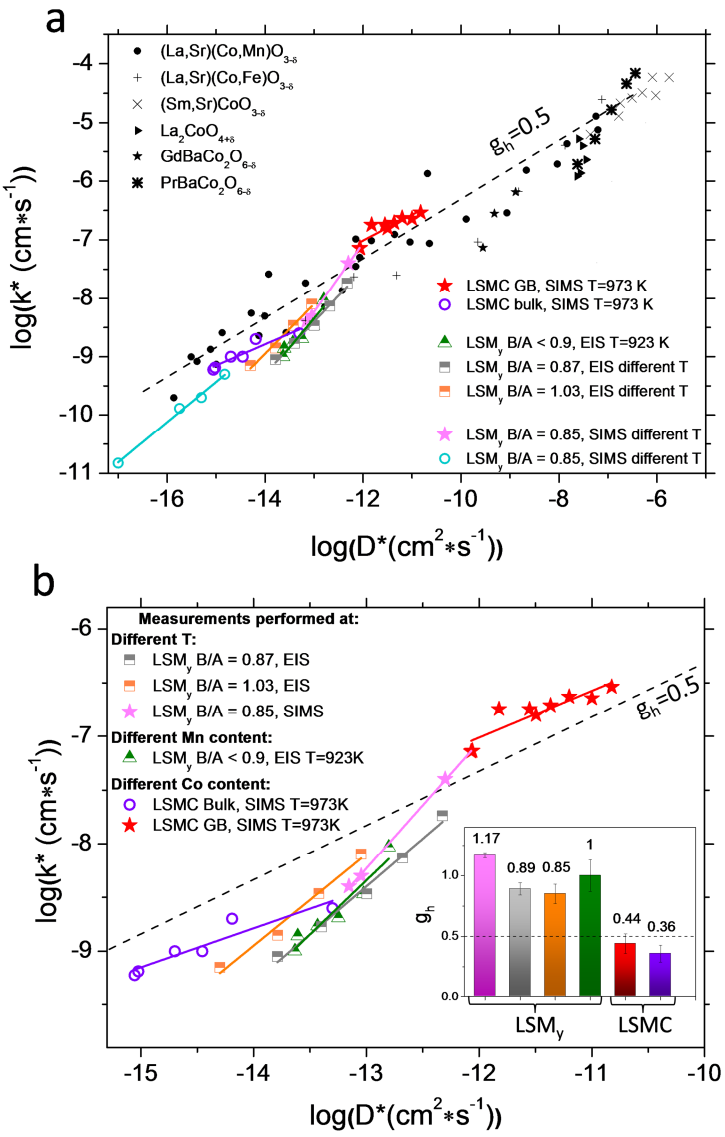

Figure 6.16 a, Correlation between the oxygen surface exchange coefficient k* and the oxygen self-exchange diffusion coefficient D*, obtained for LSMC and for LSM_y by different techniques and compared to literature data for different perovskite materials. The figure is adapted from De Souza et al.[6] and Tarancón et al.[45] **b**, Selected area of **a**, showing the gradients obtained by linear fitting of the experimental points, for LSM_y and LSMC GB-dominated films measured in this work. The inset shows a direct comparison of the obtained slopes.

Before offering a possible explanation for this behavior, the meaning of g_h is discussed. In the case of oxygen vacancies involved in the rate limiting step (*rds*) of oxygen incorporation, Merkle *et al.*[48] derived, using Maier's kinetic approach,[49] a solid

mechanistic explanation for the empirical law, which leads to the direct relation between the surface exchange and the diffusion activation energies (ΔH_k and ΔH_D respectively):

$$\Delta H_k = g_h \cdot \Delta H_D \qquad \text{Eq. 6.1}$$

The equation directly leads to a linear relation $\log D^*$ *vs.* $\log k^*$ when considering both diffusion and surface exchange mechanisms described by an Arrhenius law. [§] Considering that the diffusion activation energy is given by the sum of vacancy migration enthalpy (ΔH_m) and vacancy formation enthalpy (ΔH_f), one finds that g_h is a measure of how an increase of oxygen vacancy availability (concentration + mobility) affects the surface exchange rate. In Merkle *et al.*'s work,[48] the origin of the experimental parameter $g_h < 1$ was explained considering that, for transferring the oxygen absorbed on the surface to the first atomic layer, just a fraction of ΔH_D is necessary and not the whole diffusion activation energy of the bulk (i.e. the *rds* is not a pure ionic step but involves a transfer of not fully charged oxygen ions). Also, a value of $g_h < 1$ may indicate that other phenomena that also vary proportionally to ΔH_D, such as the electron fermi level[50] or the adsorbate energy[51], play a role in the ORR and incorporation.

In the light of these considerations, the value of $g_h \sim 1$ found for LSM_y GBs reinforces the incorporation picture proposed in Chapter **5**, with the *rds* consisting of a pure ionic step involving an oxygen vacancy approaching the adsorbed surface. It is also interesting to note that similar g_h were found either varying the temperature (for different B/A ratios) or changing the B/A ratio at fixed temperature (see **Figure 6.16b**). This corroborates the fundamental role of GB's oxygen vacancies concentration in the surface exchange reactions of LSM_y, which can be enhanced both by an increase of temperature (negative ΔH_f) or by a decrease of Mn content for B/A< 0.9 (see Chapter **5**).

In LSMC, however, the slope lower than 0.5 for both GB and bulk indicates that increasing the oxygen vacancies availability by increasing the Co content has a smaller effect on the surface exchange process than in LSM_y. Moreover, one can also note from **Figure 6.16b** that, an even weaker gradient is revealed if excluding from the series the points obtained for small Co content (y < 0.2, which in fact matches well with the results obtained for the $LSM_{0.85}$ GBs by SIMS). Many different reasons may behind this interesting behaviour. Here, it is proposed that the variation of adsorption energy increasing the Co content is at the origin of the low value of g_h. In this sense, Choi *et al.*[51] demonstrated that MIEC materials with smaller vacancy formation energy (such as LSC respect to LSM) also present smaller adsorption energy, resulting in less oxygen adsorbate species on the surface. If the same GB incorporation mechanism presented in

[§] Note that the Arrhenius equation also gives rise to a linear dependence to the pre-exponential factors in the log-log plot. Nevertheless, since the empirical law is independent of the temperature, Eq. 6.1 still holds its validity. The interested reader may find more details in [48].

Chapter **5** is considered for the whole LSMC series, the surface exchange coefficient will be proportional to $k^* \propto [V_O^{\cdot\cdot}] \cdot D_v \cdot \theta(O^-)$. This means that, even if increasing the Co content will result in a higher concentration of oxygen vacancies, decreasing the Mn content will also reduce the number of oxygen species on the surface ($\theta(O^-)$). Consequently, the positive effect of increasing the oxygen vacancy availability is reduced, giving rise to a g_h eventually smaller than 1, as obtained here. This mechanism can therefore explain the behaviour found for both the LSMC and the LSM_y systems, taken into account this last consideration. Moreover, it highlights the extraordinary properties of LSM when it is not limited by the poor concentration of oxygen vacancies, allowing attaining high oxygen exchange coefficients comparable to, or even higher than, those found in pure LSC. It should be noted that the change of g_h may also reveal that a change of mechanism of oxygen incorporation takes place in LSMC films with high Co content, suggesting that, for further improving the surface exchange properties of these materials, other strategies besides the increase of oxygen vacancies should be considered. These could include, for example, surface decoration with a more active oxide,[52,53] or enhancing the minority carriers electrons[54] directly involved in the reduction of the oxygen species.

5.5 Conclusions

In summary, in this chapter a thin film pseudo-binary system of $La_{0.8}Sr_{0.2}(Mn_{1-y}Co_y)_{0.85}O_{3\pm\delta}$ ($y \approx 0$ to 1) has been successfully deposited by combinatorial pulsed laser deposition in order to study the oxygen mass transport properties at the bulk and grain boundary levels as a function of the cobalt content. Isotope exchange depth-profiling coupled with SIMS measurement has been employed to obtain diffusion profiles and, therefore, by numerical modelling the oxygen self-diffusion (D_b^*, D_{gb}^*) and surface exchange (k_b^*, k_{gb}^*) coefficients for a large range of Co compositions at T = 600 - 700ºC (y = 0 to 0.8). While the bulk properties follow the behaviour reported in the literature, this study reveals that grain boundaries act as fast diffusion and exchange pathways for oxygen ion transport. The results presented here show how GBs enhance the transport properties of the whole material in the range of compositions under study, although for high Co concentration (y = 0.4 to 0.8) the GB effect is already concealed by the high bulk diffusion.

The in plane electrical measurements revealed that GBs dominate the electronic properties when the transport takes place through the Mn-O-Mn sub-lattice (y < 0.35), while, when Co-O-Co path start to control the conduction, a more bulk-like behaviour is found. The trend observed for the polaron activation energy and the pre-exponential factor suggests that the Co progressively accumulates at the GBs, hindering the electronic transport due to polaron localization effects. Also, the analysis of the optical absorption revealed that the electronic structure of LSMC is strongly influenced by the Co content, giving rise to different behaviour in the infrared and visible-ultraviolet ranges.

Finally, the GB's surface exchange coefficient of LSMC was combined with the results obtained in the previous chapters for LSM_y to get insights into the mechanism of oxygen incorporation in the two families. The results obtained for diffusivity and surface coefficient of bulk and GB in LSMC thin films were collected in a $\log D^*$ *vs.* $\log k^*$ plot. It is found that while in LSM_y the oxygen vacancies directly control the oxygen incorporation (with a slope $g_h \sim 1$), increasing $V_O^{\bullet\bullet}$ by rising the Co content in LSMC does not cause the same behaviour, since a slope lower than 0.5 is found. It is proposed that this change is originated by the lower surface adsorption energy of Co with respect to Mn, which results in a lower concentration of oxygen adsorbate species on the LSMC surface (partially counteracting the positive effect of increasing the oxygen vacancies with the Co content). This observation reinforce the idea of the superior electrochemical properties of LSM when it is not limited by the availability of oxygen vacancies.

References

1. Waldow, S. P. & De Souza, R. A. Computational Study of Oxygen Diffusion along a [100] Dislocations in the Perovskite Oxide $SrTiO_3$. *ACS Appl. Mater. Interfaces* **8,** 12246–12256 (2016).
2. Metlenko, V. *et al.* Do dislocations act as atomic autobahns for oxygen in the perovskite oxide $SrTiO_3$. *Nanoscale* **6,** 12864–12876 (2014).
3. Marrocchelli, D., Sun, L. & Yildiz, B. Dislocations in $SrTiO_3$: Easy to Reduce but Not so Fast for Oxygen Transport. *J. Am. Chem. Soc.* **137,** 4735–4748 (2015).
4. Sun, L., Marrocchelli, D. & Yildiz, B. Edge dislocation slows down oxide ion diffusion in doped CeO_2 by segregation of charged defects. *Nat. Commun.* **6,** 6294 (2015).
5. De Souza, R. & Kilner, J. a. Oxygen transport in $La_{1-x}Sr_xMn_{1-y}Co_yO_{3\pm\delta}$ perovskites Part I. Oxygen tracer diffusion. *Solid State Ionics* **106,** 175–187 (1998).
6. De Souza, R. A. & Kilner, J. a. Oxygen transport in $La_{1-x}Sr_xMn_{1-y}Co_yO_{3\pm\delta}$ perovskites: Part II. Oxygen surface exchange. *Solid State Ionics* **126,** 153–161 (1999).
7. Navickas, E. *et al.* Fast oxygen exchange and diffusion kinetics of grain boundaries in Sr-doped $LaMnO_3$ thin films. *Phys. Chem. Chem. Phys.* **17,** 7659–7669 (2015).
8. Saranya, A. M. *et al.* Engineering Mixed Ionic Electronic Conduction in $La_{0.8}Sr_{0.2}MnO_{3+\delta}$ Nanostructures through Fast Grain Boundary Oxygen Diffusivity. *Adv. Energy Mater.* **5,** 1500377 (2015).
9. Hornes, A., Saranya, A. M., Morata, A. & Tarancon, A. High-throughput screening of SOFC cathode materials. in *Proceedings of the 12th European SOFC & SOE forum* B1508 (2016).
10. Thursfield, A., Rossiny, J. C. H., Fearn, S., Kilner, J. A. & Metcalfe, I. S. A combinatorial approach to synthesis of the $La_{0.8}Sr_{0.2}Co_{1-y}Mn_yO_{3\pm\delta}$ family of perovskite-type mixed conducting metal oxides and characterisation of the surface oxygen mobility. *Solid State Ionics* **225,** 182–185 (2012).
11. Rossiny, J. C. H. *et al.* Combinatorial characterisation of mixed conducting perovskites. *Solid State Ionics* **179,** 1085–1089 (2008).
12. Christen, H. M. *et al.* A laser-deposition approach to compositional-spread discovery of materials on conventional sample sizes. *Meas. Sci. Technol.* **16,** 21–31 (2005).
13. Christen, H. M., Silliman, S. D. & Harshavardhan, K. S. Continuous compositional-spread technique based on pulsed-laser deposition and applied to the growth of epitaxial films. *Rev. Sci. Instrum.* **72,** 2673–2678 (2001).
14. Fukumura, T. *et al.* Rapid construction of a phase diagram of doped Mott insulators with a composition-spread approach. *Appl. Phys. Lett.* **77,** 3426–3428 (2000).
15. Greer, J. A. History and current status of commercial pulsed laser deposition equipment. *J. Phys. D. Appl. Phys.* **47,** 34005 (2014).
16. Christen, H. M. & Eres, G. Recent advances in pulsed-laser deposition of complex oxides. *J. Phys. Condens. Matter* **20,** 264005 (2008).
17. Eason, R. *Pulsed Laser Deposition of Thin Films*. (John Wiley & Sons, Inc., 2006).
18. Noh, M., Thiel, J. & Johnson, D. C. Synthesis of Crystalline Superlattices by Controlled Crystallization of Modulated Reactants. *Science (80-.).* **270,** 1181–1184 (1995).
19. Noh, M., Johnson, C. D., Hornbostel, M. D., Thiel, J. & Johnson, D. C. Control of reaction pathway and the nanostructure of final products through the design of

modulated elemental reactants. *Chem. Mater.* **8,** 1625–1635 (1996).

20. Fister, L. & Johnson, D. C. Controlling Solid-State Reaction Mechanisms Using Diffusion Length in Ultrathin-Film Superlattice Composites. *J. Am. Chem. Soc.* **114,** 4639–4644 (1992).

21. Li, Z. *et al.* Interface and surface cation stoichiometry modified by oxygen vacancies in epitaxial manganite films. *Adv. Funct. Mater.* **22,** 4312–4321 (2012).

22. Chen, J. *et al.* Plasma interactions determine the composition in pulsed laser deposited thin films. *Appl. Phys. Lett.* **105,** 114104 (2014).

23. Wandekar, R. V., Wani, B. N. & Bharadwaj, S. R. Crystal structure, electrical conductivity, thermal expansion and compatibility studies of Co-substituted lanthanum strontium manganite system. *Solid State Sci.* **11,** 240–250 (2009).

24. Petrov, A. N., Voronin, V. I., Norby, T. & Kofstad, P. Crystal Structure of the Mixed Oxides $La_{0.7}Sr_{0.3}Co_{1-z}Mn_zO_{3-y}$ ($0<z<1$). *J. Solid State Chem.* **143,** 52–57 (1999).

25. Krishna Murthy, J. *et al.* Phase Separation in $La_{2-x}A_xCoMnO6$ (A = Ca and Sr) Perovskites I. *J. Exp. Theor. Phys.* **99,** 363–369 (2004).

26. Fischer, E. & Hertz, J. L. Measurability of the diffusion and surface exchange coefficients using isotope exchange with thin film and traditional samples. *Solid State Ionics* **218,** 18–24 (2012).

27. Kilner, J. A., Skinner, S. J. & Brongersma, H. H. The isotope exchange depth profiling (IEDP) technique using SIMS and LEIS. *J. Solid State Electrochem.* **15,** 861–876 (2011).

28. Kilo, M., Argirusis, C., Borchardt, G. & Jackson, R. A. Oxygen diffusion in yttria stabilised zirconia—experimental results and molecular dynamics calculations. *Phys. Chem. Chem. Phys.* **5,** 2219–2224 (2003).

29. Kubicek, M. *et al.* Electrochemical properties of $La_{0.6}Sr_{0.4}CoO_{3-\delta}$ thin films investigated by complementary impedance spectroscopy and isotope exchange depth profiling. *Solid State Ionics* **256,** 38–44 (2014).

30. Ziese, M. & Srinitiwarawong, C. Polaronic effects on the resistivity of manganite thin films. *Phys. Rev. B* **58,** 11519–11525 (1998).

31. Gayathri, N. *et al.* Electrical transport, magnetism, and magnetoresistance in ferromagnetic oxides with mixed exchange interactions: A study of the $La_{0.7}Ca_{0.3}Mn_{1-x}Co_xO_3$ system. *Phys. Rev. B* **56,** 1345–1353 (1997).

32. Vashook, V. *et al.* Electrical conductivity and oxygen nonstoichiometry in the double B mixed $La_{0.6}Ca_{0.4}Mn_{1-x}Co_xO_3$ perovskite system. *J. Alloys Compd.* **487,** 577–584 (2009).

33. Kozhevnikov, V. L. *et al.* Conductivity and carrier traps in $La_{1-x}Sr_xCo_{1-z}Mn_zO_{3-\delta}$(x=0.3; z=0 and 0.25). *J. Solid State Chem.* **172,** 296–304 (2003).

34. Scafetta, M. D., Xie, Y. J., Torres, M., Spanier, J. E. & May, S. J. Optical absorption in epitaxial $La_{1-x}Sr_xFeO_3$ thin films. *Appl. Phys. Lett.* **102,** 81904 (2013).

35. Mildner, S., Hoffmann, J., Blöchl, P. E., Techert, S. & Jooss, C. Temperature- and doping-dependent optical absorption in the small-polaron system $Pr_{1-x}Ca_xMnO_3$. *Phys. Rev. B* **92,** 35145 (2015).

36. Nomerovannaya, L. V., Makhnev, A. A. & Rumyantsev, A. Y. Evolution of the optical properties of single-crystal $La_{1-x}Sr_xMnO_3$. *Phys. Solid State* **41,** 1322--1326 (1999).

37. Quijada, M. *et al.* Optical conductivity of manganites: Crossover from Jahn-Teller small polaron to coherent transport in the ferromagnetic state. *Phys. Rev. B* **58,** 16093–16102

(1998).

38. Cesaria, M., Caricato, A. P., Leggieri, G., Martino, M. & Maruccio, G. Optical response of oxygen deficient La0.7Sr0.3MnO3 thin films deposited by pulsed laser deposition. *Thin Solid Films* **545,** 592–600 (2013).

39. Yamaguchi, S., Okimoto, Y., Ishibashi, K. & Tokura, Y. Magneto-optical Kerr effects in perovskite-type transition-metal oxides: $La_{1-x}Sr_xMnO_3$ and $La_{1-x}Sr_xCoO_3$. *Phys. Rev. B - Condens. Matter Mater. Phys.* **58,** 6862–6870 (1998).

40. Jeong, D. W. *et al.* Dimensionality control of d-orbital occupation in oxide superlattices. *Sci. Rep.* **4,** 1–5 (2014).

41. Tokura, Y. *et al.* Thermally induced insulator-metal transition in A view based on the Mott transition. *Phys. Rev. B - Condens. Matter Mater. Phys.* **58,** R1699–R1702 (1998).

42. Rühle, S. *et al.* All-oxide photovoltaics. *J. Phys. Chem. Lett.* **3,** 3755–3764 (2012).

43. Zhou, C., O'Brien, J. E., Rajan, G., Marsillac, S. & Zhang, X. Water Splitting Using High Temperature Solid Oxide Photoelectrochemical Cell and Visible Sunlight: Searching for the Appropriate Semiconductor Materials. *J. Electrochem. Soc.* **164,** H497–H502 (2017).

44. Brunauer, G. C. *et al.* UV-Light-Driven Oxygen Pumping in a High-Temperature Solid Oxide Photoelectrochemical Cell. *Adv. Funct. Mater.* **26,** 120–128 (2016).

45. Tarancón, A., Burriel, M., Santiso, J., Skinner, S. J. & Kilner, J. A. Advances in layered oxide cathodes for intermediate temperature solid oxide fuel cells. *J. Mater. Chem.* **20,** 3799–3813 (2010).

46. Kilner, J. Isotopic exchange in mixed and ionically conducting oxides. in *Proceedings of the Second International Symposium on Ionic and Mixed Conducting Ceramics* (eds. Ramanarayanan, W. L., Worell, H. L. & Tuller, H. L.) 174–190 (The Electrochemical Society Inc, 1994).

47. De Souza, R. a. A universal empirical expression for the isotope surface exchange coefficients (k*) of acceptor-doped perovskite and fluorite oxides. *Phys. Chem. Chem. Phys.* **8,** 890–897 (2006).

48. Merkle, R., Maier, J. & Bouwmeester, H. J. M. A linear free energy relationship for gas-solid interactions: Correlation between surface rate constant and diffusion coefficient of oxygen tracer exchange for electron-rich perovskites. *Angew. Chemie - Int. Ed.* **43,** 5069–5073 (2004).

49. Maier, J. On the correlation of macroscopic and microscopic rate constants in solid state chemistry. *Solid State Ionics* **112,** 197–228 (1998).

50. Lankhorst, M. H. R., Bouwmeester, H. J. M. & Verweij, H. Use of the Rigid Band Formalism to Interpret the Relationship between O Chemical Potential and Electron concentration in $La_{1-x}Sr_xCoO_3$. *Phys. Rev. le* **77,** 2989–2992 (1996).

51. Choi, Y., Lin, M. C. & Liu, M. Rational design of novel cathode materials in solid oxide fuel cells using first-principles simulations. *J. Power Sources* **195,** 1441–1445 (2010).

52. Mutoro, E., Crumlin, E. J., Biegalski, M. D., Christen, H. M. & Shao-Horn, Y. Enhanced oxygen reduction activity on surface-decorated perovskite thin films for solid oxide fuel cells. *Energy Environ. Sci.* **4,** 3689 (2011).

53. Lynch, M. E. *et al.* Enhancement of $La_{0.6}Sr_{0.4}Co_{0.2}Fe_{0.8}O_{3-\delta}$ durability and surface electrocatalytic activity by $La_{0.85}Sr_{0.15}MnO_{3\pm\delta}$ investigated using a new test electrode platform. *Energy Environ. Sci.* **4,** 2249 (2011).

54. De Souza, R. A. Limits to the rate of oxygen transport in mixed-conducting oxides. *J.*

Mater. Chem. A **5,** 20334–20350 (2017).

55. Saranya, A. M. Integrating nanoionics concepts in micro solid oxide fuel cells. (Universitat de Barcelona, 2015).

56. Petrov, A. N. & Zuev, A. Y. Defects in doped perovskite-like lanthanum cobaltite crystals $La_{1-x}Sr_xCo_{1-y}Mn_yO_{3-\delta}$ (Me = Cu and Mn). *Russ. J. Phys. Chem. A* **80,** 1935–1942 (2006).

Conclusions

The present thesis was devoted to the investigation and the engineering of the composition and functional properties of Grain Boundaries (GB) in Mixed Ionic Electronic Conductor (MIEC) perovskite oxides ($ABO_{3\pm\delta}$) thin films. The thesis is focused in three main topics: (i.) structural and compositional characterization of grain and GBs in $La_{0.8}Sr_{0.2}Mn_yO_{3\pm\delta}$ (LSM_y) thin films; (ii.) effect of GBs on functional properties of LSM_y thin films; (iii.) effect of B-site Co substitution on the bulk and GBs functional properties of $La_{0.8}Sr_{0.2}(Mn_{1-y}Co_y)_{0.85}O_{3\pm\delta}$ (LSMC) thin films. The most relevant findings concluded in this work are listed below.

- **The presence of GB local non-stoichiometry in $La_{0.8}Sr_{0.2}Mn_yO_{3\pm\delta}$ thin films**: The analysis of LSM_y GBs revealed that a profound atomic reorganization takes place in these interfaces under the lattice distortions generated by the dislocation fields (Chapter **3**). By the deposition of LSM_y thin films with different Mn content, two main types of GB local nonstoichiometries, determined by the concentration of the relative cation ratio B/A in the grain bulk, were found, namely:
    - For B/A<0.9, the GBs are characterized by a Mn and O depletion along with a La and Sr enrichment (GB_{def}). The relative decrease of Mn and O concentration near the strained interfaces suggests a compensation mechanism based on the generation of associated defects $V_O^{\bullet\bullet} - V_{Mn}^{\prime\prime\prime}$, while the increase of La points at the formation of antisite defects La_{Mn}^{x}.
    - For B/A>0.9, the GBs are observed to present La and O depletion along with a Mn enrichment (GB_{rich}). The switch of behaviour occurs when the films are still Mn deficient, suggesting a complex interaction among the electrochemical equilibrium of cation and oxygen vacancies in the bulk and in the GBs.

  The results demonstrate that the GB composition can be modified by tuning the cationic chemical potential in the grain bulk (*i.e.* overall cationic concentration).

- **The capability engineering the functional properties in $La_{0.8}Sr_{0.2}Mn_yO_{3\pm\delta}$ thin films through GBs.** The different GB local nonstoichiometry presented a large impact on the electrical and electrochemical properties. The results can be rationalized according to the type of chemical defects that characterize these interfaces:
    - In the thin films dominated by GB_{def} (B/A<0.9), the electronic conductivity was severely hindered by the presence of these interfaces in the entire temperature range measured (83 – 873 K) (Chapter **4**). The simultaneous lack of Mn and O impedes the low temperature double exchange mechanism, giving rise to highly electronically insulating interfaces and hindering the low temperature metallic behaviour. The Mn deficiency also gives rise to a variable range hopping conduction mechanism at low temperature and a surprising n-type pO_2 behaviour at high temperature. On the other hand, the oxygen mass transport properties were found to be

substantially enhanced by the presence of these GBs, with an increase of diffusivity and surface exchange coefficient up to, respectively, three and two orders of magnitude respect to bulk reference at 923 K (see Chapter **5**). Moreover, for B/A < 0.9, a further decrease of bulk Mn content gives rise to a steep decrease of the activation energy of both diffusion and surface exchange coefficient, which similarly reduce from ~2.5 eV (for B/A = 0.9) to ~1.6 eV (for B/A = 0.85). The results suggest that the enhancement of oxygen surface coefficient is due to the increase of oxygen vacancy concentration in the GBs, which act as a sink providing $V_O^{\bullet\bullet}$ to the surface and accelerating the surface incorporation. Moreover, the GB's oxygen vacancy concentration appears to be modifiable by the decrease of bulk Mn content, corroborating the previously mentioned interrelation between $V_O^{\bullet\bullet}$ and V_{Mn}'''.

- In the thin films dominated by GB_{rich} (B/A>0.9), the electronic conductivity is substantially improved (Chapter **4**). The presence of Mn in the GBs allows the double exchange mechanism to occur, gradually restoring the low temperature metallic behaviour and decreasing the electrical resistivity of more than three orders of magnitude at 150 K (in the range B/A = 0.85 – 1.03). Also, the expected p-type pO_2 behaviour is observed for these interfaces, meaning that a bulk type equilibration mechanism takes place. Nevertheless, GB_{rich}-dominated thin films still present a substantial of increase of oxygen mass transport properties respect to the bulk LSM (up to two orders of magnitude for oxygen diffusivity and one for surface exchange coefficient at 923 K), although somehow reduced respect to GB_{def}-dominated thin films (Chapter **5**). Moreover, varying the Mn content in this compositional region (B/A = 0.9 - 1.1) was observed not to affect the diffusivity activation energy, which presented a constant value of ~2.6 eV. The results suggest that the variation of bulk cation concentration does not modify the equilibrium of oxygen vacancies in GB_{rich}. Yet, an increase of *ca.* 4 times of the surface exchange coefficient was observed increasing the bulk Mn concentration from B/A = 0.9 to B/A = 1.1. This increase of surface incorporation observed for high Mn content is believed to be related to an evolution of the surface upon the Mn insertion, rather than an effect of the variation of GB composition.

Overall, the results demonstrate the possibility of actively engineering the electrical and electrochemical properties of $La_{0.8}Sr_{0.2}Mn_yO_{3\pm\delta}$ thin films by tuning their bulk cationic composition.

- **The extension of GB effects to $La_{0.8}Sr_{0.2}(Mn_{1-y}Co_y)_{0.85}O_{3\pm\delta}$ thin films.** The effect of Co insertion in the oxygen mass transport, electrical and optical properties of LSMC polycrystalline thin films has been studied (Chapter **6**). The oxygen self-diffusion and surface exchange coefficient of grain and GBs have been measured by

finite element modelling of isotope exchange depth profiles. The results show that GBs clearly enhance the transport properties of the thin films up to a Co fraction of y = 0.4, with an improvement of oxygen diffusivity and surface exchange coefficient up to, respectively, three and two orders of magnitude respect to bulk values. For higher Co content, the high bulk diffusion conceals the GB effect, hindering the possibility of distinguishing the two pathways. The analysis of in-plane electronic transport suggests that the Co is progressively inserted in the GBs, giving rise, first, to one order of magnitude decrease of electronic conductivity between y = 0 - 0.4, and then, to a progressive improvement of electrical transport due to the onset of the Co-O-Co pathway (y = 0.4 – 1). Finally, the effect of increasing the oxygen vacancies in LSM_y and LSMC on the surface exchange coefficient is discussed, revealing that, when not limited by oxygen vacancies, the electrochemical properties of LSM are as good as, and possibly better, the one of a well-known MIEC material as LSC.

Overall, the results and conclusions derived from this thesis contribute to the controversial debate taken place within the Solid State Ionics community regarding the beneficial/deleterious role of GBs in oxygen mass transport properties. In particular, this thesis: (i.) improves the fundamental understanding of the electrical and electrochemical properties of interfaces in mixed ionic electronic oxides; (ii.) proposes that cationic bulk concentration can be used for engineering the chemical composition and functional properties of GBs in functional oxides; (iii.) opens new strategies for the application of interface dominated thin films for a collection of solid state devices, such as, among others, μSOFCs, sensors, non-volatile random-access memories and supercapacitors.

Appendixes

A. BICUVOX thin films as electrolyte for low temperature μSOFC

A.1 Introduction

In the main body of the thesis, the focus was set on the use of interfaces to improve the electrochemical performances of cathodes MIEC for solid state ionic devices. In this appendix, the enhancement of the electrolyte ionic conductivity is targeted, with special focus on approaching RT operation.

In μSOFC technology, the reduction of the operating temperature has been traditionally pursued by downscaling the traditional SOFC functional layers using thin film technology.[1] In this way, operational temperatures as low as 450 ºC could be attained with Yttria-stabilized Zirconia (YSZ) self-sustained membranes.[2–4] When compared to the typical bulk SOFC working temperatures, such a reduction in temperature undoubtedly meant a significant technological breakthrough, attaining quick and low power consuming start-up processes. However, the new temperature range still entailed important restrictions to the cell performance of TF-SOFCs. First, an operating temperature of ~450 ºC was incompatible with state-of-the-art SOFC ceramic electrodes,[5] limiting the portfolio of possible electrode materials to inherently instable porous metallic films.[3,4,6–8] Also, the integration of TF-SOFCs with additional components of the final portable powering device (reformers, post-combustors, or simply electronics)[9,10] required a full integration of the system microfabrication in CMOS-compatible Si technology, typically restricted to maximum peak temperatures of 450 ºC.[11] This limited the broad implementation of TF-SOFC (and, for similar reasons, also gas microsensors) from both a materials and a microfabrication points of view. Further lowering of the operating temperature is therefore still required, for which we are entailed to look for alternative high oxygen conducting electrolyte materials able to operate at reduced temperatures, eventually room temperature.

Clearly, the number of alternatives to YSZ is very limited, and all come at a cost. Materials with higher ionic conductivity than YSZ at intermediate temperatures usually suffer from fast degradation under reducing conditions, see e.g. ceria-based electrolytes at T > 600 ºC.[12] Among the explored alternatives, it is to be highlighted the BIMEVOX family, as the electrolyte material with the highest ionic conductivity at intermediate temperatures ever reported. Firstly described in 1990 by Abraham et al.,[13] BIMEVOX presents a layered aurivillius structure consisting of alternating $\{Bi_2O_2\}^{2+}$ and transition metal-doped perovskite $\{VO_{3.5}\square_{0.5}\}^{2-}$ layers, see Figure 1a. The high presence of disordered oxygen vacancies in the perovskite sheets is the responsible for the high oxygen mobility, which is maximized when stabilizing the tetragonal γ-phase. In the undoped parent compound $Bi_4V_2O_{11}$, temperatures below 550 ºC lead to the formation of additional monoclinic α and orthorhombic β phases with lower conductivity;[14] however, doping with different transition metals has been proved to successfully stabilize the γ-phase down to room temperature. Among the different options, BICUVOX (which stands for the corresponding BIMEVOX doped with Cu and formula $Bi_4V_{1.8}Cu_{0.2}O_{10.7}$, for a typical 10 mol. % doping) was shown to present the highest ionic conductivity.[13] However, a non-trivial electronic conductivity already at

intermediate temperatures (T ~ 500 ºC),[15] irreversible phase changes under reducing atmospheres[16] and a high thermal expansion coefficient[17] drastically hindered the broad application of the material in final cells. Consequence of this, the material was practically abandoned by the end of that decade, except for its use in oxygen separation membranes.[18,19]

However, the possibility of fabricating thin film devices, in which the operating temperature can be significantly lowered, opens the door to explore such an outstanding material in a new low temperature range (approaching RT), where the chemical instability is expected to be significantly hindered. Despite the promising possibilities for low temperature applications, three decades after the discovery of the high ionic conductivity of BIMEVOX only a few works have dealt with the thin film deposition of this material (thickness < 500 nm, low temperature processing),[20,21] and a study of the electrochemical performance at this temperature range is still lacking. In this work, we optimized the deposition of BICUVOX thin films by means of Pulsed Laser Deposition (PLD) using a large area system (LA-PLD) and we studied its electrochemical performance at T = 50 – 450 ºC. On one side, we extend previous works and show the tremendous capabilities of PLD for tuning the stoichiometry in this type of films, simply changing the deposition conditions. Then, we present the conduction properties of the optimized films, by measuring its oxygen conductivity as a function of temperature. Noting the layered crystal structure of BICUVOX with oxide ionic diffusion taking place mainly along the $\{VO_{3.5}\square_{0.5}\}^{2-}$ layers, we investigated the anisotropy in the conduction by preparing epitaxial films and measuring their conductivity in orthogonal directions (parallel and perpendicular to the perovskite sheets).

A.2 Deposition and characterization of BICUVOX thin films

A.2.1 Optimization of deposition conditions

For this thesis, BICUVOX thin films were prepared by LA-PLD. The optimization of PLD deposition of BICUVOX thin films was carried out by preparing a set of polycrystalline films Si (100) coated with Si_3N_4 (300 nm) / SiO_2 (100 nm) dielectric bilayer (thickness ranging from 100 to 300 nm) under varying depositing conditions, *viz.* background oxygen pressure (p) and target-to-substrate distance (d). Other parameters such as deposition temperature and laser fluence were previously optimized for obtaining homogeneous crystalline films and then intentionally set constant, at 600 ºC and 0.45 $J \cdot cm^{-2}$ respectively. Thin films were grown from a home-made $Bi_4V_{1.8}Cu_{0.2}O_{10.7}$ target, p was varied from 0.0067 to 0.267 mbar and two target-to-substrate distances were studied, d = 9 and 11 cm (note the longer distances typically used in LA-PLD systems compared to "standard" research-scale PLD systems).[22] Dense and homogeneous films were obtained within the whole experimental window of pressures and distances, see representative top view Scanning Electron Microscopy

(SEM) images in **Figure A.1a-f**, for selected background oxygen pressures and $d = 11$ cm.

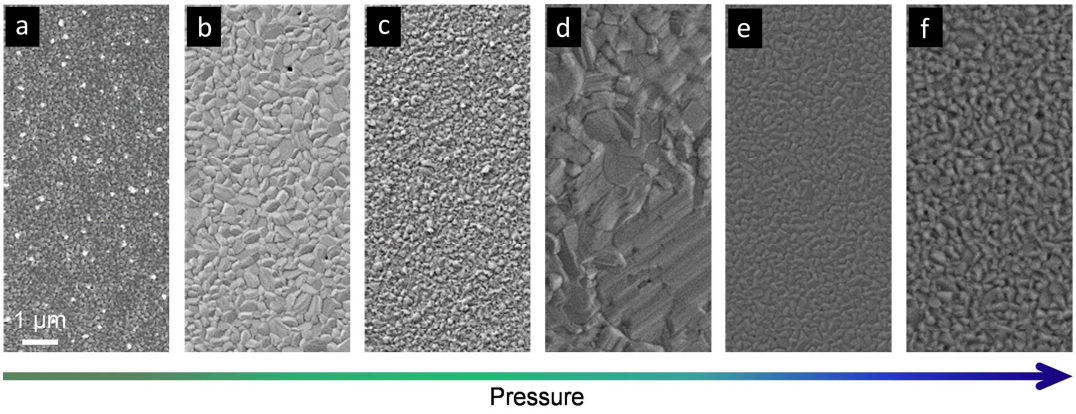

Figure A.1 Top view SEM images of representative films deposited by PLD at different background pressures (p = 0.0067 – 0.267 mbar) and a constant target-to-substrate distance of 11 cm, on top of Si substrates

After proving the full density and homogeneity of the films, we focused on the stoichiometric analysis of the deposited films, studied by Energy-Dispersive X-Ray spectroscopy (EDX), **Figure A.2a** (specific films were also measured by Wavelength Dispersive Spectroscopy, WDS, confirming the trends). Here, we observed an evolution of the cationic ratio Bi/V as a function of the pressure in analogy with similar representations in the literature involving depositions of heavy *vs.* light elements (H/L).[23] We differentiate four different regions; a first region A for low p below 0.0267 mbar, where Bi deficient films are obtained; a region B ($p \approx 0.0267$ mbar), where a good stoichiometry is maintained; a region of intermediate pressures C ($0.0267 < p < 0.187$ mbar) in which an important V deficiency is observed; and a final region D at higher pressures ($p > 0.187$ mbar), where the film approaches again the target stoichiometry. The observed trend matches well with the expected plume dynamics as a function of the background pressure, also noticed for other complex oxide materials with significantly different cationic sizes (see Chapter **2**).[23,24] In short, at lower background pressures weak scattering is expected in the laser plume for all the species independently on their size, so the stoichiometry can be well maintained. With increasing pressure, scattering is expected to affect greater to the lighter species (V in our case), giving rise to off-stoichiometric films (light element-deficient). If we keep increasing the background pressure, heavy elements (Bi) start to scatter as well and the plume ends up in a diffusion front in which the correct stoichiometry is recovered, and thus in the films (region D). In our case, two pressure regions are clearly identified as ideal for obtaining stoichiometric BICUVOX films, regions B ($p = 0.0267$ mbar) and D ($p > 0.187$ mbar).

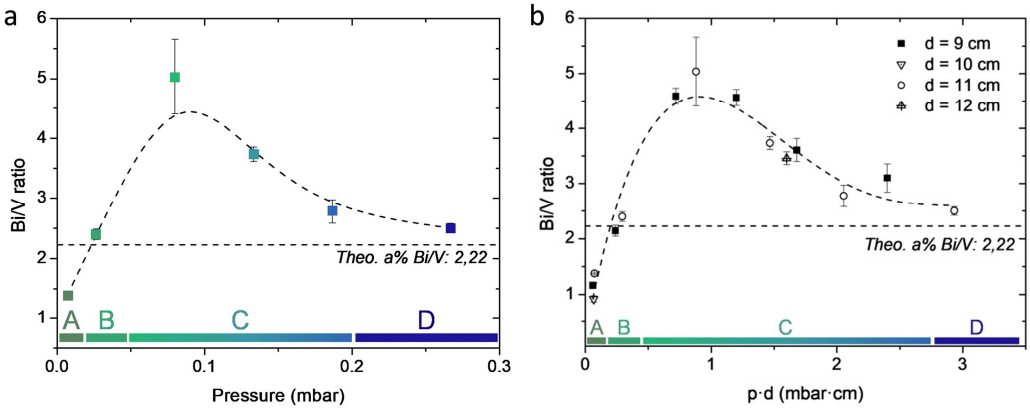

Figure A.2 a, Bi/V ratio in PLD-deposited BICUVOX films as a function of deposition pressure, at a target-to-substrate distance of 11 cm. **b**, Bi/V ratio versus p·d (background oxygen pressure times target-to-substrate distance) in PLD-deposited BICUVOX films at different distances and deposition pressure.

Interestingly, all the films deposited at different pressure and with different target-to-substrate distances fell in the same trend when plotted as a function of background oxygen pressure times target-to-substrate distance, $p{\cdot}d$ (see **Figure A.2b**). In this figure, we collected the data from the two set of samples, at d = 9 cm and d = 11 cm with varying background pressure, and we added two extra points at d = 10 cm and d = 12 cm to confirm the goodness of the hypothesis. The single trend observed in **Figure A.2b** for different target-to-substrate distances confirms the hypothesis that the thin film composition is mainly dominated by plume dynamics. Indeed, the scattering events of the plasma species with the background gas are dependent on both the pressure in the chamber and the distance travelled as the plume expands towards the substrate. This is particularly marked at high pressure, where the diffusive deposition regime starts to take place (regions C – D).

The presence of a Bi-deficient region at the lowest deposition pressure (region A) is probably related to the high volatility of Bi, which would provoke that at low background pressures, where no collisions are expected in the plume, Bi simply flies away.[25] Noteworthy, the great stoichiometric tuning capabilities achieved here with PLD is not only relevant for the deposition of BICUVOX, but it can be extended to the deposition of other relevant Bi-based complex oxides such as $BiVO_4$, $BiFeO_3$ or Bi_2Te_3 (widely used for photovoltaics,[26] magnetism[27] and thermoelectric[28] applications, respectively) and, more generally, to any solid oxide in which the atomic mass ratio between constituting cations is large.

Regarding the Cu distribution along the film series, no clear trend could be detected with the background pressure. However, we could identify the presence of homogeneously distributed Cu-rich micrometre-size particles (probably CuO) in the low-pressure regime, p = 0.0067 – 0.0267 mbar. Analogously, in these films (and opposed to the films deposited at higher pressures) it was impossible to detect Cu out of these particles, suggesting that Cu could not be successfully integrated in the material and that the films deposited at low p are composed by undoped $Bi_4V_2O_{11}$.

X-Ray Diffraction (XRD) and Raman spectroscopy were carried out in order to analyse the phase evolution through the film series, and the correlation between Bi/V ratio and phase stabilization (**Figure A.3a** and **b**). Indeed, the appearance of expectable secondary phases is clearly observed in the films with stoichiometry distant from the targeted one. Analysing the XRD pattern in **Figure A.3a**, one can observe: (*i.*) the appearance of a Bi-deficient $BiVO_4$ phase at low deposition pressures ($p < 0.0267$ mbar, region A), probably a mix of clinobisvanite and dreyerite phases,[29] and (*ii.*) the presence of Bi_2O_3 in the V-deficient region C, $0.0267 < p < 0.187$ mbar (peaks marked as *). Moreover, even though the desired stoichiometry was measured in films deposited in region B, XRD revealed the presence of additional reflections (see *e.g.* the triplet peak at $2\theta \approx 28º$), presumably due to the aforementioned non-incorporation of Cu in the aurivillius structure and a subsequent non-stabilization of the tetragonal γ-phase. Contrary, at the highest deposition pressures, $p > 0.187$ mbar, single γ-$Bi_4V_{1.8}Cu_{0.2}O_{10.7}$ phase could only be detected.

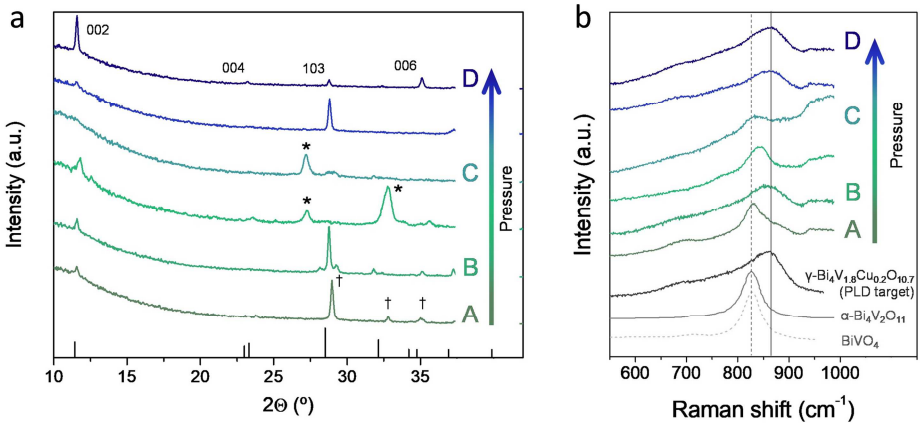

Figure A.3 a, X-Ray diffractogram obtained for the same BICUVOX film series. Main diffractions of the γ-$Bi_4V_2O_{11}$ phase are indicated (ICDD reference code 00-048-0273), as well as the appearance of secondary phases (Bi_2O_3 *, $BiVO_4$ †). **b,** Raman spectra of the BICUVOX film series, plus references for γ-$Bi_4V_{1.8}Cu_{0.2}O_{10.7}$ (measured on the pellet used as PLD target),[30] α-$Bi_4V_2O_{11}$[31] and $BiVO_4$.[29]

Similar conclusions can be drawn by Raman spectroscopy, **Figure A.3b**. In fact, it is to be highlighted the goodness of Raman spectroscopy for identifying phase formation in the $Bi_4V_2O_{11}$ family, since a clear shift in wavenumber, from ~ 860 cm^{-1} to ~ 830 cm^{-1}, happens when moving from the tetragonal γ-phase to monoclinic α-phase (see difference between the γ-$Bi_4V_{1.8}Cu_{0.2}O_{10.7}$, measured in the pellet used as PLD target and perfectly matching previous reports,[30] and the α-$Bi_4V_2O_{11}$ from ref. [31]). This way, we could clearly identify the presence of the desired tetragonal phase in the films deposited at high pressure, region D ($p > 0.187$ mbar). Meanwhile, α-$Bi_4V_2O_{11}$ was detected in the intermediate pressures, and $BiVO_4$ was presumably measured at the lowest pressure tested (note here that similar spectra have been reported for both α-$Bi_4V_2O_{11}$ and $BiVO_4$, making impossible to differentiate them by this technique). Surprisingly, at $p \approx 0.0267$ mbar Raman spectroscopy also shows the stabilization of the γ-phase, even though Cu is apparently not well incorporated in the structure. Still, we

can conclude that XRD and Raman results fully support, from a structural point of view, the stoichiometric evolution previously observed, and suggest the need of high background pressures of p > 0.187 mbar for the stabilization of the aurivillius BICUVOX γ-phase.

A.2.2 Deposition of epitaxial BICUVOX thin films

Based on this, we additionally prepared epitaxial BICUVOX films grown on (001)-oriented $SrTiO_3$ substrates (undoped – STO and doped with 1.0 at.% Nb – Nb:STO) by LA-PLD, at the optimum deposition pressure of p = 0.267 mbar. **Figure A.4a** shows a representative XRD pattern of a 36 nm-thick BICUVOX film deposited on Nb:STO. The appearance of a set of reflections corresponding to the (00L) family of planes reveals a perfect epitaxial growth of the tetragonal aurivillius γ-phase, (00L)-oriented in the c-axis. Interestingly, an additional set of low intensity peaks (at least 10^3 times lower than the main reflections) is observed in the epitaxial film between the (00L) reflections. The position of this peak and, in general, of all the set of low intensity peaks matches well with the expected positions of the odd (00L) reflections of the BICUVOX. This could be related to small alterations of the material´s symmetry derived from strain or other structural defects, or to second order effects in the crystal due to inelastic scattering. The φ-scan presented in the inset of **Figure A.4a** confirms a cube-on-cube growth of the tetragonal BICUVOX on top of Nb:STO with perfect match of the (100) planes of both materials, see schematics in **Figure A.4c**. Note the almost identical in-plane lattice parameter of BICUVOX, $a_{BICUVOX}$ = 3.907 Å,[13] as compared to the cubic STO, a_{STO} = 3.905 Å, meaning a lattice mismatch of only +0.05%. The epitaxy was confirmed by performing high resolution XRD reciprocal space maps (RSM), see **Figure A.4b**. The figure shows the coexisting reflections (-103) of the Nb:STO and (-1011) of the BICUVOX, revealing a perfect in-plane matching thanks to the very similar in-plane lattice parameters. The same conclusions holds also for the BICUVOX film deposited on undoped – STO.

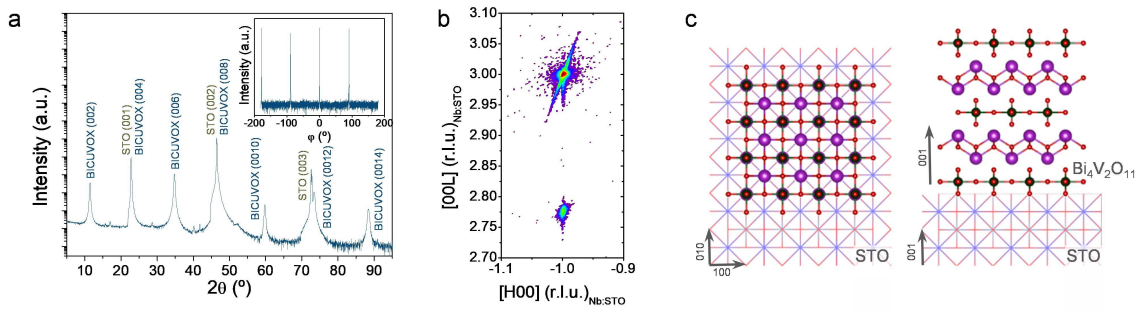

Figure A.4 a Out-of-plane θ-2θ X-Ray Diffraction pattern, where the set of peaks corresponding to the 00L reflections is visible. A φ scan around the (-103) reflection of $SrTiO_3$ is also included in the inset, showing a 4-fold symmetry corresponding to a single in-plane orientation (100) BICUVOX / (100) $SrTiO_3$. **b**, in-plane Reciprocal Space Map around the -103 reflection peak of the Nb-doped $SrTiO_3$ substrate. **c**, Schematic representations of the epitaxial growth of γ-$Bi_4V_2O_{11}$ on top of 001-oriented $SrTiO_3$ single crystals, top and cross-sectional views.

Furthermore, the quality of the films was analysed by top-view non-contact AFM images, **Figure A.5**. The images showed a clear formation of terraces, typical of layer by layer growth,[20] and a complete absence of significant defects or particulates in the top surface. The height profile obtained along the top surface (black dashed arrow in **Figure A.5b**) revealed very small steps of ~ 3.5 Å, see **Figure A.5c**. These steps are clearly smaller than the out-of-plane lattice parameter ($c_{BICUVOX}$ = 15.44 Å, as calculated from the out-of-plane XRD pattern and matching previous literature).[13] We speculate that these steps correspond to single $\{Bi_2O_2\}^{2+}$ or $\{VO_{3.5}\square_{0.5}\}^{2-}$ sub-layers, 4 every unit cell, thus matching the obtained average value. In conclusion, we were able to grow high quality epitaxial BICUVOX films in two functional substrates, one dielectric (STO), one conductive (Nb:STO), ideal for further electrochemical analysis.

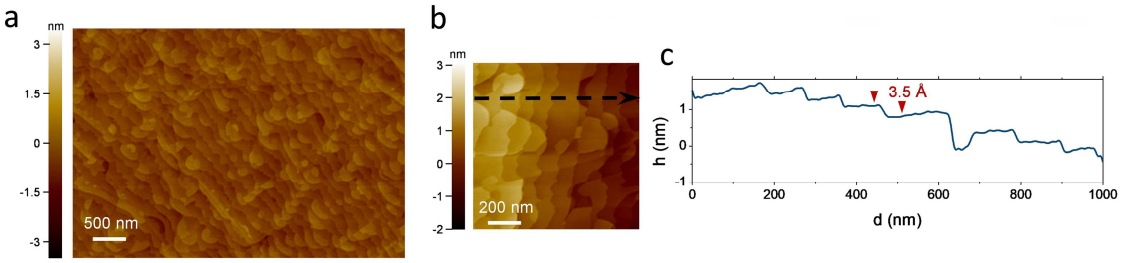

Figure A.5 a,**b** AFM images of an epitaxial BICUVOX film grown on top of Nb-doped $SrTiO_3$, with two different magnifications. **c**, Height profile corresponding to the black dashed arrow shown in figure **b**. The average step height is shown as well (only single step terraces are considered for the average calculation).

A.3 Electrical characterization of BICUVOX thin films

Ionic conductivity in the whole set of BICUVOX films was investigated by means of Electrochemical Impedance Analysis (EIS). Epitaxial (on STO-based substrates) and polycrystalline (on $Si_3N_4/SiO_2/Si$ substrates) films were measured in a temperature range from 50 to 450 ºC, under ambient conditions. The analysis presented here is restricted to the epitaxial and polycrystalline thin films deposited at the optimum pressure range, p = 0.267 mbar. **Figure A.6** collects schematics of the two measuring configurations employed, *viz.* in-plane measurements for polycrystalline (on $Si_3N_4/SiO_2/Si$ substrates) and epitaxial (on undoped STO) films, and cross-plane measurements for epitaxial films (on Nb-doped STO substrates). In all the cases, top Au microelectrodes were defined by photolithography in order to reach short electrode-to-electrode distances (for the in-plane configuration, down to d = 100 µm) or small well-defined circular shapes (for cross-plane, radius from to 50 to 500 µm).

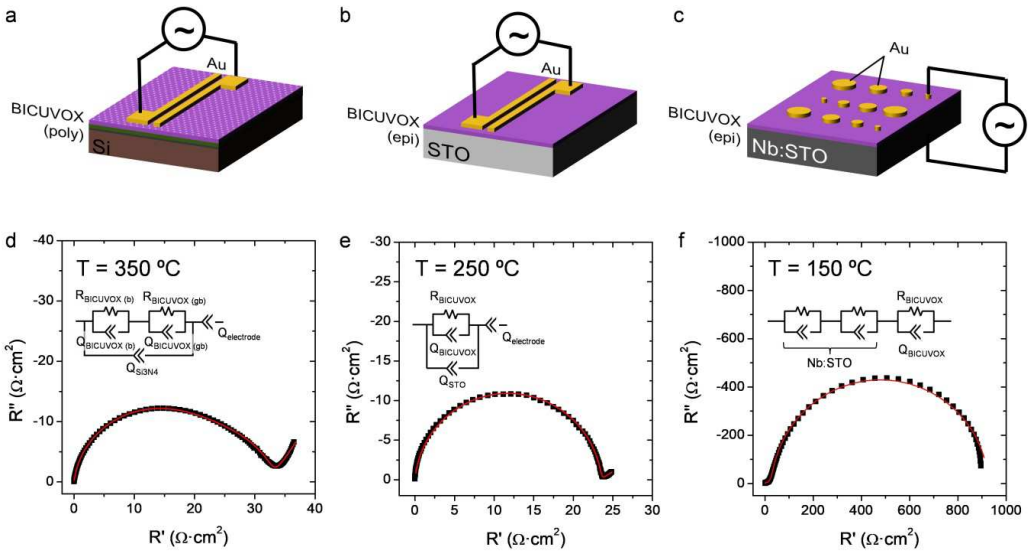

Figure A.6 Measuring configurations and representative Nyquist plots for the different types of BICUVOX films: **a**,**d** polycrystalline BICUVOX on top of $Si_3N_4/SiO_2/Si$ (in-plane measurements), **b**,**e** epitaxial BICUVOX on top of undoped STO for in-plane measurements and **c**,**f** epitaxial BICUVOX on top of Nb-doped STO for cross-plane measurements. Black squares correspond to the experimental data measured by EIS and red lines to the fitting. Equivalent circuits are included as insets and measuring temperatures are also indicated.

Representative Nyquist plots at selected temperatures are also included in the figure. In polycrystalline BICUVOX films, three different contributions could be identified, see **Figure A.6d**. Two overlapped RQ elements could be differentiated at high-to-medium frequencies, that could presumably be associated to bulk and grain boundary contributions. However, in this type of measurements the stray capacitance determined by the substrate is commonly convoluting all the single contributions from the thin film, making very difficult to interpret the results in terms of grain and grain boundary contributions. Moreover, in the case of BICUVOX different thin films orientations would determine different bulk conductivities, making challenging the confrontation among single contributions in the polycrystalline films. Therefore, in this study we decided to focus in the total resistance (sum of grain and grain boundary contributions). At low frequencies, an additional constant phase element (Q) typical of Au blocking electrodes is observed.

In the in-plane measurements of epitaxial films, only one contribution to the BICUVOX ionic conductivity is observed (**Figure A.6e**). Although again the stray capacitance of the STO might play a role masking different contributions, this matches well with the absence of grain boundaries expected for the epitaxial films. It is therefore assumed that this contribution corresponds to the bulk conductivity of BICUVOX. The contribution of the Au blocking electrodes at low frequencies is equally observed in these films. Finally, the cross-plane measurements of epitaxial BICUVOX films on top of Nb:STO (**Figure A.6f**) also shows the presence of one single contribution associated to the film. Additional small contributions are always detected at high frequencies, and are assumed to come from the Nb:STO substrate.

Figure A.7 presents the Arrhenius representation of the conductivity evolution with temperature extracted from the EIS study. The obtained results are compared with reference bulk polycrystalline BICUVOX, as well as single crystal BICUVOX in two directions (parallel and perpendicular to the $(100)_{BICUVOX}$ planes) and, finally, YSZ and Gd-doped CeO_2 (CGO) thin film conductivity.[2,32–34]

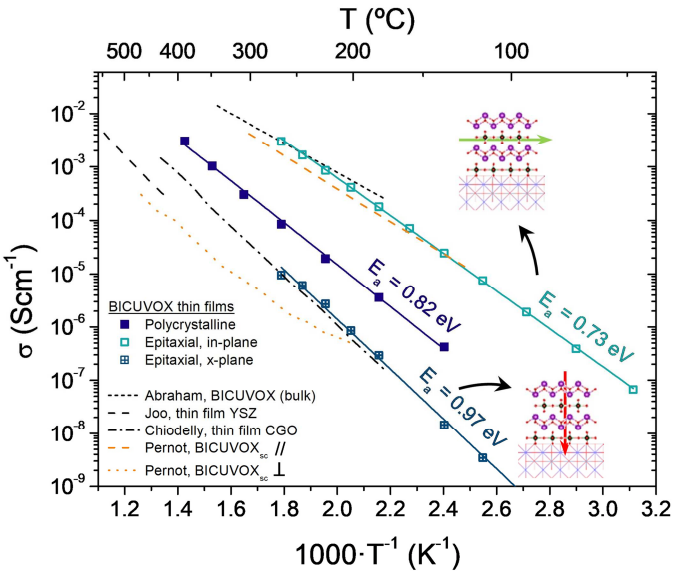

Figure A.7 a, Arrhenius representation of the evolution of ionic conductivity for different BICUVOX (polycrystalline, epitaxial) films with temperature, all deposited at p = 0.267 mbar. References for bulk polycrystalline BICUVOX,[13] single crystal BICUVOX (parallel and perpendicular to the $(100)_{BICUVOX}$ planes)[35], YSZ thin film[2,34] and CGO thin film[32,33] are included for comparison. Inset schematics show the direction of oxygen mobility in the two measuring configurations, for the epitaxial films. Activation energies (E_a) are also indicated for the measured films.

Although significant differences are found among the different films, all present an improvement in terms of ionic conduction *vs.* state-of-the-art YSZ and CGO, especially when reducing temperature (due to the lower activation energies, E_a). The highest conductivity is clearly obtained in the epitaxial BICUVOX film when measuring in-plane, followed by the polycrystalline film and, finally, the epitaxial measured cross-plane. A strong anisotropy is measured in the epitaxial films depending on the direction, with more than two orders of magnitude higher in-plane conductivity than cross-plane. This matches well with the obtained results from XRD, **Figure A.4**, since enhanced oxygen mobility in BICUVOX is known to happen along the $\{VO_{3.5}\square_{0.5}\}^{2-}$ sub-layers, *i.e.* in the direction parallel to the substrate surface (in-plane), and hindered when crossing the $\{Bi_2O_2\}^{2+}$ sub-layers, *i.e.* in the $(001)_{BICUVOX}$ direction, across the film.[35,36] As for the activation energies (E_a), one single mechanism could be observed for the whole range of measuring temperatures, with slightly higher activation energy for the cross-plane than for the in-plane conduction. The obtained values match well with previous reports in this range of temperatures,[35] pointing at the ionic nature of the conduction in the films. The slightly higher values obtained here could be related to the plausible presence of structural defects in the films or small off-stoichiometries.

Interestingly, the polycrystalline film presents an intermediate conductivity and activation energy, probably derived from the random orientation of the grains and the presence of grain boundaries.

The measured in-plane conductivity for the epitaxial film goes in line with literature values for bulk BICUVOX, confirming the outstanding oxide ionic conductivity of this material. Notably, these results position the prepared films as the thin film material with highest ionic conductivity ever reported for low temperature applications (T < 300 ºC), with important implications for their application in advanced thin film-based devices. As an example, we can forecast possible operation of a BICUVOX-based TF-SOFC at temperatures below 150 ºC, estimated on the basis of a 100 nm-thick electrolyte film and a target Area-Specific Resistance of 0.15 $\Omega \cdot cm^2$ for the electrolyte.[37] This means a reduction of approximately 300 ºC *vs.* the current state-of-the-art (~ 450 ºC) and, noteworthy, an operation within the temperature operation range of CMOS-based micro-systems. Furthermore, radically new all solid state electrochemically-driven memories based on BICUVOX and operating at room temperature can be also anticipated.

Clearly, apart from the outstanding oxide ionic conductivity, low temperature operation with BICUVOX films (especially for applications in powering devices) requires high stability in a wide range of pO_2, from oxidizing to highly reducing atmospheres. In fact, as commented before, this has been the main drawback of BICUVOX hindering its use as electrolyte material in the past. Here, we therefore study the stability *vs.* pO_2 of the utmost performing BICUVOX epitaxial film, in the new operating temperature range, T < 300ºC. **Figure A.8** presents the in-plane conductivity measured by EIS at different temperatures, from 150 ºC to 350 ºC, and oxygen partial pressures, from pO_2 = 0.21 bar (synthetic air) to $pO_2 = 10^{-19}$ bar (5 vol.% H_2 in Ar). For temperatures below 300 ºC, the figure shows great stability (flat profiles) within the whole range of pO_2 (from oxidizing to highly reducing conditions), proving the effectiveness of the material to be used in thin film-based low temperature operating devices. The maximum operating temperature for epitaxial BICUVOX is set in this study at T = 350 ºC, since a clear effect on the conductivity is observed there when reducing pO_2. It is important to note, though, that the observed trend matches well with an unexpected p-type conduction behaviour. The origin of this conduction comportment at this temperature range requires attention and will be a matter of discussion in further works.

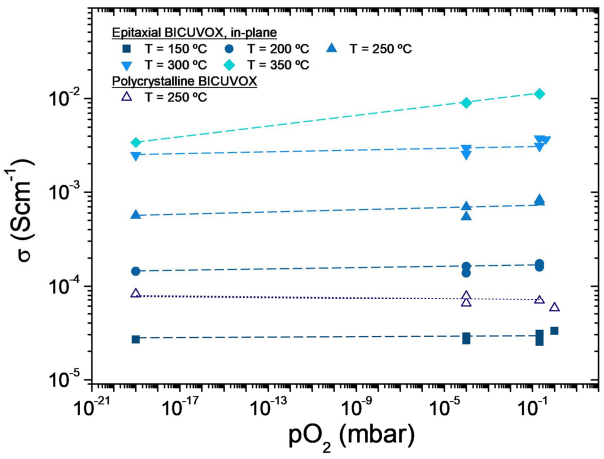

Figure A.8 pO_2 dependence of BICUVOX in-plane conductivity, measured in an epitaxial film at different temperatures (T = 150 – 350 ºC) and in a polycrystalline sample at T = 250 ºC. Oxygen partial pressure is measured by an oxygen sensor at the outlet of the gases. Dashed lines are included as guide for the eyes.

Finally, we would like to raise a flag for the BICUVOX polycrystalline films. Although not as outstanding as the in-plane conductivity measured in the epitaxial film (between one and two orders of magnitude lower), this material already represents an important reduction of ~150 ºC and ~100 ºC *vs.* YSZ and CGO respectively, with a potential operating temperature below 300 ºC. Taking into account that for certain applications this microstructure might be significantly easier to implement than an epitaxial film (*e.g.* in the already existing TF-SOFC systems), polycrystalline BICUVOX are expected to play a crucial role in future low temperature devices too. Noteworthy, we also carried out stability tests in these films, proving the viability of the material in the operating temperature range (T = 250 ºC), see the negligible conductivity changes vs. pO_2 in **Figure A.8**.

A.4 Conclusions

In conclusion, BICUVOX thin films are presented in this appendix as a superior oxygen conducting electrolyte material, for their application in low temperature operating electrochemical solid-state devices. First, epitaxial BICUVOX films proved to have the highest oxide ion conductivity ever reported at this temperature range (T < 300 ºC), when measuring parallel to the $\{VO_{3.5}\square_{0.5}\}^{2-}$ planes. The high ionic conductivity and high stability with pO_2 shown anticipates its potential use down to room temperature, in a new family of non-heated solid-state electrochemical systems. Importantly, the use of this material opens up remarkable possibilities for the fabrication of solid-state devices fully integrated in CMOS processing technologies and with possible encapsulation in plastics. Finally, it is to be highlighted as well the enormous tuning capabilities of PLD for the deposition of Bi-based complex oxides, being able to easily vary the film stoichiometry by simply changing the background pressure in the chamber.

References

1. Beckel, D. *et al.* Thin films for micro solid oxide fuel cells. *J. Power Sources* **173,** 325–345 (2007).
2. Garbayo, I. *et al.* Electrical characterization of thermomechanically stable YSZ membranes for micro solid oxide fuel cells applications. *Solid State Ionics* **181,** 322–331 (2010).
3. Kerman, K., Lai, B. & Ramanathan, S. Pt/Y 0.16 Zr 0.84 O 1.92/Pt thin film solid oxide fuel cells: Electrode microstructure and stability considerations. *J. Power Sources* **196,** 2608–2614 (2011).
4. An, J., Kim, Y.-B., Park, J., Gür, T. M. & Prinz, F. B. Three-Dimensional Nanostructured Bilayer Solid Oxide Fuel Cell with 1.3 W/cm2 at 450 °C. *Nano Lett.* **13,** 4551–4555 (2013).
5. Garbayo, I. *et al.* Porous La0.6Sr0.4CoO3-δ thin film cathodes for large area micro solid oxide fuel cell power generators. *J. Power Sources* **248,** 1042–1049 (2014).
6. Kerman, K., Lai, B. K. & Ramanathan, S. Free standing oxide alloy electrolytes for low temperature thin film solid oxide fuel cells. *J. Power Sources* **202,** 120–125 (2012).
7. Takagi, Y., Adam, S. & Ramanathan, S. Nanostructured ruthenium – gadolinia-doped ceria composite anodes for thin film solid oxide fuel cells. *J. Power Sources* **217,** 543–553 (2012).
8. Tsuchiya, M., Lai, B.-K. & Ramanathan, S. Scalable nanostructured membranes for solid-oxide fuel cells. *Nat. Nanotechnol.* **6,** 282–6 (2011).
9. Pla, D. *et al.* Is it possible to design a portable power generator based on micro-solid oxide fuel cells? A finite volume analysis. *J. Power Sources* **293,** 264–273 (2015).
10. Scherrer, B. *et al.* A thermally self-sustained micro-power plant with integrated micro-solid oxide fuel cells, micro-reformer and functional micro-fluidic carrier. *J. Power Sources* **258,** 434–440 (2014).
11. Sedky, S., Witvrouw, A., Bender, H. & Baert, K. Experimental determination of the maximum post-process annealing temperature for standard CMOS wafers. *IEEE Trans. Electron Devices* **48,** 377–385 (2001).
12. Goodenough, J. B. Oxide-Ion Electrolytes. *Annu. Rev. Mater. Res.* **33,** 91–128 (2003).
13. Abraham, F., Boivin, J. C., Mairesse, G. & Nowogrocki, G. BIMEVOX series. A new family of high performances oxide ion conductors. *Solid State Ionics* **40–41,** 934–937 (1990).
14. Abraham, F., Debreuille-Gresse, M. F., Mairesse, G. & Nowogrocki, G. Phase transitions and ionic conductivity in $Bi_4V_2O_{11}$ an oxide with a layered structure. *Solid State Ionics* **28–30,** 529–532 (1988).
15. Iharada, T. *et al.* Electrochemical characterization of BIMEVOX oxide-ion conductors. *Solid State Ionics* **48,** 257–265 (1991).
16. Guillodo, M., Fouletier, J., Dessemond, L. & Del Gallo, P. Redox stability of BIMEVOX.10 materials (ME=Co, Cu). *Electrochim. Acta* **47,** 2809–2815 (2002).
17. Steil, M. C. *et al.* Thermal stability and preparation of dense membrane ceramics of BIMEVOX. *Solid State Ionics* **176,** 2305–2312 (2005).
18. Boivin, J. C. *et al.* Electrode–electrolyte BIMEVOX system for moderate temperature oxygen separation. *Solid State Ionics* **113–115,** 639–651 (1998).

19. Paydar, M. H., Hadian, A. M. & Fafilek, G. A new look at oxygen pumping characteristics of BICUVOX.1 solid electrolyte. *J. Mater. Sci.* **41,** 1953–1957 (2006).

20. Sant, C. & Contour, J. P. Pulsed laser deposition of $Bi_2Cu_{2x}V_{2(1-x)}O_{11}$ thin films. *J. Cryst. Growth* **153,** 63–67 (1995).

21. Trzciński, K. *et al.* Optical and photoelectrochemical characterization of pulsed laser deposited $Bi_4V_2O_{11}$, BICUVOX, and BIZNVOX. *Thin Solid Films* **638,** 251–257 (2017).

22. Ojeda-G-P, A., Schneider, C. W., Döbeli, M., Lippert, T. & Wokaun, A. Plasma plume dynamics, rebound, and recoating of the ablation target in pulsed laser deposition. *J. Appl. Phys.* **121,** 135306 (2017).

23. Amoruso, S. in *Metal Oxide-Based Thin Film Structures* 133–160 (Elsevier, 2018). doi:10.1016/B978-0-12-811166-6.00006-6

24. Schneider, C. W., Wokaun, A., Lippert, T., Döbeli, M. & Ojeda-G-P, A. The importance of pressure and mass ratios when depositing multi-element oxide thin films by pulsed laser deposition. *Appl. Surf. Sci.* **389,** 126–134 (2016).

25. Havelia, S., Wang, S., Skowronski, M. & Salvador, P. A. Controlling the Bi content, phase formation, and epitaxial nature of $BiMnO_3$ thin films fabricated using conventional pulsed laser deposition, hybrid pulsed laser deposition, and solid state epitaxy. *J. Appl. Phys.* **106,** 123509 (2009).

26. Song, J. *et al.* Non-Equilibrium Deposition in Epitaxial $BiVO_4$ Thin Film Photoanodes for Improving Solar Water Oxidation Performance. *Chem. Mater.* **30,** 5673–5681 (2018).

27. Wu, J., Fan, Z., Xiao, D., Zhu, J. & Wang, J. Multiferroic bismuth ferrite-based materials for multifunctional applications: Ceramic bulks, thin films and nanostructures. *Prog. Mater. Sci.* **84,** 335–402 (2016).

28. Hu, L., Zhu, T., Liu, X. & Zhao, X. Point Defect Engineering of High-Performance Bismuth-Telluride-Based Thermoelectric Materials. *Adv. Funct. Mater.* **24,** 5211–5218 (2014).

29. Frost, R. L., Henry, D. A., Weier, M. L. & Martens, W. Raman spectroscopy of three polymorphs of $BiVO_4$: clinobisvanite, dreyerite and pucherite, with comparisons to $(VO_4)_3$-bearing minerals: namibite, pottsite and schumacherite. *J. Raman Spectrosc.* **37,** 722–732 (2006).

30. Bacewicz, R. & Kurek, P. Raman scattering in BIMEVOX (ME=Mg, Ni, Cu, Zn) single crystals. *Solid State Ionics* **127,** 151–156 (2000).

31. Kumar, S. & Sahare, P. D. Photocatalytic activity of bismuth vanadate for the degradation of organic compounds. *Nano* **08,** 1350007 (2012).

32. Chiodelli, G., Malavasi, L., Massarotti, V., Mustarelli, P. & Quartarone, E. Synthesis and characterization of $Ce_{0.8}Gd_{0.2}O_{2-y}$ polycrystalline and thin film materials. *Solid State Ionics* **176,** 1505–1512 (2005).

33. Rupp, J. & Gauckler, L. Microstructures and electrical conductivity of nanocrystalline ceria-based thin films. *Solid State Ionics* **177,** 2513–2518 (2006).

34. Joo, J. H. & Choi, G. M. Electrical conductivity of YSZ film grown by pulsed laser deposition. *Solid State Ionics* **177,** 1053–1057 (2006).

35. Pernot, E. *et al.* Structure and conductivity of Cu and Ni-substituted Bi4V2O11. *Solid State Ionics* **70–71,** 259–263 (1994).

36. Kurek, P., Dygas, J. R. & Breiter, M. W. Temperature and time dependence of conductivity of single crystals of BICUVOX. *Solid State Phenom.* **39–40,** 247–250 (1994).

37. Brandon, N. P., Skinner, S. & Steele, B. C. H. Recent advances in materials for fuel cells. *Annu. Rev. Mater. Res.* **33,** 183–213 (2003).

B. In-situ ellipsometry study of the electronic structure of $La_{0.8}Sr_{0.2}FeO_{3-\delta}$ as a function of the oxygen partial pressure

B.1 Introduction

Different techniques have been proposed for the in-situ analysis of defect chemistry in oxide thin films. The most common way to get insights into the defect chemistry is to analyse the electronic conductivity as a function of pO_2 (see Chapter **4**). Nevertheless, this method is incapable of separating the electronic charge carrier from the electronic mobility, which may both vary with the pO_2.[1] Another interesting method is the study of the chemical capacitance in a thin film deposited on an ionic conductor by EIS.[2–4] Yet, the high polarization resistance of the surface reactions (in parallel to the chemical capacitance) hinders the application of this technique at low temperature, because the large relaxation time of the process undermines the precision of the measurements. Optical transmission was also proposed to measure the concentration of point defects in acceptor- and donor-doped $SrTiO_3$[5,6] and Pr-doped Ceria.[7] This optical approach offers great advantages in the understanding of oxygen related phenomena but presents some disadvantages that limit its applicability, such as the need of a transparent substrate and the difficulties in deconvoluting the different optical transitions.

In this appendix, an ellipsometry *in-situ* analysis of the optical and electrical properties of $La_{0.8}Sr_{0.2}FeO_{3-\delta}$ (LSF) thin films as a function of oxygen partial pressure is presented. It is shown that by varying the oxygen concentration in the thin films, substantial modifications of the optical spectra develop, which can be used to qualitatively track the presence of electronic holes in the system. The results are also confronted with the behaviour of pO_2 electrical conductivity, evidencing unexpected differences in the two measurement methods. The capability of ellipsometry for the study of defect chemistry of oxides thin films is demonstrated.

B.2 Optical absorption in $La_{1-x}Sr_xFeO_{3-\delta}$

In this section, the optical properties of $La_{1-x}Sr_xFeO_{3-\delta}$ are briefly reviewed. This material has been largely studied due to its possible application in photoelectrochemical water splitting.[8,9] In particular, it must be mentioned the excellent works produced by Steven May and co-workers, who deeply analysed the optical absorption of $La_{1-x}Sr_xFeO_{3-\delta}$ thin films as a function of Sr, Fe and oxygen content.[10–13] Additionally, the electronic structure of this material family was studied by x-ray absorption spectroscopy (XAS) and x-ray photoemission spectroscopy (XPS) by Wadati *et al.*[14,15] and, recently, by Wang *et al.*[16] Smolin *et al.* studied the effect of Sr content on the absorption spectra of $La_{1-x}Sr_xFeO_{3-\delta}$ thin films (see **Figure B.1a**).[12]

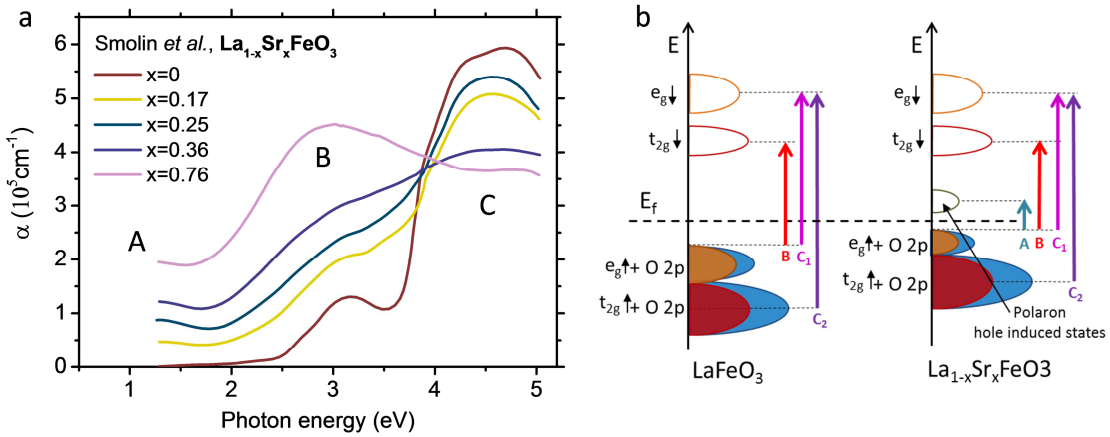

Figure B.1 Optical absorption in $La_{1-x}Sr_xFeO_{3-\delta}$ thin films for different Sr content. The data are derived by Smolin *et al.*[12] Schematic density of states and optical transition of $LaFeO_3$ and $La_{1-x}Sr_xFeO_{3-\delta}$ based on literature experimental and computational results.[10–15]

Since these thin films were oxidized in ozone prior to the measurements, the Sr content is expected to be mainly compensated by the creation of electron holes. These holes in LSF are partially localized on the Fe and partially on the O, due to the strong hybridization of the O 2p – Fe 3d orbitals.[14–16] As can be seen in the figure, three main features can be observed (A, B and C). The absorption intensities of transition A and B progressively increase with hole doping while transition C tends to decrease. The origin of transition A was attributed to strong localization effects of electronic holes, which impede the instauration of a metallic behaviour and give rise to an empty O 2p-Fe e_g band above the Fermi level.[14,16] Indeed, this transition is not present in $LaFeO_3$, where there are no nominal holes. Increasing the divalent doping in the system generates a rise of optical absorption in the low energy range, due to an increase of available states in the hole-induced empty band. Transition B is thought to be originated by an electron transfer from majority spin Fe e_g band towards the minority t_{2g} empty band.[11] Increasing the hole doping, the valence band moves towards higher energy and increase its t_{2g} character, lowering the band-gap and increasing the intensity of this feature. Finally, the transition C is probably originated by multiple transfers from O-2p states below the fermi level towards minority spin e_g band.[11] The decrease observed rising the Sr content

is not fully understood yet but it is probably related to the opposite increase of B feature (similar to the optical absorption trend observed in Chapter **6** for LSMC thin films increasing the Co content). **Figure B.1b** shows a sketch of the optical transitions in $LaFeO_3$ and $La_{1-x}Sr_xFeO_{3-\delta}$ materials. In conclusion, $La_{1-x}Sr_xFeO_{3-\delta}$ appears as a promising material for the in-situ optical study of point defect concentration as a function of pO_2.

B.3 Deposition and characterization of $La_{0.8}Sr_{0.2}FeO_{3-\delta}$ thin films

Thin films of $La_{0.8}Sr_{0.2}FeO_{3-\delta}$ (LSF) were deposited by LA-PLD on single crystal Sapphire (0001) substrates at 700ºC and under an oxygen pressure of $6.7 \cdot 10^{-3}$ mbar (see more details in Chapter **2**). The number of laser pulses was regulated to obtain a thickness of ~30 nm, which was then confirmed by ellipsometry. The structure of the thin films was study by XRD and AFM. The XRD analysis revealed a single phase pseudo-cubic polycrystalline structure, characterized by a lattice parameter of 3.93 Å (see **Figure B.2a**). The AFM study confirmed the polycrystalline nature of the layers and proved the high quality and smoothness of the LSF films deposited (see **Figure B.2b**). The cationic composition of the thin films was studied by EDS. The analysis showed that nearly stoichiometric thin films with a cationic ratio of Fe/(La+Sr)= 0.98 ± 0.04 were obtained. Please note that, contrary to the LSM thin films studied in the main text of the thesis, these LSF layers were deposited at lower oxygen pressure, which allowed reducing the B site deficiency. Overall, the thin films of LSF deposited are suitable for the ellipsometry *in-situ* study.

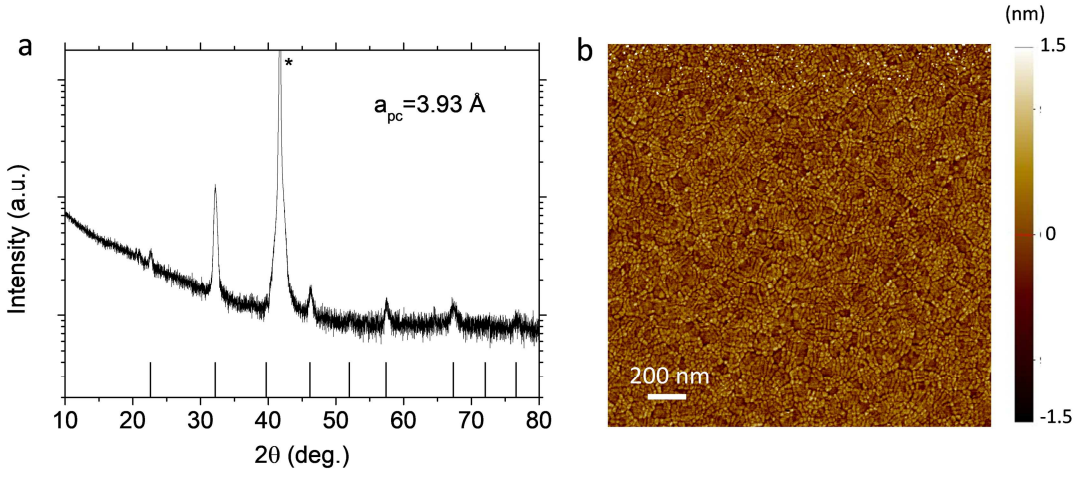

Figure B.2 a, XRD of the LSF thin films deposited on Sapphire (0001). The asterisk indicates the position of the substrate peak. The vertical lines refer to a cubic LSF structure with lattice parameter equal to 3.93 Å. **b**, AFM image of the surface of the LSF layer.

B.4 *In-situ* ellipsometry study of pO_2 behaviour

The *in-situ* ellipsometry study was carried out with the experimental setup described in Chapter **2**. The optical spectra were measured at 673 K as a function of the pO_2 in a Linkam chamber (1 - $3 \cdot 10^{-4}$ bar). The electrical resistivity of the thin films was measured by Van Der Pauw method during the optical measurements. **Figure B.3** shows the raw measurements of two vectoral components of the reflected light (I_c, I_s) recorded during the experiment (see Chapter **2** for more details on the technique). These spectra were measured after waiting for the stabilization of the thin films, which was confirmed by the electrical measurements. Both the recorded light intensities (I_c, I_s) show a relevant variation during the oxidation/reduction process, meaning that ellipsometry is indeed sensitive to the variation of point defect concentration in the LSF thin films.

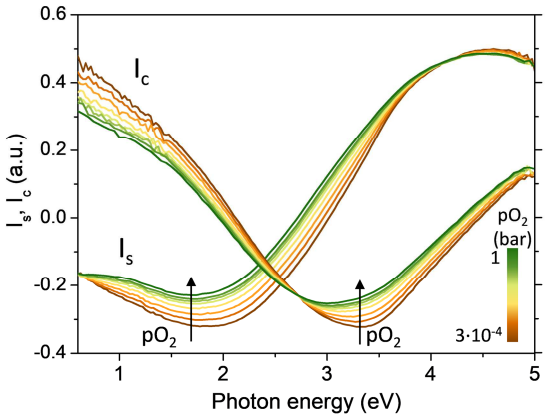

Figure B.3 Raw ellipsometry data of the LSF thin films on sapphire (0001) measured at 673 K as a function of pO_2.

The raw data were then fitted by the procedure explained in Chapter **2** and the optical constants of the material were extracted. The optical properties of LSF were simulated by 5 Lorentzian oscillators, in agreement with literature.[10] **Figure B.4** shows the optical conductivities extracted from the fittings of the raw spectra. In this study, the optical conductivity was preferred over the optical absorption because the transitions are better defined in this notation. Nevertheless, the trends described in the following yield to the same results for the two parameters. As it can be observed in **Figure B.4a**, substantial modifications of the optical properties take place when decreasing the oxygen partial pressure. In detail, the low energy transitions A and B progressively decreases their intensity lowering the pO_2 while the transition C tends to grow. The trend observed is analogous to the variation described in section **B.2** for $La_{1-x}Sr_xFeO_{3-\delta}$ thin films with different Sr content, which was ascribed to a variation of the electron holes in the system. Therefore, decreasing the pO_2 appears to lower the concentration of electronic holes, in agreement with the expected defect chemistry model described in Chapter **1**.

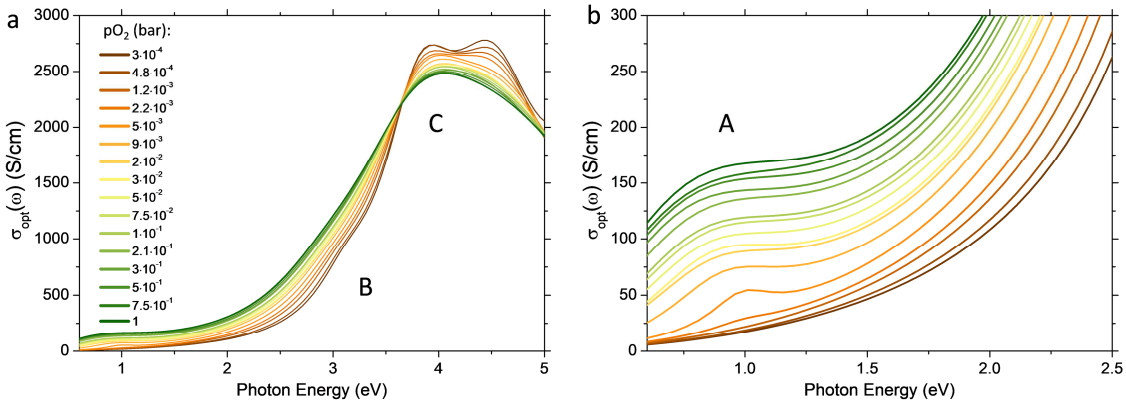

Figure B.4 a, optical conductivity of LSF thin films at 673 K as a function of pO_2. In **b**, a magnification of the low energy transition A is shown.

In order to offer more insights into the behaviour of the different transitions, the optical conductivity values at 4 different energies (1 eV, 3 eV, 3.8 eV and 4.5 eV) has been extracted and plotted against the pO_2 (see **Figure B.5**). It is possible to observe that all the transitions present a linear behaviour in a log-log plot, meaning that the optical conductivity is linked to the pO_2 with a power law ($\sigma_{opt} \propto (pO_2)^m$). The highest sensitivity is measured at low energy (1 eV), while the higher energy transitions presents progressively less pronounced slopes. Also, it is possible to note that an apparent change in behaviour is detected for the 1 eV optical conductivity at *ca.* 10^{-2} bar. Nevertheless, this is believed to be an artefact of the fitting, since for this oxygen partial pressure, the Lorentzian element inserted in the model following the transition A presents a very small intensity, likely losing its ability to correctly reproduce the raw data. Indeed, the fittings with and without this element yield to basically the same overall error for $pO_2 < 10^{-2}$ bar.

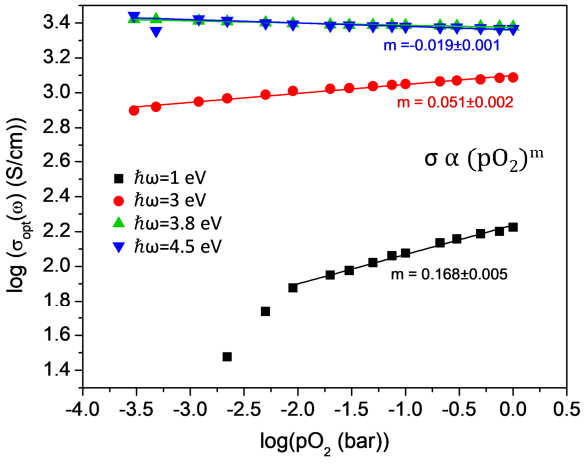

Figure B.5 Optical conductivity measured at four different energy (1 eV, 3 eV, 3.8 eV and 4.5 eV) plotted against the pO_2 in the chamber.

It is necessary to note that the behaviour shown in **Figure B.5** for the singular energies may represent a convolution among different transitions. For this reason, the evolution

of the first oscillator (corresponding to transition A) with the pO_2 has been extracted in **Figure B.6a**. This feature has been chosen because it is well separated from the others and because it is expected to be directly proportional to the concentration of holes in the system (see Section **B.2**). **Figure B.6b** shows the pO_2 behaviour of the maximum of conductivity of the transition A depicted in a log-log plot (blue dots). In this case, a slope of m = 0.22 ± 0.01 is obtained, confirming that the conductivity directly extracted from 1 eV was indeed convoluted with other high energy transitions (see **Figure B.4b**). Moreover, the slope observed is very similar to the variation of holes predicted by the defect chemistry model (m=1/4, see Chapter **1**), endorsing the hypothesis that transition A is directly related to a hole induced empty band above the fermi level.

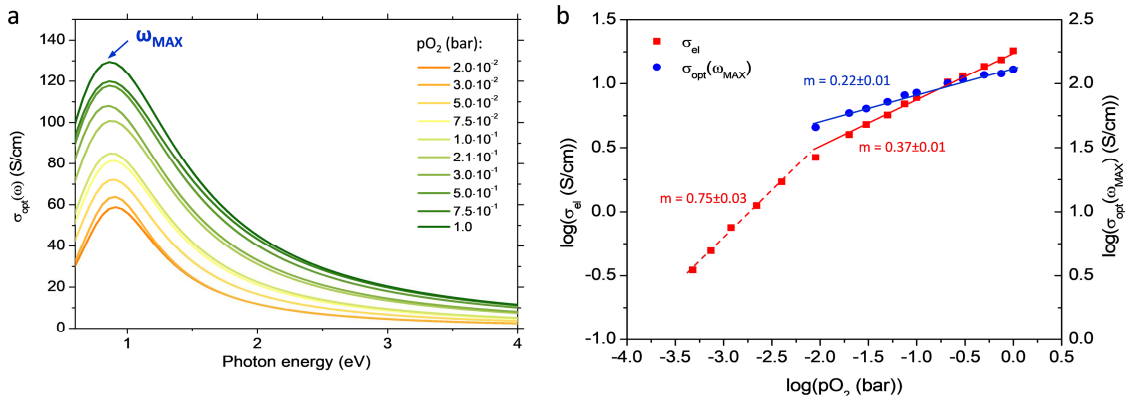

Figure B.6 a, Evolution of optical transition A as a function of pO_2. **b**, Maximum of optical conductivity of transition A (blue dots) and electrical conductivity (red squares) plotted against the pO_2 in the chamber.

Figure B.6b also shows the in-plane electronic conductivity measured *in-situ* in the ellipsometry chamber (red squares). Two unexpected features can be distinguished. First, for pO_2 higher than 10^{-2} bar, the slope observed is higher than the one expected from the defect chemistry (and the one observed for the optical conductivity). Second, for pO_2 lower than 10^{-2} bar, an unreported slope near 0.75 is found. In order to study this unusual behaviour, the pO_2 behaviour of the electrical conductivity of LSF thin films was studied in a dedicated experiment at different temperatures (see **Figure B.7**). Here, it can be noted that decreasing the temperature the m=0.75 behaviour starts at higher pO_2, basically occupying the entire oxygen partial pressure range at 300 ºC.

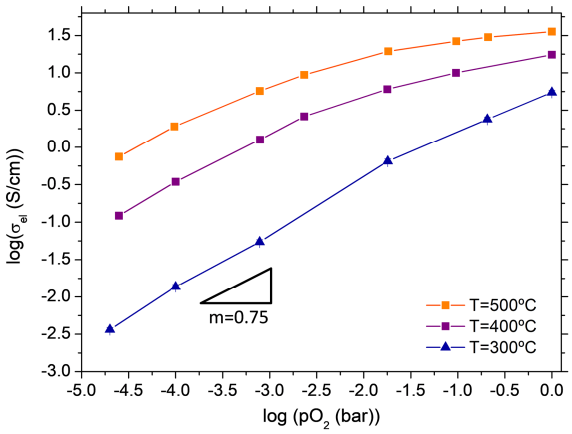

Figure B.7 In-plane electronic conductivity of LSF thin films measured at different temperatures as a function of pO_2.

The origin of this trend is out of the scope of this appendix, but it is noted that it is probably linked to a variation of charge carrier mobility taking place while modifying the point defect concentration. Indeed, we measured that the layers stabilized at 300ºC in oxygen present an activation energy for polaron transport of ~0.41 eV while the one stabilized at $pO_2=10^{-4}$ bar of ~0.56 eV.* This trend is in agreement with literature measurements of bulk $La_{1-x}Sr_xFeO_{3-\delta}$, where it was found that, increasing the Sr content, the energy barrier for polaron motion substantially decreases.[17] Therefore, it appears that in $La_{1-x}Sr_xFeO_{3-\delta}$ the polaron hopping energy is not constant but strongly depends on the electronic structure of the oxide. The change of activation energy also explains why the effect is more evident at lower temperature. Additionally, it must be noted that these films are far more reducible than literature bulk samples. For instance, if one calculates the defect concentration at 300 ºC using the entropy and enthalpy values of the equilibrium constants measured by Song *et al.*,[18] no variation of holes concentration are expected in the pO_2 window analysed here (pO_2= 1 - 10^{-5} bar). Therefore, the large change of conductivity measured appears even more peculiar and may reveal a substantial difference between thin films and bulk materials. More work is currently ongoing to understand this effect.

Finally, also the bandgaps of the various optical transitions can be used to track the presence of holes in the system. As can be observed from **Figure B.4,** the intermediate energy transition B varies not just in intensity but also its position when decreasing the pO_2. The onset energy of this transition has been calculated by linear extrapolation in a Tauc plot, see **Figure B.8a**. According to literature, the transition B has a direct forbidden character, due to the d-d nature of this feature that present Fe 3d states both in the valence and in the conduction band.[11] Therefore, a Tauc plot exponential of 3/2 has

* These measurements were performed stabilizing the sample at 300 ºC in different oxygen environments and decreasing the temperature while measuring the electrical resistivity in the thin films. The results were fitted by non-adiabatic polaron hopping and the activation energy was then extracted, in accordance with Xie *et al.*[19]

been used. **Figure B.8b** shows that the optical spectra progressively increases their band gap while decreasing the hole concentration in the system.

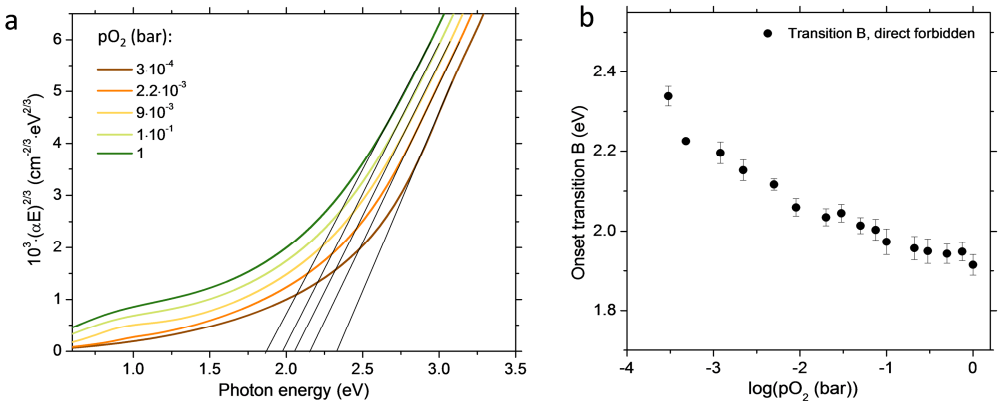

Figure B.8 a, Tauc plot of direct forbidden transition B for a selection of pO_2 at 673 K. The results obtained by the linear extrapolation of the Tauc plot are shown in **b** as a function of pO_2.

In order to confront the results obtained with the literature data, the optical absorption of two samples annealed respectively at 673 K in oxygen and at 673 K under 100 ppm of oxygen ($pO_2=10^{-4}$) was measured at room temperature (RT), see **Figure B.9a**. For comparison, two literature $La_{1-x}Sr_xFeO_{3-\delta}$ thin films with x=0 and x=0.17 are also reported in the figure.[12] The confrontation has been made at RT because, to the best knowledge of the author, no data are available for $La_{1-x}Sr_xFeO_{3-\delta}$ at 673 K. It is possible to note that the three transitions (A, B and C) are similar in the case of oxidized sample and x=0.17 literature layer as well as reduced film and undoped $LaFeO_3$ (x=0). Additionally, the bandgap of the transition B was calculated for the different films (see the Tauc plot in the inset of **Figure B.9a**).[11] Considering the literature thin films as fully oxidized, **Figure B.9b** shows the effect of hole doping on the onset of transition B. Here, due to the previous considerations, the LSF film annealed in air is considered to be entirely hole compensated ($[h^{\bullet}]=0.2$) and the one annealed under 100 ppm of oxygen completely oxygen vacancy compensated ($[h^{\bullet}]\sim0$). The good match between the band-gaps obtained varying the Sr content by Wang *et al.*[16] and Smolin *et al.*[12] and the films measured in this work after different annealing treatments suggests that the reducing conditions at 673 K effectively removes all the holes in the thin films, giving rise to an electronic structure similar to the undoped $LaFeO_3$. These measurements indicate that also the band-gaps may be used to get insights into the holes concentration in LSF thin films.

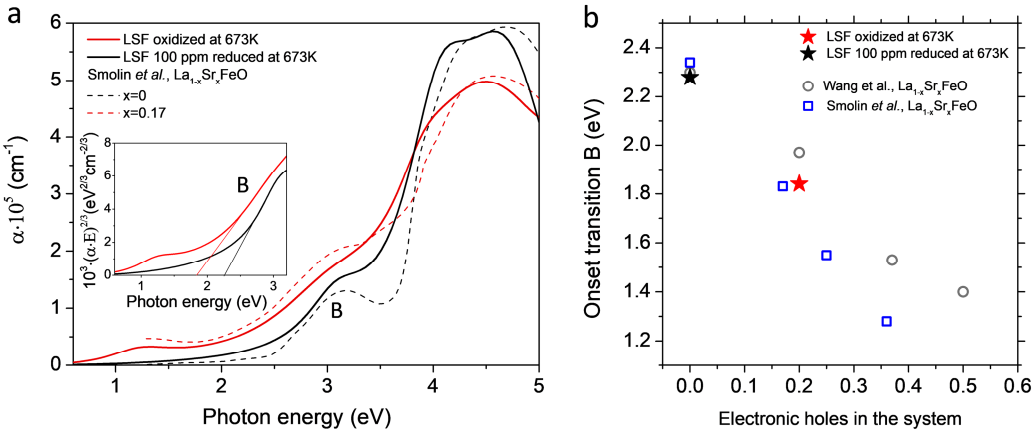

Figure B.9 a, Optical absorption of two LSF thin films measured at RT after an annealing at 673 K in oxygen and under 100 ppm of oxygen. Data corresponding to $La_{1-x}Sr_xFeO_{3-\delta}$ thin films with x=0 and x=0.17 from Smolin *et al* are also reported for comparison.[12] The inset shows the Tauc plot used for obtaining the band-gap of transition B. **b**, Onset transition of transition B obtained for the reduced and oxidized samples as a function of electronic holes in the system. The band-gaps measured by Wang *et al.*[16] and Smolin *et al.*[12] are also reported for comparison.

B.5 Conclusions and future work

In this appendix, it was shown that ellipsometry can be used to track the defect chemistry of LSF thin films. All the different optical transitions in the LSF spectra show an evolution with pO_2, related to the variation of electronic holes in the system. Decreasing the pO_2, the optical features undergoes through a change of both the absorption intensity and the bandgap, which can be used to track the presence electronic defects in the thin films. In detail, the low energy transition A was observed to vary its intensity with the pO_2 with a log-log slope of m = 0.22, similar to the hole concentration behaviour expected from defect chemistry model (m = 0.25). Moreover, also the bandgap of energy transition B was found to be sensitive to the holes concentration in the system, increasing its energy during the thin film reduction. The confrontation with literature $La_{1-x}Sr_xFeO_{3-\delta}$ thin films suggests that the Sr doping and the oxidation/reduction of LSF thin films have similar effect on the electronic transitions, which appear linked to the hole concentration in the system.

More work is needed to fully understand the impact of electronic holes on the high temperature optical properties of LSF thin films. In order to being able to offer a quantification of the point defects, films with different Sr content must be deposited and characterized. Moreover, epitaxial thin films must be considered to exclude grain boundary effects on the in-plane electronic conductivity. In this way, it may also be possible to understand the remarkable steep behaviour (m=0.75) measured for the electronic conductivity varying the pO_2 at low temperature. All considered, ellipsometry is presented as a promising tool for studying the point defect concentration in oxide thin films at low to intermediate temperature.

References

1. Patrakeev, M. V., Leonidov, I. A., Kozhevnikov, V. L. & Poeppelmeier, K. R. p-type electron transport in $La_{1-x}Sr_xFeO_{3-\delta}$ at high temperatures. *J. Solid State Chem.* **178,** 921–927 (2005).
2. Schmid, A., Rupp, G. M. & Fleig, J. Voltage and partial pressure dependent defect chemistry in (La,Sr)FeO3-δ thin films investigated by chemical capacitance measurements. *Phys. Chem. Chem. Phys.* **20,** 12016–12026 (2018).
3. Fleig, J. *et al.* The Chemical Capacitance as a Fingerprint of Defect Chemistry in Mixed Conducting Oxides. *Acta Chim. Slov.* 509–518 (2016). doi:10.17344/acsi.2016.2302
4. Chen, D., Bishop, S. R. & Tuller, H. L. Non-stoichiometry in Oxide Thin Films: A Chemical Capacitance Study of the Praseodymium-Cerium Oxide System. *Adv. Funct. Mater.* **23,** 2168–2174 (2013).
5. Merkle, R. & Maier, J. How Is Oxygen Incorporated into Oxides? A Comprehensive Kinetic Study of a Simple Solid-State Reaction with SrTiO3 as a Model Material. *Angew. Chemie Int. Ed.* **47,** 3874–3894 (2008).
6. Perry, N. H., Pergolesi, D., Bishop, S. R. & Tuller, H. L. Defect chemistry and surface oxygen exchange kinetics of La-doped Sr(Ti,Fe)O3−α in oxygen-rich atmospheres. *Solid State Ionics* **273,** 18–24 (2015).
7. Kim, J. J., Bishop, S. R., Chen, D. & Tuller, H. L. Defect Chemistry of Pr Doped Ceria Thin Films Investigated by in Situ Optical and Impedance Measurements. *Chem. Mater.* **29,** 1999–2007 (2017).
8. Stoerzinger, K. A. *et al.* Linking surface chemistry to photovoltage in Sr-substituted LaFeO3 for water oxidation. *J. Mater. Chem. A* **6,** 22170–22178 (2018).
9. Shao-Horn, Y. *et al.* Perovskites in catalysis and electrocatalysis. *Science (80-.).* **358,** 751–756 (2017).
10. Scafetta, M. D., Xie, Y. J., Torres, M., Spanier, J. E. & May, S. J. Optical absorption in epitaxial $La_{1-x}Sr_xFeO_3$ thin films. *Appl. Phys. Lett.* **102,** 081904 (2013).
11. Scafetta, M. D., Cordi, A. M., Rondinelli, J. M. & May, S. J. Band structure and optical transitions in LaFeO3: Theory and experiment. *J. Phys. Condens. Matter* **26,** (2014).
12. Smolin, S. Y. *et al.* Static and Dynamic Optical Properties of $La_{1-x}Sr_xFeO_{3-\delta}$: The Effects of A-Site and Oxygen Stoichiometry. *Chem. Mater.* **28,** 97–105 (2016).
13. Scafetta, M. D. & May, S. J. Effect of cation off-stoichiometry on optical absorption in epitaxial $LaFeO_3$ films. *Phys. Chem. Chem. Phys.* **19,** 10371–10376 (2017).
14. Wadati, H. *et al.* Strong localization of doped holes in $La_{1-x}Sr_xFeO_3$ from angle-resolved photoemission spectra. *Phys. Rev. B* **74,** 115114 (2006).
15. Wadati, H. *et al.* Hole-doping-induced changes in the electronic structure of $La_{1-x}Sr_xFeO_3$: Soft x-ray photoemission and absorption study of epitaxial thin films. *Phys. Rev. B - Condens. Matter Mater. Phys.* **71,** 1–7 (2005).
16. Wang, L. *et al.* Hole-induced electronic and optical transitions in $La_{1-x}Sr_xFeO_3$ epitaxial thin films. *Phys. Rev. Mater.* **3,** 1–8 (2019).
17. Jung, W. H. & Iguchi, E. Polaronic transport properties in $La_{1-x}Sr_xFeO_3$ systems (0.05<or=x<or=0.3). *J. Phys. Condens. Matter* **7,** 1215–1277 (1995).
18. Song, S.-J., Singh, B., Im, H.-N., Kim, I.-H. & Bae, H. Thermodynamic Quantities and Defect Chemical Properties of $La_{0.8}Sr_{0.2}FeO_{3-\delta}$. *J. Electrochem. Soc.* **165,** F641–F651

(2018).

19. Xie, Y. J. *et al.* Electronic phase diagram of epitaxial $La_{1-x}Sr_xFeO_3$ films. *Appl. Phys. Lett.* **105,** 062110 (2014).

C. Defect chemistry model of $La_{0.2}Sr_{0.8}MnO_{3\pm\delta}$

C.1 Introduction

The concentration of point defects in oxides strongly influences their oxygen transport, electronic, structural and magnetic properties. For this reason, defect chemistry models are fundamental for the understanding and the design of functional properties of these materials. In Chapter **1**, a qualitative defect chemistry model valid for the $La_{1-x}Sr_xMO_{3\pm\delta}$ perovskites family was presented.[1,2] Although this model has the advantage of offering a simple and correct overview of the point defects evolution as a function of the oxygen partial pressure (pO_2), for the quantification of defects concentration more sophisticated models must be considered.

In this appendix, the defect chemistry models presented by Poulsen[3] and Nowotny *et al.*[4] are considered for calculating the concentration of point defects of $La_{0.2}Sr_{0.8}MnO_{3\pm\delta}$ (LSM) at 923 K. The results were used as a reference in the main text of the thesis for comparing the expected behaviour of bulk stoichiometric LSM with the one observed in LSM_y thin films.

C.2 Calculation of defect concentration of LSM at 923 K

The main assumptions of the defect chemistry model are:[3] (i.) random distribution of point defects; (ii.) negligible association between the defects; (iii.) the presence of interstitial oxygen and cationic anti-site defects are not considered; (iv.) cationic ratio Mn/(La+Sr)=1; (v.) the electronic charges are localized on the Mn atoms (polaron model). The species contributing to the model are: $V_{La}^{'''}, La_{La}^{x}$ at the A site, $V_{Mn}^{'''}, Mn_{Mn}^{x}, Mn_{Mn}^{\bullet}, Mn_{Mn}^{'}$ at the B site and O_O^x, $V_O^{\bullet\bullet}$ at the oxygen site. The three chemical reactions involved in the defect equilibrium are shown in **Table C.1,** along with the equilibrium constant equations. One must note that other models in literature combines the Schottky reaction and the oxygen incorporation,[4,5] with overall reaction:

$$V_{Mn}^{'''} + V_{La}^{'''} + 3O_O^x + 6Mn_{Mn}^{\bullet} \leftrightarrow 6Mn_{Mn}^{x} + 3/2\ O_2 \qquad \text{Eq. C.1}$$

Nevertheless, the equilibrium constant of this reaction is equal to $K_2 = K_r^3/K_s$, meaning that considering equation **2.24** or the Schottky reaction is indeed equivalent.

Taking into account the additional charge and ion balances of **Table C.2**, the system has then 8 equations and 8 variables and can therefore be solved. The values of the equilibrium constants were extrapolated to 923 K from the corresponding enthalpy and entropy values measured by Nowotny *et al.*[4] ($K_r = 7.27 \cdot 10^{-12}, K_s = 8.69 \cdot 10^{-36}, K_i = 6 \cdot 10^{-2}$). The algorithm developed by Poulsen[3] was implemented in an excel data sheet for simplifying the calculation of the point defect concentration as a function of pO_2.

Table C.1 Main reactions involved in the defect equilibrium of LSM.

Phenomenon	Reaction	Equilibrium
Oxygen incorporation	$O_O^x + 2Mn_{Mn}^{\bullet} \leftrightarrow V_O^{\bullet\bullet} + 2Mn_{Mn}^x + 1/2\ O_2$	$K_r = \frac{[Mn_{Mn}^x]^2[V_O^{\bullet\bullet}]pO_2{}^{1/2}}{[O_O^x][Mn_{Mn}^{\bullet}]^2}$
Schottky-reaction	$nil \leftrightarrow 3V_O^{\bullet\bullet} + V_{Mn}'''' + V_{La}''''$	$K_s = [V_O^{\bullet\bullet}]^3[V_{Mn}''''][V_{La}'''']$
Charge disproportiona-tion	$2Mn_{Mn}^x \leftrightarrow Mn_{Mn}^{\bullet} + Mn_{Mn}'$	$K_i = \frac{[Mn_{Mn}^{\bullet}][Mn_{Mn}']}{[Mn_{Mn}^x]^2}$

Table C.2 Charge and ion balances of the LSM system.

Electroneutrality	$2[V_O^{\bullet\bullet}] + [Mn_{Mn}^{\bullet}] = [Sr_{La}^{`'}] + [Mn_{Mn}'] + [V_{Mn}''''] + [V_{La}'''']$
A-site balance	$[La_{La}^x] + [Sr_{La}^{`'}] + [V_{La}''''] = 1$
B-site balance	$[Mn_{Mn}^x] + [Mn_{Mn}^{\bullet}] + [Mn_{Mn}'] + [V_{Mn}''''] = 1$
O-site balance	$[V_O^{\bullet\bullet}] + [O_O^x] = 3$
Dopant content	$[La_{La}^x]/([La_{La}^x] + [Sr_{La}^{`'}]) = 0.2$

The Brouwer diagram of main species calculated at 923 K is shown in **Figure C.1a**. Three regimes can be observed. In oxidizing atmospheres ($pO_2 = 10^0 - 10^{-6}$ bar), the $[V_O^{\bullet\bullet}]$ is extremely low and the defects equilibrium is dominated by cation vacancies. This eventually give rise to a slight increase of $[Mn_{Mn}^{\bullet}]$, for compensating the additional negative charges. It is important to note that the cationic defects V_{Mn}'''' and V_{La}'''' are calculated to be present in the same concentration, since neither anti-site defect formation nor preferential vacancy specie equilibrium is considered. Decreasing the pO_2, the cation vacancies rapidly decrease and the system enters in a plateau ($pO_2 = 10^{-6} - 10^{-20}$ bar). In this region, the concentration of positive oxygen vacancies, which grows proportional to $(pO_2)^{1/2}$, is still not high enough to modify the Mn valence. For low values of pO_2 ($pO_2 < 10^{-20}$ bar), $[V_O^{\bullet\bullet}]$ starts to be relevant, giving rise to an increase of Mn_{Mn}' and a decrease of $Mn_{Mn}^{\bullet}$ as a mechanism of compensation of the new positive charges introduced in the system. **Figure C.1b** shows an enlargement of the Brouwer diagram for the high values of species concentration. These results are used as a bulk reference to compare the evolution of in-plane electrical conductivity (chapter **4**) and out of plane oxygen diffusion (chapter **5**) in the LSM_y thin films, as a function of pO_2.

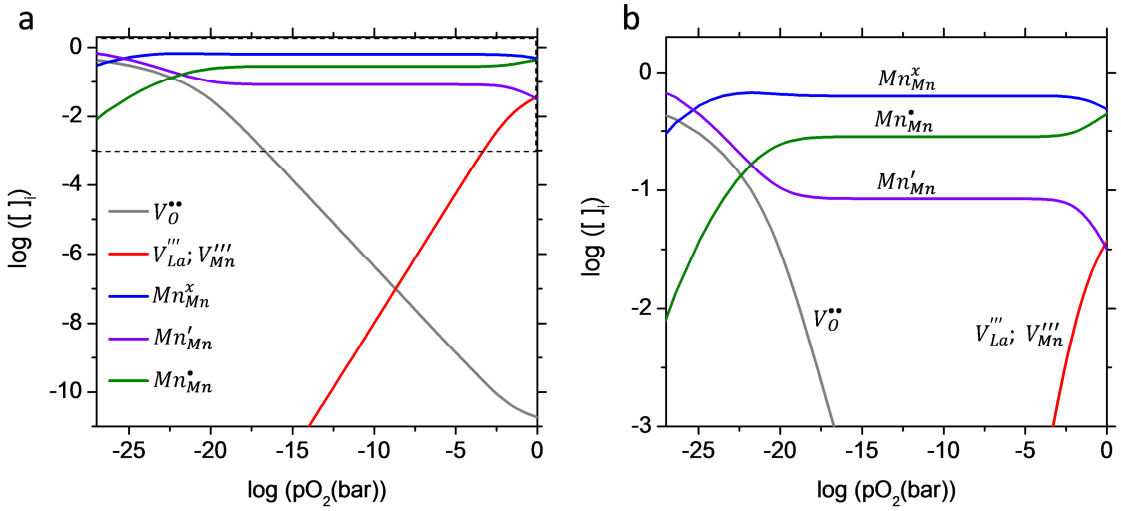

Figure C.1 a, Brouwer diagram of bulk LSM calculated extrapolating Nowotny *et al.*[4] equilibrium constants to 923 K. **b**, enlargement of the black dashed square depicted in **a**.

References

1. Anderson, H. U., Zhou, X.-D. & Dogan, F. in *Mixed Ionic Electronic Conducting Perovskites for Advanced Energy Systems* (eds. Orlovskaya, N. & Browning, N.) 303–312 (Springer Netherlands, 2004). doi:10.1007/978-1-4020-2349-1_30

2. Anderson, H. U. Defect chemistry of p-type perovskites. in *Proceedings of the 14th Risø International Symposium on Materials Science* (eds. Poulsen, F. W., Bentzen, J. ., Jacobsen, T., Skou, E. & Østergard, M. J. .) 1–18 (The Electrochemical Society, 1994).

3. Poulsen, F. Defect chemistry modelling of oxygen-stoichiometry, vacancy concentrations, and conductivity of $(La_{1-x}Sr_x)_yMnO_{3+\delta}$. *Solid State Ionics* **129,** 145–162 (2000).

4. Nowotny, J. & Rekas, M. Defect Chemistry of (La,Sr)MnO_3. *J. Am. Ceram. Soc.* **81,** 67–80 (1998).

5. Mizusaki, J. *et al.* Oxygen nonstoichiometry and defect equilibrium in the perovskite-type oxides $La_{1-x}Sr_xMnO_{3+d}$. *Solid State Ionics* **129,** 163 (2000).

Scientific Contributions

Publications

Peer-reviewed scientific journals

1. F. Chiabrera, I. Garbayo, D. Pla, M. Burriel, F. Wilhelm, A. Rogalev, M. Núñez, A. Morata, A. Tarancón, Unraveling bulk and grain boundary electrical properties in $La_{0.8}Sr_{0.2}Mn_{1-y}O_{3\pm\delta}$ thin films, *APL Materials* 7 (2019) 013205

2. F. Chiabrera, I. Garbayo, L. López-Conesa, G. Martín, A. Ruiz-Caridad, M. Walls, L. Ruiz-González, A. Kordatos, M. Núñez, A. Morata, S. Estradé, A. Chroneos, F. Peiró, A. Tarancón*;* Engineering Transport in Manganites by Tuning Local Nonstoichiometry in Grain Boundaries*, Advanced Materials*, 31 (2018) 1805360

3. A. M. Saranya, A. Morata, D. Pla, M. Burriel, F. Chiabrera, I. Garbayo, A. Hornés, J. A. Kilner and A. Tarancón, Unveiling the Outstanding Oxygen Mass Transport Properties of Mn-Rich Perovskites in Grain Boundary-Dominated $La_{0.8}Sr_{0.2}(Mn_{1-x}Co_x)_{0.85}O_{3\pm\delta}$ Nanostructures*, Chemistry of Materials*, 30, (2018) 5621−5629

4. F. Chiabrera, A. Morata, M. Pacios, A. Tarancón, Insights into the enhancement of oxygen mass transport properties of strontium-doped lanthanum manganite interface-dominated thin films*, Solid State Ionics*, 299 (2017) 70-77

Chapters in books

1. F. Chiabrera, I. Garbayo, A. Tarancón, Nanoionics And Interfaces For Energy And Information Technologies, a chapter in: Metal Oxide-Based Thin Film Structures, 409-439, Elsevier, 2018

Conference proceedings

1. F. Chiabrera, I. Garbayo, N. Alayo, A. Tarancón, Micro Solid Oxide Fuel Cells: A New Generation Of Micro-Power Sources For Portable Applications, *Proceedings of SPIE*, 10246, (2017)

2. A. Tarancón, A. Morata, D. Pla, A. M. Saranya, F. Chiabrera, I. Garbayo, A. Cavallaro, J. Canales-Vázquez, J. A. Kilner, and M. Burriel, Grain Boundary Engineering to Improve Ionic Conduction in Thin Films for micro-SOFCs, *ECS Transactions* 69 (2015) 1256-1262

Contributions in meetings and conferences[1]

1. N. Alayo, I. Garbayo, M. Bianchini, F. Chiabrera, M. Salleras, L. Fonseca, A. Tarancón, Large area free-standing membranes supported by doped silicon slabs for micro power sources, 44th International Conference on Micro and Nanoengineering (MNE) 2018, Copenhagen (Denmark), Oral presentation.

2. F. Baiutti, A. Morata, N. Alayo, I. Garbayo, F. Chiabrera, L. Fonseca, J. R. Morante, A. Tarancón, Fully integrated electrochemical sensors: a disruptive alternative compatible with microelectronics procedures, 17th International Meeting on Chemical Sensors, Vienna (Austria), Oral presentation.

3. F. Chiabrera, I. Garbayo, A. Chroneos, A. Kordatos, L. López-Conesa, A. Morata, A. Ruiz-Caridad, S. Estradé, F. Peiró, A. Tarancón, Grain boundaries in strontium-doped lanthanum manganite thin films: the origin of mixed ionic-electronic conduction, EMRS Spring Meeting, Strasbourg (France), June 2018. Oral presentation.

4. F. Chiabrera, A. Hornés, I. Garbayo, A. Morata, A. Tarancón, Characterization of combinatorial $La_{0.8}Sr_{0.2}MO_{3\pm\delta}$ (M = Co, Mn, Fe) thin films for SOFC cathode materials, EMRS Spring Meeting, Strasbourg (France), June 2018. Poster.

5. I. Garbayo, F. Chiabrera, N. Alayo, A. Morata, A. Tarancón, Superior oxide-ion conducting thin film electrolytes for low temperature μSOFC operation, EMRS Spring Meeting, Strasbourg (France), June 2018. Oral presentation.

6. F. Chiabrera, L. López-Conesa, I. Garbayo, A. Morata, A. Ruiz-Caridad, S. Estradé, F. Peiró, A. Tarancón, Grain boundary dominated strontium-doped lanthanum manganite thin films for enhanced mixed ionic-electronic conduction properties, COST TO-BE Spring Meeting, Sant Feliu de Guìxols (Spain), March 2018. Poster.

7. I. Garbayo, F. Chiabrera, N. Alayo, A. Morata, A. Tarancón. $Bi_2V_{0.9}Cu_{0.1}O_{5.35}$ thin films as alternative electrolytes for low temperature μSOFC, COST TO-BE Spring Meeting, Sant Feliu de Guìxols (Spain), March 2018. Poster.

8. N. Alayo, T. Leung, I. Garbayo, F. Chiabrera, A. Morata, A. Tarancón, Micro Solid Oxide Fuel Cells, towards a new generation of miniaturized portable power generators, MNE 2017, Braga (Portugal), September 2017. Oral presentation.

9. I. Garbayo, F. Chiabrera, N. Alayo, A. Morata, A. Tarancón, Advances in silicon-integrated Micro Solid Oxide Fuel Cells: Towards a new family of ultra-

[1] In this section, the underlining specifies the presenting author

thin portable power sources. XXVI International Materials Research Congress, Cancún (Mexico), August 2017. Invited talk.

10. I. Garbayo, F. Chiabrera, N. Alayo, A. Morata, A. Tarancón, BICUVOX materials for low temperature μ-solid oxide fuel cells. 3rd Functional Oxide Thin Films for Advanced Energy and Information Technology Conference, Rome (Italy), July 2017, Poster.

11. I. Garbayo, F. Chiabrera, N. Alayo, A. Morata, A. Tarancón, Revisiting classical superior ionic conducting materials for low temperature μSOFC. 21st International Conference on Solid State Ionics, Padua (Italy), June 2017. Poster.

12. F. Chiabrera, A. M. Saranya, D. Pla, A. Morata, A. Cavallaro, J. Canales-Vázquez, L. López-Conesa, A. Ruiz-Caridad, S.Estradé, F. Peiró, J. A. Kilner, M. Burriel, A. Tarancón, Interface-dominated MIECs for integration in solid state ionics device. 21st International Conference on Solid State Ionics, Padua (Italy), June, 2017. Invited talk.

13. F. Chiabrera, L. López-Conesa, A. Morata, A. Ruiz-Caridad, S. Estradé, F. Peiró, A. Tarancón, Grain boundary dominated thin films of strontium-doped lanthanum manganite for μSOFCs, 10th International Conference on Diffusion in Materials (DIMAT), Haifa (Israel), May 2017. Oral presentation.

14. F. Chiabrera, I. Garbayo, N. Alayo, A. Tarancón, Micro solid oxide fuel cells: a new generation of micro-power sources for portable applications, SPIE Microtechnologies, Barcelona (Spain), May 2017. Invited talk.

15. F. Chiabrera, I. Garbayo, N. Alayo, A. M. Saranya, D. Pla, A. Morata , M. Salleras, A. Cavallaro, J. Canales-Vázquez, L. López-Conesa, A. Ruiz-Caridad, S.Estradé, F. Peiró, J. A. Kilner, M. Burriel, L. Fonseca, A. Tarancón, Towards a new generation of fully integrated in silicon solid state devices based on Interface-dominated MIECs, International FOSXI conference, Vienna (Austria), May 2017. Invited talk.

16. F. Chiabrera, A. Saranya, D. Pla, A. Morata, A. Cavallaro, J. Canales-Vazquez, J. Kilner, M. Burriel, A.Tarancón, Oxygen transport phenomena at the grain boundary level in MIEC thin films, Electronic material and Applications meeting, Orlando (Florida), January 2017. Invited talk.

17. F. Chiabrera, I. Garbayo, D. Pla, M. Salleras, J. R. Morante, A. Tarancón, A. Morata, Micro lambda sensor based on free standing YSZ thin membranes integrated on micro machined Silicon platforms, COST TO-BE FALL MEETING, Ljubljana (Slovenia), September 2016. Poster.

18. I. Garbayo, D. Pla, F. Chiabrera, M. Salleras, L. Fonseca, A. Morata, A. Tarancón, Integration of thin film functional oxides for micro Solid Oxide Fuel

Cells applications, COST TO-BE FALL MEETING, Ljubljana (Slovenia), September 2016. Oral presentation.

19. F. Chiabrera, A. M. Saranya, D. Pla, A. Morata , A. Cavallaro, J. Canales-Vázquez, J. A. Kilner, M. Burriel, A. Tarancón, Interface dominated thin films of strontium-doped lanthanum manganite for micro electrochemical devices, COST TO-BE FALL MEETING, Ljubljana (Slovenia), September 2016. Oral presentation.

20. A. Tarancón, A. Morata, D. Pla, A. M. Saranya, F. Chiabrera, I. Garbayo, A. Cavallaro, J. Canales-Vázquez, J. A. Kilner, and M. Burriel, Grain Boundary Engineering of Oxide Thin Films for Improving their Performance in Solid State Devices, 2nd Functional Oxide Thin Films for Advanced Energy and Information Technology Conference, Cancun (Mexico), March 2016, Invited talk.

21. A. M. Saranya , D. Pla , A. Morata , A. Cavallaro , J. Canales-Vázquez , F. Chiabrera, J. A. Kilner , M. Burriel, A. Tarancón, Artificial mixed ionic electronic conductors by grain boundary engineering, EMRS Spring meeting, Lille (France), May 2016. Invited talk.

22. D. Pla, A. Morata, A. M. Saranya, A. Cavallaro, J. Canales-Vázquez, F. Chiabrera, J. A. Kilner, M. Burriel, A. Tarancón, Evaluation of the Mass Transport Properties of $La_{0.8}Sr_{0.2}MnO_{3\pm\delta}$ nanostructures by Finite Element Method (FEM) Simulations, EMRS Spring meeting, Lille (France), May 2016. Poster.

23. F. Chiabrera, I. Garbayo, D. Pla, M. Salleras, J. R. Morante, A. Tarancón, A. Morata, Free standing YSZ thin membranes integrated on micro machined Silicon platforms for Oxygen sensors and μSOFC, EMRS Spring meeting, Lille (France), May 2016. Poster.